NASA/CR-2003-208934

National Aeronautics and Space Administration/ American Society of Engineering Education Summer Faculty Fellowship Program – 2000

Richard B Bannerot, Editor
University of Houston
Houston, Texas

Donn G. Sickorez, Editor
Lyndon B. Johnson Space Center
Houston, Texas

March 2003

The NASA STI Program Office . . . in Profile

Since its founding, NASA has been dedicated to the advancement of aeronautics and space science. The NASA Scientific and Technical Information (STI) Program Office plays a key part in helping NASA maintain this important role.

The NASA STI Program Office is operated by Langley Research Center, the lead center for NASA's scientific and technical information. The NASA STI Program Office provides access to the NASA STI Database, the largest collection of aeronautical and space science STI in the world. The Program Office is also NASA's institutional mechanism for disseminating the results of its research and development activities. These results are published by NASA in the NASA STI Report Series, which includes the following report types:

- TECHNICAL PUBLICATION. Reports of completed research or a major significant phase of research that present the results of NASA programs and include extensive data or theoretical analysis. Includes compilations of significant scientific and technical data and information deemed to be of continuing reference value. NASA's counterpart of peer-reviewed formal professional papers but has less stringent limitations on manuscript length and extent of graphic presentations.

- TECHNICAL MEMORANDUM. Scientific and technical findings that are preliminary or of specialized interest, e.g., quick release reports, working papers, and bibliographies that contain minimal annotation. Does not contain extensive analysis.

- CONTRACTOR REPORT. Scientific and technical findings by NASA-sponsored contractors and grantees.

- CONFERENCE PUBLICATION. Collected papers from scientific and technical conferences, symposia, seminars, or other meetings sponsored or cosponsored by NASA.

- SPECIAL PUBLICATION. Scientific, technical, or historical information from NASA programs, projects, and mission, often concerned with subjects having substantial public interest.

- TECHNICAL TRANSLATION. English-language translations of foreign scientific and technical material pertinent to NASA's mission.

Specialized services that complement the STI Program Office's diverse offerings include creating custom thesauri, building customized databases, organizing and publishing research results . . . even providing videos.

For more information about the NASA STI Program Office, see the following:

- Access the NASA STI Program Home Page at ***http://www.sti.nasa.gov***

- E-mail your question via the Internet to help@sti.nasa.gov

- Fax your question to the NASA Access Help Desk at (301) 621-0134

- Telephone the NASA Access Help Desk at (301) 621-0390

- Write to:
  NASA Access Help Desk
  NASA Center for AeroSpace Information
  7121 Standard
  Hanover, MD 21076-1320

NASA/CR-2003-208934

National Aeronautics and Space Administration/ American Society of Engineering Education Summer Faculty Fellowship Program – 2000

Richard B Bannerot, Editor
University of Houston
Houston, Texas

Donn G. Sickorez, Editor
Lyndon B. Johnson Space Center
Houston, Texas

National Aeronautics and
Space Administration

Johnson Space Center
Houston, Texas 77058-3696

March 2003

Available from:

NASA Center for AeroSpace Information
7121 Standard
Hanover, MD 21076-1320

National Technical Information Service
5285 Port Royal Road
Springfield, VA 22161

This report is also available in electronic form at http://techreports.larc.nasa.gov/cgi-bin/NTRS

CONTENTS

MATHEMATICAL MODELING OF FOOD SUPPLY FOR LONG TERM SPACE MISSIONS USING ADVANCED LIFE SUPPORT

John Cruthirds
University of South Alabama
SF 5
10 August 2000

Vickie Kloeris
Space Human Factors Branch
Flight Projects Division
Space and Life Sciences Directorate

John Cruthirds

John Cruthirds

Vickie Kloeris

Vickie Kloeris

MATHEMATICAL MODELING OF FOOD SUPPLY FOR LONG TERM SPACE MISSIONS USING ADVANCED LIFE SUPPORT

Final Report

NASA/ASEE Summer Faculty Fellowship Program – 2000

Johnson Space Center

Prepared By:	John E. Cruthirds, Ph.D.
Academic Rank:	Associate Professor of Mathematics
University & Department:	University of South Alabama Department of Mathematics & Statistics Mobile, Alabama 36688

NASA/JSC

Directorate:	Space and Life Sciences
Division:	Flight Projects Division
Branch:	Space Human Factors
JSC Colleague:	Vickie Kloeris
Date Submitted:	August 10, 2000
Contract Number:	NAG 9-867

ABSTRACT

A habitat for long duration missions which utilizes Advanced Life Support (ALS), the Bioregenerative Planetary Life Support Systems Test Complex (BIO-Plex), is currently being built at JSC. In this system all consumables will be recycled and reused. In support of this effort, a menu is being planned utilizing ALS crops that will meet nutritional and psychological requirements. The need exists in the food system to identify specific physical quantities that define life support systems from an analysis and modeling perspective. Once these quantities are defined, they need to be fed into a mathematical model that takes into consideration other systems in the BIO-Plex. This model, if successful, will be used to understand the impacts of changes in the food system on the other systems and vice versa.

The Equivalent System Mass (ESM) metric has been used to describe systems and subsystems, including the food system options, in terms of the single parameter, mass. There is concern that this approach might not adequately address the important issues of food quality and psychological impact on crew morale of a supply of fresh food items. In fact, the mass of food can also depend on the quality of the food.

This summer faculty fellow project will involve creating an appropriate mathematical model for the food plan developed by the Food Processing System for BIO-Plex. The desired outcome of this work will be a quantitative model that can be applied to the various options of supplying food on long-term space missions.

INTRODUCTION

When humans conduct long range space missions such as the establishment of permanent bases on the Lunar surface or travel to Mars, they will continue to need food, water and air. For long term missions it will not be feasible to resupply these life support elements from Earth. Systems will need to be developed to produce food, purify the water supply and regenerate oxygen. Of significant importance is the development of agricultural systems to produce food, convert carbon dioxide to oxygen through photosynthesis, provide potable water through evapo-transpiration and recycle organic wastes.

The Bioregenerative Planetary Life Support Systems Test Complex (BIO-Plex) is a habitat for long duration missions which utilizes Advanced Life Support (ALS). In this system all consumables will be recycled and reused. In support of this effort, a menu is being planned utilizing ALS crops that will meet nutritional and psychological requirements. The baseline ALS crops are wheat, soybeans, peanuts, rice, potato, sweet potato and various salad plants.

The need exists in the food system to identify specific physical quantities that define life support systems from an analysis and modeling perspective. This model, if successful, will be used to understand the impacts of changes in the food system on the other systems and vice versa.

Within ALS the Equivalent System Mass (ESM) metric has been used to describe systems and subsystems, including the food system options, in terms of the single parameter, mass. The technique is described in the Baseline Values and Assumptions Document (BVAD) (Drysdale, et. al., June, 1999). It is possible this approach does not adequately address the important issues of food quality and psychological impact on crew morale of a supply of fresh food items.

The objective of the proposed project will be the development, within the ESM framework, of a quantitative modeling perspective relative to the food processing subsystem for long-term space missions. More precisely, work will proceed on two primary issues. Firstly, a modified computation of the ESM for wheat will be studied which adequately credits the air and water regeneration capabilities of the wheat crop. Such a modified ESM computation will be particularly useful in comparing different cultivars of wheat as potential ALS crops. Secondly, a food metric will be proposed which includes both food quality and the ESM metric as essential factors.

This report will conclude with a discussion of several topics for further study concerning the ALS food plan for long-term space missions.

MODIFIED ESM COMPUTATION FOR WHEAT

The standard ESM computation for food does not generally consider the air and water regeneration capabilities of crops being grown as part of the food system for a long duration space mission. A modification of the ESM computation will be introduced that hopefully gives adequate mass credits for air and water regeneration to crops. Data exists concerning the performance of wheat for air revitalization and food production during the Phase III test of the Lunar-Mars Life Support Test Project (Barta & Henderson, 1998). This data is a suitable basis for the study of wheat production during the BIO-Plex experiments, and, more generally, for the study of wheat production on the surface of the moon or Mars.

The Mars scenarios described in the Advance Life Support Systems Modeling and Analysis Reference Missions Document (JSC-39502) all include an approximate stay on the surface of 600 days. Consequently, the examples considered in this report will focus on a 600-day period of crop growth of wheat. The modified ESM for wheat will be denoted by ESM_{wheat} and the details of its computation follow.

Modified ESM for Wheat:

$ESM_{wheat} = M_E + Pow_P + V_P + \text{Biomass} - CO_2 \text{ Credit} - H_2O \text{ Credit}$, where

M_E = mass of equipment used for growing/harvesting the wheat crop

Pow_P = Power Mass Penalty based on the Advanced Life Support Systems Modeling and Analysis Reference Missions Document (JSC-39502)

V_P = Volume Mass Penalty based on the Advanced Life Support Systems Modeling and Analysis Reference Missions Document (JSC-39502)

Biomass = total mass of the wheat crop over the course of the mission

CO_2 Credit = mass credit for CO_2 uptake by the wheat crop computed using the Air data in the ALS Reference Missions document

H_2O Credit = mass credit for H_2O transpiration by the wheat crop computed using the Water data in the ALS Reference Missions document

It is appropriate to comment on the means by which these quantities will be computed. Some of the quantities will almost certainly be the same no matter which cultivar of wheat is grown. In particular, the same equipment will be used no matter which cultivar is used. Similarly, the power requirements of the wheat crop will likely be independent of the particular cultivar being grown. Consequently, M_E and Pow_P will be considered as constants that are independent of cultivar. M_E could at best be approximated at this stage since the particular equipment to be used in growing, maintaining, and harvesting wheat grown on the Mars surface has yet to be completely determined. In fact, perhaps a fractional amount, based on the portion of the growing area devoted to wheat, of the mass of the equipment might be more appropriate since it is reasonable to assume that crop-growing/harvesting equipment will be designed for more than one type of crop. Biomass for wheat can be easily computed by known characteristics of the particular cultivar of wheat being used. Much data is available concerning the Apogee wheat and a recent seminar held at Johnson Space Center by Dr. Bruce Bugbee (Bugbee, 2000) contained additional information about the Perigee wheat as a possible replacement for the Apogee wheat. V_P can readily be computed using the ESM volume mass penalty (9.08 kg/m^3) developed in the ALS Reference Missions document by simply computing the volume of the space taken up by the growing plants.

The CO_2 Credit is computed using the rate at which the wheat assimilates carbon dioxide per unit area per day (0.098 kg/m^2 per day for Apogee wheat (Barta and Henderson)) and the appropriate proportional amount of the ESM from Table 3.1.1 of Drysdale, Maxwell, et.al. for Air. A similar computation using the Water data from the same Table 3.1.1 together with the rate at which wheat transpires water (600 grams of water for each gram of seed yield (Bugbee)) is done to compute the value of the H_2O Credit. More precisely,

$$CO_2 \text{ Credit} = (0.098\ kg/m^2/day)*(\text{growing area})*(\text{total number of days})*(10.5/5760)$$

and

$$H_2O \text{ Credit} = 600*(\text{grain yield per day per } m^2)*(\text{growing area})*(\text{total number of days})*(3.8/64512)$$

It should be noted that a careful study of Table 3.1.1 of Drysdale, Maxwell, et.al. shows that 5760 kg of revitalized CO_2 (1 kg/person/day for a crew of 6 for 960 days) corresponds to an ESM for Air of 10.5 metric tons. In a similar way, 64512 kg of water (11.2 kg/person/day (based on Lange and Lin (1998)) for 6 people for 960 days) corresponds to an ESM value of 3.8 metric tons for Water. The units of CO_2 Credit and H_2O Credit will be metric tons. The data in Table 1 below will allow for a comparison of the ESM_{wheat} values for Apogee and Perigee wheat for a 600-day mission. In Table 1 the crop growing areas have been adjusted to produce the same total amount of grain yield for the two crops. The H_2O data in Table 1 comes form Dr. Bugbee's seminar, while the other Apogee data in Table 1 comes from the Phase III report of Barta and Henderson. It appears that the Perigee wheat has not yet been grown under the strict conditions under which the Apogee wheat was grown during the Phase III test, but Dr. Bugbee's seminar and a subsequent phone conversation with him lead to the data listed for Perigee. In particular, Perigee's grain yield and CO_2 uptake capability are assumed to be 90% of the corresponding figures for Apogee wheat.

Table 1. Summary of Apogee and Perigee Wheat Characteristics

characteristic	Apogee Wheat	Perigee Wheat
height	50 cm	45 cm
harvest index	35%	35%
grain yield	1.74 kg/m^2	1.57 kg/m^2
growing cycle	80 days	80 days
CO_2 uptake	0.098 kg/m^2/day	0.090 kg/m^2/day
H_2O transpiration	600∗(1.74/80 kg/ m^2/day)	600∗(1.57/80 kg/ m^2/day)
growing area	20 m^2	22.2 m^2
total harvest (600 d)	261 kg	261 kg

The information in Table 1 leads to the following computations:

Apogee wheat:

$$\begin{aligned}ESM_{wheat} = {} & M_E + Pow_P + (.00908\ MT/m^3)*(20\ m^2)*(.5\ m) + \\ & (600/80)*(1.74\ kg/m^2)(1/.35)*(20\ m^2) - \\ & (0.098\ kg/m^2\ /day)*(20\ m^2)*(600\ days)*(10.5\ MT/5760\ kg) - \\ & 600*(1.74/80\ kg/m^2/day)*(20\ m^2)*(600days)*(3.8\ MT/64512\ kg) \\ = {} & M_E + Pow_P + .0908 + .746 - 2.14 - 9.22\ \text{(metric tons)} \\ = {} & M_E + Pow_P - 10.52\ \text{(metric tons)}\end{aligned}$$

Perigee wheat:

$$\begin{aligned}ESM_{wheat} = {} & M_E + Pow_P + (.00908\ MT/m^3)*(22.2\ m^2)*(.45\ m) + \\ & (600/80)*(1.57\ kg/m^2)(1/.35)*(22.2\ m^2) - \\ & (0.090\ kg/m^2\ /day)*(22.2\ m^2)*(600\ days)*(10.5\ MT/5760\ kg) - \\ & 600*(1.57/80\ kg/m^2/day)*(22.2\ m^2)*(600days)*(3.8\ MT/64512\ kg) \\ = {} & M_E + Pow_P + .0907 + .747 - 2.19 - 9.24\ \text{(metric tons)} \\ = {} & M_E + Pow_P - 10.59\ \text{(metric tons)}\end{aligned}$$

Assuming Apogee and Perigee wheat have very similar nutritional values, and they are grown and harvested using the same types of equipment, the numbers above indicate that Perigee wheat would be a slightly better choice. In any event, the credits for air and water regeneration were significant factors.

DEVELOPMENT OF A FOOD METRIC

There are three primary variables to include in the design of a food metric which can be applied to any potential food plan for long duration space travel: nutritional value, palatability (sometimes called food quality), and variation in the diet. A Food Quality Index (*FQI*) rating will be introduced which includes these variables. Subsequent to that, a food metric will be proposed which includes the Food Quality Index and the ESM metric as essential factors.

Food Quality Index

The following letters represent the three key variables mentioned above.

- n denotes the nutritional value (based on RDA) of the food plan, where $0 < n \leq 10$.
- p denotes the palatability (based on a Hedonic scale) of the food plan, where $0 < p \leq 10$.
- v denotes the cycle length in days of the diet, where $0 < v \leq 20$.

We let *FQI* denote the Food Quality Index. It is defined as the function of the three variables n, p, v given by

$$FQI\,(n, p, v) = n * \text{Log}\,(p^{\sqrt{(5v)}})$$

Prior to an analytic study of *FQI*, it is appropriate to consider the qualitative properties of the above function. This function has value zero when $n = 0$ or $p = 1$, and has maximum value of 100 when $n = 10, p = 10, v = 20$. The *FQI* function places heavy emphasis on nutritional value n and diet cycle length v, but it is jointly dependent on all three variables. If any one of the three variables n, p, v are very low in value then the value of *FQI* is low. Algebraically, the Log (p) factor indicates that palatability values in the upper range of the scale are not considered significantly different from one another. Table 2 below contains a sampling of values of *FQI* for a variety of values of n, p, and v. The values in Table 2 are sorted by increasing *FQI* values and are used to indicate the general properties of the *FQI* rating. Some of the listed combinations of n, p, and v values (for example, $n = 2, p = 5, v = 8$) would not match an actual space mission food plan because of unacceptably low n or p values. It is important to demonstrate, however, that the proposed *FQI* gives low ratings to such combinations.

Table 2. Sample *FQI* Values for Various n, p, v Values

n	p	v	$FQI\,(n, p, v)$
4	1	3	0.00
8	1	20	0.00
2	5	8	8.84
7	6	1	12.18
8	10	1	17.89
7	2	20	21.07
6	4	7	21.37
5	5	10	24.71
8	10	3	30.98
7	8	5	31.61
8	10	5	40.00
8	10	6	43.82
8	10	8	50.60
10	7	10	59.76
8	7	20	67.61
10	7	18	80.17
10	7	20	84.51
10	9	20	95.42
10	10	20	100.00

The values in this table show, for example, that a food plan with $n = 8, p = 7, v = 20$ rates better than a plan with $n = 8, p = 10, v = 8$. The *FQI* rating is particularly valuable in rating one food plan against another. Since the *FQI* function is nonlinear it is not necessarily the case that a food plan with an *FQI* rating of, say 80, is twice as good as a food plan with an *FQI* rating of 40. However, the food plan with the higher rating would definitely be preferable to the one with the lower rating.

The *FQI* rating can be applied to a food system with prepackaged food as well as to a food system consisting of a mixture of fresh ALS crops and some amount of resupply items. In fact, the *FQI* rating can be applied to any food system as long as the appropriate values for $n, p,$ and v are obtained from the food science group.

Details of a Proposed Food Metric

A food metric based on the Equivalent System Mass (ESM) metric and the Food Quality Index (*FQI*) rating is proposed. It is reasonable to assume that as mass goes down the value of *FQI* does not increase. Consequently, the ratio of *FQI* to ESM will give a metric which rates highly food plans which simultaneously have low mass and high food quality index values. More precisely, denoting the food metric value by FMV, for a food plan A with ESM value E_A and *FQI* rating FQI_A the food metric computation for plan A is given by

$$\text{FMV for plan } A = \frac{FQI_A}{E_A}$$

In this computation the quantity E_A can be computed using the traditional ESM approach for prepackaged food systems or using the modified ESM method proposed in this document if there is a component of crop growth in the food plan. The units of ESM (usually, metric tons) and *FQI* are not the same but the magnitudes of their values are comparable. So, the value of FMV should be thought of as a numerical value to be used for comparison purposes when comparing one food plan against another. Higher FMV values are better in the sense that between two plans with equal mass factors the better plan is the one with higher *FQI*, and between two plans with equal *FQI* factors the better plan is the one with the lower mass.

CONCLUSIONS

The models proposed here are significant in that they contain the important factors of food quality and nutritional value as important components. The work described in this paper should be thought of as early work in the development of an appropriate mathematical model describing the food system for long duration space missions. A natural process in the formulation of a mathematical model is the testing and refinement of the proposed model. The models described here are ready to be studied carefully by means of the testing/refinement process. The traditional ESM metric does not sufficiently take the factors of food nutrition and quality into account. Consequently, a food metric that considers food quality and nutrition along with mass could be very valuable in the overall rating of different food plans, especially if that metric can be applied to food systems with a mixture of packaged items and fresh crops. The food metric put forth in this paper has precisely these attributes.

TOPICS FOR FURTHER STUDY

The work described herein leads to several natural areas of further work. Foremost would be the extension of the modified ESM computation for wheat to the other ALS crops. This project would involve the gathering of data similar to that listed in Table 1 for the other ALS crops. Once this work is completed the modified ESM numbers could be used to study the problem of which crop scenario would be most beneficial for the BIO-Plex experiments and various ones of the Mars mission scenarios. It seems certain the food plans developed for these various scenarios will be crop driven rather than menu driven in the sense that what meals are prepared depends on the crops available, more so than having the menu items determine the cropping scenario. This is somewhat contrary to the approach used by Hunter, et. al. (Hunter, et. al., 1998).

Much work can be done in the area of the testing and refining of the food metric proposed in this paper. It is very important to consider food quality and nutrition in any metric applied to food systems. Of course, in the case of space missions, the mass of the various systems is also a crucial factor. To date the model does not take into account the psychological benefits of a supply of fresh food items for long duration space missions. There seems to be little firm data concerning this possibly significant component of the overall food plan. Consequently, a suitable metric could eventually be quite different from the food metric put forth in this paper, but the food metric proposed here is a functioning model upon which to base further study.

REFERENCES

Bugbee, Bruce, Frantz, Jonathan, (July 13, 2000), Seminar, "Environmental Factors Affecting Plant Growth in BIO-Plex", Johnson Space Center, Houston, Texas

Drysdale, A.E., Hanford, A.J., Ewert, M.K., Lin, C.H., Henninger, D.L., Behrend Jr., A.F. (June, 1999) "Advanced Life Support Systems Modeling and Analysis Project Baseline Values and Assumptions Document", JSC 39317 (CTSD–ADV–371) National Aeronautics and Space Administration, Johnson Space Center, Houston, Texas.

Drysdale, A.E., Hanford, A.J., Ewert, M.K., Lin, C.H., Henninger, D.L., Behrend Jr., A.F. (November, 1999) "Advanced Life Support Research and Development Metric – Baseline", JSC 39503 (CTSD-ADV-384) National Aeronautics and Space Administration, Johnson Space Center, Houston, Texas.

Drysdale, A.E., Maxwell, S., Hanford, A.J., Ewert, M.K., Lin, C.H., Henninger, D.L., Behrend Jr., A.F. (December, 1999) "Advanced Life Support Systems Modeling and Analysis Reference Missions Document", JSC 39502 (CTSD–ADV–383) National Aeronautics and Space Administration, Johnson Space Center, Houston, Texas.

Barta, D.J., Henderson, K. (1998), "Performance of Wheat for Air Revitalization and Food Production During the Lunar-Mars Life Support Test Project Phase III Test", SAE paper 981704, 28th International Conference on Environmental Systems, Society of Automotive Engineers, Danvers, Massachusetts.

Hunter, J., Olabi, A., Spies, R., Rovers, A., Levitsky, D. (1998),"Diet Design and Food Processing for Bioregenerative Life Support Systems", SAE paper 982365, 28th International Conference on Environmental Systems, Society of Automotive Engineers, Danvers, Massachusetts.

Lange, K. E., and Lin, C. H. (1998) "Advanced Life Support Program: Requirements Definition and Design Consideration," JSC-38571 (CTSD-ADV-245, Rev. A) National Aeronautics and Space Administration, Johnson Space Center, Houston, Texas.
http://peer1.idi.usra.edu/peer_review/prog/ALSREQ98.PDF

Diagnostics of Carbon Nanotube Formation in a Laser Produced Plume:
An Investigation of the Metal Catalyst
by Laser Ablation Atomic Fluorescence Spectroscopy

Gary De Boer.
LeTourneau University
ES
August 4, 2000

Carl Scott
Thermal Branch
Structures and Mechanics Division
Engineering Directorate
NASA/JSC

Gary De Boer 8/3/00

Carl Scott 8/2/00

Diagnostics of Carbon Nanotube Formation in a Laser Produced Plume: An Investigation of the Metal Catalyst by Laser Ablation Atomic Fluorescence Spectroscopy

Final Report
NASA/ASEE Summer Faculty Fellowship Program – 1999
Johnson Space Center

Prepared By:	Gary D. De Boer, Ph.D.
Academic Rank:	Assistant Professor
University & Department	LeTourneau University Division of Natural Science

NASA/JSC	
Directorate:	Engineering
Division:	Structures and Dynamics Division
Branch:	Thermal
JSC Colleague	Carl Scott
Date Submitted	August 4, 2000
Contract Number	NAG-9-867

ABSTRACT

Carbon nanotubes, elongated molecular tubes with diameters of nanometers and lengths in microns, hold great promise for material science. Hopes for super strong light-weight material to be used in spacecraft design is the driving force behind nanotube work at JSC. The molecular nature of these materials requires the appropriate tools for investigation of their structure, properties, and formation. The mechanism of nanotube formation is of particular interest because it may hold keys to controlling the formation of different types of nanotubes and allow them to be produced in much greater quantities at less cost than is currently available.

This summer's work involved the interpretation of data taken last summer and analyzed over the academic year. The work involved diagnostic studies of carbon nanotube formation processes occurring in a laser-produced plume. Laser ablation of metal doped graphite to produce a plasma plume in which carbon nanotubes self assemble is one method of making carbon nanotube. The laser ablation method is amenable to applying the techniques of laser spectroscopy, a powerful tool for probing the energies and dynamics of atomic and molecular species.

The experimental work performed last summer involved probing one of the metal catalysts, nickel, by laser induced fluorescence. The nickel atom was studied as a function of oven temperature, probe laser wavelength, time after ablation, and position in the laser produced plume. This data along with previously obtained data on carbon was analyzed over the academic year. Interpretations of the data were developed this summer along with discussions of future work.

The temperature of the oven in which the target is ablated greatly influences the amount of material ablated and the propagation of the plume. The ablation conditions and the time scale of atomic and molecular lifetimes suggest that initial ablation of the metal doped carbon target results in atomic and small molecular species. The metal atoms survive for several milliseconds while the gaseous carbon atoms and small molecules nucleate more rapidly. Additional experiments and the development of *in situ* methods for carbon nanotube detection would allow these results to be interpreted from the perspective of carbon nanotube formation.

INTRODUCTION

Nanotechnology, the use of materials with dimensions of nanometers, represents engineering at the molecular scale. Many of the promises of nanotechnology have focussed on the use of nanometer scaled tubes discovered in 1991. [1] These tubes with dimension of nanometers in diameter and microns in length can be described as elongated fullerenes, and are often referred to as "nanotubes." Though nanotubes can be composed of combinations of carbon, nitrogen, and boron, [2] it is the pure carbon nanotube that has dominated discussions and has been the focus of the research at NASA/JSC. The molecular structure of the carbon nanotube is the source of its unique properties and technological promise. [3-16] The physical properties associated with a network of chemical bonds and aspect ratios of several orders of magnitude imply that incredibly strong, lightweight composite materials can be formed using nanotubes. [4-6] Another application of nanotubes may include hydrogen storage with potential benefits to fuel cell development. [7,8] Nanotubes have conductivity ranging from that of insulator to metallic conductor as a function of their geometry and size [9-13] leading to exciting implications for electronic applications. Because of the promising potential of carbon nontubes, NASA has made a commitment to take an active part in this cutting edge research and is currently producing, purifying, characterizing, and performing composite studies with carbon nanotubes.

Though promising methods have been developed recently for the large-scale production of nanotubes, the reality of gross quantities of inexpensive materials has remained elusive. Therefore, to advance NASA's objective of developing nanotube materials for space applications, processes that provide reproducible, inexpensive, bulk materials with specific properties are needed.

The objective of this work has been to obtain a better understanding of carbon nanotube formation for purposes of increasing production and enabling further research into composites and other materials. The self-assembly of carbon nanotubes involving species at the atomic and molecular level requires the use of appropriate tools. The most powerful tools of chemists and molecular physicists are those of atomic and molecular spectroscopy. Carbon nanotube production by laser ablation provides an environment for the spectroscopic probing of carbonaceous materials and metal atoms. Specific spectroscopic techniques employed include resolved emission and laser induced fluorescence. Atomic fluorescence spectroscopy is an extremely sensitive means of detecting a variety of metals [17-22] including nickel. [23-25] In this work atomic fluorescence spectroscopy has been employed to probe the metal catalyst during the production of carbon nanotubes by laser ablation. The metal signal was measured as a function of the same parameters used in previous carbonaceous studies at JSC allowing the carbonaceous and metal data to be complementary.

EXPERIMENTAL

The nanotube production setup at JSC follows that developed at Rice University [26] described previously by Arepalli, *et al.* [27, 28] Briefly, the setup includes a carbon target (19 mm diameter) which is doped with 1% nickel and 1% cobalt and is supported on a rod in an oven which is heated to 1473 K during normal production. The target and rod are centered within a 50.8 mm quartz tube. A smaller 25.4 mm quartz tube is centered within the 50.8 mm tube and extends to 6 mm of the target. Argon flows through the tubes toward the target at a pressure of 67 kPa and a flow rate of 100 sccm. Two Nd:YAG ablation lasers follow a path through the inner tube to strike the flat end of the target at normal incidence. The green (532 nm) Nd:YAG laser fires 50 ns prior to the IR (1064 nm) Nd:YAG laser. The ablations lasers, which generally operate at 60 Hertz, were operated at 10 Hertz for these experiments with an average power output of 1.5 watts and an energy density of 1.6 J/cm^2 per pulse for a laser spot size diameter of 3.4 mm. A third Nd:YAG laser (355 nm) operating at 10 Hz is used to pump a Lambda Physik FL 3002 dye laser. The dye (Coumarin 120) laser output was frequency doubled with a BBO1 crystal and was tuned to the atomic lines of nickel over the wavelength range of 224.2 nm to 226.2 nm.

Two SRS digital delay generators and a 60-hertz to 10-hertz converter synchronized the lasers. Fluorescence from nickel metal atoms was focussed by a 200 mm focal length lens onto a 1 mm pinhole in front of a Hamamatsu R928 photomultiplier tube (PMT). Fluorescence spectra were acquired by monitoring the PMT signal as a function of dye laser wavelength, laser energies, PMT position, and pump-probe delay. The signals were averaged through a boxcar and the averaged signals were recorded with a PC. The time decay of nickel fluorescence was monitored with a LeCroy transient digitizer and a Tektronix digital oscilloscope. Emission was also collected with an optical fiber and a Spex 270M spectrophotometer that was used to resolve the emission. The resolved emission was recorded with an ICCD.

Wavelengths shorter than 350 nm for excitation and emission of the nickel atom were chosen to avoid spectral interference due to black body radiation produced by the oven and the carbonaceous emissions resulting from ablation. Also, the PMT is more sensitive in this range. The nature of the production setup results in a great deal of scattered incident radiation from the ablation and probe lasers. To reduce the detection of scattered probe radiation a combination of excitation and fluorescent lines was chosen to allow detection of only the fluorescing radiation. The excitation wavelength was varied from 224.2 and 226.2 nm while collecting fluorescence transitions between 290-310 nm. A Solar Blind (SB300) filter centered at 300 nm was placed in front of the PMT, allowing detection of the 300 nm fluorescence, while minimizing the detection of scattered ablation light, scattered dye laser light, and black body radiation. A diagram of the diagnostic setup and physical principles appear in Figures 1 and 2.

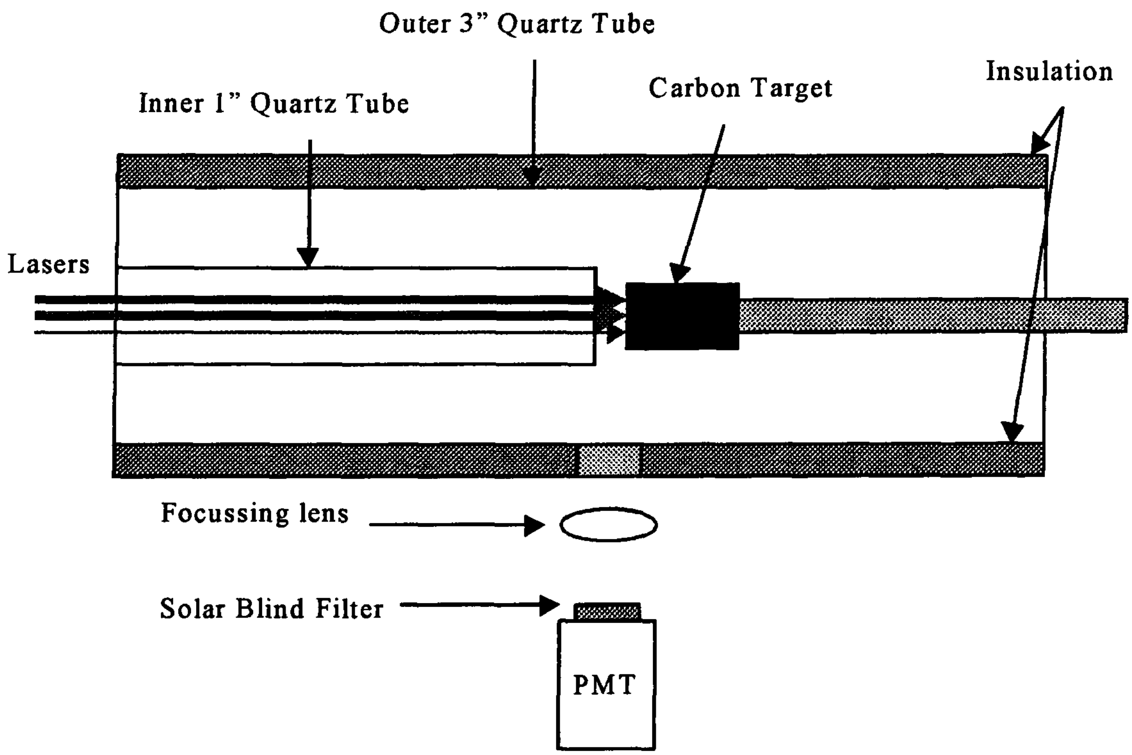

Figure 1. Diagnostics Setup

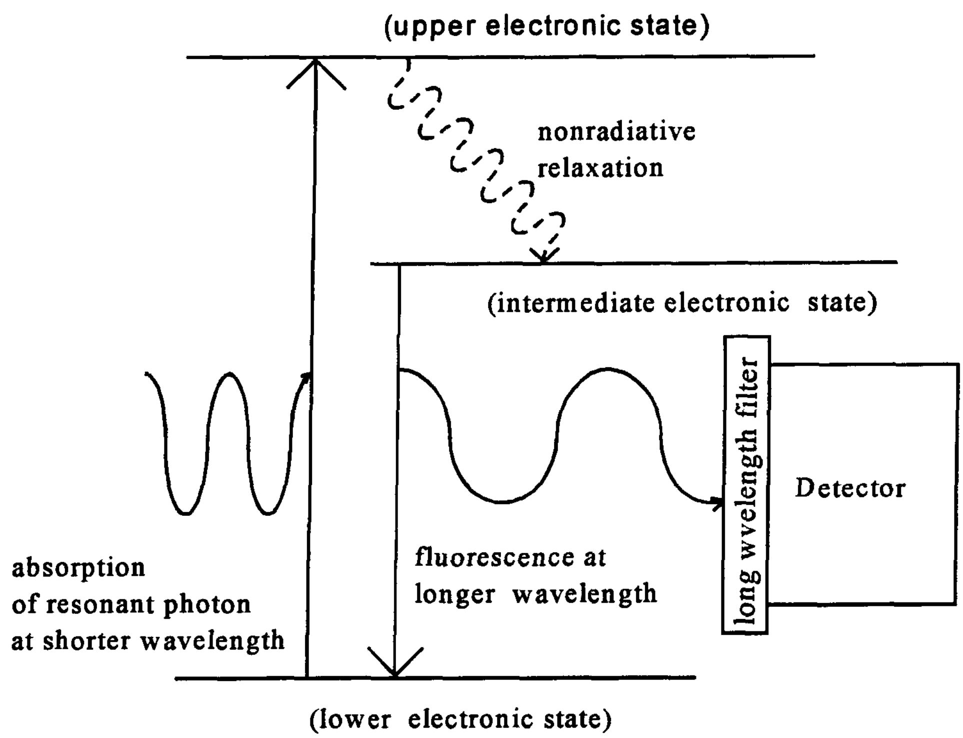

Figure 2. Illustration of Physical Principles

RESULTS

The nickel signal was recorded as a function of the pump-probe delay while positioning the PMT to collect the plume image 1 mm from the target surface, Figure 3. The nickel signal is seen even when probing within nanoseconds of the second ablation laser, though interference from the ablation lasers make quantifying the nickel fluorescence difficult. For the room temperature solid nickel target, Figure 3 inset, the nickel signal soon diminishes within a few microseconds, then increases only to diminish again within 20 μs of ablation. At an oven temperature of 1473 K the pump-probe time profile for the composite target appears to be quite different as it results in a long-lived signal of over several milliseconds, Figure 3. It can also be seen that the temporal peak of the nickel signal comes later in time as we probe farther from the target's surface. Imaging the plume at a distance of 1 mm, 2 mm, and 3 mm from the surface results in a change in the temporal profile implying a propagation velocity of about 10 m/s.

Wavelength spectra were taken over 224.2 nm to 226.2 nm. The transitions within this region involve electronic transitions from 3d to 4p atomic orbitals. Given that our line intensities are proportional to the intensity of the excitation transition, the line intensity can be related to the population of the lower states if the transition probabilities and degeneracies of the lower states are known. A distribution of the population of the lower states can be fit to a Maxwell-Boltzmann distribution to determine an electronic excitation temperature. The result of such an analysis at two different pump-probe delays for the composite target at 1473 K, along with a comparison to synthetic spectra of indicated temperature appears in Figure 4. The upper spectrum, A, in Figure 4 was taken at a pump probe delay which corresponds to the peak of the nickel signal intensity. The experimental data, circles, is compared to a synthetic spectrum generated with an electronic temperature of 1500 K. The lower spectrum, B, in Figure 4 was taken at a much earlier pump-probe delay which corresponds to much lower nickel signal intensity. The experimental data in B is compared with a synthetic spectrum generated with an electronic temperature of 225 K. Warmer electronic temperatures are associated with greater nickel atom signal intensities. This is true of both the solid nickel target at room temperature and the composite target heated to 1473 K by use of the oven.

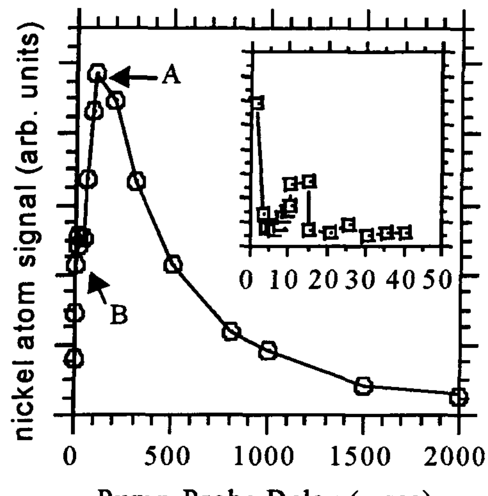

Figure 3

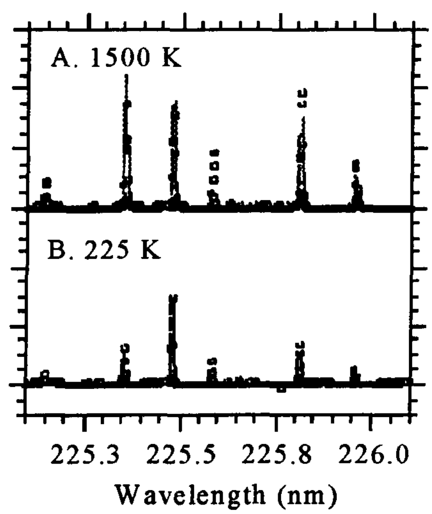

Figure 4

A similar analysis of previously obtained C_2 LIF spectra was also done. The analysis indicates a shorter lifetime for the C_2 species and cooler temperatures than for the nickel atom. The cooler temperatures are likely the result of only one laser being used for ablation, while two lasers were used in the nickel work. But as with the nickel data, the higher signal intensities relate to warmer temperatures, see Figures 5 and 6. The data in Figure 5 were collected at a pump-probe delay of 1 μs while the data in Figure 6 were collected with a fixed imaging distance of 1.75 mm.

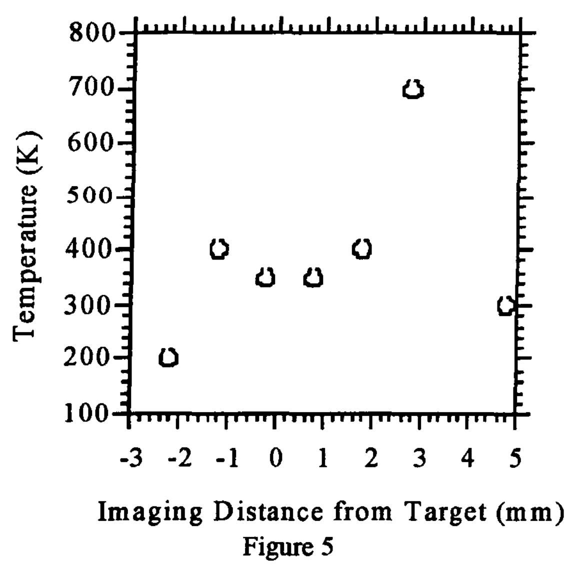

Figure 5

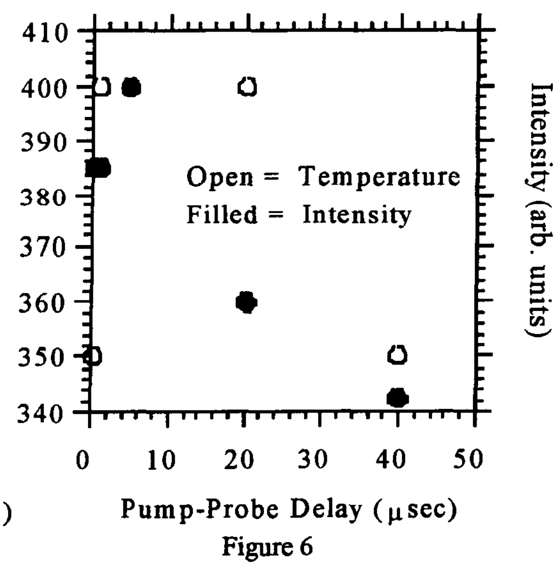

Figure 6

The LIF of both the C_2 and the nickel atom both are much lower by some thousands of Kelvin than the temperature indicated by C_2 emission. C_2 emission is more closely related to the plasma temperature.

DISCUSSION AND INTERPRETATION

Since metal catalysts are essential to carbon nanotube formation, several studies have focussed on the behavior of the metal. Yudasaka *et al* [29] have shown, by inspection of targets, that when Nd:YAG pulsed lasers are used there is poor metal ablation at room temperature and carbon nanotubes do not form. However, when the target is heated to 1473 K carbon nanotubes form and the metal is ablated from the target. Yudasaka also notes that when a CO_2 laser is used at room temperature carbon nanotubes are also formed, implying that the elevated ambient gas temperature is not necessary for nanotube assembly, but rather for metal ablation. [30] The microsecond CO_2 laser has a much longer pulse than the nanosecond Nd:Yag or excimer lasers. It is possible that the longer heating time of the CO_2 laser allows for better ablation so that elevated oven temperatures are not necessary. This work is consistent with an increase in nickel metal ablation at elevated oven temperatures. This work also indicates that the electronic temperature of nickel atoms produced by laser ablation is at least 1500 K in the center of the plume regardless of oven temperature and becomes much lower outside of the plume. The propagation and the lifetime of nickel atoms clearly change when the oven is used to elevate the target temperature.

Temperatures obtained from the nickel and carbon LIF spectra are much cooler than those indicated by the C_2 emission. Similar LIF and emission studies done by Brinkman [31] in a DC arcjet for purposes of analyzing diamond deposition found similar temperature differences between C_2 emission and LIF. Temperature measurements based on a variety of methods in other systems appear to give similar temperature variations for the electronically excited state and ground state species. [32-34] Brinkman postulates that the quenching of the excited electronic C_2 species is much faster than a multiple collision process necessary for reaching vibrational and rotational thermal equilibrium. The hot C_2 emission has a lifetime of about 60 μs implying that during this time short-lived C_2 species are being formed.

Laser produced plumes associated with carbon have been studied. [35-37] These studies indicate that the carbonaceous emission results primarily from recombination of atomic carbon to produce hot C_2 emission spectra. Arepalli *et al.* [38] have also explored the possibility that C_2 emission can result from the photodissociation or "shrinkage" of fullerenes. Both of these sources and possibly others are likely contributors to the hot C_2 emissions.

Computational studies based on analysis of the endcaps of carbon nanotubes formed in the DC arc indicate that the growth of carbon nanotubes occurs at between 700-1800 K, rather than the much higher temperatures of the plasma. [39] The dependence of nanotube diameter on oven temperature would also indicate that oven temperatures have a role in the formation process. [40] Arepalli et al. [28] have shown that oven temperature influences plume propagation, size and lifetime when Nd:YAG lasers are used for ablation. They have also shown that target position relative to the inner tube can affect the plume propagation. The empirically determined optimal target position for the formation of carbon nanotubes also relates to the position in which the plume appears to have the slowest rate of propagation. No doubt the distance of the target from the inner tube influences the argon gas flow characteristics around the target. Yudasaka et al. [41] also notes that nickel ablation has a gas pressure dependency, though they attribute this dependency to effects on ablation rather than plume propagation. The ablation process very much influences the propagation of the plume and so it is difficult analyze them independently.

In regards to the metal species within the plume, whether they are atomic or large micrometer sized particle or melts, works to characterize plumes produced by laser ablation can be elucidative. [35-37, 42-46] Plumes associated metals, including nickel, have also been studied. [43-46] In general, it has been found that higher laser energy densities and gas pressures appear to be necessary to create metallic nanoparticles or liquid droplets by laser ablation. [43-45] Given the conditions of our experiments it seems likely that initial ablation results in atomic and small molecular species with the larger particles and droplets being less prevalent.

Dillon *et al* [47] have addressed the specific question of carbon nanotube formation as a function of laser parameters. They studied the formation of carbon nanotubes using pulsed lasers at 3 to 24 kHz with various pulse energies and continuous wave lasers indicate that tubes are formed at higher laser powers, but with lower pulse energies and higher pulse frequency, consistent with smaller species being ablated. This implies that the formation of carbon nanotubes is favored by species that are in the vapor phase.

Lifetimes of the C_2 and nickel atoms reported in this work indicate that nickel atoms are more prevalent than nickel particles or droplets. The long lifetime of the nickel atom signal would suggest that the presence of the atomic species is more prevalent than nickel particles or droplets. Lifetimes of emission and LIF of C_2 are shorter than the lifetime of the nickel LIF signal which may indicate that the nucleation process for carbon is faster than for the nickel metal. Geohegan observed a similarly long lifetime for the cobalt atom,[48] consistent with the suggestion that more metal atoms rather than metal clusters or particles are present during the first several milliseconds after ablation.

Maiti reports experimental nanotube growth rates of 1-500 A/ms for the DC arc process and calculates a growth rate of 8.2E2 A/ms at 1500 K and 1.9E4 A/ms at 2000 K based on molecular dynamics simulations. [49] This would imply a growth time of one to many milliseconds for a micron long tube. Smalley [50] and Scott *et al.* [51] propose much shorter microsecond times for nanotube formation during laser ablation, while Puretz *et al* [52] propose formation times of as long as seconds. Time scales on the order of milliseconds and longer would allow for metal nucleation during nanotube formation. The nucleation of metals into small bimetallic clusters may be the reason for a bimetallic dependence of the metal catalyst. Clearly, additional efforts to determine the growth rates of nanotubes and the presence of nanotubes during the formation process are necessary.

This work demonstrates that nickel metal catalyst can be monitored *in situ* during carbon nanotube formation. Elevation of the oven temperature increases the amount of ablation and also appears to influence plume expansion and propagation. The distribution of energies in the nickel atom and the rotational energies of the ground electronic state of the C_2 species inferred from the LIF spectra, imply that the temperatures of these species are much lower than the plasma temperature. The temperatures determined by LIF are more closely related to the ambient oven temperature. Laser power densities, gas pressures, as well as metal and C_2 lifetimes are consistent with an atomic or small molecule presence upon ablation. Nucleation of bimetallic clusters during the time frame of nanotube growth is possible. The inner tube and gas properties may play an important role in the confining of reactive species during the formation process. Additional experiments including LIF studies of C_2 using two ablation lasers, additional LIF studies of nickel and cobalt as a function of various system parameters, and an *in situ* method to monitor nanotube growth would be beneficial to this work.

REFERENCES

1 Iijima, *Nature* **354**, 56 (1991).

2 S. IIjima, H. G. Zhang, and K. Suenaga, *Chemical Physics Letters* **279**, 264 (1997).

3 P. Calvert, in *Carbon Nanotubes Preparation and Properties*, edited by T. W. Ebbesen (NEC Research Institute, Princeton, New Jersey, 1996).

4 P. Calvert, *Nature* **399**, 210 (1999).

5 H. D. Wagner and O. Lourie, *Applied Physics Letters* **73**, 3527 (1998).

6 C. Bower, R. Roson, L. Jin, J. Han, and O. Zhou, *American Institute of Physics* **74**, 3317 (1999).

7 N. M. Rodriguez, A. Chambers, C. Park, and T. K. Baker, *The Journal of Physical Chemistry B* **102**, 4253 (1998).

8 A. C. Dillon, K. M. Jones, T. A. Bekkedah, C. H. Klang, D. S. Bethune, and M. J. Heben, *Nature* **386**, 377 (1997).

9 R. Smalley, J. W. G. Wildoer, L. C. Venema, A. G. Rinzler, and C. Dekker, *Nature* **391**, 59 (1998).

10 M. Burghard, A. Y. Kasumov, R. Deblock, M. Kociak, B. Reulet, H. Bouchiat, I. I. Khodos, Y. B. Gorbatov, V. T. Volkov, and C. Journet, *Science* **284**, 1508 (1999).

11 N. Hamada, *Material Science and Engineering* **B19**, 181 (1993).

12 J.-C. Charlier, *J. Mater. Res.* **13**, 2368 (1998).

13 J.-C. Charlier and P. Lambin, *The American Physical Society* **57**, 57 (1998).

14 C. Dekker, *Physics Today*, 22 (1999).

15 T. W. Ebbesen, *Carbon Nanotubes Preparation and Properties* (NEC Research Institute, Princeton, New Jersey, 1996).

16 J. Sloan, J. Cook, and M. Green, *Chemisty and Industry* **16**, 600 (1996).

17 W. Sdorra and K. Niemax, *Inst. Phys. Conf. Ser.* **11**, 463 (1990).

18 Y. Oky, T. Tani, N. Kidera, and M. Maeda, *Optics Communications* **110**, 298 (1994).

19 J. D. Winefordner, S. J. Weeks, and H. Haraguchi, *Analytical Chemistry* **50**, 360 (1978).

20 R. G. Michel, J. X. Zhou, X. Hou, and S.-J. J. Tsai, *Analytical Chemistry* **69**, 490 (1997).

21 R. g. Michel, J. P. Dougherty, and F. R. Preli, *Journal of Analytical Atomic Spectrometry* **2**, 429 (1987).

22 M. Maeda, Y. Oki, and E. Tashiro, *Analytical Chemistry* **65**, 2096 (1993).

23 J. D. Winfordner, M. S. Epstein, J. Bradshaw, S. Bayer, J. Bower, and E. Voigtman, *Applied Spectroscopy* **34**, 372 (1980).

24 O. Axner, A. Marunkov, N. Cherkalin, and J. Enger, *Spectrochimica Acta* **49B**, pp. 1385 (1994).

25 O. Axner, A. Marunkov, N. Chekalin, and J. Enger, *Spectrochimica Acta* **49B**, 1385 (1994).
26 R. E. Smalley, A. Thess, R. Lee, P. Nikolaev, D. Hongjie, P. Petit, J. Robert, C. Xu, Y. H. Lee, S. G. Kim, A. G. Rinzler, D. T. Colbert, G. E. Scuseria, D. Tomanek, and J. E. Fischer, *Science* **273**, 483 (1996).
27 S. Arepalli and C. D. Scott, *Chemical Physics Letters* **302**, 139 (1998).
28 S. Arepalli, P. Nikolaev, W. Holmes, and C. D. Scott, *Applied Physics A* **70**, 125 (2000).
29 M. Yudasaka, R. Kikuchi, O. Yoshimasa, O. Etsuro, and S. Yoshimura, *Appl. Phys. Lett.* **70**, 1817 (1997).
30 M. Yudasaka, S. Iijima, F. Kokal, K. Takahashi, R. Yamada, N. Sensui, and T. Ichihashi , *Journal of Physical Chemistry* **103**, 3576 (1999).
31 E. A. Brinkman, G. A. Ralche, M. S. Brown, and J. B. Jeffries, *Appl. Phys. B* **64**, 689 (1996).
32 J. A. Pobst, I. J. Wysong, and R. A. Spores, *IEPC* **95**, 203 (1995).
33 G. A. Raiche and J. B. Jeffries, *Appl. Opt.* **32**, 4629 (1993).
34 A. G. Gaydon, *The Spectroscopy of Flames, 2nd ed.* (Haisted, New York, 1974).
35 c. Parigger, D. H. Plemmons, J. O. Hornkohl, and J. W. L. Lewis, *J. Quant. Spetrosc. Radiat. Transfer* **52**, 707 (1994).
36 S.-i. Aoqui, t. Ikegami, Y. Yamagaa, and K. Ebihara, *Thin Solid Films* **316**, 40 (1998).
37 J. Seth, R. Padiyath, and S. V. Babu, *Appl. Phys. Lett.* **63**, 126 (1993).
38 S. Arepalli, C. D. Scott, P. Nikolaev, and R. E. Smalley, *Chemical Physics Letters* **320**, 26 (2000).
39 V. H. Crespi, *Physical Review Letters* **82**, 2908 (1998).
40 S. Bandow, S. Asaka, Y. Saito, A. M. Rao, L. Grigorian, E. Richter, and P. C. Eklund, *Phys. Rev. Lett.* **80**, 3779 (1998).
41 M. Yudasaka, T. Komatsu, Y. Ichihashi, Y. Achiba, and S. Iijima, *J. Phys. Chem. B* **102**, 4892 (1998).
42 C. Miller, *Laser Ablation Principles and Applications* (Springer, Berlin, 1994).
43 M. F. Becker, J. R. Brock, H. Cai, D. E. Henneke, J. W. Keto, J. Lee, W. T. Nichols, and H. D. Glicksman, *NanoStrucured Materials* **10**, 853 (1998).
44 K. H. Song and X. Xu, *Applied Surface Science* **127-129**, 111 (1998).
45 J. A. Aguilera, C. Aragon, and F. Penalba, *Applied Surface Science* **127-129**, 309 (1998).
46 M. Tanaka, Y. Fujisawa, T. Nakajima, Y. Tasaka, and K. Ota, *J. Appl. Phys.* **83**, 3379 (1998).
47 A. C. Dillon, P. A. Parilla, K. M. Jones, g. Riker, and M. J. Heben, *Advances in Laser Ablation of Materials (USA)*, 403 (1998).
48 A. A. Puretzky, D. B. Geohegan, X. Fan, and S. J. Pennycook, *Appl. Phys. Letts.* **76**, 182 (2000).

49 A. Maiti, C. J. Brabec, C. Ronald, and J. Bernholc, *Phys. Rev., Condens. Matter.* **52**, 14850 (1995).
50 R. E. Smalley, *Accounts of Chemical Research* **25**, 98 (1992).
51 C. D. Scott, S. Arepalli, P. Nikalaev, and R. Smalley, *to be published*, (2000).
52 A. A. Puretzky, D. B. Geohegan, X. Fan, and S. J. Pennycook, *Appl. Phys. A* **70**, 153 (2000).

Development of a Multi-Channel, High Frequency QRS Electrocardiograph

Jude L. DePalma
Department of Engineering
University of Southern Colorado
Pueblo, CO 81001
SD
August 4, 2000

Todd T. Schlegel, M.D.
Life Sciences Research Laboratories
Medical Sciences Division
Space and Life Sciences Directorate

Jude L. DePalma

Jude L. DePalma, Ph.D.

Todd T. Schlegel, MD

Todd T. Schlegel, M.D.

Development of a Real-Time, High Frequency QRS Electrocardiograph

Final Report
NASA/ASEE Summer Faculty Fellowship Program – 2000

Johnson Space Center

Prepared by:	Jude L. DePalma, Ph.D.
Academic Rank:	Assistant Professor
University & Department	University of Southern Colorado Department of Engineering Pueblo, CO 81001

NASA/JSC	
Directorate:	Space and Life Sciences
Division:	Medical Sciences Division
Branch:	Life Sciences Research Laboratories
JSC Colleague:	Todd T. Schlegel, M.D.
Date Submitted:	August 4, 2000
Contract Number:	NAG –9-867

ABSTRACT

With the advent of the ISS era and the potential requirement for increased cardiovascular monitoring of crewmembers during extended EVAs, NASA flight surgeons would stand to benefit from an evolving technology that allows for a more rapid diagnosis of myocardial ischemia compared to standard electrocardiography. Similarly, during the astronaut selection process, NASA flight surgeons and other physicians would also stand to benefit from a completely noninvasive technology that, either at rest or during maximal exercise tests, is more sensitive than standard ECG in identifying the presence of ischemia. Perhaps most importantly, practicing cardiologists and emergency medicine physicians could greatly benefit from such a device as it could augment (or even replace) standard electrocardiography in settings where the rapid diagnosis of myocardial ischemia (or the lack thereof) is required for proper clinical decision-making.

A multi-channel, high-frequency QRS electrocardiograph is currently under development in the Life Sciences Research Laboratories at JSC. Specifically the project consisted of writing software code, some of which contained specially-designed digital filters, which will be incorporated into an existing commercial software program that is already designed to collect, plot and analyze conventional 12-lead ECG signals on a desktop, portable or palm PC. The software will derive the high-frequency QRS signals, which will be analyzed (in numerous ways) and plotted alongside of the conventional ECG signals, giving the PC-viewing clinician advanced diagnostic information that has never been available previously in all 12 ECG leads simultaneously. After the hardware and software for the advanced digital ECG monitor have been fully integrated, plans are to use the monitor to begin clinical studies both on healthy subjects and on patients with known coronary artery disease in both the outpatient and hospital settings. The ultimate goal is to get the technology out into the clinical world, where it has the potential to save lives.

BACKGROUND

The Electrocardiogram (ECG)

The conventional surface ECG has long been used as a diagnostic tool for detecting problems with the heart. A representative tracing from a conventional surface ECG in a healthy subject is shown in Figure 1.

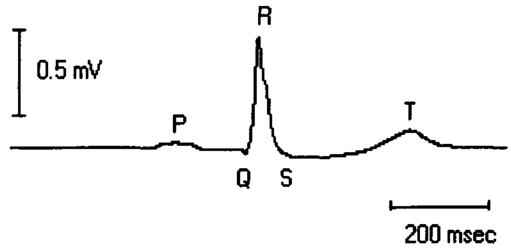

Figure 1: A Conventional Surface ECG Signal From a Healthy Subject

Plots of the conventional surface ECG generally require sampling rates of 100 Hz or less. To detect frequencies >100 Hz within the ECG complex, a much higher sampling rate is required. For the present project, we utilized ECG recordings that had been collected using an A/D converter with sampling rate of 1000 Hz. The electrocardiographic point of interest for our study was the QRS complex. Traditionally a clinician will look at changes in the ST segment of the conventional ECG as a potential indicator for myocardial ischemia, or a lack of oxygen/blood supply to an area of the heart. However, a diminution of the higher frequency components present within the QRS complex is a more sensitive indicator for myocardial ischemia than ST-segment changes in the conventional ECG [1], [2], [3]. These higher frequency components are not visible in the conventional ECG, but can be seen when an ECG acquired at sampling rates of $\geq$ 500 Hz is filtered with a bandpass filter which passes only frequencies from 150 - 250Hz. An example of a high frequency QRS signal from a healthy subject is shown in Figure 2.

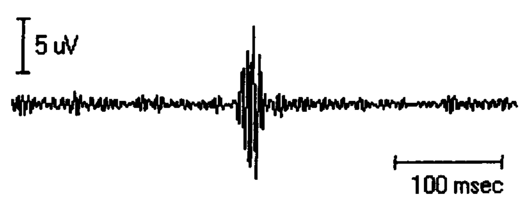

Figure 2. High Frequency QRS Signal in a Healthy Subject With No Myocardial Ischemia

Note that the amplitude of the high frequency components filtered between 150 – 250 Hz is in microvolts (Figure 2) rather than millivolts (Figure 1).

Figure 3 shows a high frequency QRS signal from a patient with myocardial ischemia. Notice the reduced voltage scale (compared to Figure 2) as well as the fact that there are

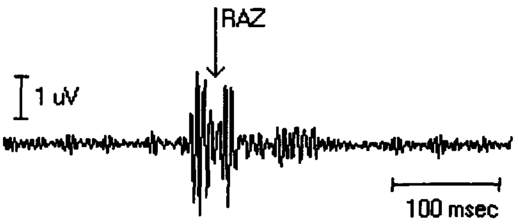

Figure 3. High Frequency QRS From a Patient With Myocardial Ischemia

two peaks in the envelope of the high frequency QRS signal rather than the single peak in Figure 2. The dip in the envelope pointed to by the arrow in the figure is denoted as a reduced amplitude zone (RAZ) [1]. When a RAZ is present it may be indicative of dead or ischemic cardiac tissue.

Spectrum of the High Frequency QRS

The spectrum of the high frequency QRS can also be examined for the possible presence of ischemia [1]. If no ischemia is present the spectrum will generally exhibit only one peak as shown in Figure 4.

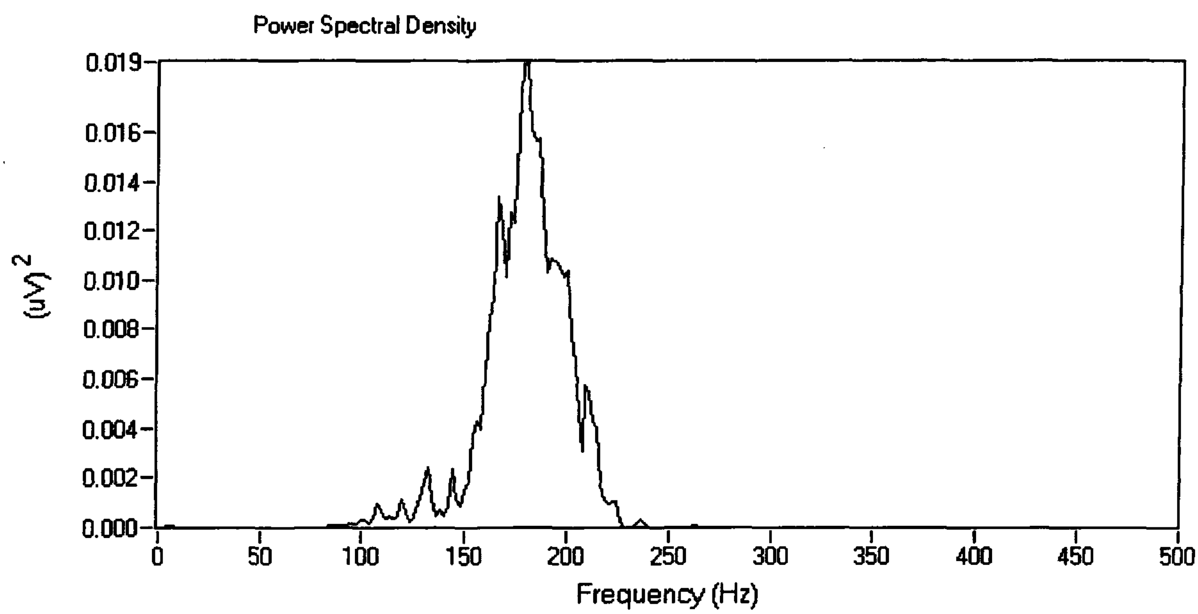

Figure 4. Spectrum of High Frequency QRS of Subject With No Ischemia

However, if a RAZ is present in the high frequency QRS signal and/or ischemia is present, the spectrum may have two peaks as shown in Figure 5.

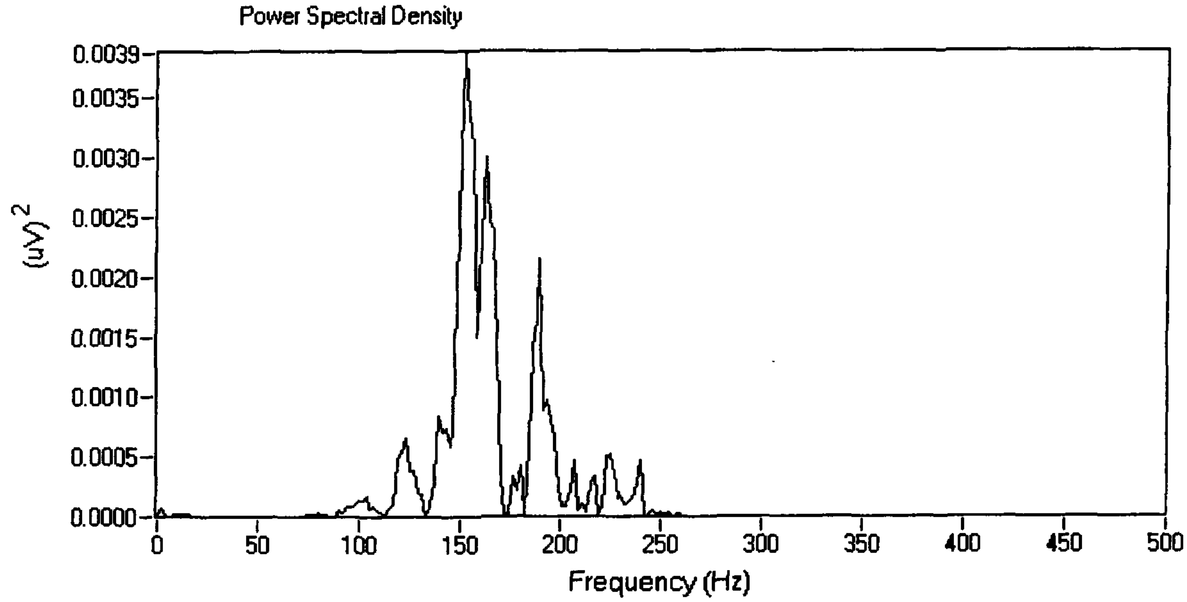

Figure 5. Spectrum of High Frequency QRS of Subject With Ischemia

Numerical Measures

Several numerical measures of the high frequency QRS have been proposed that show a decrease when ischemia is present [1], [2], [4]. One of these measures is the root mean square (RMS) voltage of the filtered QRS signal, which can be defined as

$$RMS = \sqrt{\frac{\sum_{i=fqon}^{fqoff} X_i^2}{FQRSD}}, \tag{1}$$

where X_i is the filtered voltage at a given sampling point, *fqon* and *fqoff* are the onset and offset, respectively, of the high frequency QRS signal, and FQRSD is the filtered QRS-interval duration as defined by *fqon* and *fqoff*. The onset and offset of the filtered QRS occur when the voltage exceeds some multiple of the average noise level (AVNL) in an isoelectric portion of the filtered ECG (i.e., in the ST or PR segment).

SYSTEM IMPLEMENTATION

Introduction

In order to implement the system, various software elements had to be developed. The elements were incorporated into a overall software package that read in ECG data from a binary file. The elements include an R-wave detector, alignment of the R-waves for averaging, a bandpass filter, and RAZ detection. A description of how these elements were implemented follows. These elements will be incorporated into an existing commercial software program that is already designed to collect, plot and analyze conventional 12-lead ECG signals on a desktop, portable or palm PC.

R-wave Detection

In order to average the ECG signal, the R-waves must be detected first. The following algorithm was developed to detect R-waves [5], [6], [7]. The R-wave was detected in lead II. First the raw ECG data was passed through two finite impulse response (FIR) digital filters to isolate the R-wave peak. A lowpass and a highpass filter were combined to effectively create a bandpass filter. The filters were designed using the LabWindows™ Signal Processing Toolset v. 5.0. The passband response for both filters was flat to within –3.01dB. The stopband attenuation for both filters was –28dB. The passband frequency for the lowpass filter was 11 Hz and the stopband frequency was 80 Hz. The filter order was 17. For the highpass filter, the passband frequency was 6 Hz and the stopband frequency was 0.5 Hz. The filter order was 129. After filtering the signal the first derivative of the signal is estimated using the difference equation

$$y(nT) = \frac{1}{10T}\left[2x(nT) + x(nT - T) - x(nT - 3T) - 2x(nT - 4T)\right], \tag{5}$$

where T is the sampling period. The first derivative of the signal is then squared point by point. Then the squared signal is integrated using a moving-window integration. The equation for the moving window integration is

$$y(nT) = \frac{1}{N}\left[x(nT - (N-1)T) + x(nT - (N-2)T) + \ldots + x(nT)\right], \tag{6}$$

where N is the number of samples in the integration window. N is chosen so that the window is 150 ms, the width of the widest possible QRS complex. Peaks are then searched for in the integrated waveform. In order to eliminate multiple peaks caused by ripple in the integrated waveform is peak maximal levels are stored since the last peak detection. A peak is defined only after a level is reached that is half of the maximal or peak level. The fiducial mark of the R-wave is then set to the largest peak in the bandpass filtered signal in an interval of 225 to 125 ms preceding a peak found in the integrated waveform. Thresholds must now be set to determine if the peak is an R-wave or a noise peak. The value of a peak is defined as *PEAKI.* The intermediate variables determining thresholds are

$$SPKI = 0.125PEAKI + 0.875SPKI, \tag{7}$$

if *PEAKI* is the signal (R-wave) peak and

$$NPKI = 0.125PEAKI + 0.875NPKI, \tag{8}$$

if *PEAKI* is a noise peak. The thresholds are then

$$THRESHOLDI1 = NPKI + 0.25(SPKI - NPKI) \tag{9}$$

and

$$THRESHOLDI2 = 0.5THRESHOLDI1 . \tag{10}$$

If a peak is above $THRESHOLDI1$, it is an R-wave peak. Whenever an R-wave is not detected within a certain interval, a searchback routine is used. If it is used, then if a peak is above $THRESHOLDI2$, it is an R-wave peak. The thresholds are applied to both the integrated waveform and the bandpass filtered waveform. The value of the peak must exceed the threshold in both waveforms for it to be identified as an R-wave.

The searchback routine works by defining two RR-interval averages. They are

$$RRAVERAGE1 = 0.125(RR_{n-7} + RR_{n-6} + \ldots + RR_n) \tag{11}$$

and

$$RRAVERAGE2 = 0.125(RR'_{n-7} + RR'_{n-6} + \ldots + RR'_n), \tag{12}$$

where the RR'_n values are RR-intervals that fall within the limits

$$RRLOWLIMIT = 92\% \times RRAVERAGE2 \tag{13}$$

and

$$RRHIGHLIMIT = 116\% \times RRAVERAGE2 . \tag{14}$$

If an R-wave has not been detected for the interval of

$$RRMISSEDLIMIT = 166\% \times RRAVERAGE2, \tag{15}$$

then the R-wave is the peak found above $THRESHOLDI2$ and below $THRESHOLDI1$.

Aligning the R-wave Signals

Since noise is present it is crucial that the beats are aligned correctly on a single point before averaging. However, the R-wave peak may not be the best point upon which to align the signals. In order to determine a better point upon which to align the signals, a normalized cross correlation of the first beat with the subsequent beats to be averaged was computed. The normalized cross correlation, $\rho_{xy}(\tau)$, was computed as

$$\rho_{xy}(\tau) = \frac{R_{xy}(\tau)}{\sqrt{R_{xx}(0)R_{yy}(0)}}, \tag{16}$$

where $R_{xy}(\tau)$ is the cross correlation of signals x and y and $R_{xx}(\tau)$ is the autocorrelation of a signal x with itself. The waveforms were aligned upon the point of the maximum of $\rho_{xy}(\tau)$ computed for the first beat with the subsequent beat to be aligned. The user could select whether or not to use the cross correlation method to align the beats for averaging. If not, the beats were averaged by aligning the R-wave peaks.

Bandpass Filter Design

Since the final system functions in real time, speed was an important consideration in all numerical computations. Speed was especially important for the design of the bandpass filter. The lower the filter order the less the numerical computation and the faster the filtering of the data. However, there is a trade off in filter order vs. desired filter response. Specifically, as the filter order is decreased, several non-optimal characteristics are introduced. These include more ripple in the bandpass response, increased transition interval from bandpass to stopband, and an increase in undesired frequencies through the filter because of the increased stopband level. With consideration of these tradeoffs, a filter was designed using the LabWindows™ Signal Processing Toolbox v. 5.0. with the following characteristics: *1*) The passband response was flat to within 4.5dB from 146 to 240 Hz; *2*) The stopband attenuation was –100dB; *3*) The stopband frequencies were 47.4 Hz and 327.7 Hz; and *4*) The filter order was 32.

RAZ Detection

Software was written to determine if a RAZ was present in the high frequency QRS signal. First the envelope of the high frequency QRS was defined as the line segments connecting the local minima and maxima in the signal. A local maxima was defined if the amplitude at a sample point exceeded the amplitudes of the three sample points before and after it. Similarly, a local minima was defined if the amplitude at a sample point was less than the amplitudes of the three points before and after it. A RAZ was defined if at least two local maxima or minima of the envelope were found [1].

Power Spectrum Estimation

The spectrum of the high frequency QRS was estimated using the periodogram method. First a Hamming window was applied to the signal. Then the FFT of the signal was computed. The spectrum was then calculated as the magnitude squared of the resulting FFT.

Multi-channel System

A multi-channel system was developed which incorporated all of the previously noted elements. The system reads in ECG data from a binary file in which the data is stored as integers that are two bytes long. The initial display window of the program showing the standard 12-lead ECG is shown in Figure 6. The display window for the averaged ECG is shown in Figure 7. Next the display window for the high frequency QRS is shown in

Figure 8. And finally the display of the high frequency QRS spectrum is shown in Figure 9.

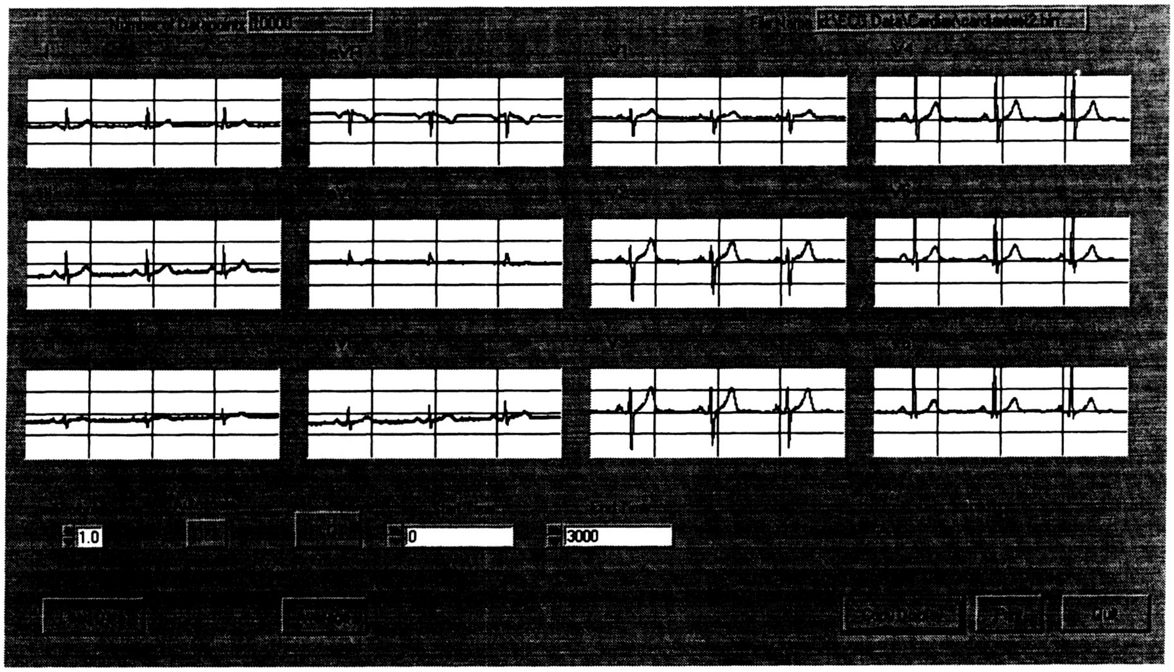

Figure 6. Initial Display of Program

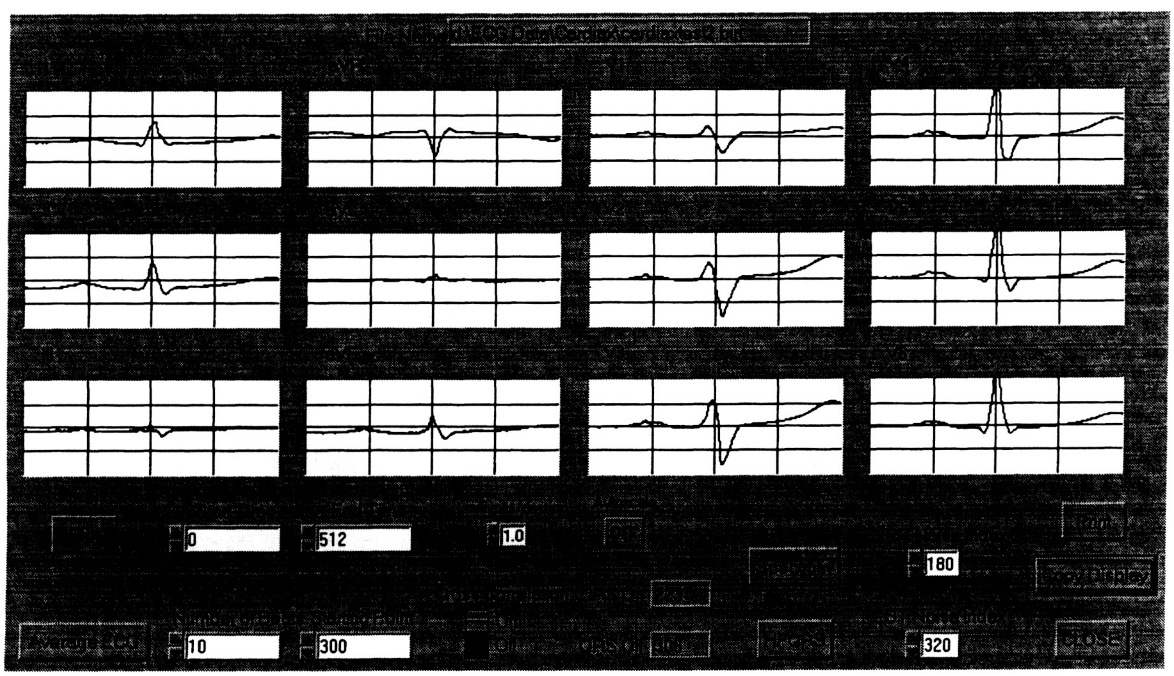

Figure 7. Display of Averaged ECG Data

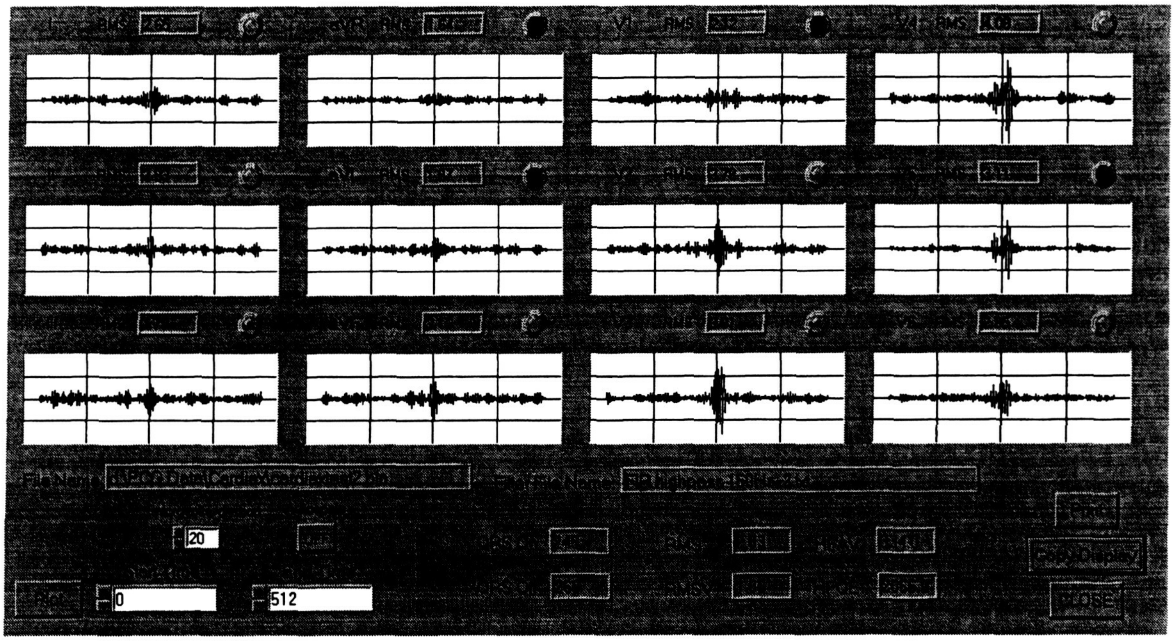

Figure 8. Display of High Frequency QRS

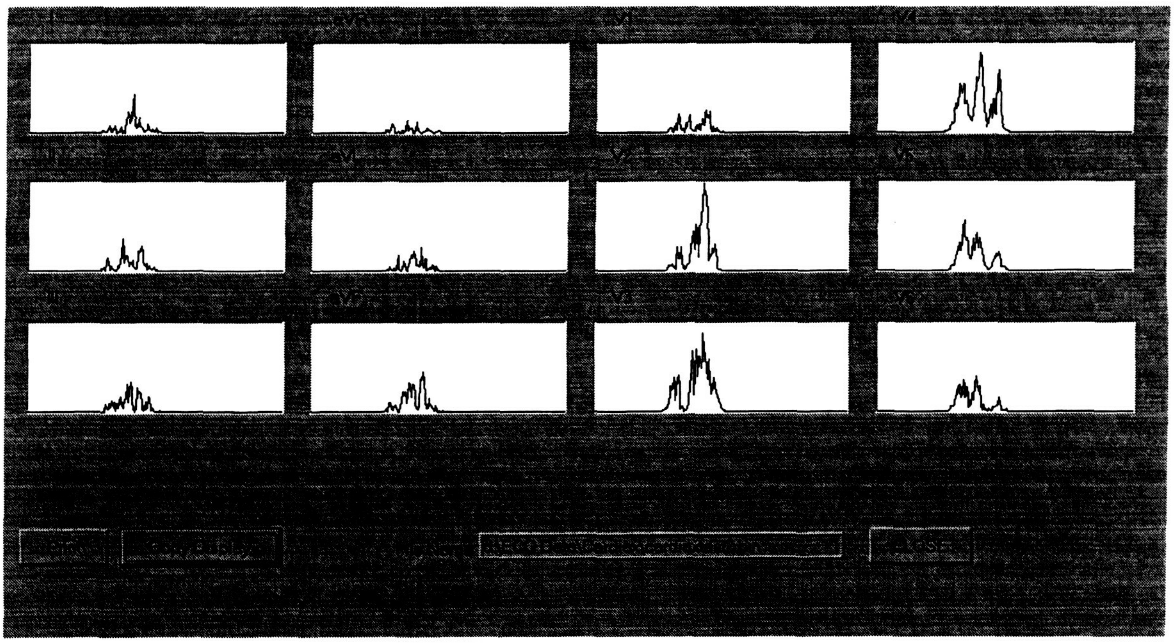

Figure 9. Display of High Frequency QRS Spectrum

Conclusion

The software for a multi-channel high frequency electrocardiograph has been developed which incorporates the latest advances used in this area of electrocardiography. Unfortunately, the developed software could not be incorporated into the commercially available ECG software this summer because of delays in obtaining interface software from the commercial ECG software supplier. Current plans are to finish the software integration during the upcoming academic year. The system designed is both a diagnostic and experimental system. It will be used to collect more data to help refine the high frequency QRS method. Since the system is software based, changes can easily be made as further knowledge and experience is gained in this area. The system should prove to be a valuable tool in the diagnosis of myocardial ischemia.

REFERENCES

[1] S. Abboud, "High-Frequency Electrocardiogram Analysis of the Entire QRS in the Diagnosis and Assessment of Coronary Artery Disease," *Progress in Cardiovascular Diseases*, vol. XXXV, pp. 311-328, 1993.

[2] A. Beker, A. Pinchas, J. Erel, and S. Abboud, "Analysis of High Frequency QRS Pontential During Exercise Testing in Patients with Coronary Artery Disease and in Healthy Subjects," *PACE*, vol. 19, pp. 2040-2050, Dec. 1996, Part I.

[3] S. Abboud, R. J. Cohen, A. Selwyn, P. Ganz, D. Sadeh, and P. L. Friedman, "Detection of transient myocardial ischemia by computer analysis of standard and signal-averaged high-frequency electrocardiograms in patients undergoing percutaneous transluminal coronary angioplasty," *Circulation*, vol. 76, no. 3, pp. 585-596, Sept. 1987.

[4] Q. Xue, B. R .S. Reddy, and T. Aversano, "Analysis of High-frequency Signal-averaged ECG Measurements," *Journal of Electrocardiography*, vol. 28 Supplement, pp. 239-245, 1995.

[5] W. J . Thompkins, editor, *Biomedical Digital Signal Processing*, Upper Saddle River, New Jersey, USA: Prentice Hall PTR, 1995.

[6] J. Pan and W. J. Tompkins, "A Real-Time QRS Detection Algorithm," *IEEE Transactions on Biomedical Engineering*, vol. BME-32, no.3, pp. 230-236, Mar. 1985.

[7] P. S. Hamilton and W. J. Tompkins, "Quantitative Investigation of QRS Detection Rules Using the MIT/BIH Arrhythmia Database," *IEEE Transactions on Biomedical Engineering*, vol. BME-33, no.12, Dec. 1986.

Deformation and Flexibility Equations
For Idealized ARIS Umbilicals,
Under Planar End-Loading Conditions

R. David Hampton
University of Alabama in Huntsville
OZ3
18 August 2000

Naveed Quraishi
OZ3/Hardware and Software Engineering
OZ/Space Station Payloads Office
OA/International Space Station

R. David Hampton
R. David Hampton

Naveed Quraishi
Naveed Quraishi

Deformation and Flexibility Equations
For Idealized ARIS Umbilicals,
Under Planar End-Loading Conditions

Final Report

NAS/ASEE Summer Faculty Fellowship Program—2000

Johnson Space Center

Prepared By:	R. David Hampton, Ph.D., P.E.
Academic Rank:	Associate Professor
University & Department:	University of Alabama in Huntsville Mechanical and Aerospace Engineering Huntsville, Alabama 35899

NASA/JSC

Directorate:	OA/International Space Station
Division:	OZ/Space Station Payloads Office
Branch:	OZ3/Hardware and Software Engineering
JSC Colleague:	Naveed Quraishi
Date Submitted:	August 18, 2000
Contract Number:	NAG 9-867

ABSTRACT

The International Space Station (ISS) relies on the Active Rack Isolation System (ARIS) as the central component of an integrated, station-wide strategy to isolate microgravity space-science experiments. ARIS uses electromechanical actuators to isolate an International Standard Payload Rack (ISPR) from disturbances due to the motion of the ISS. Disturbances to microgravity experiments on ARIS-isolated racks are primarily transmitted via the ARIS power and vacuum umbilicals. Recent experimental tests indicate that these umbilicals resonate at frequencies outside the ARIS controller's bandwidth, at levels of potential concern for certain microgravity experiments. Reduction in the umbilical resonant frequencies could help to address this issue.

This report develops equations for the in-plane deflections and flexibilities of an idealized umbilical (thin, flexible, cantilever beam) under end-point, in-plane loading (inclined-force and moment). The effect of gravity is neglected due to the on-orbit application. The analysis assumes an initially straight, cantilevered umbilical with uniform cross-section, which undergoes large deflections with no plastic deformation, such that the umbilical terminus remains in a single quadrant and the umbilical slope changes monotonically. The analysis is applicable to the ARIS power and vacuum umbilicals, under the indicated assumptions.

NOMENCLATURE

Lower case

c_ξ	Cosine of angle ξ
p	Modulus of elliptic integral
s	Distance along umbilical from cantilevered end
s_ξ	Sine of angle ξ
y	Position coordinate
y_c	Position coordinate of umbilical terminus (point C)
z	Position coordinate
z_c	Position coordinate of umbilical terminus (point C)
α_i, α_{ij}	Normalized loads
β_i	Flexibility integrals
η	Shape kernel
ξ	Angle of umbilical tangent at arbitrary point R
ξ_c	Angle of umbilical tangent at terminal point C
ϕ	Amplitude of elliptic integral

Upper case

C_1	Integration constant
E	Young's modulus of elasticity
EI	Flexural rigidity
$F(p, \phi)$	Legendre's incomplete elliptic integral of the 1st kind
I	Area moment of inertia with respect to beam neutral axis
$K(p)$	Legendre's complete elliptic integral of the 1st kind
L	Umbilical length
M	Internal moment
M_x	Terminally applied moment about the x-axis
Q_y	Terminally applied force, y-direction
$-P_z$, Q_z	Terminally applied force, z-direction
R	Arbitrary point along umbilical

INTRODUCTION

The Active Rack Isolation System (ARIS) serves as the central component of an integrated, station-wide strategy to isolate microgravity space-science experiments on the International Space Station (ISS). ARIS uses eight electromechanical actuators to isolate an International Standard Payload Rack (ISPR) from disturbances due to the motion of the ISS; eleven ARIS racks are being developed for the ISS. Disturbances to microgravity experiments on ARIS-isolated racks are primarily transmitted via the (nominally thirteen) ARIS umbilicals, which provide power, data, vacuum, cooling, and other miscellaneous services to the experiments. The two power umbilicals and, to a lesser extent, the vacuum umbilical, serve as the primary transmission paths for acceleration disturbances. Experimental tests conducted by the ARIS team (December 1998) [1] indicate that looped power umbilicals resonate at about 10 Hz; unlooped power umbilicals resonate at about 4 Hz. In either case, the ARIS controller's limited bandwidth (about 2 Hz) admits only limited active isolation at these frequencies. Reduction in the umbilical resonant frequencies could help to address this problem.

Analytical studies of the nonlinear bending and deflection of a flexible cantilever beam (originally horizontal) have been conducted for a variety of loading conditions, including concentrated terminal transverse (vertical) loading [2, 3, 4, 5]; uniformly distributed vertical loading [2, 6, 7]; uniformly distributed normal loading [8]; concentrated terminal inclined loading [9, 10]; multiple concentrated vertical loads [11]; and concentrated terminal vertical and moment loading [11]. (See the thesis of Christopher Rojahn [12] for a thorough summary of the history up to 1968.) Typical exact solutions involve complete and incomplete elliptic integrals [e.g., 2, 11, 4, 5].

Equations for the case of general terminal in-plane loading (i.e., including both inclined-force and moment loads) have apparently not been determined. These and the corresponding in-plane flexibility (or stiffness) equations would be of particular interest toward umbilical design for microgravity-isolation purposes. The equations could be used to help optimize umbilical flexibilities and resonant frequencies for microgravity applications.

This paper develops equations for the in-plane deflections and flexibilities of an idealized umbilical (thin, flexible, cantilever beam) under terminal in-plane loading (inclined-force and moment). The effect of gravity can be neglected due to the on-orbit application. The analysis is applicable to an initially straight, cantilevered umbilical with uniform cross-section, which undergoes large deflections with no plastic deformation, such that the umbilical terminus remains in a single quadrant and the umbilical slope changes monotonically. The analysis would be applicable to the ARIS power and vacuum umbilicals, under the indicated assumptions.

PROBLEM STATEMENT

Consider an idealized umbilical of length L with end-points O and C and arbitrary intermediate point R (Figure 1). Let R be located at distance s along the umbilical, measured from the cantilevered end, with coordinates (z, y); the coordinates of point C are (z_c, y_c). The coordinates have been chosen to be consistent with the coordinate system in use for the existing analyses of ARIS, for dynamic-modeling and controller-design purposes; point O, then, is the umbilical point-of-attachment to the ISS, and point C is the point-of-attachment to the ISPR. Let ξ be the angle, at R, of the tangent to the umbilical; and let ξ_c represent the end-point angle, at C. Assume a specified flexural rigidity EI.

This paper accomplishes the following fundamental tasks: (1) to derive equations for the umbilical length, coordinates at arbitrary point R, and terminal coordinates (at C); and (2) to use these equations to derive useful equations for the six in-plane umbilical flexibilities. These nine equations will be expressed in terms of the angle ξ_c, and of the in-plane loads at C. These loads are as follows: forces Q_y and Q_z, in the positive y- and z-directions, respectively, and counter-clockwise (positive) moment M_x, about the positive x-axis.

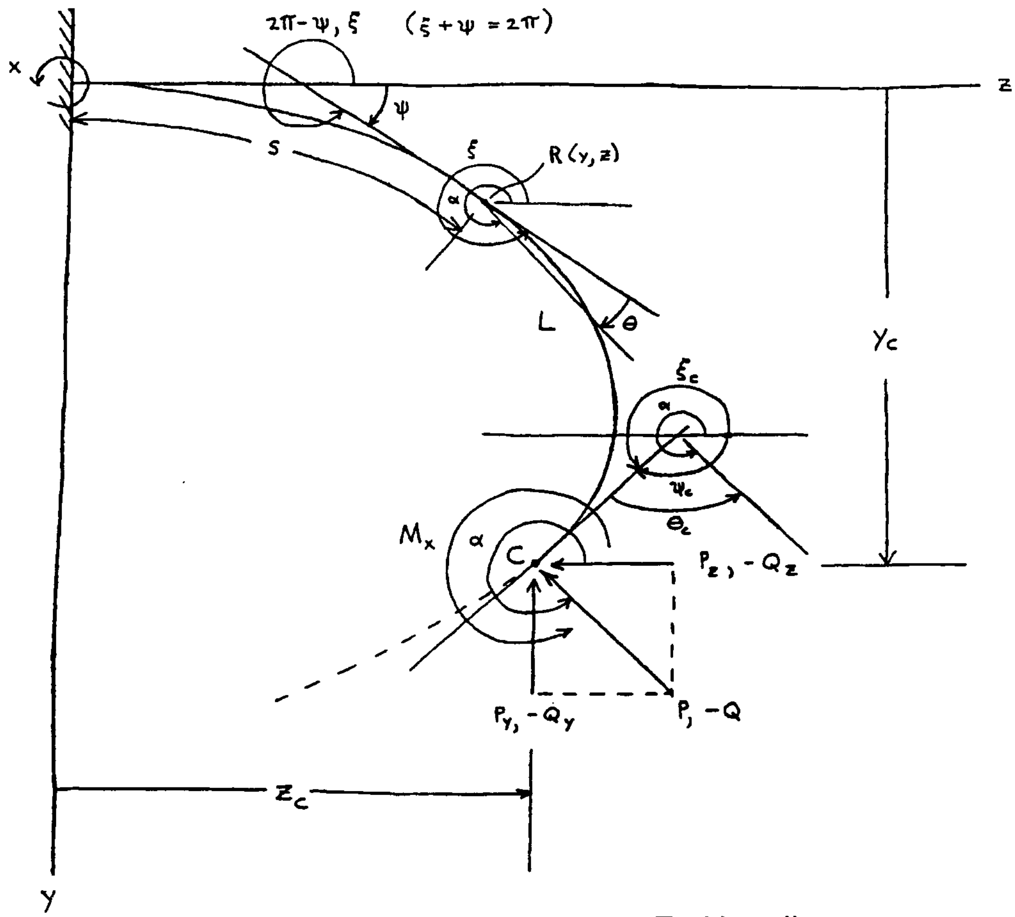

Figure 1. Flexible Umbilical under End Loading

EQUATIONS OF UMBILICAL GEOMETRY

At R the moment equation is $$M = EI\frac{d\xi}{ds} = M_x + Q_z(y_c - y) - Q_y(z_c - z). \tag{1}$$

Differentiating twice, observing that $$\frac{dy}{ds} = -\sin\xi \tag{2}$$

and $$\frac{dz}{ds} = \cos\xi, \tag{3}$$

and using the shorthand notation $s_\xi = \sin\xi$ and $c_\xi = \cos\xi$, one obtains

$$\frac{d^2\xi}{ds^2} = \frac{Q_z}{EI}s_\xi + \frac{Q_y}{EI}c_\xi. \tag{4}$$

Integration of Equation (4) yields $$\frac{1}{2}\left(\frac{d\xi}{ds}\right)^2 = \frac{1}{EI}\left(Q_y s_\xi - Q_z c_\xi\right) + C_1, \tag{5}$$

where C_1 is an integration constant. At point C, Equation (1) becomes

$$M_x = EI\left.\frac{d\xi}{ds}\right|_{R\to C}. \tag{6}$$

Applying this boundary condition to Equation (5), one has

$$C_1 = \frac{1}{2}\left(\frac{M_x}{EI}\right)^2 - \frac{1}{EI}\left(Q_y s_{\xi_c} - Q_z c_{\xi_c}\right), \tag{7}$$

so that Equation (5) can now be solved for $\frac{d\xi}{ds}$:

$$\frac{d\xi}{ds} = -\left\{\frac{2}{EI}\left[Q_y\left(s_\xi - s_{\xi_c}\right) - Q_z\left(c_\xi - c_{\xi_c}\right)\right] + \left(\frac{M_x}{EI}\right)^2\right\}^{1/2} = -\eta^{1/2}, \tag{8}$$

where the radicand $$\eta = \frac{2Q_y}{EI}\left(s_\xi - s_{\xi_c}\right) - \frac{2Q_z}{EI}\left(c_\xi - c_{\xi_c}\right) + \left(\frac{M_x}{EI}\right)^2. \tag{9}$$

Equation (8) applies under the assumption that the radicand η is nonnegative, or equivalently, that $\frac{d\xi}{ds}$ is nonpositive.

From Equation (8), $$ds = -\eta^{-1/2}d\xi, \tag{10}$$

which can be integrated to yield an expression for the umbilical length:

$$L = \int_0^L ds = \int_{2\pi}^{\xi_c} -\eta^{-1/2}d\xi = \int_{\xi_c}^{2\pi}\eta^{-1/2}d\xi. \tag{11}$$

From Equation (2), $$dy = s_\xi \eta^{-1/2}d\xi, \tag{12}$$

so that $$y = -\int_\xi^{2\pi}\eta^{-1/2}s_\xi d\xi \quad \text{and} \quad y_c = -\int_{\xi_c}^{2\pi}\eta^{-1/2}s_\xi d\xi. \tag{13, 14}$$

Likewise, Equation (3) yields $$z = \int_\xi^{2\pi}\eta^{-1/2}c_\xi d\xi \quad \text{and} \quad z_c = \int_{\xi_c}^{2\pi}\eta^{-1/2}c_\xi d\xi. \tag{15, 16}$$

Together, Equations (11) and (13) through (16) describe the umbilical geometry as functions of the terminal angle ξ_c; terminal loads Q_y, Q_z, and M_x; and integration-, or "shape" kernel η.

VALIDATION (SPECIAL CASES)

The umbilical geometric equations, (11) and (13) through (16), can be used to derive equations for umbilical in-plane flexibilities. First, however, it will be shown as a check of the mathematics that the geometric equations simplify in some special cases to known forms [11].

Horizontal Cantilever with Vertical Point Load at Free End

Consider the case where Q_y and M_x are both zero; this is Frisch-Fay's "basic strut" [11, p. 41].

Define, for convenience, $$P_z = -Q_z. \tag{17}$$

Equation (11) becomes $$L = \left(\frac{EI}{2P_z}\right)^{1/2} \int_{\xi_c}^{2\pi} \left(c_\xi - c_{\xi_c}\right)^{-1/2} d\xi, \tag{18}$$

which can be rewritten as $$L = \left(\frac{EI}{8P_z}\right)^{1/2} \int_{\xi_c}^{2\pi} \left(\sin^2\frac{\xi_c}{2} - \sin^2\frac{\xi}{2}\right)^{-1/2} d\xi. \tag{19}$$

Let $$p = \sin\frac{\xi_c}{2} \tag{20}$$

and select ϕ such that $$p\sin\phi = \sin\frac{\xi}{2}. \tag{21}$$

Taking the differential of the above, $$p\cos\phi\, d\phi = \frac{1}{2}\cos\frac{\xi}{2}\, d\xi. \tag{22}$$

From Equations (20) and (21), $$\sin^2\frac{\xi_c}{2} - \sin^2\frac{\xi}{2} = p^2\left(1 - \sin^2\phi\right); \tag{23}$$

as ξ varies from ξ_c to 2π, ϕ varies from $\frac{\pi}{2}$ to π. In this range,

$$-\cos\phi = \left(1 - \sin^2\phi\right)^{1/2} \text{ and } -\cos\frac{\xi}{2} = \left(1 - p^2\sin^2\phi\right)^{1/2}, \tag{24, 25}$$

so that $$d\xi = \frac{-2p\cos\phi\, d\phi}{\left(1 - p^2\sin^2\phi\right)^{1/2}}. \tag{26}$$

Finally, using Equations (23) and (26) in Equation (19), and simplifying, one obtains the following result:

$$L = \frac{1}{k}K(p), \tag{27}$$

where $$k^2 = \frac{P_z}{EI}, \tag{28}$$

and $$K(p) = F(p, \pi/2) = \int_0^{\pi/2} \left(1 - p^2\sin^2\varsigma\right)^{-1/2} d\varsigma. \tag{29}$$

$K(p)$ and $F(p, \phi)$, respectively, are Legendre's complete and incomplete elliptic integrals of the 1st kind [11, p. 5].

Horizontal Cantilever with Inclined Point Load at Free End

Consider next the case where Q_z and M_x are both zero. Equation (11) becomes

$$L = \left(\frac{EI}{2Q_y}\right)^{1/2} \int_{\xi_c}^{2\pi} \left(s_\xi - s_{\xi_c}\right)^{-1/2} d\xi. \tag{30}$$

Introduce ϕ and positive parameter p such that $$p^2 = \left(1 - \sin\xi_c\right)/2 \tag{31}$$

and $$\sin\phi = \left(\frac{1 - \sin\xi}{2p^2}\right)^{1/2}. \tag{32}$$

Squaring the above yields $$1-\sin\xi = 2p^2\sin^2\phi. \tag{33}$$

Taking the differential, $$\cos\xi\, d\xi = -4p^2\sin\phi\cos\phi\, d\phi, \tag{34}$$

so that $$d\xi = \frac{-4p^2\sin\phi\cos\phi}{\left(1-\sin^2\xi\right)^{1/2}}\, d\phi. \tag{35}$$

From Equation (33) one obtains $$1+\sin\xi = 2\left(1-p^2\sin^2\phi\right). \tag{36}$$

Equations (33) and (36) together yield

$$\left(1-\sin^2\xi\right)^{1/2} = 2p\sin\phi\left(1-p^2\sin^2\phi\right)^{1/2}. \tag{37}$$

As ξ varies from ξ_c to 2π, ϕ varies from $\frac{\pi}{2}$ to $\frac{1}{p\sqrt{2}}$. Using Equation (37) in (35) yields

$$d\xi = \frac{-2p\cos\phi\, d\phi}{\left(1-p^2\sin^2\phi\right)^{1/2}}. \tag{38}$$

Obtaining expressions for $\sin\xi_c$ and $\sin\xi$ from Equations (31) and (33), respectively, and substituting from these and Equation (35) into Equation (30), one obtains the following result:

$$L = \left(\frac{EI}{Q_y}\right)^{1/2} \int_m^{\pi/2} \left(1-p^2\sin^2\phi\right)^{-1/2} d\phi \tag{39}$$

where $$m = \sin^{-1}\frac{1}{p\sqrt{2}}. \tag{40}$$

In terms of elliptic integrals,

$$L = \left(\frac{EI}{Q_y}\right)^{1/2} \left[K(p) - F(p,m)\right], \tag{41}$$

the solution previously reported in [11], page 42.

EQUATIONS OF UMBILICAL FLEXIBILITY

The Nature of the Dependencies on Flexural Rigidity EI

It will now be shown that, for constant values of L, ξ_c, y_c, and z_c (i.e., umbilical length and terminal geometry), the following expressions are also constants: $\frac{Q_y}{EI}$, $\frac{Q_z}{EI}$, and $\frac{M_x}{EI}$. These facts will have important implications for umbilical shapes and flexibilities.

Define the following, for two umbilicals $(i = 1, 2)$ having the same flexural rigidity and terminal angle, but with but different terminal loads:

$$L_i = L(\eta_i) = \int_{\xi_c}^{2\pi} \eta_i^{-1/2} d\xi > 0, \tag{42}$$

$$y_{ci} = y_c(\eta_i) = \int_{\xi_c}^{2\pi} \eta_i^{-1/2} c_\xi d\xi > 0, \tag{43}$$

and
$$z_{ci} = z_c(\eta_i) = \int_{\xi_c}^{2\pi} \eta_i^{-1/2} s_\xi d\xi > 0, \tag{44}$$

where
$$\eta_i = 2\alpha_{1i}\left(s_\xi - s_{\xi_c}\right) + 2\alpha_{2i}\left(c_\xi - c_{\xi_c}\right) + \alpha_{3i}^2 > 0, \tag{45}$$

for
$$\alpha_{1i} = \frac{Q_{yi}}{EI}, \tag{46}$$

$$\alpha_{2i} = \frac{Q_{zi}}{EI}, \tag{47}$$

and
$$\alpha_{3i} = \frac{M_{xi}}{EI}. \tag{48}$$

The terminal angle is assumed to be arbitrary, fixed between π and 2π. Then the following obtains:

$$\left.\begin{matrix} L_1 = L_2 \\ y_{c1} = y_{c2} \\ z_{c1} = z_{c2} \end{matrix}\right\} \Leftrightarrow \eta_1 = \eta_2 \Leftrightarrow \left\{\begin{matrix} \alpha_{11} = \alpha_{12} \\ \alpha_{21} = \alpha_{22} \\ \alpha_{31} = \pm\alpha_{32} \end{matrix}\right. . \tag{49}$$

The former "if-and-only-if" statement is true based on the orthogonality of the constant, cosine, and sine functions. As for the latter, using Equation (45),

$$\eta_1(\xi) = \eta_2(\xi) \ \forall \pi \le \xi_c \le 2\pi \Leftrightarrow \left\{\begin{matrix} \alpha_{11} = \alpha_{12}, \\ \alpha_{21} = \alpha_{22}, \quad \text{and} \\ \alpha_{31}^2 - \alpha_{11}s_{\xi_c} - \alpha_{21}c_{\xi_c} = \alpha_{32}^2 - \alpha_{12}s_{\xi_c} - \alpha_{22}c_{\xi_c}. \end{matrix}\right. \tag{50}$$

The third right-hand-side equation will be true if and only if $\alpha_{31}^2 = \alpha_{32}^2$, (51)

since the first two right-hand-side equations must hold. Since $\frac{Q_y}{EI}$, $\frac{Q_z}{EI}$, and $\frac{M_x}{EI}$ are constants (for fixed umbilical length and terminal geometry), changing the flexural rigidity by some factor γ changes all of the terminal loads by the same factor. Further, from Equations (13) and (15) the umbilical shape will also remain unchanged. The implications for in-plane umbilical stiffnesses will be explored in the next section.

Basic Flexibility Equations

For given terminal geometry (ξ_c, y_c, and z_c), Leibnitz' Rule can now be applied to Equations (11), (14), and (16) to yield expressions for the six in-plane flexibilities. Applying Leibnitz' Rule to Equations (14) and (16), one obtains the following initial expressions for the flexibilities:

$$\frac{\partial y_c}{\partial Q_y} = \frac{1}{EI}\int_{\xi_c}^{2\pi} \eta^{-3/2} s_\xi \left[\left(s_\xi - s_{\xi_c}\right) - \mu \frac{\partial \xi_c}{\partial Q_y}\right] d\xi + \frac{EI}{M_x}\frac{\partial \xi_c}{\partial Q_y}, \tag{52}$$

$$\frac{\partial y_c}{\partial Q_z} = \frac{-1}{EI}\int_{\xi_c}^{2\pi} \eta^{-3/2} s_\xi \left[\left(c_\xi - c_{\xi_c}\right) + \mu \frac{\partial \xi_c}{\partial Q_z}\right] d\xi + \frac{EI}{M_x}\frac{\partial \xi_c}{\partial Q_z}, \tag{53}$$

$$\frac{\partial z_c}{\partial M_x} = \frac{-1}{EI}\int_{\xi_c}^{2\pi} \eta^{-3/2} c_\xi \left[\left(\frac{-M_x}{EI}\right) + \mu \frac{\partial \xi_c}{\partial M_x}\right] d\xi + \frac{EI}{M_x}\frac{\partial \xi_c}{\partial M_x}, \tag{54}$$

$$\frac{\partial z_c}{\partial Q_y} = \frac{-1}{EI}\int_{\xi_c}^{2\pi} \eta^{-3/2} c_\xi \left[\left(s_\xi - s_{\xi_c}\right) - \mu \frac{\partial \xi_c}{\partial Q_y}\right] d\xi - \frac{EI}{M_x}\frac{\partial \xi_c}{\partial Q_y}, \tag{55}$$

$$\frac{\partial z_c}{\partial Q_z} = \frac{1}{EI}\int_{\xi_c}^{2\pi} \eta^{-3/2} c_\xi \left[\left(c_\xi - c_{\xi_c}\right) + \mu \frac{\partial \xi_c}{\partial Q_y}\right] d\xi - \frac{EI}{M_x}\frac{\partial \xi_c}{\partial Q_y}, \tag{56}$$

and

$$\frac{\partial z_c}{\partial M_x} = \frac{1}{EI}\int_{\xi_c}^{2\pi} \eta^{-3/2} c_\xi \left[\left(\frac{-M_x}{EI}\right) + \mu \frac{\partial \xi_c}{\partial M_x}\right] d\xi - \frac{EI}{M_x}\frac{\partial \xi_c}{\partial M_x}; \tag{57}$$

where

$$\eta = \frac{2Q_y}{EI}\left(s_\xi - s_{\xi_c}\right) - \frac{2Q_z}{EI}\left(c_\xi - c_{\xi_c}\right) + \left(\frac{M_x}{EI}\right)^2, \tag{58}$$

and

$$\mu = c_{\xi_c} Q_y + s_{\xi_c} Q_z. \tag{59}$$

The partial derivatives on the right-hand-sides of Equations (52) through (57) can be found by applying Leibnitz' Rule to Equation (11), to yield the following:

$$\frac{\partial \xi_c}{\partial Q_y} = \frac{\dfrac{-M_x}{(EI)^2}\displaystyle\int_{\xi_c}^{2\pi} \eta^{-3/2}\left(s_\xi - s_{\xi_c}\right) d\xi}{1 - \dfrac{M_x}{(EI)^2}\mu \displaystyle\int_{\xi_c}^{2\pi} \eta^{-3/2}\, d\xi}, \tag{60}$$

$$\frac{\partial \xi_c}{\partial Q_z} = \frac{\dfrac{-M_x}{(EI)^2}\displaystyle\int_{\xi_c}^{2\pi} \eta^{-3/2}\left(c_\xi - c_{\xi_c}\right) d\xi}{1 - \dfrac{M_x}{(EI)^2}\mu \displaystyle\int_{\xi_c}^{2\pi} \eta^{-3/2}\, d\xi}, \tag{61}$$

and

$$\frac{\partial \xi_c}{\partial M_x} = \frac{\dfrac{-M_x^{\,2}}{(EI)^3}\displaystyle\int_{\xi_c}^{2\pi} \eta^{-3/2}\, d\xi}{1 - \dfrac{M_x}{(EI)^2}\mu \displaystyle\int_{\xi_c}^{2\pi} \eta^{-3/2}\, d\xi}. \tag{62}$$

Substituting from Equations (60) through (62) into Equations (52) through (57), one finally obtains the desired expressions for the flexibilities. For example, substituting from Equation (60) into Equation (52) yields

$$\frac{\partial y_c}{\partial Q_y} = \frac{1}{EI}\left\{\int_{\xi_c}^{2\pi} \eta^{-3/2} s_\xi \left(s_\xi - s_{\xi_c}\right) d\xi \right.$$
$$\left. - \frac{1 - \dfrac{M_x}{EI}\times\dfrac{\mu}{EI}\displaystyle\int_{\xi_c}^{2\pi} \eta^{-3/2} s_\xi\, d\xi}{1 - \dfrac{M_x}{EI}\times\dfrac{\mu}{EI}\displaystyle\int_{\xi_c}^{2\pi} \eta^{-3/2}\, d\xi} \times \int_{\xi_c}^{2\pi} \eta^{-3/2}\left(s_\xi - s_{\xi_c}\right) d\xi \right\}. \tag{63}$$

Note that the expression in the curly brackets is invariant with *EI*. Corresponding expressions for the other flexibilities can be found in similar manner; each will have a similar form [see Equations (75) through (80) below.] The flexibilities, then, are all inversely proportional to the flexural rigidity.

Simplified Flexibility Equations

For convenience define the following normalized loads and flexibility integrals:

$$\alpha_1 = \frac{Q_y}{EI}, \tag{64}$$

$$\alpha_2 = \frac{Q_z}{EI}, \tag{65}$$

$$\alpha_3 = \frac{-M_x}{EI}, \tag{66}$$

$$\alpha_4 = \frac{\mu}{EI} = c_{\xi_c}\alpha_1 + s_{\xi_c}\alpha_2, \tag{67}$$

$$\beta_1 = \int_{\xi_c}^{2\pi} \eta^{-3/2} d\xi, \tag{68}$$

$$\beta_2 = \int_{\xi_c}^{2\pi} \eta^{-3/2} c_\xi d\xi, \tag{69}$$

$$\beta_3 = \int_{\xi_c}^{2\pi} \eta^{-3/2} s_\xi d\xi, \tag{70}$$

$$\beta_4 = \int_{\xi_c}^{2\pi} \eta^{-3/2} c_\xi^2 d\xi, \tag{71}$$

$$\beta_5 = \int_{\xi_c}^{2\pi} \eta^{-3/2} c_\xi s_\xi d\xi, \tag{72}$$

and

$$\beta_6 = \int_{\xi_c}^{2\pi} \eta^{-3/2} s_\xi^2 d\xi, \tag{73}$$

where

$$\eta = 2\alpha_1\left(s_\xi - s_{\xi_c}\right) - 2\alpha_2\left(c_\xi - c_{\xi_c}\right) + \alpha_3^2. \tag{74}$$

Using these symbols the in-plane flexibility equations are as follows:

$$\frac{\partial y_c}{\partial Q_y} = \frac{1}{EI}\left[\left(\beta_6 - s_{\xi_c}\beta_3\right) - \left(\beta_3 - s_{\xi_c}\beta_1\right)\left(\frac{1+\alpha_3\alpha_4\beta_3}{1+\alpha_3\alpha_4\beta_1}\right)\right], \tag{75}$$

$$\frac{\partial y_c}{\partial Q_z} = \frac{-1}{EI}\left[\left(\beta_5 - s_{\xi_c}\beta_3\right) - \left(\beta_2 - c_{\xi_c}\beta_1\right)\left(\frac{1+\alpha_3\alpha_4\beta_3}{1+\alpha_3\alpha_4\beta_1}\right)\right], \tag{76}$$

$$\frac{\partial y_c}{\partial M_x} = \frac{-\alpha_3}{EI}\left[\beta_3 - \beta_1\left(\frac{1+\alpha_3\alpha_4\beta_3}{1+\alpha_3\alpha_4\beta_1}\right)\right], \tag{77}$$

$$\frac{\partial z_c}{\partial Q_y} = \frac{-1}{EI}\left[\left(\beta_5 - s_{\xi_c}\beta_2\right) - \left(\beta_3 - s_{\xi_c}\beta_1\right)\left(\frac{1+\alpha_3\alpha_4\beta_2}{1+\alpha_3\alpha_4\beta_1}\right)\right], \tag{78}$$

$$\frac{\partial z_c}{\partial Q_z} = \frac{1}{EI}\left[\left(\beta_4 - c_{\xi_c}\beta_2\right) - \left(\beta_2 - c_{\xi_c}\beta_1\right)\left(\frac{1+\alpha_3\alpha_4\beta_2}{1+\alpha_3\alpha_4\beta_1}\right)\right], \tag{79}$$

and

$$\frac{\partial z_c}{\partial M_x} = \frac{\alpha_3}{EI}\left[\beta_2 - \beta_1\left(\frac{1+\alpha_3\alpha_4\beta_2}{1+\alpha_3\alpha_4\beta_1}\right)\right], \tag{80}$$

where α_3 and the square-bracketed expressions are all invariant with EI. This means physically that changing the flexural rigidity by some factor γ changes all of the in-plane stiffnesses by the same factor.

IMPLICATIONS FOR UMBILICAL DESIGN

The foregoing equations can be used as an aid for designing umbilicals to minimize stiffness. First, as previously noted, each of the flexibility equations can be expressed in a form showing it to be inversely proportional to the flexural rigidity [Eqs. (75) through (80)]. Consequently, reductions in flexural rigidity will produce proportional reductions in all in-plane stiffnesses. Second, it was shown that for a fixed umbilical geometry, changes in flexural rigidity will produce proportional changes in all of the terminal (in-plane) loads. Third, for given umbilical length L, and end-point conditions ξ_c, z_c, and y_c, Equations (11), (14), and (16) can be solved for the loads Q_y, Q_z, and M_x. These loads can be determined and used iteratively in Equations (75) through (80) to maximize umbilical flexibilities (or, equivalently, to minimize the corresponding stiffnesses) using L as a parameter. And fourth, the umbilical designer can use the preceding equations to determine optimal L, ξ_c combinations. Although the angle ξ_c is fixed at about 225° for ARIS (in the "home," or centered, position); L, ξ_c optimization could suggest better angles for future designs.

CONCLUSION

In summary, this paper presented equations for the shape and flexibility of an umbilical on orbit (i.e., such that gravity can be neglected), under terminal in-plane loading conditions of even sufficient magnitude to cause large deformations. The umbilical was assumed to be initially straight, to have a uniform cross-section, and to undergo no plastic deformation. All in-plane stiffnesses were shown to be proportional to the flexural rigidity EI. An approach was offered for using umbilical length and terminal geometry (end-point locations and slopes) to optimize these umbilical stiffnesses. The basic equations were shown to reduce to previously published results for special loading conditions.

REFERENCES

1) Edberg, Donald L., and Wilson, Bruce W., "Design and Testing of Reduced-Stiffness Umbilicals for Space Station Microgravity Isolation," AIAA 2000-1408, Apr. 2000.
2) Hummel, F. H., and Morton, W. B., "On the large deflection of thin flexible strips and the measurement of their elasticity," *Philosophical Magazine*, Series 7, Vol. 17, 1927, pp. 348-357.
3) Gross and Lehr, *Die Federn*, Berlin V. D. I. Verlag, 1938.
4) Barten, H. J., "On the deflection of a cantilever beam," *Quarterly of applied Mathematics*, Vol. 2, 1944, pp. 168-171; Vol. 3, 1945, pp. 275-276.
5) Bisshopp, K. E., and Drucker, D. C., "Large deflections of cantilever beams," *Quarterly of Applied Mathematics*, Vol. 3, Oct. 1945, pp. 272-275.
6) Bickley, W. G., "The heavy elastica," *Philosophical Magazine*, Series 7, Vol. 17, 1934, pp. 603-622.
7) Rohde, F. V., "Large deflections of a cantilever beam with a uniformly distributed load," *Quarterly of Applied Mathematics*, Vol. 11, 1953, pp. 337-338.
8) Mitchell, T. P., "The non-linear bending of thin rods," *Journal of Applied Mechanics*, Vol. 26, Trans. ASME, Vol 81, Series E, 1959, pp. 40-43.
9) Beth, R. A., and Wells, C. P., "Finite deflections of a cantilever strut," *Journal of Applied Physics*, Vol. 22, 1951, pp. 742-746.
10) Massoud, M. F., "On the problem of large deflection of a cantilever beam," *International Journal of Mechanical Sciences*, Vol. 8, Feb. 1966, pp. 141-143.
11) Frisch-Fay, R., *Flexible Bars*, Butterworth and Co., Limited, Great Britain, 1962.
12) Rojahn, C., "Large Deflections of Elastic Beams," thesis for the Degree of Engineer, Stanford University, June 1968.

Design of a Gas-SWNT Interaction Test Module

Robert Hauge
Rice University
Department of Chemistry
Dec. 12, 2000

Alice Lee
SR&QA Office
Technology Division, NX

Robert H. Hauge

Alice Lee

Design of a Gas-Single Wall Nanotube (SWNT) Interaction Test Module

Final Report
NASA/ASEE Summer Faculty Fellowship Program
Johnson Space Center

Prepared by:	Robert H. Hauge
Academic Rank:	Distinguished Faculty Fellow
University & Department:	Rice University Department of Chemistry Houston,Tx
NASA/JSC	
Directorate:	SR & QA Office
Division:	Technology Division (NX)
JSC Colleague:	Alice Lee

Date submitted:	Dec. 12, 2000
Contract Number:	NAG 9-867

DESIGN OF A GAS-SWNT INTERACTION TEST MODULE

Robert H. Hauge
Rice University

Abstract

A gas-SWNT interaction test module was designed and constructed. The purpose of the module is to quantitatively measure the electrical response of SWNTs to a variety of gases. This is accomplished by monitoring the electrical response of a SWNT packed column to specific gases. The apparatus is similar to a gas chromatograph with the difference that the movement of gas is tracked by monitoring the electrical resistivity at the beginning and end of the column. The change in electrical resistivity as a function of the amount of gas injected, the time required to transit the column and their respective dependence on temperature will be documented.

INTRODUCTION

Rice university investigators have led the way with respect to production and characterization of single wall carbon nanotubes. New production methods sponsored by NASA are now coming on line that will dramatically increase the availability and decrease the price of single wall carbon nanotubes. Methods to separate nanotubes by diameter and length are also funded and ongoing at Rice. Thus development of sensor applications that utilize the availability of nanotubes is timely.

Single wall carbon nanotubes are a new material with a very unusual property in that all carbon atoms are surface atoms. Thus anything that adsorbs on the surface will significantly affect the electrical and optical properties of single wall carbon nanotubes. These changes can be monitored such that parts per thousand of a monolayer on the nanotubes are detectable. This translates into parts-per-billion sensitivity for toxic species.

The unique sensitivity of the electrical properties of SWNTs to gas adsorption is expected to lead to the development of sensors that rapidly and continuously detect very low levels of toxic gases such as ammonia, hydrazine, halogens, nitrogen oxides and acids. Measurement of the responsivity of SWNTs to specific concentrations of various gases is needed for evaluation of the potential of SWNTs gas sensors. We have designed and built a gas chromatograph with a unique SWNT column that provides a measure of relative responsivities for various gases. This gas-SWNT interaction test module is described in the following section.

GAS-SWNT TEST MODULE

An intial version of the test module has been built during the summer and is currently being instrumented for controlled gas flow and accurate resistivity measurements. The module consists of a packed column of silica microspheres that have been coated with SWNTs. Surface area measurements were performed on the SWNT material used to make the column. These measurements show that the SWNT materials have a surface area between 300 and 600 square meters per gram. This large surface area makes SWNTs ideal for gas sensing.

A voltage drop is imposed along the column by two electrodes placed at the beginning and end of the column. Additional electrodes with a spacing of approximately one millimeter are placed near the beginning and end of the column to measure resistivity changes as a gas pulse passes through the column. Inert gas is continuously passed through the column in a temperature-controlled environment. Operation involves injecting a sample into the inert gas stream and following the change in conductivity at the beginning of the column and at the end of the column. The time that a gas requires to move through the column, the dependence on column temperature and the smallest detectable amount of gas will be determined for a variety of gases and volatile liquids. .

The test module will be operated jointly with NASA and Rice personnel during the next year. Measurements will be made that allow the prediction of the ultimate sensitivity of sensors that use single wall carbon nanotubes as both the adsorbing and sensing element. These measurements will be used to construct a database characterizing the response of SWNTs to different gases. This database will be utilized to design and qualify SWNT based sensors.

USER AND TASK ANALYSIS OF THE FLIGHT SURGEON CONSOLE AT THE MISSION CONTROL CENTER OF THE NASA JOHNSON SPACE CENTER

Kathy A. Johnson
Assistant Professor

Molly C. Shek
Graduate Student

University of Texas, Houston
JSC Mail Code SD
August 2000

Patrick J. McGinnis, M.D.
Medical Operations Branch
Medical Sciences Division
Space and Life Sciences Directorate

Kathy A. Johnson, Ph.D.

Molly C. Shek, graduate student

Patrick McGinnis, M.D.

USER AND TASK ANALYSIS OF THE FLIGHT SURGEON CONSOLE AT THE MISSION CONTROL CENTER OF THE NASA JOHNSON SPACE CENTER

Final Report

NASA/ASEE Summer Faculty Fellowship Program—2000

Johnson Space Center

Prepared By:	Kathy. A. Johnson, Ph.D.
Academic Rank:	Assistant Professor
Prepared By:	Molly Shek, graduate student
University & Department:	University of Texas Health Science Center at Houston
	7000 Fannin, Suite 690
	Houston, Texas 77030
NASA/JSC	
Directorate:	Space & Life Sciences
Division:	Medical Sciences
Branch:	Medical Operations
JSC Colleague:	Patrick McGinnis, M.D.
Date Submitted:	August 11, 2000
Contract Number:	NAG 9-867

ABSTRACT

Astronauts in a space station are to some extent like patients in an intensive care unit (ICU). Medical support of a mission crew will require acquisition, transmission, distribution, integration, and archiving of significant amounts of data. These data are acquired by disparate systems and will require timely, reliable, and secure distribution to different communities for the execution of various tasks of space missions. The goal of the Comprehensive Medical Information System Project at Johnson Space Center Flight Medical Clinic is to integrate data from all Medical Operations sources, including the reference information sources and the electronic medical records of astronauts. A first step toward the full CMIS implementation is to integrate and organize the reference information sources and the electronic medical record with the Flight Surgeons' console. In order to investigate this integration, we need to understand the usability problems of the Flight Surgeon's console in particular and medical information systems in general. One way to achieve this understanding is through the use of user and task analyses whose general purpose is to ensure that only the necessary and sufficient task features that match users' capacities will be included in system implementations.

The goal of this summer project was to conduct user and task analyses employing cognitive engineering techniques to analyze the task of the Flight Surgeons and Biomedical Engineers (BMEs) while they worked on Console. The techniques employed were user interviews, observations and a questionnaire to collect data for which a hierachical task analysis and an information resource assessment were performed. They are described in more detail below. Finally, based on our analyses, we make recommendations for improvements to the support structure.

INTRODUCTION

Astronauts in a space station are to some extent like patients in an intensive care unit (ICU). Medical support of a mission crew will require acquisition, transmission, distribution, integration, and archiving of significant amounts of data. These data are acquired by disparate systems and will require timely, reliable, and secure distribution to different communities for the execution of various tasks of space missions. The goal of the Comprehensive Medical Information System Project at Johnson Space Center Flight Medical Clinic is to integrate data from all Medical Operations sources, including the reference information sources and the electronic medical records of astronauts. A first step toward the full CMIS implementation is to integrate and organize the reference information sources and the electronic medical record with the Flight Surgeons' console. In order to investigate this integration, we need to understand the usability problems of the Flight Surgeon's console in particular and medical information systems in general. One way to achieve this understanding is through the use of user and task analyses whose general purpose is to ensure that only the necessary and sufficient task features that match users' capacities will be included in system implementations.

The goal of this summer project was to conduct user and task analyses employing cognitive engineering techniques to analyze the task of the Flight Surgeons and Biomedical Engineers (BMEs) while they worked on Console. The techniques employed were user interviews, observations and a questionnaire to collect data for which a hierachical task analysis and an information resource assessment were performed. They are described in more detail below. Finally, based on our analyses, we make recommendations for improvements to the support structure.

Our project supports the NASA Strategic Plan For Medical Informatics: Telemedicine and Telehealth, January 2000. According to the Executive Summary, the last several years have seen a rapid evolution in technology in communications, information systems, and medical care. The evaluation and ongoing efforts to integrate these three domains continue to be the focal point of NASA's telemedicine, telehealth, and medical informatics development. Medical informatics will become the center of medical care and not simply a tool for medical care.

METHODS

Review of Johnson Space Center Information

Johnson Space Center is like any large organization that has its distinct culture. In order to understand the background and the operations of the study subjects, the analysts started by reviewing the manuals and documents that the subjects use or are trained with. A description of these resources may be obtained from the researchers. Many of these documents have an acronym attachment due to the fact that many acronyms are context specific – i.e. the same acronym may be used in more than one area to mean different things. The document review provided the analysts with excellent views of the intricate procedures and diverse functions of the various aspects of space flight. In addition to the document review, the analysts gained background and context information by attending seminars, workshops, and tours of Johnson Space Center. This provided them with improved understanding and profound appreciation of the Mission, Vision, the monumental accomplishments, and the tremendous challenges of Johnson Space Center and NASA.

Task Data Collection Methods

Data collection is a prerequisite of any form of task analysis (Kirwan, & Ainsworth, 1992). We collected data by the following methods: Observation, Questionnaire, and Unstructured Interview.

Observation

The objective was to obtain data by directly observing the activity and behavior of the Flight Surgeons and BMEs while they were working on console. The analysts attended simulations of both shuttle missions and international space station missions and observed Flight Surgeons and Biomedical Engineers while they worked on console. One analyst would observe the Flight Surgeon in Mission Control while another analyst would observe the BMEs in the Multi-purpose Service Room. The subjects were informed that the analysts were there to observe unobtrusively. Questions could be asked of the subjects and the subjects would only respond if that did not interfere with their job performance.

Videotape was made of the BMEs while they worked on two shuttle mission simulations. These tapes were later reviewed for useful information. While this is generally a good data collection method, the particular simulations observed in this manner had sparse activity and so the videotapes provided no additional information over the notes taken during observation. Discussion of future use of this technique will be presented in the recommendations section.

Unstructured Interview

Unstructured interviews were used during all stages of information gathering. (Kirwan, & Ainsworth, 1992). The analysts performed some unstructured interviews during mission simulations. Additional interviews were scheduled with Flight Surgeons and BMEs to investigate specific issues such as a) what set of information resources is available in paper form; b) how are updates to the information resources performed; c) what electronic resources are available; d) what are the differences in resources between shuttle and ISS; and e) what is the current state of the electronic patient record.

Questionnaire

The questionnaire was designed for the Flight Surgeons and BMEs in order to determine which information resources are being used and what types of support might be useful. The information gleaned from the unstructured interviews was used to design this questionnaire. A copy of the survey may be obtained from the researchers. The criteria were:

- To make the questions direct and informative
- Use multiple choice questions with comment sections for adding information
- The answer selections must include a full range of significant alternatives

- The questionnaire must be anonymous; and must not require more than ten minutes to complete.

The questionnaire was distributed to Flight Surgeons in hardcopy form and collected during a regular meeting. Additional results were collected using a web-based survey form. The questionnaire was administered to BMEs through the web-based survey. Responses were obtained from 70% of the Flight Surgeons. Data collection has not yet been completed for the BMEs.

RESULTS

Information Assessment Index

The Information Assessment Index was utilized to organize the huge amount of information that was gathered (William Pena, 1979). There are two major components to this index: Function and Form. For each, the goals, facts, concepts, needs, and issues are listed. This may be obtained from the researchers.

Task Analysis of Flight Surgeon and Biomedical Engineer on Console

A hierarchical task analysis was performed. Results are presented here for the Flight Surgeon portion of the task analysis. Flight Surgeons and BMEs have intersecting task sets. The primary differences are:

1) The BME sets up the equipment and materials for the Private Medical Conference (PMC) and serves as a resource locator rather than performing the PMC which is the task of the Flight Surgeon.
2) The BME is the person who is primarily responsible for diagnosing medical equipment problems.

It should also be noted that there are differences in the resources available for Shuttle and ISS. Although many of the same types of resources are available, the terminology used is often different (e.g. EECOM for Shuttle versus ECLSS for ISS).

The hierarchical task analysis is displayed in two forms. Figure 1 shows a graphical representation of the task/subtask hierarchy. Following that, Table 1 gives the specific descriptions of the higher level tasks.

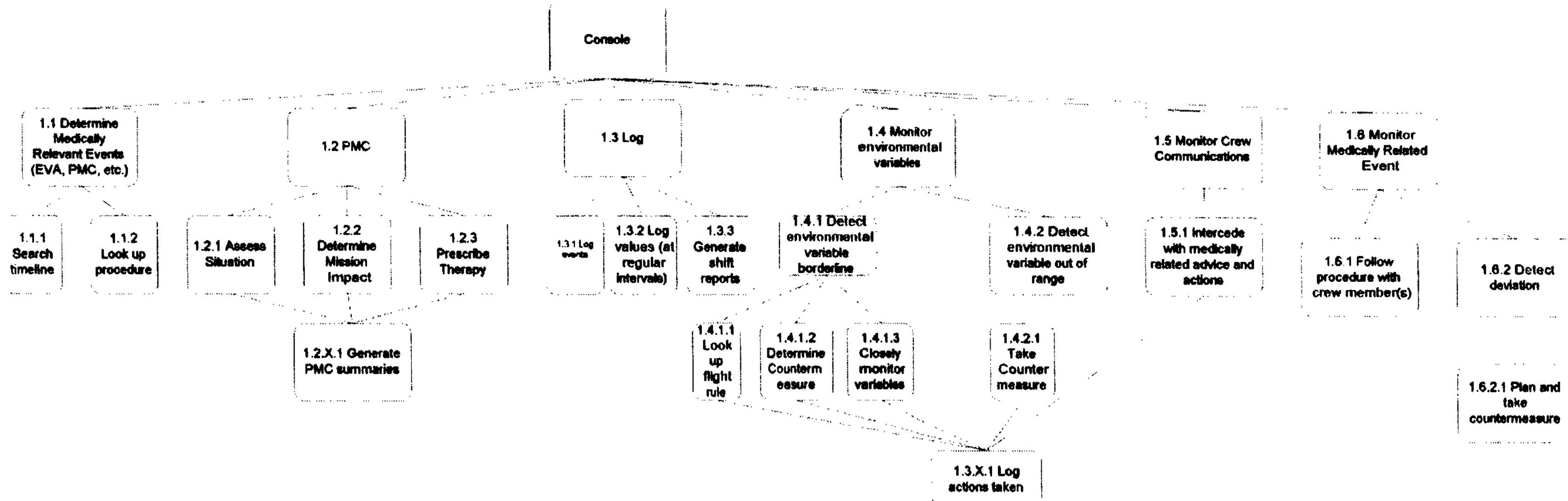

Figure 1: Flight Surgeon Task Hierarchy

Table 1 Task descriptions

Task Element	
1.1 Determine medically relevant events (EVA, PMC etc.)	**Purpose** To determine events that would fall within the purview of the Flight Surgeons and BMEs (i.e. have medical implications or use medical devices) These generally have the potential to develop into abnormal situations.
	Decision Alternatives Make knowledge based decision for actions.
	Displays Timelines on PC (ISS – interactive, STS – static)
	Actions Monitor Timelines. Look up procedures in flight rules and Missions Information Package
	Information Sources Timelines, Flight rules, Mission Information Package
1.4 Monitor Environmental Variables	**Purpose** To monitor environmental variables that have the potential to develop into abnormal situations
	Decision Alternatives Determine if environmental variables are near range boundaries or out of range. Locate in information materials the constraints or counter measures involved. Make knowledge based decisions.
	Displays Environmental variables on DEC Alpha Timeline on PC (ISS – interactive, STS – static) Procedures on PC
	Actions Take appropriate actions based on flight rules Log the actions taken
	Information Sources Flight Rules, Timelines, Flip File, DCS manual, Medical Record, Environmental Display, log, SOMS/CHeCS Reference, Medical References/texts, Toxicology Web Site, Toxicology Ref (TOMES), Radiation Web Sites, Mission Support Medical Operations JSC Web Site.
1.4.1 Detect environmental controls near range boundary	**Purpose** To make timely decisions and take appropriate counter measures to maintain crewmembers' health and safety. To prepare for the possibility that actions may become necessary due to environmental changes.
	Decision Alternatives Make decisions on whether to initiate counter measures to maintain crew members' health and safety

	Display Orange value in environmental display on DEC Alpha
	Actions Maintain close monitor of those environmental controls. Log values/times. Look up appropriate rules. Determine actions that may become necessary. Determine materials necessary to take countermeasures. Locate materials. Locate crewmembers procedures if necessary. (e.g. method for replacing CO2 filter).
	Information Sources DEC Alpha environmental displays, Flight Rules (hardcopy)
1.4.2 Detect environmental controls out of range boundary	**Purpose** To initiate counter measures.
	Decision Alternatives Make decisions to initiate counter measures to maintain crew members' health and safety
	Display Red value in environmental display on DEC Alpha
	Actions Take counter measure actions. Monitor crew performance. Continue to monitor/log values.
	Information Sources DEC Alpha environmental displays, Flight Rules (hardcopy)
1.5 Monitor crew communications	**Purpose** To keep abreast of the mental and physical conditions of the crew and detect any factors that may affect the health and safety of the crew members
	Decision Alternatives Decide when and where to intercede with medically related advice and actions
	Display Maintain open channels on DVIS between crewmembers and CAP COM, CAP COM and Flight Director and others as appropriate.
	Action Take actions to maintain the health and safety of the crew members
	Information Sources DVIS, DEC Alpha environmental displays
1.6 Monitor Medically Related Events: EVA, use of medical devices	**Purpose** To react promptly and efficiently and to act within Flight Rule Guidelines BME to detect and handle mechanical/device problems
	Decision Alternatives When deviations from planned procedures occur, decide on

	actions to safe guard crews' health and also impact on the mission.
	Display Timeline on PC. DEC Alpha bioenvironmental displays.
	Action Detect deviations. Follow procedures in Flight Rules. Take counter measures when indicated.
	Information Sources DVIS, DEC Alpha, Timeline on PC, Flight Rules (hardcopy), MIP (Mission Information Packet – hardcopy),
1.2 PMC routine (weekly in case of ISS)	**Purpose** To perform a checkup of a crewmember for various purposes including: routine physical (weekly on ISS), pre-EVA; post-EVA, or crewmember has requested one. To detect any deviations from the Astronauts' general health status.
	Decision Alternatives No change in daily schedule. Modification of work or exercise schedules. Prescribe the necessary medications. Determine mission impact.
	Display OCA communications. DVIS. Ku band
	Action Flight Surgeon go to MPSR to perform PMC. Modification of work or exercise schedules. Prescribe medications. Inform Flight Controller of Mission Impact. Generate PMC summary.
	Information Sources Flight Rules. Timelines. Flip Chart. DCS manual. Medical Record. Environmental Displays. Log. SOM/CHeCS References. Medical References/texts. Toxicology We sites. Toxicology Ref (TOMES). Radiation Web Sites.
1.3 Log	**Purpose** To keep records of events, environmental variables, decisions, results of actions, and generate shift reports..
	Decision Alternatives Make decisions to enter pertinent information into log
	Displays PC displays template for log or use paper log form.
	Actions Document events, decisions, and results of those decisions along with the times that they occurred. Document environmental variables at intervals. Generate shift reports.
	Information Sources Flight Rules, Timelines, Flip File, DCS manual, Medical Record, Environmental Display, log, SOMS/CHeCS Reference, Medical References/texts, Toxicology Web Site, Toxicology Ref (TOMES), Radiation Web Sites, Mission

	Support Medical Operations JSC Web Site.

Questionnaire Results

A preliminary analysis of the questionnaire data shows that Flight Surgeons do indeed use most of the resource materials that the analysts found and that the list of materials documented here is relatively comprehensive. There is also strong evidence that there are several areas of support that survey participants would like to see improved. 1) The majority of the respondents expressed a wish for the capability to automatically time stamp log entries. Although this capability can be used, it requires that the person know where to obtain the appropriate template and the reliability of the tool appears to be low. 2) An overwhelming majority of respondents indicated that a combination of electronic resources and paper resources would be beneficial. 3) Many respondents indicated that a key issue is finding reference materials more quickly. 4) Several respondents requested that the crewmember medical record be electronically available while on console

Issues Identified

The following key issues were identified during this project:

1) Not all participants have knowledge of the availability of all information resources and tools.
2) There is a lack of ease of access to information resources.
3) Manual copying of information is time-intensive and prone to errors. For example, logging the environmental variables is accomplished by reading the displays on the DEC Alpha and writing or typing the values into a log.
4) The organization of information material not task oriented. For example, the flight rules are organized by functional unit. If the oxygen concentration (an environmental variable) registers high, the person monitoring must look up the relevant flight rule. In this particular case, the flight rule is not dictated by Medical Operations but is instead a safety issue related to fire hazards. Thus the person monitoring has a difficult time finding the appropriate flight rule.
5) BMEs do not have clinical training but may be required to be the liaison between crew and the Flight Surgeon who may be off site during ISS mission.
6) There are few medical emergency scenarios during simulations.
7) There is a lack of communication of DEC Alpha with the PC. It is not possible at this time to send data between the two systems.
8) There is a mismatch between amount of information to display and screen real estate. There are 3 or 4 DEC Alpha screens (the number is different for ISS vs STS) and only one PC screen when most of the tools that the Flight Surgeon and BME use are on the PC.
9) The current console is designed for a person to actively monitor variables and events and requires that their eyes be looking at the screen and that the data to be monitored is displayed. Long uneventful periods can cause a lack of attention to the screen.

10) Much of the time spent on console is relatively slow. However, when a medical emergency does arise, the nature of the tasks becomes time-critical.

11) The crewmember medical record is currently a standardized summary of medical information presented on paper. Often this summary does not include previous mission data.

Potential Solutions

It is not within the scope of this project to identify the solutions to all of the issues raised above or even to identify the best solutions. However, some discussion of the potential solutions is worthwhile. The most beneficial support change would be a centralization of resources. There is already a very extensive web site that contains links to many of the resources; however, each resource must be searched individually. Further electronification and centralization would enable the addition of a search capability at a global level – not only searching an individual document, but searching all the documents that are potentially relevant. It would also enable alternate indices for the materials. It would be particularly useful to implement a task-based index as this would facilitate quick and accurate access to the appropriate information. This same area could also be used to centralize a description of capabilities for use both in training and while working the console. For example, the analysts found that it IS possible to receive an audio indication of environmental variables reaching threshold values. Enabling this capability would help to alleviate issue 9 above (inattention to values during uneventful periods). However, this capability is unknown to most Flight Surgeons and BMEs.

Time could be saved and more accurate information collected if there were a way to automatically log the environmental variables periodically. Also, it was apparent from some of the simulations that having access to recent unlogged values could be useful. For example, when it is noticed that an environmental variable reaches a threshold value, knowledge of exactly when the event occurred and how quickly the variable was changing is useful in determining the actions to be taken.

Integration of the electronic patient record into the console environment would provide easy access to the most recent data on a crewmember and would serve to consolidate and coordinate all the information collected. For example, a medical problem that occurs during an EVA may be better solved if the Flight Surgeon has access to logs about previous missions. In the current environment, this information may not be available in the paper patient record that is used on the console.

CONCLUSIONS

The console environment used by Flight Surgeons and Biomedical Engineers is very complex. There are numerous information resources including computer displays of information, web-based materials, paper documentation, personnel, etc. The tasks that the Flight Surgeons and Biomedical Engineers do can also be complicated and at times quite time-critical. There are clearly some areas where support for these users and tasks can be improved. We have identified what seem to be the most critical issues and have generated some potential solutions. Future work may include implementation and testing of some of these solutions.

REFERENCES

Pena, W. (1979). *Problem Seeking.*: American Institutes of Architects Press.

Kirwan, B., & Ainsworth, L. (1992). *A Guide to Task Analysis: The Task Analysis Working Group.*: Taylor & Francis, Limited.

Robotic Mars Sample Return
Risk Assessment and Analysis Report

Thomas R. Lalk
Cliff A. Spence
Texas A&M University
EX 13
September 26, 2000

H. Mandell and D. Neubek
Exploration Office
Advanced Development Office
Engineering Directorate

Thomas R. Lalk

Humboldt Mandell

Cliff A. Spence

Deborah Neubek

ROBOTIC MARS SAMPLE RETURN
RISK ASSESSMENT AND ANALYSIS REPORT

Final Report

NASA/ ASEE Summer Faculty Fellowship Program—2000

Johnson Space Center

Prepared by:	Thomas R. Lalk, Ph.D., P.E. Cliff A. Spence, B.S.
Academic Rank:	Associate Professor and Graduate Student
University & Department:	Texas A&M University Mechanical Engineering College Station, Texas 77843

NASA/ JSC

Directorate:	Engineering
Division:	Advanced Development Office
Branch:	Exploration Office
JSC Colleague:	Humboldt Mandell
Date Submitted:	September 26, 2000
Contract Number:	NAG 9-867

ABSTRACT

A comparison of the risk associated with two alternative scenarios for a robotic Mars sample return mission was conducted. Two alternative mission scenarios were identified, the Jet Propulsion Lab (JPL) reference Mission and a mission proposed by Johnson Space Center (JSC). The JPL mission was characterized by two landers and an orbiter, and a Mars orbit rendezvous to retrieve the samples. The JSC mission (Direct/SEP) involves a solar electric propulsion (SEP) return to earth followed by a rendezvous with the space shuttle in earth orbit. A qualitative risk assessment to identify and characterize the risks, and a risk analysis to quantify the risks were conducted on these missions. Technical descriptions of the competing scenarios were developed in conjunction with NASA engineers and the sequence of events for each candidate mission was developed. Risk distributions associated with individual and combinations of events were consolidated using event tree analysis in conjunction with Monte Carlo techniques to develop probabilities of mission success for each of the various alternatives.

The results were the probability of success of various end states for each candidate scenario. These end states ranged from complete success through various levels of partial success to complete failure. Overall probability of success for the Direct/SEP mission was determined to be 66% for the return of at least one sample and 58% for the JPL mission for the return of at least one sample cache. Values were also determined for intermediate events and end states as well as for the probability of violation of planetary protection. Overall mission planetary protection event probabilities of occurrence were determined to be 0.002% and 1.3% for the Direct/SEP and JPL Reference missions respectively.

INTRODUCTION

It has become increasingly important to the planning of space missions to include risk management as an integral part of the process, because of the increased emphasis on efficiency of operation in terms of performance, schedule and cost. Risk management provides a means to identify sources and magnitude of risk, and actions to reduce it, as well as a criterion for trading-off alternative designs or solutions. Risk management includes qualitative risk assessment to identify and characterize risks, a risk analysis to quantify the risks, and risk mitigation and tracking. Although these activities increase the time and effort necessary in the early planning stages of a mission, they are valuable to the decision process for selecting an alternative to pursue and can result in greater likelihood of mission success. Risk analysis may also be used to identify events and sub systems critical to mission success and possible revisions to a scenario, or to develop additional alternatives.

Several alternative scenarios have been proposed for a robotic Mars sample return mission and a major criterion for selecting among them is the risk associated with each candidate. This resulted in the following need statement for the project described herein:

> ***To Compare Alternative Concepts for Mars Robotic Sample Return Missions, Based On Risk***

Two alternative mission scenarios were identified, the Jet Propulsion Lab (JPL) reference Mission and a mission proposed by Johnson Space Center (JSC). The JPL mission was characterized by two landers and an orbiter, and a Mars orbit rendezvous to retrieve the samples. The JSC mission (Direct/SEP) involves a solar electric propulsion (SEP) return to earth followed by a rendezvous with the space shuttle in earth orbit. Technical descriptions of the candidate scenarios were determined and the sequence of events for each was developed. Distributions of the risk associated with individual and combinations of events, functions or sub-systems were determined and combined using event tree and fault tree analysis in conjunction with Monte Carlo techniques to develop the probability of success of various end states for each candidate scenario. These end states range from complete success through various levels of partial success to complete failure.

The procedure used, including that for the risk assessment and for the quantitative analysis are described, followed by presentation of the results and discussion in terms of comparisons of the probabilities of success for various mission end states as well as for individual events, such as planetary protection. In addition, critical events or functions were identified. The findings are summarized and conclusions drawn and presented before concluding with recommendations.

PROCEDURE

There were three main phases of the procedure: Risk Assessment –identification and characterization of risks, Risk Analysis – quantification of the risks, and presentation and interpretation of the results. Each of these is described below.

Risk Assessment

The first step of the risk assessment was a functional decomposition of a general robotic Mars sample return mission and development of a function structure to display the relationship among the various functions. Following the identification of the top-level functions and functional requirements a top-level event tree, with the sequence of events for a general mission, was developed. Specific missions to analyze and compare were identified and a matrix developed of top-level functional requirements and how each candidate mission is proposed to satisfy each requirement. Design parameters associated with each of the events were identified, which aided in identifying mission specific requirements and potential failure modes. Major areas of difference between the JPL reference mission and Direct/SEP were identified. The function structure was further decomposed by identifying sub-events that would be required for specific missions, particularly those events that differed between the candidate missions. The probabilities of success of these sub-events could then be consolidated to determine the mission probability of success. These probabilities were quantified during the risk analysis.

Risk Analysis

The risk analysis was initiated by developing time-lines designating event times throughout the mission for each candidate mission including sub-events specific to each. This resulted in a different event tree for each candidate mission. This also allowed identification of various end states for each candidate mission, that is, several successful or unsuccessful outcomes. Then, general sub-systems, which would be required for most events throughout the mission, were determined by considering what sub-systems would be necessary to provide the functions identified from the functional decomposition of a general mission. These were avionics, power, thermal management, structure, propulsion and mechanisms. This was done while recognizing that not all sub-systems and sub-systems types would necessarily be needed for all events, and that usage may differ from event to event. This could result in different risk values associated with these sub-systems for the various events and sub-events of the two candidate missions. Failure rates associated with the various sub-systems were determined from several sources, although primarily from a risk data base developed for the International Space Station (ISS), because this source included data for space rated systems. Additional component failure rate data was taken from The Nonelectronic Parts Reliability Data – 1995 (NPRD-95). The data for the various sub-systems was in the form of failure rates or mean time between failure and had to be converted into probabilities for the various sub-systems during each event. This was done by assuming a constant failure rate reliability model (exponential) shown below, where $R(t)$ is the reliability (probability of success), t is the time for the event and M is the mean time between failure.

$$R(t) = e^{\frac{t}{M}} \tag{1}$$

The reliability for a particular sub-system in use during a particular event was determined by using this equation with the mean time between failure, M (hours), for the particular sub-system such as avionics, and the time for the event in hours. The reliability for the entire event was determined by multiplying the sub-system reliabilities. If a particular sub-system was determined to not be in use during a particular event it was assumed to have a failure rate two orders of magnitude lower than when it was in use (multiply M by 100). Also, if a particular sub-system was in use only part of the time during an event this was accommodated by reducing the time used in the equation. This reliability model was used only for events that were greater than one hour in duration. For events shorter than one hour some other method of determining the reliability such as using actual data (for example, solid rocket booster data) or estimating was used.

Once the reliabilities for all of the sub-systems for each event had been determined they could be multiplied together to determine a reliability for the entire event. The reliabilities for the events connecting to particular end states could be, in turn, multiplied to determine the probabilities of these end states. Before doing so the uncertainty associated with the mean time between failures, M, was accounted for by assuming an uncertainty range. That is, distributions of the value of M about the nominal values obtained from the database were assigned and used to obtain values to use for each sub-system, for each event. A triangular distribution was assumed about each nominal value of M, with a range of a half order of magnitude on either side of the nominal value obtained from the database. These distributions were then used to conduct a Monte Carlo analysis, whereby a random value was selected from the applicable distribution for each sub-system, within each event, for each iteration. The simulation was run for 5000 iterations to obtain distributions of the probabilities of success for each of the end states analyzed. Thus mean values for the probabilities of success were determined. In addition, plots of the distributions of probability values about the mean values and standard deviations for these distributions were determined.

The results in terms of the mean values and distributions of probabilities of various final end states and individual events throughout the mission were compared for each candidate mission. In particular, various end states involving violation of planetary protection were determined and compared. These results are presented and discussed in the following section.

RESULTS AND DISCUSSION

The results are presented in two sections. Results of the qualitative risk assessment are presented first because the activities producing these results preceded the risk analysis and, in fact, lead into and are necessary for a better understanding of the results of the risk analysis. The quantitative risk analysis results are presented in the following section in the form of plots, tables and charts providing the basis for the comparisons between the two candidate missions analyzed.

Qualitative Risk Assessment

The results presented in this section are those produced during the process of identifying and characterizing the risks associated with a robotic Mars sample return mission and determining means for quantifying these risks.

Table 1 shows the critical top level events for a robotic Mars sample return mission and how each candidate mission is proposed to accomplish them. These events were determined from the functional decomposition of a general Mars sample return mission and identification of top-level functional requirements coupled with the identification of alternative mission scenarios being proposed. This table also serves to describe the two missions and how they differ. Several events that would be necessary for the mission are not shown on this Table because they would be essentially the same for both. The major areas of difference between the two missions are summarized in Table 2. This shows that the two missions differ primarily in how the samples are to be acquired (activities on the Mars surface) and returned to earth. The events identified were used to construct event trees described below.

Event trees are used to depict initiating events and combinations of successes and failures. For a mission composed of a sequence of events, any one of the events can be viewed as an initiating event whose success or failure could result in complete or partial failure or complete or partial success of the mission. This is shown by the example event tree for the Direct/SEP mission in Figure 1. Starting with any event there are alternative paths that could be taken depending on the success or failure of the event. For example, some events are mission critical such that their failure results in mission termination, which is an end state, while their success may result in a number of paths to various levels of success or failure. The event numbers are given across the top of each tree. Some of these events are described, for each mission, on Table 1. Each event tree has several top-level event numbers listed across the top. Each of these events also has sub-events that must be at least partially completed if the event is to be at least partially successful. This is illustrated by the large number of options (end states) for mission outcome that are listed along the side of the tree. Some of these outcomes are success end states (various levels of success) and some failure end states. These will be explained in more detail in the risk analysis results. It should also be noted that each of the events has a probability of success associated with it. To determine the success of a particular end state the probabilities for the events leading to it would be multiplied. These event trees were developed to do just that – determine the probabilities of various end states.

Table 1. How Candidate Missions Are Proposed to Accomplish Critical Top Level Events

	Launch	*To Mars*	*Mars Landing*	*Sample Acquisition*	*Mars Ascent*	*To Earth*	*Sample Recovery*
JPL	2 launches Delta & Ariane	Chemical Direct	Direct entry, parachutes, propulsion, legs	2 landers 2 rovers, 2 Deedri, multi MAV interfaces	2 stage to orbit, solid prop, partial guidance	Mars orbit rendezvous x 2, chem/direct	Ballistic entry and impact x 2
Direct/SEP	Ariane	Chemical Direct	Mid L/D entry, parachutes, propulsion, legs	1 lander, 2 arms, 3 sampling end effectors, multi-master cache/single ascent vehicle interface	2 stage to orbit, CH4/LOX fully guided	SEP	Earth orbit rendezvous with shuttle, shuttle landing

Table 2. Major Areas of Difference Between the Candidate Mars Sample Return Missions

1. Means of acquiring the samples from the Mars surface
2. Means of transferring samples to MAV and to Earth return vehicle
3. Means of ascent from Mars surface
4. Means for returning to Earth
5. Means to avoid Earth contamination from returned samples

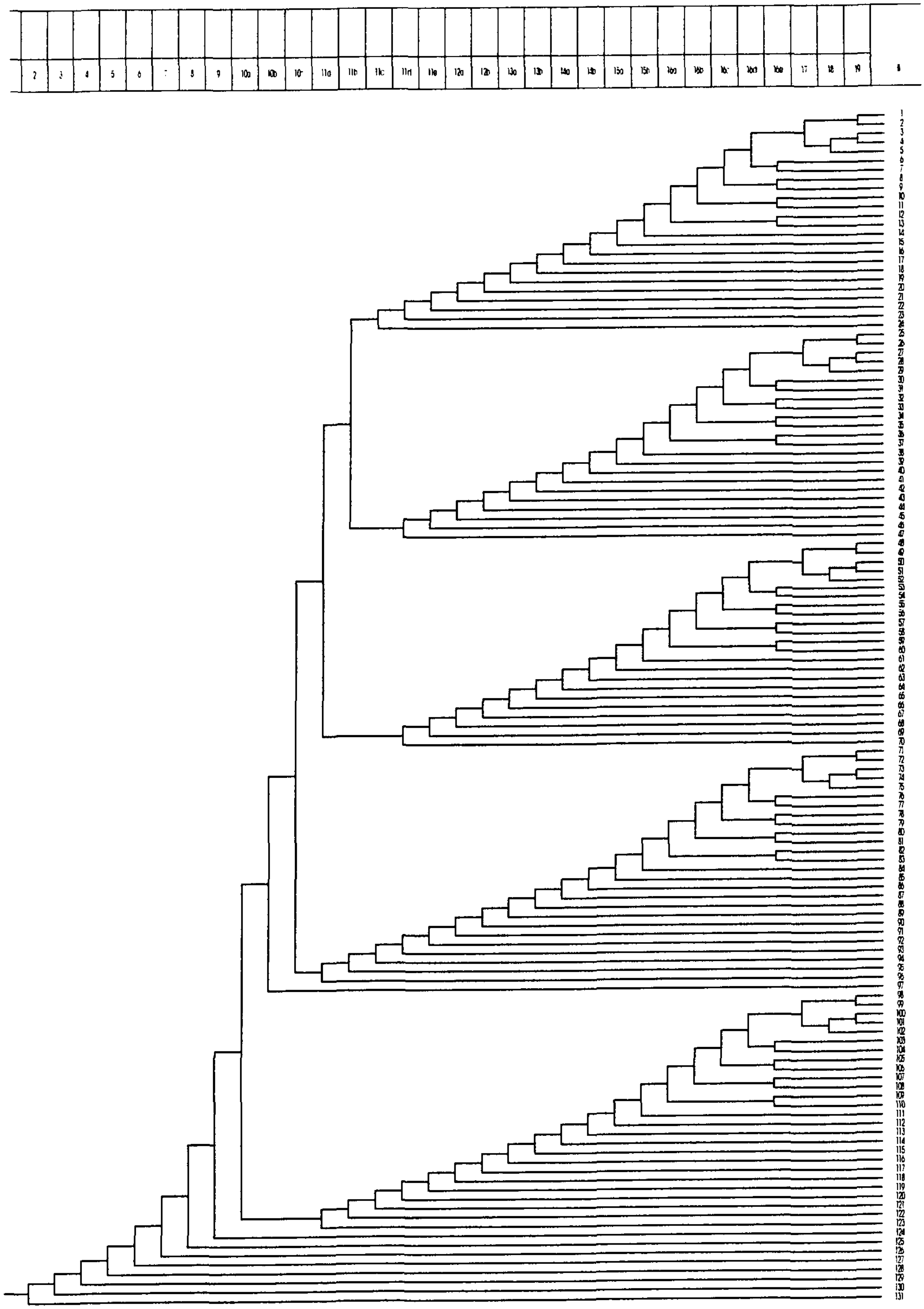

Figure 1. Example Event Tree for the Direct/SEP Mission Showing the Event Numbers (Top) and End States (Right)

Risk Analysis Results

The purpose of the risk analysis was to quantify the risks associated with each candidate mission to provide a method to differentiate between the risk of each. Several quantitative results that can be used to provide a comparison of the risks between the two candidate missions and also identify critical areas of risk were developed. The values that were produced should be used for comparison purposes only, and not interpreted to represent an absolute risk of the missions. The risk analysis was focused on producing an answer to two questions; 1) which of the two candidate missions had a higher probability of success and 2) which of the two candidate missions was least likely to violate planetary protection requirements. Many additional results could have been determined from the analysis conducted, however, due to time constraints only these two questions were directly addressed in any detail. It should also be noted that only technical risk was considered with no attempt to quantify financial, programmatic or any other type of risk.

The probabilities of success for various end states for the direct/SEP and JPL Reference missions are presented in figures 2&3. The mean values are presented as well as the distributions about the mean values and the standard deviations for each end state. The first values to compare between the two figures are the middle entries, which are the values for the probabilities of success for the return of one sample (Direct/SEP) and at least one sample cache (JPL Reference). The act of collecting and transferring one sample cache during one sortie for the JPL mission was considered to be functionally similar to collecting and transferring one sample into the cache for the Direct/SEP mission. These values indicate that the Direct/SEP mission is more likely to return at least one sample to Earth than the JPL Reference returning one sample cache (66% as compared to 58%). These distributions have non-overlapping confidence intervals, so there is a statistically significant difference between the two options. For this particular case it can be stated with 99.9% confidence that the mean values are truly different.

The first and third entries on Figures 2&3 display the results for probability of mission success for additional end states of the two mission scenarios. Comparing the results for these end states also indicates that the direct/SEP mission has higher probability of success than the JPL Reference mission. As expected, for both mission scenarios, the probabilities of success for obtaining only one sample or cache, and at least one sample or cache are higher than those for obtaining two or more samples or caches. This is to be expected because it will be more difficult to achieve success if sampling and transfer actions must be repeated to obtain additional samples or caches.

Figure 4 provides a comparison of the probabilities of success for various functionally similar phases of the missions, which differed in the manner they were accomplished. The major difference between the two missions lies in the rendezvous technique employed to obtain the samples. The success probabilities associated with these two events differed by almost 20%, meaning that a successful transfer is much more likely with the Earth orbit Shuttle combination. The only other relatively significant difference in risk was with the sample acquisition systems due to the perceived relative simplicity of the scoop system of the Direct/SEP mission compared to the drilling systems of JPL.

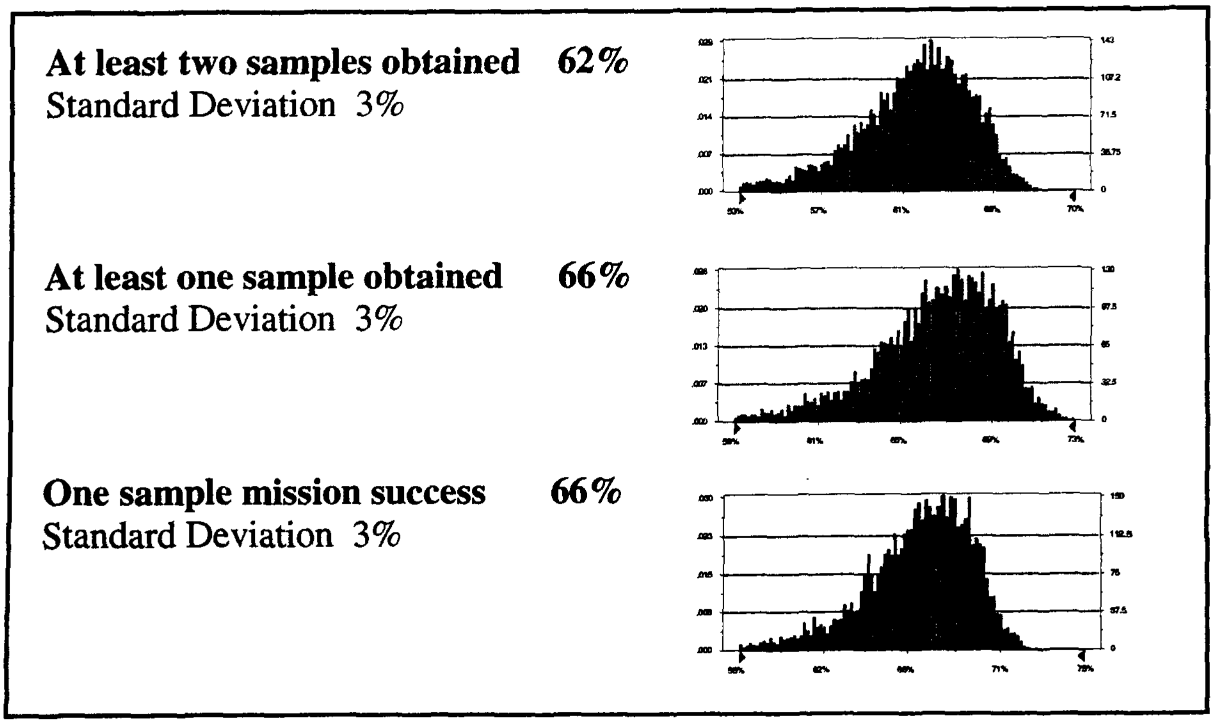

Figure 2. Direct/ SEP Probability of Mission Success for Various End States

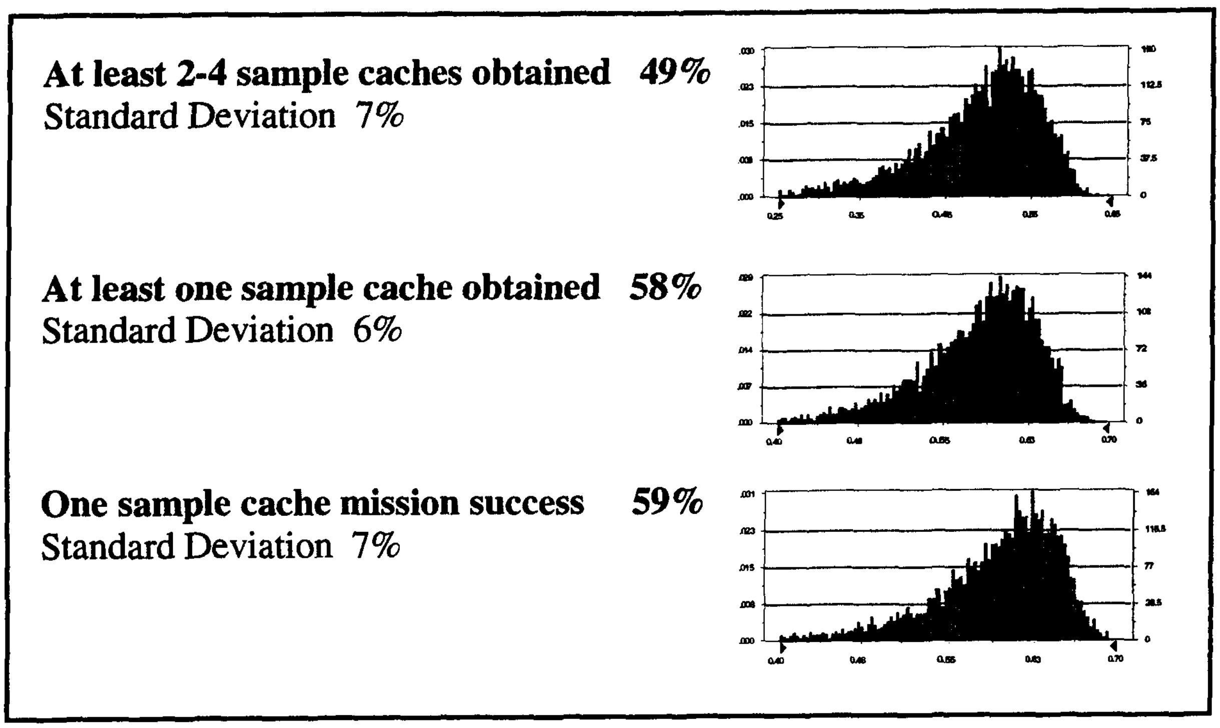

Figure 3. JPL Reference Mission Probabilities of Success of Various End States

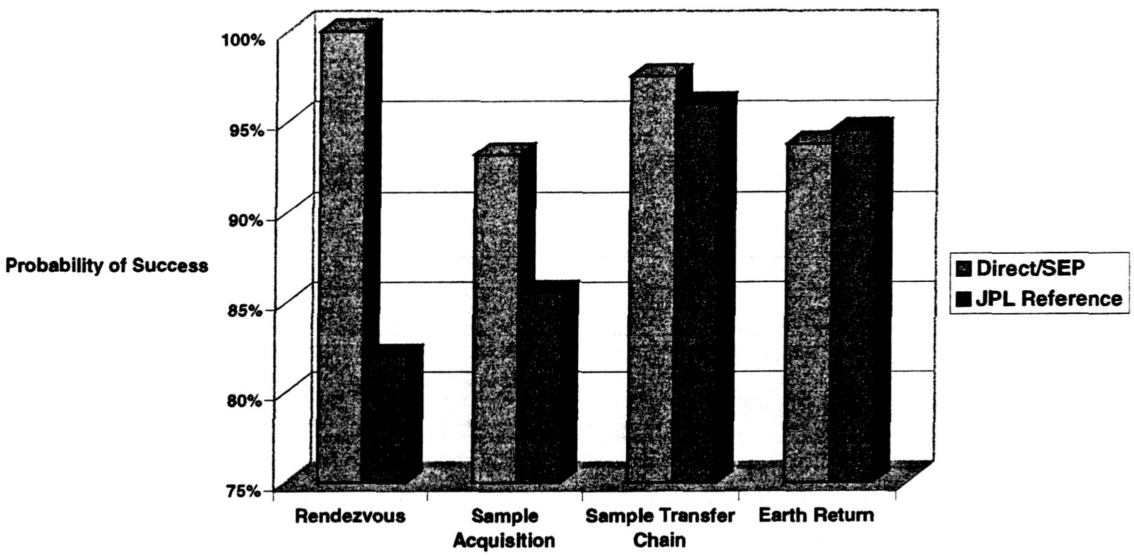

Figure 4. Comparison of the Probabilities of Success for Functionally Similar Phases of the Mission

Planetary Protection Results

Results are presented in Figure 5 and Tables 3 and 4 for the risk associated with the planetary protection events during the complete missions, and for the most critical planetary protection events of each mission.

The overall probability that a planetary protection event will occur for each mission is presented in Figure 5. The values that were determined for each mission were 0.002 % and 1.3% for the Direct/SEP and JPL Reference mission, respectively. The Direct/SEP had a much lower probability of a planetary protection event occurring as explained below. The overall planetary protection probability was calculated by consolidating the five most critical planetary protection end state probabilities found from the risk analysis. These are listed in Tables 3 and 4.

Comparing the planetary protection event tables (Tables 3 and 4) it is apparent that the majority of planetary protection event probabilities of the Direct/SEP mission are several orders of magnitude lower than for the JPL Reference mission. This is due to the redundant planetary protection systems that are designed into the Direct/SEP mission hardware and mission operation and the use of proven technology (shuttle). Also, the planetary protection risks increase with the use of two Earth return vehicles (ERVs) used in the JPL Reference mission. All planetary protection probabilities were desired to be lower than "one in a million" or have a probability of success of 0.999999 (1.0 E-6 failure probability). From Tables 3 and 4, it can be seen that four out of the five most critical JPL Reference end states had probabilities greater than the 1.0 E-6 range, while the Direct/SEP only had one end state that was greater than this target. An improved method that has been devised for shuttle sample casket sealing and disposable shuttle end effector would most likely result in the redundancy necessary to reduce this risk to meet the goal of one in a million. It was found that a similarity between the missions was the relatively high probability that the initial seal for the samples may not succeed and that the sample would be returned to Earth without knowing that the seal had failed.

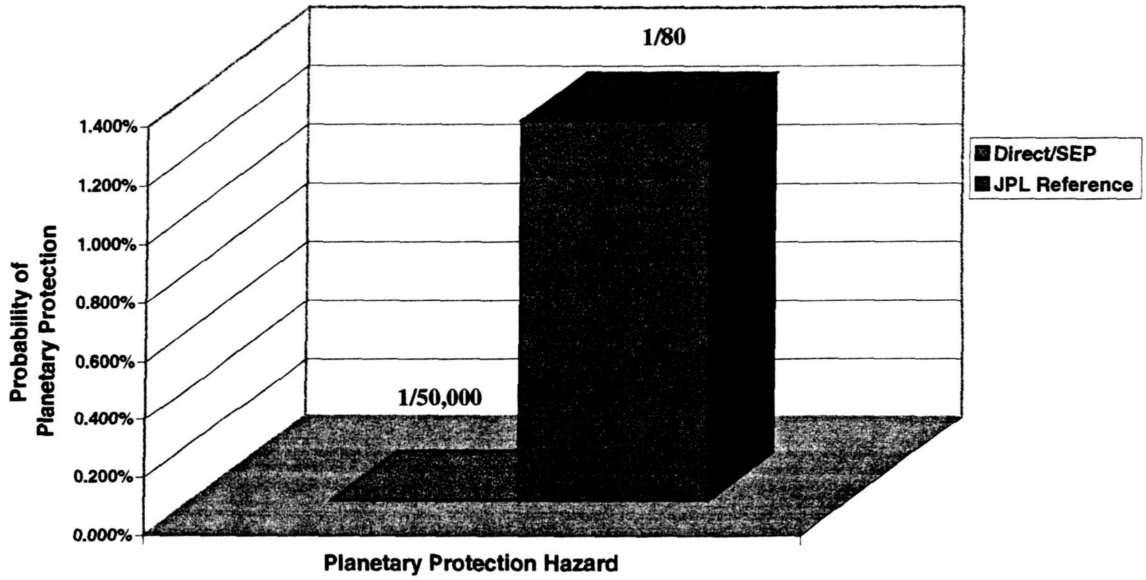

Figure 5. Comparison of the Probability of Violating Planetary Protection During Mission

Table 3. Direct/ SEP Mission- Planetary Protection Details

Planetary Protection End State	Probability
Shuttle landing fails and containment cask fails to contain sample	5.9×10^{-7}
Failure to contain sample in shuttle after rendezvous, two more failed mission attempts, and Earth Return Vehicle (ERV) fails to abort at low orbit	2.3×10^{-9}
Failure to rendezvous with shuttle after three mission attempts and ERV fails to abort at low orbit	6.3×10^{-9}
Failure to seal sample at Mars and failure to verify planetary protection threat before rendezvous with shuttle •	1.6×10^{-5}
Failure to deploy, pyro, or remove solar cells before rendezvous and failure of ERV to abort at low Earth Orbit	8.8×10^{-10}

• *Dependent on sealing method and method of verification*
Currently, PP Seal- 0.995 Success & Verification- 0.995 Success

Table 4. JPL Reference Mission- Planetary Protection Details

Planetary Protection End State	Probability [illegible]	Probability [illegible]
Mission completed as expected, but planetary protection seal did not work	$1.1x10^{-2}$	$5.1x10^{-3}$
Loss of sample containment at impact – at desired impact location	$2.3x10^{-4}$	$1.0x10^{-4}$
Sample containment on impact, but impact occurs in undesirable but recoverable location	$1.1x10^{-3}$	$5.1x10^{-4}$
Loss of sample containment on impact at incorrect impact site	$2.3x10^{-4}$	$1.0x10^{-4}$
EEV loses integrity during Earth entry	$3.3x10^{-6}$	$3.0x10^{-6}$

*Earth Entry Vehicle

Cumulative Risk and Effect of Redundancy on Mission Risk

The cumulative risk for each mission was determined during the analysis to identify any events that resulted in a critical increase in risk. This was accomplished by tracking the mission risk to determine each event's contribution to the overall mission risk. Critical drops in risk can then be identified and the associated events targeted for design or operational changes to reduce the risk to the mission. Also examined was the effect that redundancy had on the overall mission risk. This was accomplished by plotting the mission risk for each event with redundant systems and without redundant systems. Large changes in risk due to the loss of the redundant system means that the redundancy significantly reduces overall mission risk. Figure 6 shows that the major contributions to risk associated with the Direct/SEP system, with the redundant arm, occur during the cruise to Mars, sample transfer chain, launch from Mars and travel back to Earth. The cruise to Mars and return to Earth have relatively high risks because of the lengths of time involved. The redundant arm only makes a difference in the mission risk during the surface operations of sample acquisition and transferring of the samples. The overall mission probability was 67% for the successful return of one sample and decreased to 62% with the redundant arm and 57% without the redundant arm. Figure 7 shows the major contributions to risk associated with the JPL Reference mission occurred during the events of cruise to Mars, Mars rendezvous and Earth return. The largest decrease in the overall success probability occurred for the Mars rendezvous event. The effect of redundancy on the mission success probability is much more pronounced than seen for the Direct/SEP mission. This is because a greater degree of redundancy has been added by having two almost identical landers. Without the redundant lander, the mission success probabilities start to decrease almost immediately and become pronounced by the time the surface events have been completed. The overall mission success probability of obtaining at least one sample was 58% with the redundant lander and dropped to 38% without the redundant lander. For retrieving at least two sample caches, the overall mission success probability with the redundant lander was 48% and dropped to 12% without the second lander. This means the loss of redundancy greatly impacts the JPL Reference mission's ability to collect multiple samples.

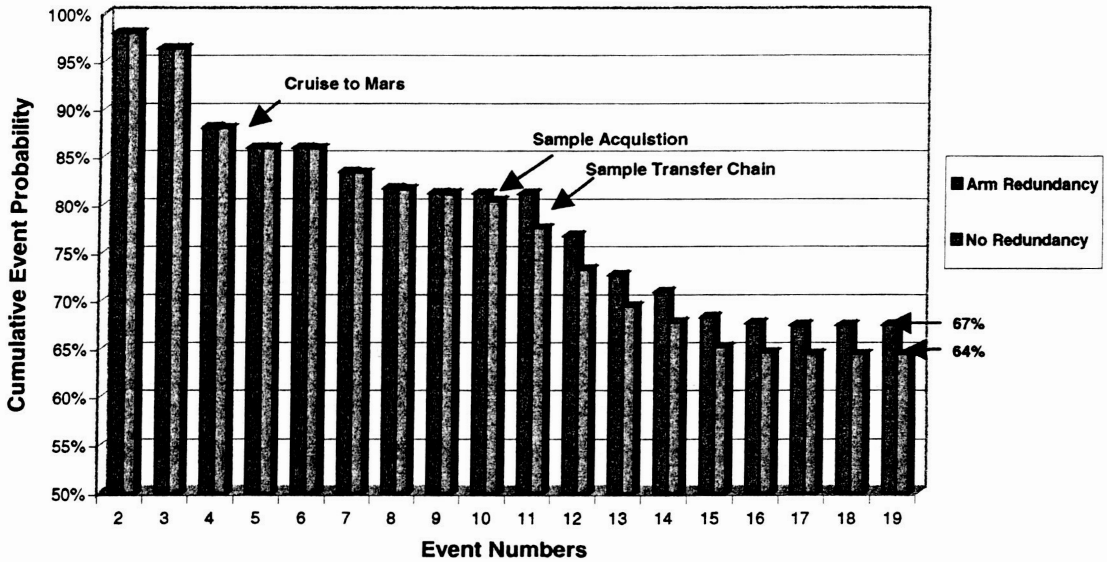

Figure 6.Cumulative Effect of Individual Events on the Probability of Obtaining At Least 1 Sample Type Including the Effect of Redundancy -- Direct/SEP Mission

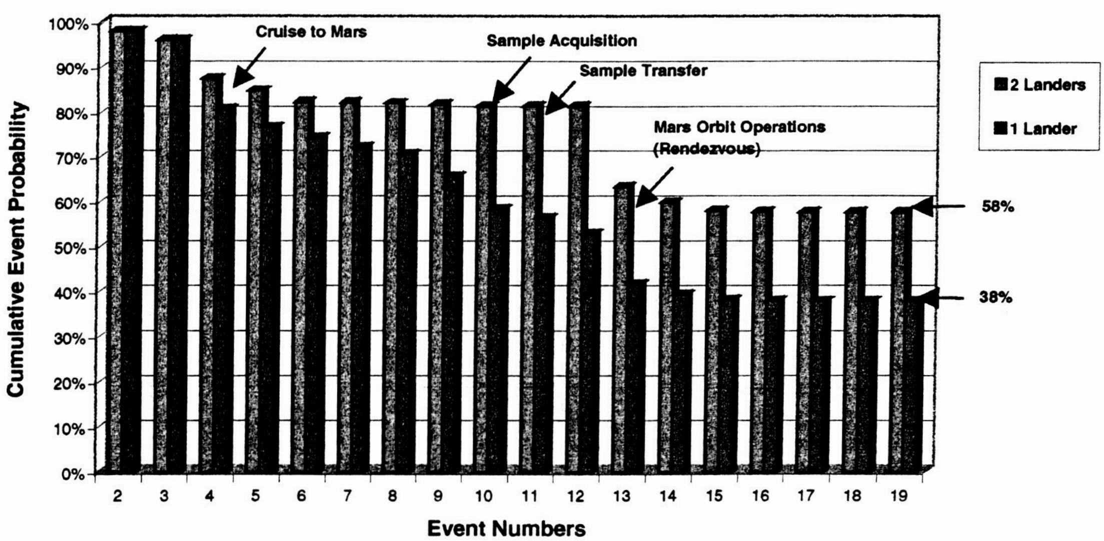

Figure 7. Cumulative Effect of Individual Events on the Probability of Obtaining At Least 1 Sample Cache Including the Effect of the Number of Landers -- JPL Reference Mission

SUMMARY AND CONCLUSIONS

Summary of Results

- Direct/SEP probability of mission success was determined to be significantly higher than JPL reference mission.
- Direct/SEP risk of a planetary protection violation event was determined to be significantly lower than JPL reference mission.
- Most planetary protection end states have a low probability (< 1/1,000,000) for the Direct/SEP mission. The driver is sealing verification.
- Further refinement in the analysis is necessary to increase confidence in overall mission success estimate.
- For the Direct/SEP mission there is negligible increase in risk associated with acquiring additional samples after the first.
- Use of shuttle for rendezvous and sample recovery significantly increases reliability, compared to robotic Mars rendezvous.
- No statistical difference determined between risk for return SEP and chemical stages.
- Sub-system redundancy contributes to risk mitigation and reduction of mission risk. Added redundancy to sub-systems, operations and contingency events may further reduce risks at low cost.
- Use of two EEVs on the JPL Reference mission increased the probability of mission success but also increased the probability of a planetary protection violation.

Conclusions

The risk analysis conducted was a first order effort at quantifying the risks associated with alternative designs for a robotic Mars Sample Return Mission. Only general, top level conclusions should be drawn from this analysis, because of the short duration of the study and the lack of information relating to the designs, which were in the early phase of the design process. The conclusions that were drawn are summarized below.

- The Direct/SEP mission should have a higher probability of returning one or multiple samples to Earth than the JPL Reference mission.

- The Direct/SEP should pose a lower risk of a planetary protection violation than the JPL Reference mission because of it use of redundant systems.

- A dual spacecraft design is desirable, though it is recognized that additional cost and benefit analysis is needed to help make a design decision of this magnitude.

- Several areas that may require attention to increase the probability of mission success or decrease the probability of a planetary protection event from occurring can be identified from this level of risk analysis and this risk analysis in particular.

- The use of redundancy does not necessarily achieve both the goals of mission success and avoidance of planetary protection events.

HUMAN PERIPHERAL BLOOD MONONUCLEAR CELLS CULTURED IN NORMAL AND HYPERGLYCEMIC MEDIA IN SIMULATED MICROGRAVITY USING NASA BIOREACTORS

Final Report

NASA/ASEE Summer Faculty Fellowship Program 2000

Johnson Space Center

Prepared by:	Brother DeSales Lawless, PhD,
Academic Rank	Professor
Department	Natural Science
University	Fordham University, New York, N.Y., 10023
	Adjunct Faculty The Rockefeller University, New York, N.Y., 10021

NASA/JSC

Directorate:	Space and Life Science
Division:	Medical Sciences
JSC Colleague	Dennis R. Morrison, PhD
Date Submitted	August 3, 2000
Contact Number	NAG 9-867

ABSTRACT

We sought answers to several questions this summer at NASA Johnson Space Center. Initial studies involved the in vitro culture of human peripheral blood mononuclear in cells in different conditioned culture media. Several human cancer clones were similarly studied to determine responses to aberrant glycosylation by the argon laser. The cells were grown at unit gravity in flasks and in simulated microgravity using NASA bioreactors.

The cells in each instance were analyzed by flow cytometry. Cell cycle analysis was acquired by staining nuclear DNA with propidium iodide. Responses to the laser stimulation was measured by observing autofluorescence emitted in the green and red spectra after stimulation.

Extent of glycosylation correlated with the intensity of the laser stimulated auto-fluorescence.

Our particular study was to detect and monitor aberrant glycosylation and its role in etiopathogenesis.

Comparisons were made between cells known to be neoplastic and normal cell controls using the same Laser Induced Autofluorescence technique.

Studies were begun after extensive literature searches on using the antigen presenting potential of dendritic cells to induce proliferation of antigen specific cytotoxic T-cells. The Sendai virus served as the antigen.

Our goal is to generate sufficient numbers of such cells in the simulated microgravity environment for use in autologous transplants of virally infected individuals including those positive for hepatitis and HIV.

INTRODUCTION

Carbohydrates are ubiquitous in living systems. Glycosylation is the most extensive of all the postranslational modifications and has important functions in secretion and antigenicity. (1) Carbohydrates .account for the structural diversity of organisms and for differentiation and development. Several factors influence the extent of glycation; one is the ambient glucose concentration. Long term hyperglycemia is a factor contributing to the accumulation of Advanced Glycosylated End Products (AGEs) on tissue macromolecules. (2) AGEs are the result of non-enzymatic glycosylation of proteins. The interaction between reactive terminal amino group and the carbonyl group of a reducing sugar results in a Shiff base adduct, which can undergo an Amadori rearrangement to form a ketoamine adduct (3) These products can undergo multiple rearrangements to become the irreversibly bound, chemically reactive AGE. These insoluble products are responsible for the symptomology associated with the aging process and with diabetes. Aberrant glycosylation in some instances is involved in the formation of tumor antigens., (4)

A physical property associated with AGEs is the emission of 570 nm or 630nm light energy (autofluorescence following the absorption of 448 nm energy associated with argon laser. .The induction of Laser Induced Fluorescence (LIF) was compared in tumor cell lines of various lineages, and found to be distinguish lymphoid tumor cells from normal. Notable variations in induced fluorescent intensity were noted in normal murine lymphocytes cultured in excess glucose. Human peripheral blood mononuclear cells (PBMC) demonstrated similar fluctuations in autofluorescence emission speectra when grown in the presence of excess glucose at either unit gravity or in simulated microgravity.

Our results indicate that cells altered by aberrant glycosylation can be distinguished by LIF. It follows that varioius therapies to reverse or prevent aberrant glycosylation can similarly be monitored in a brief time with the flow cytometer and its laser energy source. In previous studies we demonstrated that AGEs responsible for some of the diabetic symptomology can be reversed using hyperbaric oxygen protocols. .

MATERIALS AND METHODS

Cells and Media

Normal human blood was obtained from the Gulf Coast Regional Blood Center, Houston, Texas. The peripheral blood mononuclear cells were isolated on a Ficoll-Hypaque gradient (Pharmacia LKB, Piscataway, N>J>). washed three tim4s in PBS and resuspended in complete RPMI-1640 (GIBCO-BRL), Grand Island, N.Y. supplemented with 10% heat-inactivated fetal bovine serum (Hyclone Labs, Logan, Utah) and penicillin (100 U/ml).-streptomkycin (100 ug/ml, GIBCO-BRL). Cell counts were determined with a a hemacytometer and cell viability by trypan blue excluision. Glucose, Na+, K+, Cl- concentrations in the media were checked using the Portable Clinical Analyzer, I-Stat from I-STAT Corporation, Princeton, N.J. Cell concentrations were adjusted to 1 x 10^6 cells/ml. The glucose concentration was 100 mg% in the control study and 400 mg% in hyperglycemic medium. Cell conditions in both instances were maintained at 37°C in 5% CO_2

RWV Bioreactor

One of the bioreactors devised by NASA scientists is the Rotating Wall Vessel (RWV) Bioreactor known as the HARV (High Aspect Rotating Vessel). This instrument creates an environment for cells which simulates some aspeacts of microgravity. The HARV with a volume of 10 ml and a rotation speed of 14 rpm was used in tese studies.

Flow Cytometry Analysis

Cell data were acquired on a Beacton Dickinson FACS-Calibur Flow Cytometer and analyzed with the ModFit Software program (Verity, Inc., Maine). 10,000 events were recorded as dot plots with side scatter vs forward scatteer ordinates. In all experiments, cells exhibited 90 degree scatter were eliminted; dead and large granular cells were excluded from analysis by gating.

Altered Glucose Concentrations

Cell concentrations were adjusted to 1 x 10^6 cells/ml. Cells in control studies were cultured in complete medium which containead apoproximately 100 mg% glucose. In the test study, glucose concentrations were adjusted to 400 mg% glucose. We wanted to learn if the hyperglyicemic medium affected cell cycle. All cell suspensions were maintained at 37° C in 5% CO_2 atmosphere. Data were analyzed on a Becton Dickinson FACS-Calibur Flow Cytometer from aliquots using side scatter vs log FL-1 (green) emitted fluorescence. Overlay histograms plots of FL-1 values for control vs test indicated the extent that cells absorbed the lser energy and retransmitted it as light in the green spectrum. Our data measured Mean Fluorescence Intensity (MFI) in response to argon laser stimulation for the suspensions at normal and at reduced gravity and at both normal and elevated glucose.

Cell Cycle Determinations

The procedure of Shapiro for DNA staining was followed. (5) Cells were pelleted, washed and resuspended in 70% cold ethanol overnight. The ethanol fixative was removed and 100 ul Propidium Iodide in buffer was added for ten minutes. Residual RNA was eliminated by ribonuclease contained in the PI buffer. The cells were then stimlated by the argon laser of the flow cytometer. Fluorescence intensity was recorded in histogram graphs of side scatter vs linear FL-2. The linear scale permitted us to read 2N (diploid) and 4N (tetraploid – dividing) cells. Cells undergoing apoptosis (programmed cell death appeared as hypodiploid. Software statistical analysis was completed with the ModFit Softtward Program (Verity, Inc., Maine) and yielded cell cycle percentages inclding diploid, tetraploid cells and percentage of cells in apoptosis.

Distinguishing malignant Cells from Normal Cells

When Jurkat Cancer Cells (Clone EC-1) were stimulated by the argon laser of the flow cytometer, they emitted fluorescent light in the green (570nm) and red (630 nm) regions of the visible spectrum. The cells were suspended in HBSS and 3% FCS. The cytometer was set at side scatter vs log FL-1 or log FL-2 and data were recorded in histograms. Normal human T-cells served as controls. Control T-cells did not show appreciable autofluorescence under laser stimulation. The results confirmed our hypothesis that LIF could be used as an early assay for malignancy and aberrant glycosylation. The conclusion was based on the assumption that a tumor glycoconjugate antigen or other aberrant glycosylation was involved in the etiopathogenesis of the cancer. Other cancer cell lines that were found to autofluoresce under LIF were Daudi (B Lymphoblasts from human Burkitts Lymphoma), Raji, (Human Lymphoid-like line, K-560, Human melogenous leukemia), and HL-60, Human Lymhoma.

The Raji B cell line demonstratated significantly higher emission in both spectra than any other cell line in this panel. Jurkat demonstrated lowered emission within the green spectra when compared to the B and myeloid lineage tumors, but higher emissions as compared to normal lymphocytes. Cellular autofluorescence has been attributed primarily to the presence of reduced flavins and pyridine nucleotides. We therefore attribute the reported differences in autofluorescence to be representative of the higher metabolic activit characteristic within this tumor panel may be indicative of additional differences in cellular glycosylation

Cell Cycle Analysis by Flow Cytometry of Human Peripheral Blood Lymphocytes in Media of Normal glucose concentration and hyperglycemia.

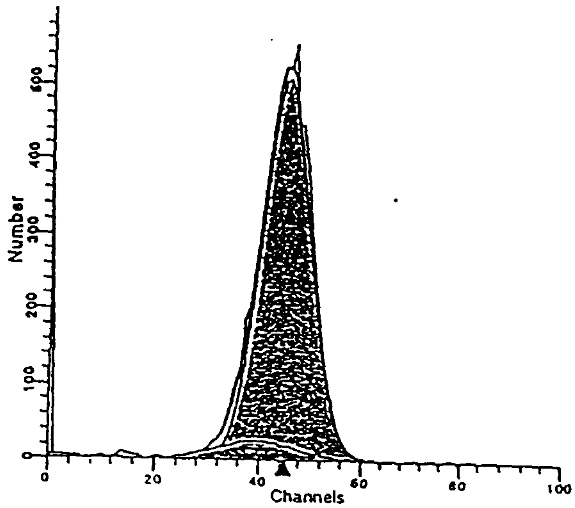

Fig 1
Cells in unit gravity - high glucose
0.45% Tetraploid 99.5% Diploid
0.00% Apoptosis

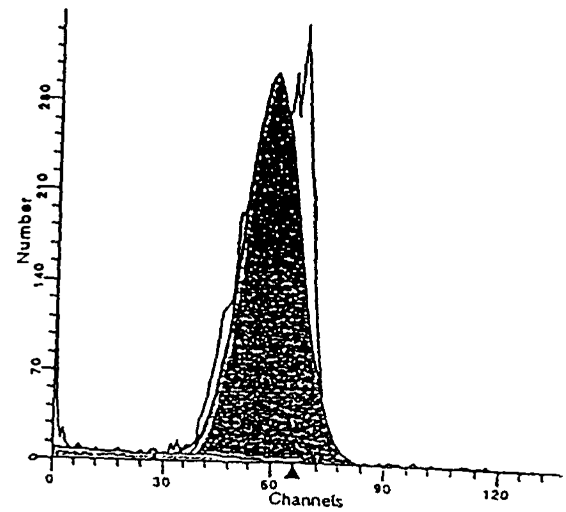

Fig 2
Cells in unit gravity - normal glucose
0.59% Tetraploid 99..28%
0.12T% Apoptosis D.ploid

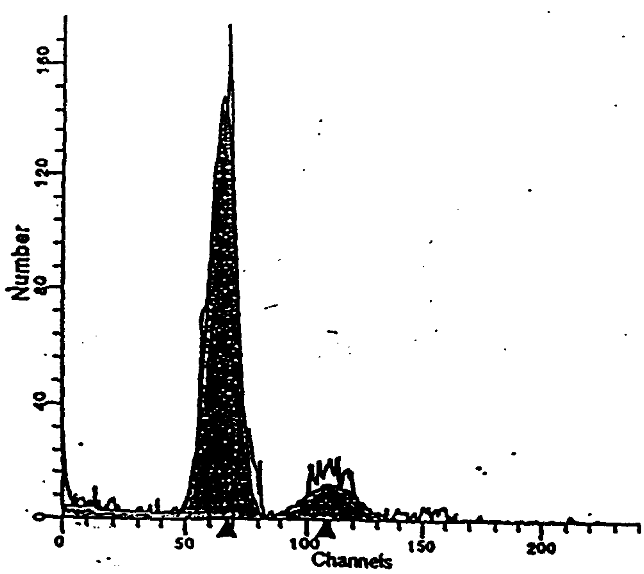

Fig 3
Cells in simulated microgravity - normal glucose
14.05% Tetraploid 85.95% Diploid
0.00% Apoptosis

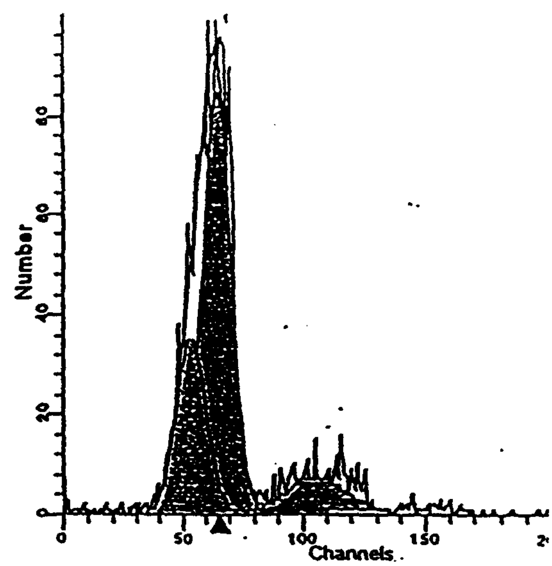

Fig 4
Cells in simulated microgravity - high gluc
14.99% Tetraploid 85.01% Dip
27.04% Apoptosis

Argon laser stimulation of PBMCs at unit gravity and in simulated microgravity.

Green fluorescence of PBMCs after stimulation by the argon laser of the flow cytometer. Fluorescence intensity is proportional to the glucose concentration and is more pronounced in microgravity.

---- = normal glucose concentration (100 mg%)

—— = elevated glucose concentration (400 mg%)

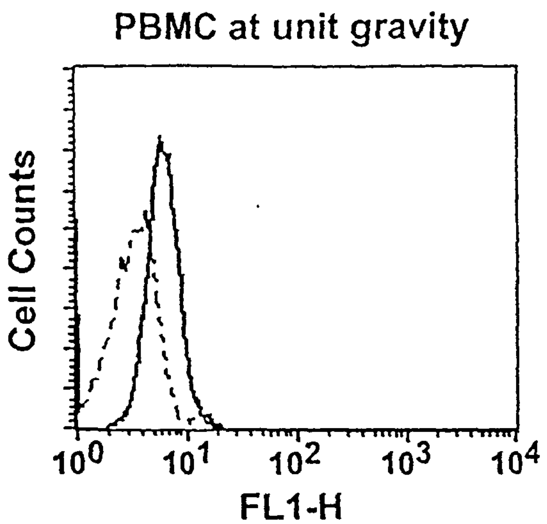

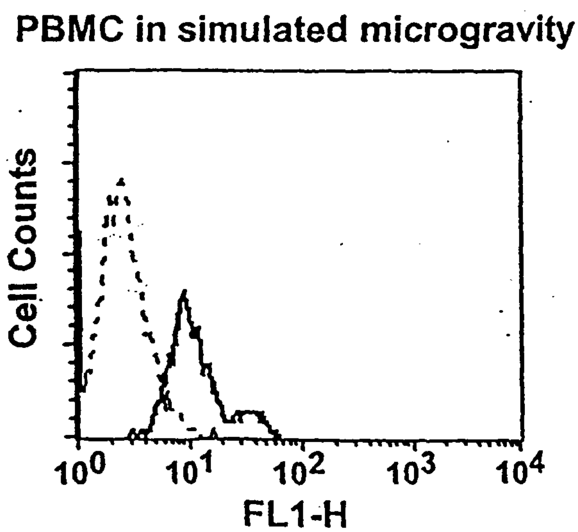

MATERIALS AND METHODS

Cells and Media

Normal human blood was obtained from the Gulf Coast Regional Blood Center, Houston, Texas. The peripheral blood mononuclear cells were isolated on a Ficoll-Hypaque gradient (Pharmacia LKB, Piscataway, N>J>). washed three tim4s in PBS and resuspended in complete RPMI-1640 (GIBCO-BRL), Grand Island, N.Y. supplemented with 10% heat-inactivated fetal bovine serum (Hyclone Labs, Logan, Utah) and penicillin (100 U/ml).-streptomkycin (100 ug/ml, GIBCO-BRL). Cell counts were determined with a a hemacytometer and cell viability by trypan blue excluision. Glucose, Na+, K+, Cl- concentrations in the media were checked using the Portable Clinical Analyzer, I-Stat from I-STAT Corporation, Princeton, N.J. Cell concentrations were adjusted to 1 x 10^6 cells/ml. The glucose concentration was 100 mg% in the control study and 400 mg% in hyperglycemic medium. Cell conditions in both instances were maintained at 37°C in 5% CO_2

RWV Bioreactor

One of the bioreactors devised by NASA scientists is the Rotating Wall Vessel (RWV) Bioreactor known as the HARV (High Aspect Rotating Vessel). This instrument creates an environment for cells which simulates some aspeacts of microgravity. The HARV with a volume of 10 ml and a rotation speed of 14 rpm was used in tese studies.

Flow Cytometry Analysis

Cell data were acquired on a Beacton Dickinson FACS-Calibur Flow Cytometer and analyzed with the ModFit Software program (Verity, Inc., Maine). 10,000 events were recorded as dot plots with side scatter vs forward scatteer ordinates. In all experiments, cells exhibited 90 degree scatter were eliminated; dead and large granular cells were excluded from analysis by gating.

Laser Induced Fluorescence (LIF) in Normal Human T Cells and in Four Human Cancer Cell Lines

Four cancer cell lines and normal T cells exposed to argon laser stimulation.

Wave lengths:	Argon Laser stimulation	- 448 nm
	FL-1 green emission	- 570 nm
	FL-2 red emission	- 630 nm

M = Mean Fluorescence Intensity (MFI)

The cancer cell lines show positive LIF and control T cells do not.

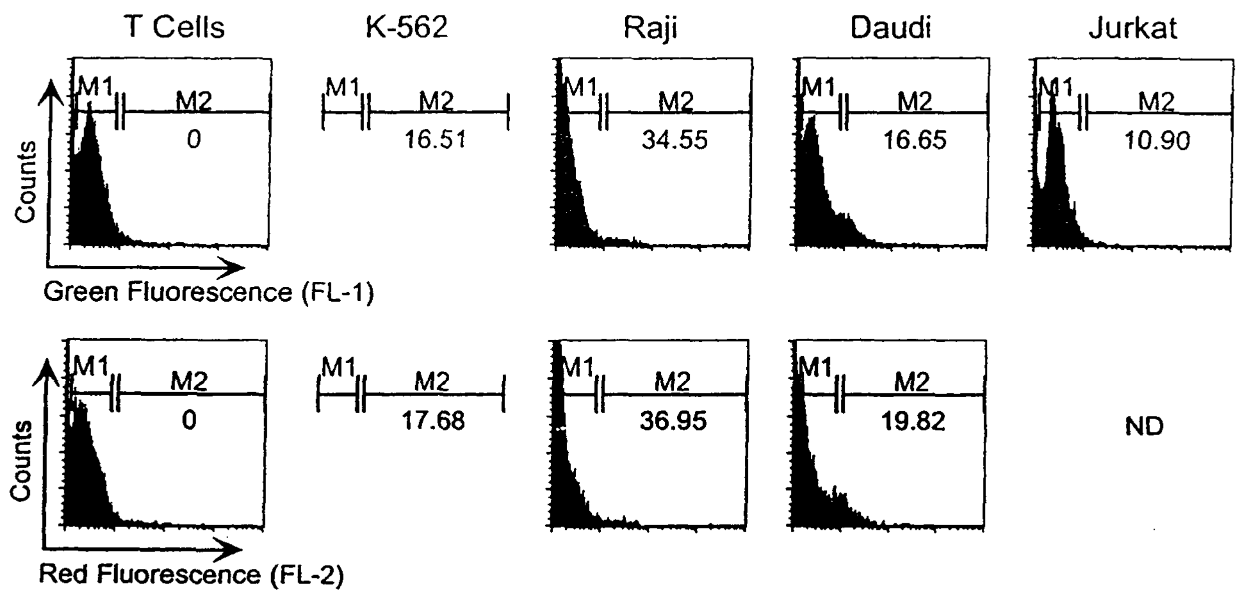

DISCUSSION

In the present work, the inherent autofluorescent characteristic of tumor cells was measured as well as autofluorescence of cells affected by environmental influences. All cells autofluoresce to some degree when stimulated by the appropriate electromagnetic energy. Laser-induced autofluorescenc has been attributed to the emission of excitation energy by substances such as flavins, porphyrins and aromatic structures within the cell. The absorption of 360 nm energy by the coenzyme $NADH_2$ results in an emission maxima at 460 nm. Riboflavin emission has been reported at 530 nm. Thus , differences in autofluorescent spectra have been used to appraise the oxidative state of the cell.

Recent investigations have demonstrated the usefulness of this distinction \in diagnosis of tumors in situ. eliminating the need for biopsy in some instances . Thus , early detection of colon cancer cells has been detected by LIF on in situ tissues. (Dus). Bladder cancer has likewise been regnized (Koienig).

These assays were performed histochemically. Cellular biopsies could be performed on in vitro cell suspensions as well as by a single investigation with flow cytometry.

Cells that autofluoresce by absorbing the laser energy can be saparated from cells that absorb the energy to a slesser extent. The exploitation of this characteristic provides the basis for the chareacterizartion of distinct cell types. Researchers have separated dendritic cells from macrophages in this manner. (10)

Splenic macrophages and murine Kuppfer cells have also been separated. (11)

Aberrant glycosylation in the formation of AGEs has been firmly implicated in the symptomology of diabetes and the aging process (2) The presence of AGE formation is readily detected with LIF. The effectiveness of methodologies which prevent or reverse glycosylation can likewise be monitored since the intensity of emitted fluorescence from simulated lased energy is proportional to the extent of glycosylation.

In a previous investigation we showed hyperbaric oxygen therapy can be used to treat non-healing wounds of diabetics by reversing AGE formation. Others have used aminoguanidine or butyrate successfully. (9) The deglycosylation in these procedures can be monitored by LIF.

All cells autofluoresce to some degree when stimulated by appropriate electromgnetic energy. In addition to cell surface glycoproteins, LIF detects the presence of the reduced flavin and nicotinamide coenzyms, $FADH_2$ and $_{NADH2}$. These compounds appraise the oxidate state of the cell. They are pronounced in cancer cells.

Cells that autofluoresce by absorbing various amounts of laser energy can be separated from cells that absorb such energy to a lesser extent. Researchers have separated dendritic cells from macrophages in this manner. (10). Splenic macrophages and murine Kuppfer cells have been also separated using the technique. (11)

Early detection of colon cancer cells has been detected by LIF (12). Bladder cancer has also been recognized (13). Cellular biopsies can be performed on in vitro cell suspensions by a single investigation with flow cytometry.

When we stimulated Jurkat Cells (Clone E6-1 acute T Cell Leukemia, human) with the argon laser, they emitted fluorescent light in the green, (570 nm) and red, (630nm) regions of the visible spectrum. the other cancer lines which we examined in this research showed similar results. Normal human T-cells served as our controls, and they did not show appreciable autofluorescence under laser stimulation. The results confirmed our hypothesis that LIF can be used as an indicator of malignancy and aberrant glcosylation

This concluision was based on the premise that a tumor glycogonjugate antigen or other aberrant glycation was involved in the etiopathogenesis of these cancers.

Murine splenocytes and bone marrow cells cultured in excess glucose exhibited greater autofluorescence when compared to cultures grown in normal glucose. The induction of increased metabolism was verified by quantitation of the cellular DNA. Human peripheral blood mononuclear cells (PBMC) demonstrated similar fluctuaions in autofluorescence emission spectra when grown in the presence of elevated glucose in both unit gravity and in simulated microgravity. Taken together, these findings show new potentiala s of LIF in cell biology and flow cytometry.

BIBLIOGRAPHY

1- Nigel, Jenkins, Parekh, Raj.B and James ,David C., "Getting the glycosylation right: implication
for biotechnology industry." Nature Biotechnology,14: 975-981, 1996 Aug.

2- Brownlee, M., "Glycosylation of proteins and microangiopathy." Hosp.Prac., 27(1):46-50, 1992, Feb.

3- Sharon, Nathan and Halina Lis, "Carbohydrates in cell recognition" Scientific American, 822-89, 1993, Jan.

4- Dennis, J.W., "Swainsonine prototype for a new class of anticancer agents," Clinical Cancer Research, 1: 935-944, 1995.

5- Shapiro, Howard M., Practical Flow Cytometry, Wiley-Liss, New York, 1995.

6- Taylor –Papaditriou, J., Epenetos, A.A., "Exploiting altered glycosylation patterns in cancer." Trends in Biotechnology, 12(6):277-33,1994, June

7- Dablelsteen, E., "Carbohydrate antigens and cancer." Ugeskr Laeger: 155(17): 1270-1275, 1993, April 26.

8- Koenig, K, and Shneckenburger, H., "Laser induced autofluorescence for medical \diagnosis." –Journal of Fluorescence,4(1): 17-25, 1994.

9- Kimbrell, P>N>, Lawless, B.D., "Hyperbaric oxygenation treatment alters immune response in non-healing wounds of patients with diabetes." Aviation Space and Environmental Medicine, 66 (5): 488, 1995.

10- Carin, E.G., et al., "Separation of Alveolar Macrophages and Dendrite Cells via autofluorescence: phenotypical and functional characteization." J.Leukoc. Biol.- 53: 504-510, 1993.

11- TenHagen, T.L., "Isolation and characterization of murine Kupffer cells and splenic macrophages." J. Immunol. Meth., 14 (1): 81-91, 1996, June.

EPILOGUE

A half century ago, Vannevar Bush wrote “Science: The Endless Frontier”. Alexander Pope wrote, “Hill peeps o’er hill and Alp on Alp arise”. These two classics haunt me at the conclusion of these investigations. The research has revealed some answers but most importantly it has given rise to further questions. And that is science: asking the right question.

Laser Induced Autofluorescence as shown in this work has tremendous analytical potential. It monitors glycosylation and deglycosylation, measures the rate of cellular metbolism, in the instances cited distinguishes cancer cells from normal ones. It potentially can be a tool for the oncologist to show the effectiveness of particular therapies. Conceivably, it can show that deglycosylation can convert cancer cell to normalcy.

LIF has established itself in assay protocol and determining etiopathogenesis in some instances. The argon laser of the flow cytometer readily determines rates of apoptosis and cell prolifertion in the cell cycles. It does more: when coupled with other techniques, it shows the influences that alter cell cycle.

The most valuable contribution of this summer research is to “ask the right question” and now to seek the answer to that question.

We are grateful for having had this opportunity.

August 4, 2000

Important background papers to support this research proposal:

GETTING THE GLYCOSYLATION RIGHT: IMPLICATIONS FOR THE BIOTECHNOLOGY INDUSTRY
Nigel Jenkins, Raj B Parekh and David C James
NATURE BIOTECHNOLOGY, Vol 14, August 1996

TUMOR MALIGNANCY DEFINED BY ABERRANT GLYCOSYLATION AND SPHINGO-GLYCOLIPID METABOLISM
Sen-itiroh Hakomori,
CANCER RESEARCH 56, 5309-5318, Dec 1, 1996

ANTIGEN PRESENTATION. ABERRANT GLYCOSYLATION AND TUMOR PROGRESSION.
G.V. Glinsky
CRITICAL REVIEWS IN ONCOLOGY/HEMATOLOGY,
17 (1994) 27-51

DIRECT ACTIVATION OF CD8+ CYTOTOXIC T LYMPHOCYTES BY DENDRITIC CELLS.
Kayo Inaba, James W. Young, and Ralph M. Steinman
J. EXP. MED., 166 July 1987 182-194

MECHANISMS OF MOUSE SPLEEN DENDRITIC CELL FUNCTION IN THE GENERATION OF INFLUENZA-SPECIFIC, CYTOLYTIC T LYMPHOCYTES.
Ruta Nonacs, Cornelia Humborg, James P. Tam and Ralph M. Steinman.
J.EXP.MED., 176, Aug 1992, 519-529

ALTERATION IN HUMAN MONONUCLEAR LEUCOCYTES FOLLOWING SPACE FLIGHT.
R.T. Meehan, L.S. Neale, E.T. Kraus,C.A. Stuart, M.L. Smith, N.M. Cintron, and C.F.Sams. IMMUNOLOGY, 22 March, 1992, 491-497.

PROTEIN GLYCOSYLATION IN DEVELOPMENT AND DISEASE.
James W. Dennis, Maria Granovsky, and Charles E. Warren.
BIOASSAYS 21, 412-421, 1999

INACTIVATED INFLUENZA VIRUS, WHEN PRESENTED ON DENDRITIC CELLS ELICITS HUMAN CD8+ CYTOTOXIC T CELL RESPONSES.
Arman Bender, Long Kim Bui, Mary A.V. Feldman, Maraie Larson, and Nina Bhardwaj. J. EXP MED 182, Dec 1995, 1663-1671.

CARBOHYDRATES IN CELL RECOGNITION, Nathan Sharon and Halina Lis,
SCIENTIFIC AMERICAN, January, 1992 82-89

SPACEFLIGHT ALTERS MICROTUBULES AND INCREASES APOPTOSIS IN HUMAN LYMPHOCYTES (Jurkat). Marian L. Lewis, B. DeSales Lawless, E Piepmeier, et al., FASEB JOURNAL, 12, August, 1998.

USING TRI-AXIAL ACCELEROMETERS TO ASSESS THE DYNAMIC CONTROL OF HEAD POSTURE DURING GAIT

John H. Lawrence III, Ph.D.
Center for Biomedical Engineering, University of Kentucky
SD3
August 2, 2000

Jacob J. Bloomberg, Ph.D. & Ajit Mulavara, Ph.D.
Life Sciences Research Laboratories
Medical Sciences Division
Space & Life Sciences Directorate

John Lawrence, Faculty Fellow

8/3/00
Jacob Bloomberg, JSC Colleague

8/3/00
Ajit Mulavara, JSC Colleague

Shannon Belcher
Shannon Belcher, NASA-ASEE
Summer Intern

USING TRI-AXIAL ACCELEROMETERS TO ASSESS THE DYNAMIC CONTROL OF HEAD POSTURE DURING GAIT

Final Report

NASA/ASEE Summer Faculty Fellowship Program – 2000

Lyndon B. Johnson Space Center

Prepared By:	John H. Lawrence III, Ph.D.
Academic Rank:	Assistant Professor
University & Department:	University of Kentucky Center for Biomedical Engineering Lexington, KY 40506-0070

NASA/JSC

Directorate:	Space & Life Sciences
Division:	Medical Sciences
Branch:	Life Sciences Research Laboratories
JSC Colleagues:	Jacob J. Bloomberg, Ph.D. Ajit Mulavara, Ph.D.
Date Submitted:	August 3, 2000
Contract Number:	NAG 9-867

ABSTRACT

Long duration spaceflight is known to cause a variety of biomedical stressors to the astronaut. One of the more functionally destabilizing effects of spaceflight involves microgravity-induced changes in vestibular or balance control. Balance control requires the integration of the vestibular, visual, and proprioceptive systems. In the microgravity environment, the normal gravity vector present on Earth no longer serves as a reference for the balance control system. Therefore, adaptive changes occur to the vestibular system to affect control of body orientation with altered, or non-present, gravity and/or proprioceptive inputs.

Upon return to a gravity environment, the vestibular system must "re-incorporate" the gravity vector and gravity-induced proprioceptive inputs into the balance control regime. The result is often a period of postural instability, which may also be associated with "space motion sickness" (oscillopsia, nausea, and vertigo). Previous studies by the JSC Neuroscience group have found that returning astronauts often employ alterations in gait mechanics to maintain postural control during gait. It is believed that these gait alterations are meant to decrease the transfer of heel strike shock energy to the head, thus limiting the contradictory head and eye movements that lead to gait instability and motion sickness symptoms.

We analyzed pre- and post-spaceflight tri-axial accelerometer data from the NASA/MIR long duration spaceflight missions to assess the heel to head transfer of heel strike shock energy during locomotion. Up to seven gait sessions (three preflight, four postflight) of head and shank (lower leg) accelerometer data was previously collected from six astronauts who engaged in space flights of four to six months duration. In our analysis, the heel to head transmission of shock energy was compared using peak vertical acceleration (**a**), peak jerk (**j**) ratio, and relative kinetic energy (KE). A host of generalized movement variables was produced in an effort to isolate those that best highlighted vestibular adaptation due to spaceflight.

Data suggest that astronauts used either head or body centered control to reduce the effects of heel strike shock on head position during normal walking at self-selected speeds. Moreover, the form of that control appears to fall under one of two categories: homeostatic or adaptive. Homeostatic control refers to tight constraint (small error) over the value of a given variable before and after spaceflight with little or no "adaptive" changes. Adaptive control refers to lesser constraint over a given movement variable with clear adaptation to earth gravity upon return from spaceflight.

Heel strike shock absorption (ratio of heel to head peak acceleration) best-discriminated head and body centered control strategies. Further, peak jerk data was useful for illustrating pre- and postflight differences in segmental (shank versus head) movement energy. Results from kinetic energy analysis show high consistency between subjects and across test dates. Whether this result highlights a control strategy or is an artifact of approximating body segments using anthropometric tables is, at this point, unclear.

METHODS

Data Collection

Data for this study was collected from six NASA astronauts who flew on long duration space flights aboard the MIR space station. The experimental protocol involved a total of seven test sessions. Three preflight and four postflight gait sessions (see Table 1) were scheduled. Not every astronaut participated in each of the seven test sessions.

Subjects were instrumented with reflective markers for 3-D kinematic analysis, electromyography electrodes to monitor leg muscle activity, and tri-axial accelerometers to measure head and shank accelerations. While kinematic (movement), electromyographic, and dynamic (force, acceleration) data were being collected, subjects walked across the test floor at their self-selected gait speed. Accelerometer data was synchronized to force plate and kinematic data for accurate timing of individual subject gait cycles and stored for later analysis using Bioware software (Kistler Instruments). Data was also collected at both 80% and 120% of self-selected speed, but that data was not analyzed for this project.

Table 1. Key for NASA/MIR Gait Test Sessions

A	practice session	60+ days preflight
B	preflight session 1	30+ days preflight
C	preflight session 2	7+ days preflight
D	R + 0	day of return from spaceflight
E	R + 1	one day after return
F	R + 4	3-6 days after return
G	R + 8	7-9 days after return

Signal Processing

For the present study, the time trace, vertical force plate data, and accelerometer (up to six channels) data were imported from Bioware into a novel signal-processing algorithm written by Dr. Lawrence for use under the Matlab (Mathworks, Inc.) environment. The time trace was converted into millisecond units based upon the data sampling frequency (500-1020 Hz). Vertical force and accelerometer data were filtered at 50 and 100 Hz, respectively. The temporal onset of heel strike was calculated from the vertical force trace. From this, a "heel strike window" of approximately 65 ms (15 ms before heel strike, 50 ms after) was set for subsequent analysis of head and shank accelerometer waveforms (Fig. 1). All data was analyzed over the established heel strike window (different for each data trial) to model the transmission of heel strike shock energy to the head during walking.

Data Analysis

A series of previously defined movement variables was produced from head and shank accelerometer waveforms falling within the designated heel strike window. Figure 1 provides a generalized description of the heel strike window. Note the heel strike window begins prior to the actual heel strike event as peak shank acceleration usually preceded heel strike. The algorithm calculated the peak head and shank accelerations, peak head and shank jerk and head and shank kinetic energy (see Appendix). Jerk, the time rate of change of acceleration, was calculated by taking the derivative of the head and shank acceleration traces (vertical and 3-D magnitude) over the heel strike window. Kinetic energy for the head and shank was modeled as proportional to mv^2, where subject mass m equaled subject weight divided by the acceleration of gravity and velocity v was calculated as the integral of the head and shank acceleration traces over the heel strike window (see Appendix for equations). Anthropometric data (Winter, 1990) was used to approximate head mass for HKE calculation.

Vertical Ground Reaction Force

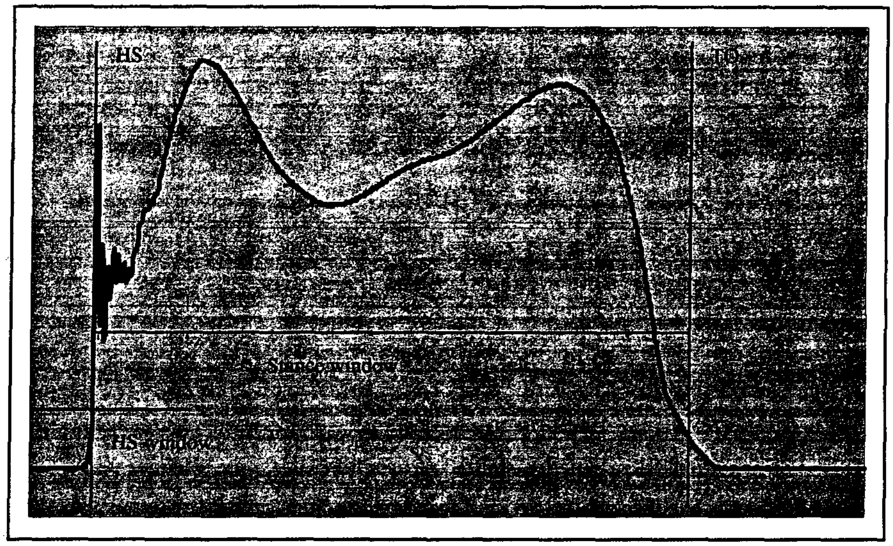

Figure 1. Typical vertical ground reaction force trace illustrated with key epochs in the gait cycle. Horizontal lines approximate the interval set for the heel strike analysis window. This window corresponded temporally to accelerometer traces. HS denotes the heel strike; TO denotes toe-off. The time interval between heel strike and toe-off defines the stance phase of gait.

The algorithm also calculated energy absorption values for acceleration, jerk, and kinetic energy. Absorption values were expressed as either ratios or percentages, modeling the proportion of heel strike shock that was "absorbed" by the body tissues prior to reaching the subject's head. Note the latency between peak shank and head vertical accelerations was calculated to accurately determine absorption values (Smeathers 1989). Peak absorption expressed the ratio of shank to head peak acceleration. Jerk absorption denoted the ratio of shank to head jerk, while RMS jerk ratio denoted the percentage of shank or heel strike jerk reaching the head. Kinetic energy absorption values expressed the percentage of heel strike kinetic energy manifested in head kinetic energy.

Generalized Gait Control Models

Analysis of shock energy variables over the heel strike window suggests the utilization of two generalized models for the control of head position during walking. The first of these control models is the head-centered strategy. Subjects most concerned with minimizing changes in head positioning during walking utilized this strategy. On the other hand, subjects most concerned with minimizing changes in energy transfer throughout the body during walking utilized the body-centered strategy.

Within each strategy, variables were further stratified based upon whether homeostatic or adaptive control was employed. Homeostatic control refers to resisting change in the value of the movement variables with changing environmental conditions. Adaptive control refers to alteration in the value of movement variables during environmental change.

RESULTS

Preliminary results suggest that two of the six astronauts employed a body-centered strategy based upon adaptive control. Figure 2 shows the peak absorption across test sessions (four trials per session) for the two astronaut subjects (9104 and 9015). Note the much higher absorption of heel strike shock upon return from spaceflight (session E) compared to pre- and postflight sessions. Moreover, these astronauts appeared to actively control the magnitude and variability (decrease the error) of shock absorption through the body during Earth-g locomotion.

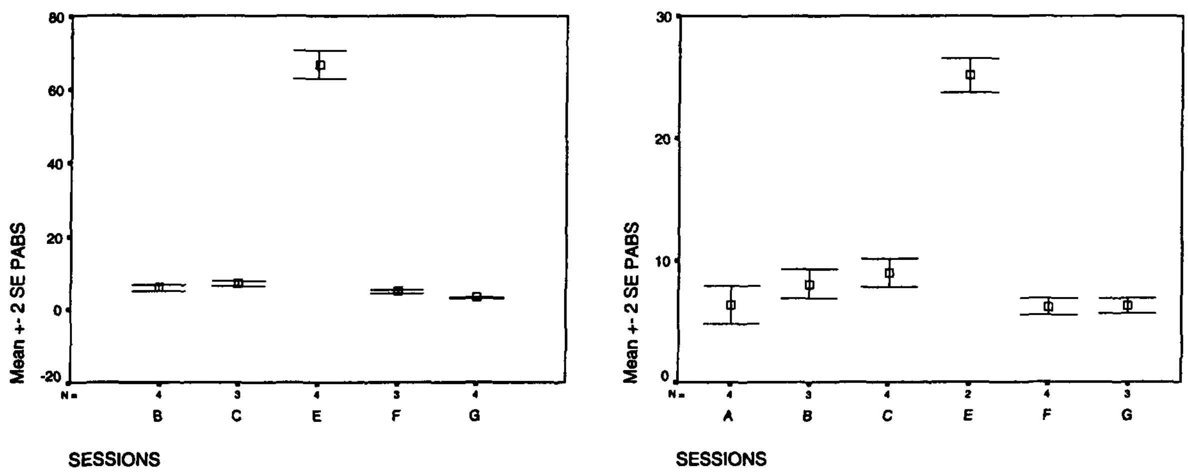

Figure 2. Plots of peak shock absorption across test sessions for two of the MIR astronauts (*l*-9014, *r*-9015). Values are *mean* ± *standard error (n=4).* Note the higher heel strike shock absorption at one day after return (session E, or R+1) as compared to preflight (A-C) and later postflight sessions F and G.

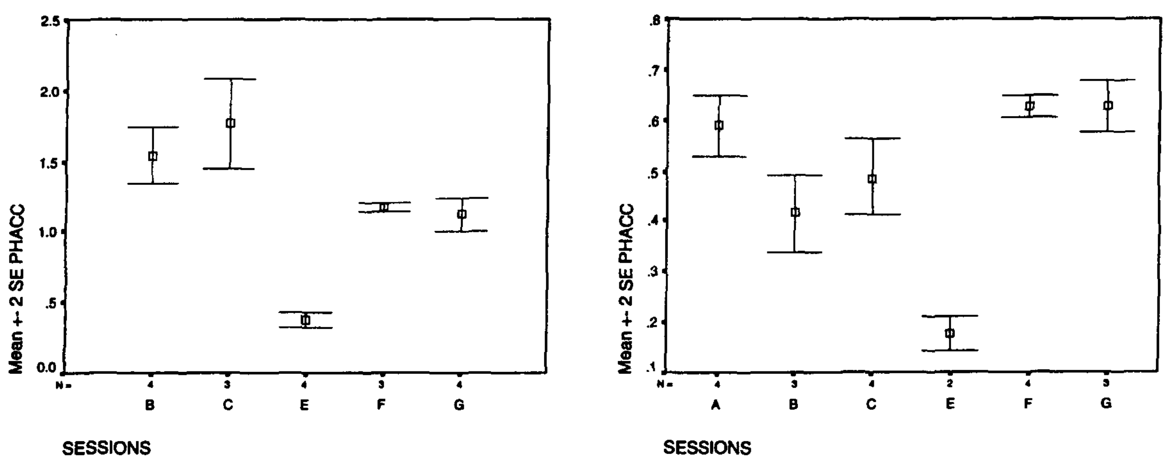

Figure 3. Peak head accelerations resulting from heel strike for astronauts 9014 (*left*) and 9015 (*right*). Note the much-reduced values recorded one day after return (session E). By session F, astronauts had re-adapted to preflight levels. Values are mean ± standard error (n=4).

The interplay between peak head and shank acceleration further illustrate head-centered adaptive control by astronauts 9014 and 9015 (Fig. 3). Note in Figure 3 how both subjects adapted to long duration spaceflight with vast reductions in head acceleration at heel strike (session E), returning to preflight levels upon re-adaptation. Shank acceleration data (not shown) suggests that these astronauts varied lower limb kinematics at heel strike to offset variability in head vertical accelerations; thus minimizing changes in absorption values.

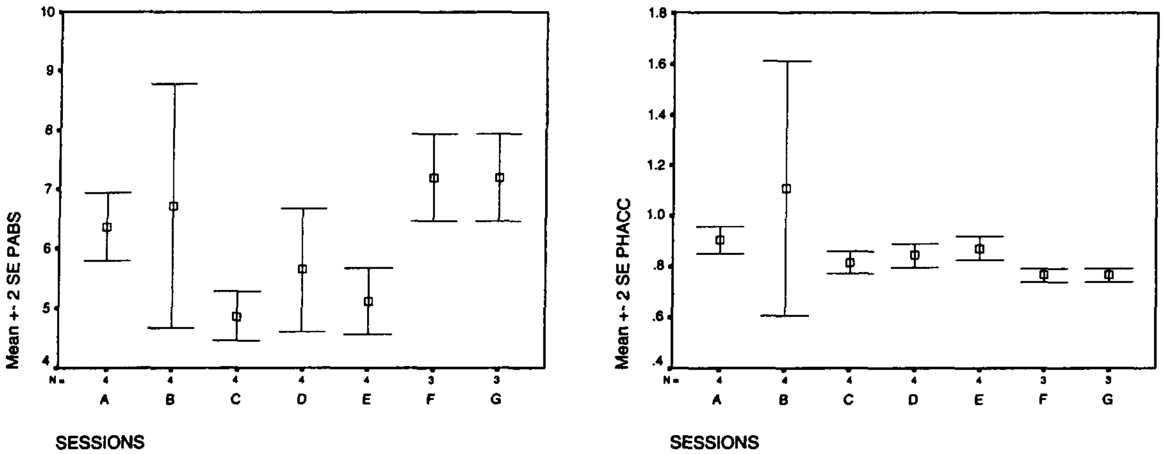

Figure 4. Interplay between shock absorption (left) and head acceleration (right) for NASA/MIR astronaut 1120. Values represent peaks over the heel strike time window (mean ± standard error, n=4).

The control strategy shown utilized by astronaut 1120 (Fig. 4) contrasted with that seen for the above astronauts. Note the absence of a distinct alteration in absorption upon return from spaceflight (sessions D/E vs. C and F. This astronaut appears to utilize a homeostatic head-centered strategy, sacrificing control of total body absorption to instead control peak head acceleration across test day (A-C, E-F) and against changes in environmental condition (pre- vs. post-flight). Data suggest that variations in peak absorption were related to alterations in peak shank acceleration (not shown).

DISCUSSION

One of the principal goals of the JSC Neuroscience Group is to design countermeasures to spaceflight induced gait instability. A series of studies developed to address that issue centers on the role of adaptability in reducing the effects of spaceflight on gait control. In this regard, researchers posit that the ability of a person to adapt to changing circumstances, as well as the form of that adaptation, defines how well that person will re-adapt to gravity environments after prolonged space flight. An example of this can be seen in the responses modern athletes make to variable stimuli. A good soccer player may utilize a simple control regime to standardize motions when performing a sport. Yet she also responds, or adapts, well to unexpected perturbations imposed on those desired movements either by other athletes or playing conditions. Similarly, astronauts must physically adapt to changing environmental conditions to adequately perform spaceflight missions.

Vertical and rotational head oscillations naturally occur during normal walking (Reschke at al. 1994c). Recent evidence shows the vestibular system to play an integral part in assuring gaze stabilization during such head movements (McDonald at al. 1997, Reschke at al. 1994b). Heel strike shock analysis suggests that one method utilized by astronauts to control head position during gait is regulation of shock transmission. Heel strike shock can be modeled a number of ways: using either dynamic (acceleration) or state (energy) functions. We chose to investigate head control regimes by analyzing the dynamic regulation of shock energy transfer by NASA/MIR long duration spaceflight astronauts.

Our analysis results led us to focus on absorption (translation and vibration) and head acceleration as variables most indicative of an astronaut's chosen method for controlling head movements after spaceflight induced gait instability. Lower leg or shank acceleration (and therefore jerk) was linked to either absorption or head acceleration control. Kinetic energy data was impressive in its consistency, but was likely an artifact to use of anthropometric approximations. Evidence that two astronauts showed striking re-adaptation to preflight levels of shock absorption illustrates well the body-centered approach to adaptive control. They varied head and/or vertical shank acceleration during heel strike to control/maintain shock transmission characteristics both preflight and postflight (after re-adaptation). These astronauts greatly increased shock absorption during the re-adaptation phase (sessions D and E or up to 3-4 days after return) to limit head movements that can lead to instability and space sickness symptoms.

Although preliminary results are promising, further analysis of long-duration space flight results is warranted to refine characterization of astronaut adaptive control strategies. A common control theme might emerge for the other four astronauts once rigorous analysis using the absorption variables is applied. Anecdotally, jerk analysis also shows potential as an adaptive gait control assessment tool as. Finally, a study of possible interactive relationships between some of the heel strike shock variables calculated here might prove beneficial.

References

McDonald, P. Vernon, Bloomberg, Jacob J., Layne, Charles S. A review of adaptive change in musculoskeletal impedance during space flight and associated implications for postflight head movement control. *Journal of Vestibular Research*, Vol. 7, Nos. 2/3, 239-250, 1997.

Reschke, Millard F., Harm, Deborah L., Parker, Donald E., Sandoz, Gwenn R., Homick, Jerry L., Vanderploeg, James M. Neurophysiologic aspects: space motion sickness. In: Space Physiology and Medicine. Lea & Febiger, 3rd edition, Chapter 12, 228-260, 1994(a).

Reschke, Millard F., Bloomberg, Jacob J., Harm, Deborah L., Paloski, William H. Space flight and neurovestibular adaptation. *Journal of Clinical Pharmacology*, 34: 609-617, 1994(b).

Reschke, Millard F., Bloomberg, Jacob J., Paloski, William H., Harm, Deborah L., Parker. Neurophysiologic aspects: sensory and sensory-motor function. In: Space Physiology and Medicine. Lea & Febiger, 3rd edition, Chapter 13, 261-285, 1994(c).

Smeathers, J. E. Transient vibrations cased by heel strike. *Proceedings of the Institution for Mechanical Engineers*, Vol. 203, pp. 181-186.

Valiant, Gordon A. Transmission and attenuation of heelstrike accelerations. In: Biomechanics of distance running, P. R. Cavanagh editor, pp. 225-247, 1990.

Voloshin, Arkady S. Shock absorption during running and walking. *Journal of the American Podiatric Medical Association*, Vol. 78, No. 6, 295-299, 1988

Voloshin, A., Wosk, J., Brull, M. Force wave transmission through the human locomotor system. *Journal of Biomechanical Engineering*, Vol. 103, pp. 48-50, 1981.

Winter, D. A. Biomechanics and motor control of human movement. Wiley Interscience, 2nd edition, Chapter 3, 56-57, 1990.

APPENDIX

Analysis variables calculated over the heel strike interval:

peak head acceleration (PHACC)
peak shank acceleration (PSACC)
head kinetic energy HKE
shank kinetic energy SKE
peak head jerk (PHJ)
peak shank jerk (PSJ)

Absorption variables calculated over the heel strike interval:
peak absorption: heel strike shock energy absorbed by the body (PABS)
kinetic energy absorption: heel strike kinetic energy absorbed by the body (KEABS)
jerk absorption: heel strike vibration energy absorbed by the body (JABS)
RMS jerk ratio: percentage of heel strike jerk reaching the head (JRAT)

Mathematical techniques for calculating variables:

Acceleration:	$\mathbf{a}$, measured directly using a tri-axial (3-D) array of linear accelerometers
Jerk:	$\mathbf{j} = {}^{da}/_{dt}$, time rate of change of acceleration
Kinetic Energy:	proportional to mv^2, where velocity $\mathbf{v} = \int \mathbf{a} \cdot dt$ (over the heel strike interval)
PABS:	$\mathbf{a}_{shank}/\mathbf{a}_{head}$, ratio of peak shank to peak head heel strike acceleration
KEABS:	$(KE_{shank} - KE_{head})/KE_{shank}$, percentage of heel strike KE absorbed by the body
JABS:	$\mathbf{j}_{shank}/\mathbf{j}_{head}$, ratio of peak shank to peak head heel strike jerk
JRAT:	$(jRMS_{shank} - jRMS_{head})/jRMS_{shank}$, percentage of heel strike jerk (root mean square) reaching the head

Growth and Metabolism of the Green Alga, *Chlorella Pyrenoidosa,* in Simulated Microgravity

W. R. Mills
University of Houston-Clear Lake
SD3
September 19, 2000

D. L. Pierson
Life Sciences Research Laboratories
Medical Sciences Division
Space and Life Sciences Directorate

W. R. Mills

D. L. Pierson

Attachment 2

Growth and Metabolism of the Green Alga, *Chlorella Pyrenoidosa,* in Simulated Microgravity

Final Report

NASA/ASEE Summer Faculty Fellowship Program--2000

Johnson Space Center

Prepared By:	W. Ronald Mills, Ph.D.
Academic Rank:	Professor
University & Department:	University of Houston-Clear Lake Programs in Biology and Chemistry Houston, Texas 77058

NASA/JSC

Directorate:	Space and Life Sciences
Division:	Medical Sciences
Branch:	Life Sciences Research Laboratories
JSC Colleague:	Duane L. Pierson, Ph.D.
Date Submitted:	September 19, 2000
Contract Number:	NAG 9-867

Abstract

The effect of microgravity on living organisms during space flight has been a topic of interest for some time, and a substantial body of knowledge on the subject has accumulated. Despite this, comparatively little information is available regarding the influence of microgravity on algae, even though it has been suggested for long duration flight or occupancy in space that plant growth systems, including both higher plants and algae, are likely to be necessary for bioregenerative life support systems.

High-Aspect-Ratio Rotating-Wall Vessel or HARV bioreactors developed at Johnson Space Center provide a laboratory-based approach to investigating the effects of microgravity on cellular reactions. In this study, the HARV bioreactor was used to examine the influence of simulated microgravity on the growth and metabolism of the green alga, *Chlorella pyrenoidosa.*

After the first 2 days of culture, cell numbers increased more slowly in simulated microgravity than in the HARV gravity control; after 7 days, growth in simulated microgravity was just over half (58%) that of the gravity control and at 14 days it was less than half (42%). Chlorophyll and protein were also followed as indices of cell competence and function; as with growth, after 2-3 days, protein and chlorophyll levels were reduced in modeled microgravity compared to gravity controls.

Photosynthesis is a sensitive biochemical index of the fitness of photosynthetic organisms; thus, CO_2-dependent O_2 evolution was tested as a measure of photosynthetic capacity of cells grown in simulated microgravity. When data were expressed with respect to cell number, modeled microgravity appeared to have little effect on CO_2 fixation. Thus, even though the overall growth rate was lower for cells cultured in microgravity, the photosynthetic capacity of the cells appears to be unaffected.

Cells grown in simulated microgravity formed loose clumps or aggregates within about 2 days of culture, with aggregation increasing over time. Presently, the basis for, or significance of, the cell aggregation is unknown.

The results from this study suggest that cell growth and morphological characteristics of green algae may be altered by culture in simulated microgravity. The data obtained to date should provide a solid basis for additional experimentation regarding the influence of modeled microgravity on cell morphology, physiological activity, protein production and possibly gene expression in algal and plant cell systems. The final aim of the study is to provide useful information to elucidate the underlying mechanism for the biological effects of microgravity on cells.

INTRODUCTION AND BODY OF REPORT

Microgravity

The effect of microgravity on living organisms during space flight has been a topic of interest for some time, and a substantial body of knowledge on the subject has accumulated. Despite this, comparatively little information is available regarding the influence of microgravity on algae, even though it has been suggested that for long duration flight or occupancy in space, plant growth systems, including both higher plants and algae, are likely to be necessary for bioregenerative life support systems [13, 14]. Moreover, it has been stated that "an elucidation of the range and mechanisms of the biological effects of microgravity is one of the urgent fundamental tasks in space biology" [7].

The term "microgravity" is generally accepted as a condition in which the absolute sum of all mass-dependant accelerations does not exceed a certain small noise level, typically 10^{-5} g to 10^{-4}g. Cell cultures exposed to microgravity are influenced by at least three relevant factors: a) three dimensional cell assembly, b) low shear and turbulence, and c) co-spatial arrangement of different cell types and substrates [5].

Generation of Simulated Microgravity

A major advance for microgravity studies in cell culture has been the development of Rotating Wall Vessel or RWV bioreactors at NASA-Johnson Space Center [11]. The RWV bioreactors produce an environmental condition variously called "simulated or modeled microgravity" in which the gravitational vectors are randomized over the surface of the cells, resulting in an over-all-time-averaged gravitational vector of about 10^{-2} g [1]. This reduction in gravity creates a sustained low-shear environment for cell growth and is intended to model in the laboratory some effects of weightlessness or microgravity on cells (5,6).

A particularly useful form of RWV bioreactor is the High-Aspect-Ratio Rotating-Wall Vessel or HARV bioreactor. Figure 1 below illustrates how the HARV bioreactors may be oriented to grow cells under conditions of "simulated microgravity" (Fig. 1A) or normal gravity (1 x g) (Fig. 1B). When the unit is completely filled with liquid, gas bubbles cannot cause turbulence and a HARV, with its axis of rotation perpendicular to gravity, simulates microgravity by nullifying the downward gravity vector. A second HARV may be placed in a horizontal position. In this case, the axis of rotation is parallel to the gravity vector and the gravity vector is no longer nullified, thus serving as a "gravity control".

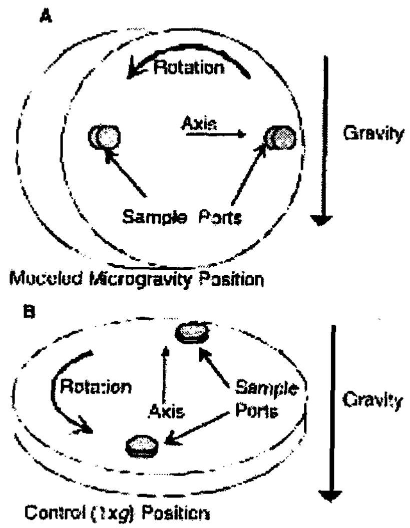

Figure 1. High-Aspect-Ratio Rotating-Wall Vessel Bioreactor (HARV). A HARV bioreactor in the modeled or simulated microgravity orientation (A) and in the normal gravity "control" position (B) is shown. Figure taken from Nickerson, et al. [8].

Previous Microgravity Studies in Algae

Over the last few years, rotating bioreactors have been used to study the effects of simulated microgravity on mammalian cells (see [12] for a review) and in bacteria [2-4]. By contrast, little work on the growth of algal and plant cells in modeled microgravity has been carried out using HARV or other RWV bioreactors.

The green alga, *Chlorella pyrenoidosa* has been used in a limited number of experiments in both space and clinostat studies. In these cases, *Chlorella* cells have been cultured in semiliquid and solid aseptic media, both under light and dark conditions. Under these conditions, an increase in biomass, reproduction and viability of *Chlorella* was observed when cells were grown in microgravity on space vehicles. The microgravity conditions not only affected growth but also structural and biochemical indices, suggesting that weightlessness may have diverse and important influences on growth and vital functions of physiologically active *Chlorella* [11].

A typical feature of *Chlorella* vegetative cells is the large cup-shaped chloroplast that occupies most of the cell's volume. Under autotrophic conditions, the thylakoids are joined in bundles and form the granae in separate chloroplast areas. The pyrenoid is perforated with one to three thylakoids and surrounded by amylogenic coating. When grown in darkness on an organic medium, the granae are absent and bundles of thylakoids often bend [9]. Changes in the ultrastructure of *Chlorella* cells were seen in space experiments of different duration [10]. In short duration, 4.5 day, studies with *Chlorella* strain LARG-1 cultivated on a semiliquid medium, there was a decrease in the relative volume of thylakoids and starch grains in chloroplasts, and the cytoplasmic membrane had more complex folds. In 10.5 – 18 day flights, there were alterations in cytokinesis and dilation of the intrathylakoid membrane space. In addition, with the decrease in the thylakoid volume there was a simultaneous decrease in chlorophyll *a* and *b* content. There was an increase in condensed chromatin, which accumulated along the nuclear periphery, as well as an increase in cell vacuolization and number of mitochondria per cell. Finally, a doubling of specific amylases compared to ground control was seen [9, 10].

Specific Aims of the Study

The goal of this study was to examine the effect of microgravity on growth, morphological and biochemical characteristics of a green alga, in this case *Chlorella pyrenoidosa.* The specific aims of the research were the following:

1. To examine the effect of simulated microgravity on growth of *Chlorella* cells.
2. To study the effect of simulated microgravity on morphology of *Chlorella* cells.
3. To examine the effect of simulated microgravity on the production of chlorophyll and protein by *Chlorella* cells.
4. To study the effect of simulated microgravity on photosynthetic capacity of *Chlorella* cells.
5. To examine the effect of simulated microgravity on the protein expression of *Chlorella* cells.
6. To examine the effect of simulated microgravity on the gene expression of the *Chlorella* cells.

Results

Results from simulated microgravity studies with *Chlorella pyrenoidosa* are illustrated in Figures 2-12, as well as Table 2, below. Cultures were grown in either simulated microgravity or HARV gravity control conditions (see Figure 1 above). In addition, a culture grown in a non-rotating flask was used as an alternative gravity control.

Figure 2 shows growth data as determined by cell number. Cell numbers in simulated microgravity were similar to those in the HARV gravity control for the first 2 days. After that time, cells grew more slowly in simulated microgravity than in the HARV gravity control; by day 7 the growth in simulated microgravity was approximately half (58%) that in the HARV gravity control and by day 14 day it was less than half (42%). Interestingly, growth was substantially greater in the stationary flask gravity control (see Figure 2) than either the HARV gravity control or in simulated microgravity. Chlorophyll and proteins levels were also followed as indices of growth and cell viability; after 2-3 days of culture, both chlorophyll and protein were lower in cultures grown in simulated microgravity than in gravity controls (Figures 3 and 4).

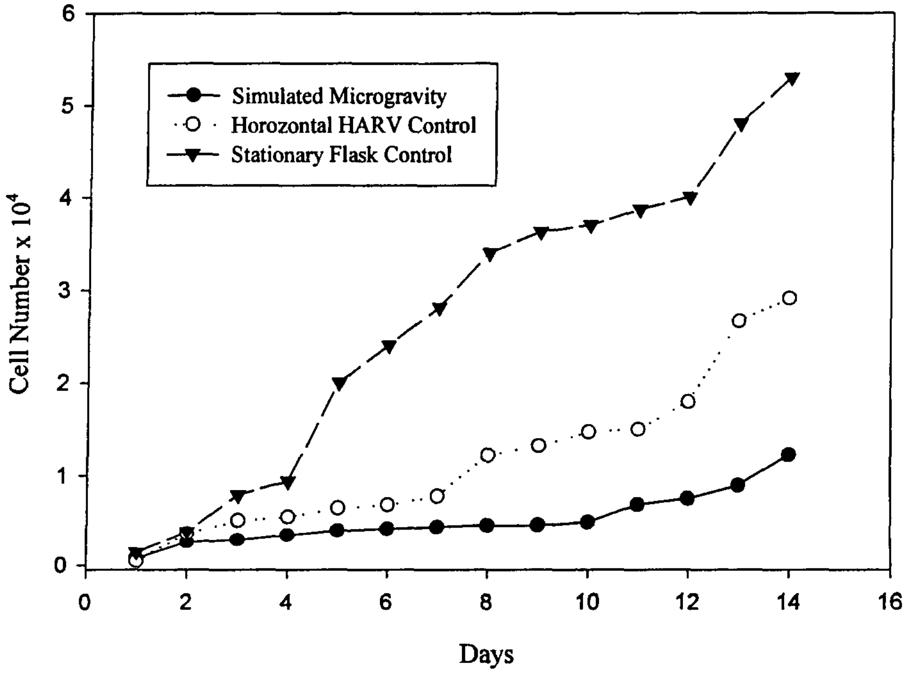

Figure 2. Effect of Simulated Microgravity on Growth of *Chlorella pyrenoidosa* Cells.

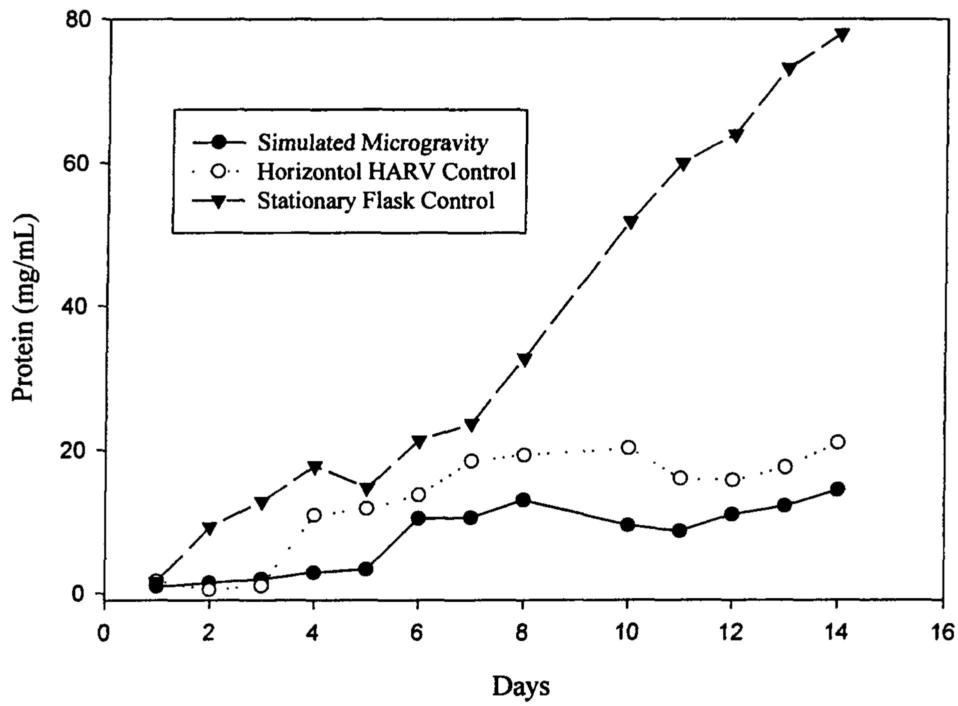

Figure 3. Effect of Simulated Microgravity on Protein Production in *Chlorella pyrenoidosa* Cells.

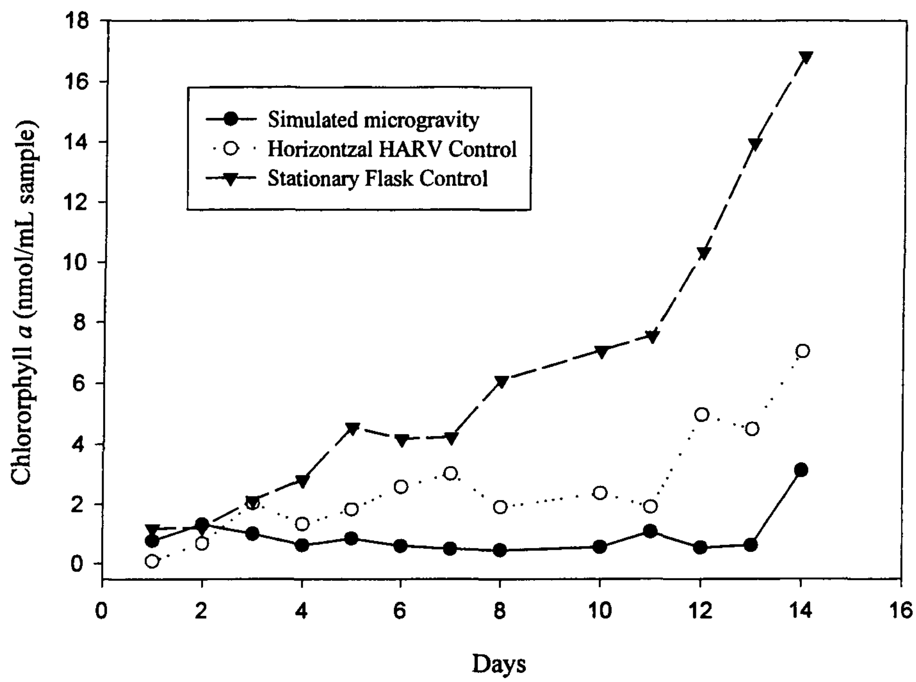

Figure 4. Effect of Simulated Microgravity on Chlorophyll *a* Production in *Chlorella pyrenoidosa* Cells

As noted above, *Chlorella* cells grew more slowly in the HARV under simulated microgravity than in the gravity control (Figure 2). These results are in contrast with the increase in growth, reproduction and viability of *Chlorella* cells seen in true microgravity when cultured on solid medium in space vehicles [9,10]. On the other hand, the decline in chlorophyll content of the *Chlorella* cells observed in simulated microgravity (Figure 4) is consistent with a corresponding decline in chlorophyll content seen when *Chlorella* cells were grown for 10.5 or 18 days in space on semiliquid medium.

CO_2 photoassimilation is often used as an index of the fitness of photosynthetic organisms. Table 2 illustrates the effect of simulated microgravity on CO_2-dependent O_2 evolution, which is a measure of CO_2 fixation capacity. The data are represented as O_2 evolution per cell or per unit chlorophyll. With either index, O_2 evolution rates were relatively similar for all samples. Thus, even though the growth rate was lower for cells cultured in simulated microgravity, the photosynthetic capacity of the cells appears to be unaffected.

Table 2. Effect of Simulated Microgravity on Photosynthetic Activity in *Chlorella pyrenoidosa* Cells as Determined by CO_2-Dependent O_2 Evolution.

Treatment	Photosynthetic activity (μmol O_2 evolved/min/ mg chlorophyll *a*)	Activity (% of stationary flask control)	Photosynthetic activity (μmol O_2 evolved /min/10^7 cells)	Activity (% of stationary flask control)
Stationary flask control	5.51	100	17.5	100.0
Horizontal HARV control	5.79	105.1	14.0	80.0
Simulated microgravity	5.47	99.3	14.1	80.9

An additional interesting finding is that cells grown in simulated microgravity form loose clumps or aggregates within 2 days of culture (Figure 5 and 6), with aggregation increasing with time of cell growth (Figures 7-12). A limited amount of cell clumping is also seen in cultures grown in the gravity control; however, the aggregation occurs later, for example after 7-14 days of growth, and only to a limited extent (Figures 7-12). At present, the basis for, or significance of, the cell aggregation is unknown.

Due to time limitations, proposed protein and gene expression studies were not completed. However, cell samples grown for 7 or 14 days under control and simulated microgravity conditions have been collected and stored in the ultracold; they will be used for subsequent experiments on protein and gene expression.

Conclusions

The initial results from this study suggest that cell growth and morphological characteristics of green algae may be affected by culture in simulated microgravity. The results obtained thus far should provide a solid basis for additional experiments regarding the effects of simulated microgravity on cell morphology, physiological activity, protein production and possibly gene expression in algal and plant systems. The final aim of the study is to provide useful information in elucidating the underlying mechanisms for the biological effects of microgravity on plant cells.

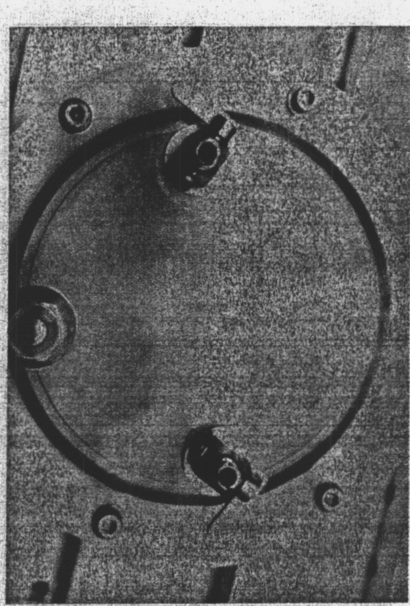

Figure 5. Appearance of *Chlorella* Cell Cultures Grown for 2 Days in a HARV Bioreactor Under Gravity Control Conditions.

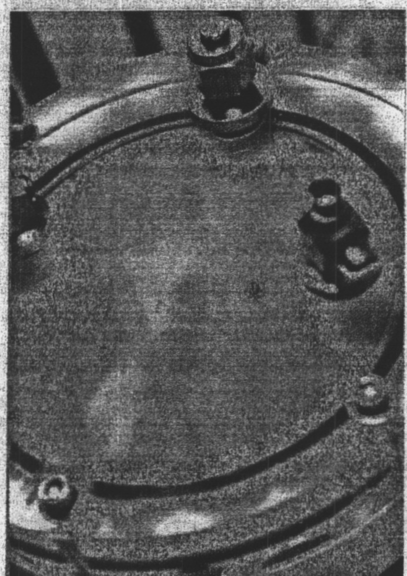

Figure 6. Appearance of *Chlorella* Cell Cultures Grown for 2 Days in a HARV Bioreactor Under Simulated Microgravity Conditions.

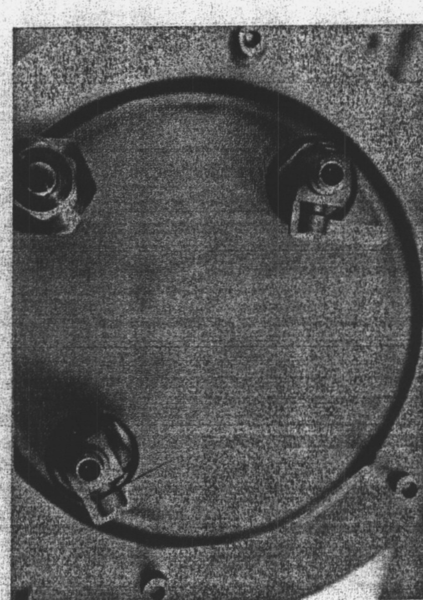

Figure 7. Appearance of *Chlorella* Cell Cultures Grown for 7 Days in a HARV Bioreactor Under Gravity Control Conditions.

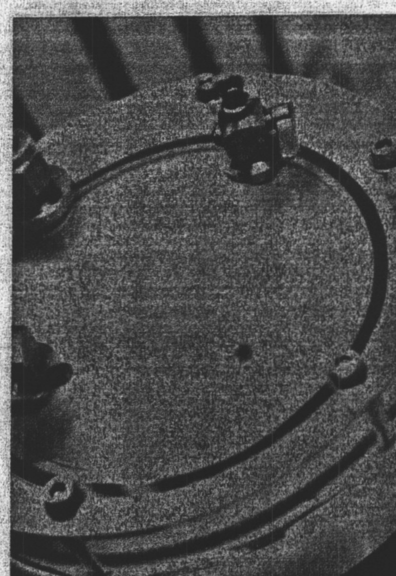

Figure 8. Appearance of *Chlorella* Cell Cultures Grown for 7 Days in a HARV Bioreactor Under Simulated Microgravity Conditions.

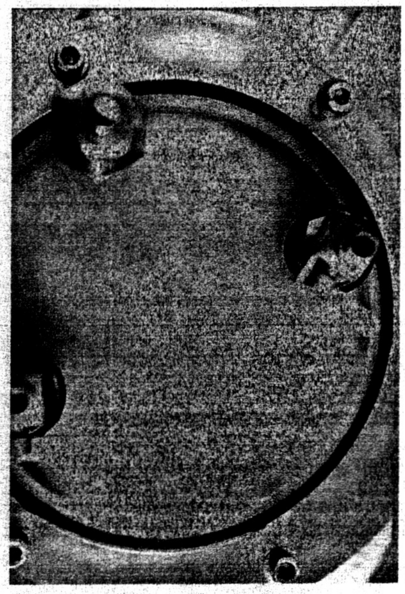

Figure 9. Appearance of *Chlorella* Cells Grown for 14 days in HARV Bioreactor Under Gravity Control Conditions.

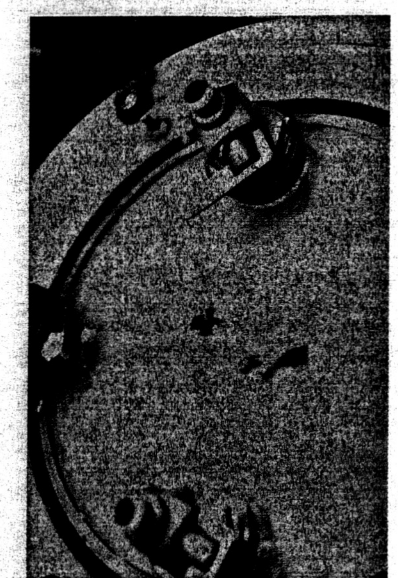

Figure 10. Appearance of *Chlorella* Cell Cultures Grown for 14 Days in HARV Bioreactor Under Simulated Microgravity Conditions.

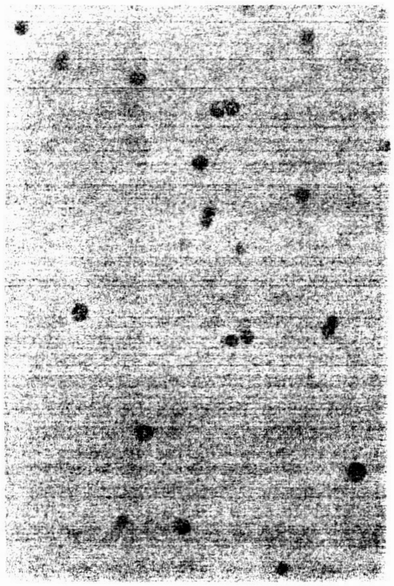

Figure 11. Microscopic Appearance of *Chlorella* Cells Grown for 14 Days in a HARV Bioreactor Under Gravity Control Conditions.

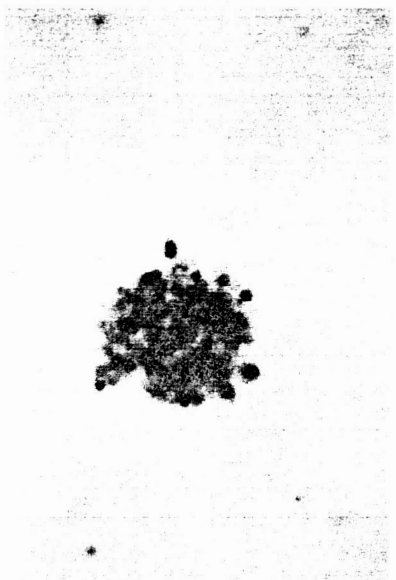

Figure 12. Microscopic Appearance of *Chlorella* Cells Grown for 14 Days in a HARV Bioreactor Under Simulated Microgravity Conditions.

References

[1] Dunn, M.J. 1996. Two-dimensional polyacrylamide gel electrophoresis. *Methods Enzymol.* 271:177-203.

[2] Fang, A., Pierson, D.L. Mishra, S.K., Koenig, D. W., and Demain, A. L. 1997. Secondary metabolism in simulated microgravity: β-lactam production in *Streptomyces clavuligerus. J. Indust. Micro. Biotech.* 18: 22-25.

[3] Fang, A., Pierson, D.L. Mishra, S.K., Koenig, D. W.,and Demain, A. L. 1997. Gramicidin S production by *Bacillus brevis* in simulated microgravity. *Current Microbiol.* 34: 199-204.

[4] Fang, A., Pierson, D.L., Koenig, D. W., Mishra, S.K., and Demain, A. L. 1997. Effect of simulated microgravity and shear stress on microcin B17 production by *Escherica coli* and on its excretion into the medium. *Applied Envr. Microbiol.* 63: 4090-4092.

[5] Gray, S.W., and Edwards, B.F. 1968. The effect of weightlessness on wheat seedling and morphogenesis and histochemistry. *Bioscience* 18: 638-655.

[6] Hammond, T.G., Lewis, F.C., Goodwin, T.J., Linnhan, R.M., Wolf, D.A., Hike, K.P., Campbell, W.C., Benes, E., O'Reilly, K.C., Globus, R.K., and Kaysen, J.H.1999. Gene expression in space. *Nat. Med.*, 4: 359.

[7] Kordyum, E.L., 1997. Biology of plant cells in microgravity and under clinostating. *Int. Rev. Cytol.*, 171: -78.

[8] Nickerson, C.A., Ott, C. M., Mister, S.J., Morrow, B.J., Burns-Keliher, L., and Pierson, D.L. 2000, Microgravity as a novel environmental signal affecting *Salmonella enterica* serovar typhimurium virulence, *Infect. Immunology.* 68: 3147-3152.

[9] Popova, A.F., Kordyum, E.L., and Shnykova, E.I. 1993. Ultrastructure of chloroplasts and amylase activity in *Chlorella* cells under space flight conditions. *Dokl. Akad. Nauk. UkrSSr Ser. Biol.* 11: 152-156.

[10] Popova, A.F., Kordyum, E.L., and Sytnik, K.M. 1995. Plastid ultrastructure, fractional composition and activity of amylases in *Chlorella* cells in microgravity. *J. Gravit. Physiol.* 2: 159-160.

[11] Schwarz, P.R., Goodwin, T.J., and Wolf, D.A. 1992. Cell culture for three-dimensional modeling in rotating-wall vessels: An application of simulated microgravity. *J. Tiss. Cult. Meth.* 14: 51-58.

[12] Space science in the twenty-first century, imperatives for the decades 1995-2015. Space Science Board, Commission on Physical Sciences, Mathematics, and Resources. National Research Council. National Academy Press. 1988.

[13] Unsworth, B.R., and Lelkes, P.I. 1998.Growing tissues in microgravity. *Nature,* 4: 901-907.

[14] Wolf, L. 1996. Bioregeneration in space. *Advances in space biology and medicine.*5: 341-356.

EVA Robotic Assistant Project: Platform Attitude Prediction

Kevin Nickels
Trinity University
ER4
August 10, 2000

Kenneth Baker
ER4/Robotic Systems Technology Branch
Automation, Robotics, & Simulation Division
Engineering Directorate

Kevin Nickels

Kenneth Baker

EVA Robotic Assistant Project:

Platform Attitude Prediction

Final Report

NASA/ASEE Summer Faculty Fellowship Program — 2000

Johnson Space Center

Prepared By:	Kevin M. Nickels, Ph. D.
Academic Rank:	Assistant Professor
University & Department:	Trinity University
	Department of Engineering Science
	San Antonio TX 78212

NASA/JSC

Directorate:	Engineering
Division:	Automation, Robotics & Simulation Division
Branch:	Robotic Systems Technology Branch
JSC Colleague:	Kenneth Baker
Date Submitted:	August 10, 2000
Contract Number:	NAG 9-867

ABSTRACT

The Robotic Systems Technology Branch is currently working on the development of an EVA Robotic Assistant under the sponsorship of the Surface Systems Thrust of the NASA Cross Enterprise Technology Development Program (CETDP). This will be a mobile robot that can follow a field geologist during planetary surface exploration, carry his tools and the samples that he collects, and provide video coverage of his activity.

Prior experiments have shown that for such a robot to be useful it must be able to follow the geologist at walking speed over any terrain of interest. Geologically interesting terrain tends to be rough rather than smooth. The commercial mobile robot that was recently purchased as an initial testbed for the EVA Robotic Assistant Project, an ATRV Jr., is capable of faster than walking speed outside but it has no suspension. Its wheels with inflated rubber tires are attached to axles that are connected directly to the robot body. Any angular motion of the robot produced by driving over rough terrain will directly affect the pointing of the on-board stereo cameras. The resulting image motion is expected to make tracking of the geologist more difficult. This will either require the tracker to search a larger part of the image to find the target from frame to frame or to search mechanically in pan and tilt whenever the image motion is large enough to put the target outside of the image in the next frame.

This project consists of the design and implementation of a Kalman filter that combines the output of the angular rate sensors and linear accelerometers on the robot to estimate the motion of the robot base. The motion of the stereo camera pair mounted on the robot that results from this motion as the robot drives over rough terrain is then straightforward to compute.

The estimates may then be used, for example, to command the robot's on-board pan-tilt unit to compensate for the camera motion induced by the base movement. This has been accomplished in two ways: first, a standalone head stabilizer has been implemented and second, the estimates have been used to influence the search algorithm of the stereo tracking algorithm. Studies of the image motion of a tracked object indicate that the image motion of objects is suppressed while the robot *is crossing rough* terrain.

This work expands the range of speed and surface roughness over which the robot should be able to track and follow a field geologist and accept arm gesture commands from the geologist.

INTRODUCTION

The focus of this work is to develop a high-fidelity estimate of the angular orientation and angular velocity of the robot base. Sensors that are utilized to arrive at this estimate include three mutually orthogonal gyrometers, three mutually orthogonal linear accelerometers, and a magnetic compass.

The estimates may then be used, for example, to command the robot's on-board pan-tilt unit to compensate for the camera motion induced by the base movement. This has been accomplished in two ways: first, a standalone head stabilizer has been implemented and second, the estimates have been used to influence the search algorithm of the stereo tracking algorithm.

Rover Hardware

The rover is a modified ATRV Jr., from RWI. The wheels have been mounted on extensions to provide adequate ground clearance, and a tower has been added to the top for the stereo vision hardware. Figure 1 shows a cartoon of the rover.

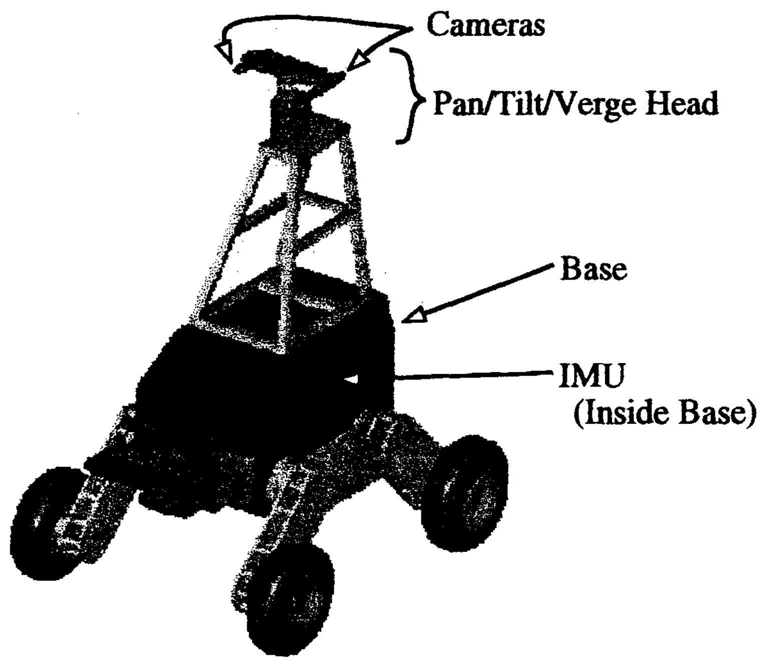

Figure 1: The EVA Robotic Assistant testbed

The rover comes equipped with a magnetic compass, an Inertial Measurement Unit (IMU), and two on-board computers. It has been augmented to include a pan-tilt-verge head and two cameras with framegrabbers. The relevant components are described briefly below, and mathematical models are given later in the report.

Sensors Used

The sensors considered in this report are three mutually orthogonal gyrometers, three mutually orthogonal linear accelerometers, and a magnetic compass.

A gyrometer measures angular velocity about a single axis. These measurements are corrupted by gyro biases [3]. These biases are commonly estimated for purposes of compensation (see below for mathematical sensor models used.) After compensation, the angular rates recovered can be integrated to arrive at an estimate of the rotation of a body relative to some fixed initial orientation.

A linear accelerometer measures acceleration along a single axis. The accelerations can be integrated to arrive at linear velocities, and integrated again to arrive at position relative to some initial position. In this work, the accelerometers were not used in this fashion, but were used to measure the direction of the gravitational vector while the rover was at rest. See [5] for more discussion on inertial data.

The linear accelerometers and gyros used in this project were packaged in a single Inertial Measurement Unit (IMU), the DMU-6X from Crossbow. A magnetic compass yields a bearing with respect to magnetic north. The magnetic compass used in this project was the TCM2 from Precision Navigation.

Actuators Used

The stereo pan-tilt-verge (PTV) heads considered in this report are the Zebra Vergence from Pyxis Corp (formerly Helpmate, formerly TRC) and the Biclops from Metrica. Each of these heads accepts movement commands via a serial port from an external computer. Each head supports two cameras, which are used for image acquisition.

Kalman filtering

This section briefly introduces Kalman filtering, the data processing algorithm used to filter the data in this project. Many excellent references on Kalman filtering are available, [1] and [2] are recommended.

Possibly the simplest way to estimate an unknown vector $\mathbf{x}$ from observed vector data $\mathbf{z}$ (with a known transform from $\mathbf{x}$ to $\mathbf{z}$) is *mean-square estimation*, where the estimate $\hat{\mathbf{x}}$ is chosen to minimize the expected value of the Euclidean norm squared of the error $E[(\mathbf{x}-\hat{\mathbf{x}})^T(\mathbf{x}-\hat{\mathbf{x}})]$. This can easily be extended to estimate functions of the quantity $\mathbf{x}$. The Kalman filter implements a recursive least squares fit to the data, given some assumptions about the system that produced the data.

We consider a general linear discrete system

$$\mathbf{x}_{k+1} = \mathbf{F}\mathbf{x}_k + \mathbf{w}_k \qquad \text{(Motion Model)}$$
$$\mathbf{y}_k = \mathbf{H}\mathbf{x}_k + \mathbf{v}_k \qquad \text{(Measurement Model)}$$

Both the *process noise*, $\mathbf{w}_k$, and *measurement noise*, $\mathbf{v}_k$, are assumed to be sequences of zero-mean Gaussian white noise such that $Var(\mathbf{w}_k) = \mathbf{Q}_k$[1] and $Var(\mathbf{v}_k) = \mathbf{R}_k$ are positive definite matrices, and $E(\mathbf{w}_k\mathbf{v}_l^T) = 0$ for all k and l.

In a physical system, the *state* can be any set of relevant parameters. Formally, relevant parameters are defined as those parameters needed to uniquely determine the output of a system, given the input to the system. For example, in a robotic arm, the state might be the configuration of

[1]The variance of a vector is simply the covariance matrix of the vector with itself ($Var(\mathbf{v}) = Cov(\mathbf{v},\mathbf{v})$).

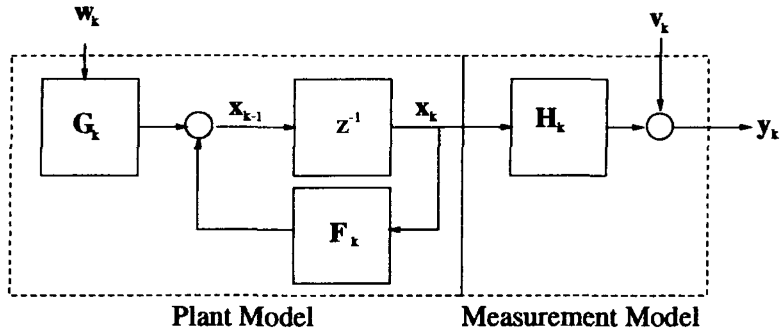

Figure 2: Plant and measurement models.

the robot. A configuration of an object is a set of numbers that give a specification of the position of every point on the object. Configuration space is defined to be the space of all possible configurations of a object.

This work utilizes six one-dimensional Kalman filters (or equivalently, one six-dimensional Kalman filter with a diagonal system covariance P_k.) The six quantities estimated are the three drifts associated with the three gyros and the three roll-pitch-yaw angles.[2]

Use of Estimates

Estimates of angular velocity and angular position (net rotation since initialization) can be used to correct for *ego-motion* in images. Ego-motion is defined to be image motion due to the movement of the camera in the world. This is distinct from object motion, which is image motion caused by the movement of the tracked object in the world. Object motion is not addressed in this report.

Given the base orientation and current PTV configuration (pan, tilt, and verge angles), a homogeneous transform (see, e.g. [4]) can be created that relates an object of interest in the world coordinate system to that object in a camera coordinate system. In a "standalone" configuration, a command is sent to the PTV to send the object of interest to a fixed point in the camera coordinate system (for example, directly centered in front of the camera).

If interaction with the stereo tracking software is desired, the ego-motion estimate described above can be used to influence the selection of the search area. The stereo tracking software is searching in each image for an object. Typically, this search begins at the last known (image) location of the object. If the estimates described above are used, the search begins at the predicted (image) location of the object, accounting for ego-motion. The residuals (difference between beginning of search and final location of object) in the images should be less when the rover is undergoing significant transients and stereo tracking is working in this mode.

SENSOR MODELS

The section describes our assumptions about the relevant sensors on the robot, and the mathematical models used for these sensors.

[2]Orientation given by roll-pitch-yaw angles is defined by taking a base coordinate system, rotating about the x axis by the roll angle, rotating about the (new) y axis by the pitch angle, and finally rotating about the (new) z axis by the yaw angle. See [4] for more discussion.

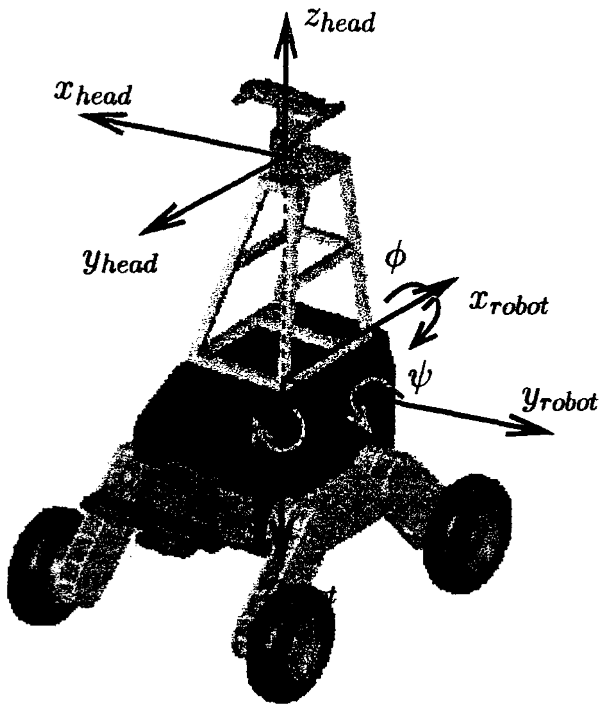

Figure 3: Coordinate System Definitions

Gyrometers

The gyrometers (commonly known as gyroscopes, but this is a more general term which does not imply rotating machinery) measure velocities about the orthogonal x, y, z axes of an inertial reference frame. Unfortunately, there is a reasonably constant[3] drift associated with each axis. This drift (often referred to as a *bias*) needs to be estimated and this estimate used for compensation.

Often, these angular velocities are integrated to arrive at an attitude (also called angular position) estimate. Defining the roll-pitch-yaw angles ϕ, ψ, θ to be positive (according to the right hand rule) rotations about the x, y, z axes, as shown in Figure 3, the models we use for the gyroscopes are:

$$\dot{\phi}_g(t) = \dot{\phi}(t) + d_\phi(t) \quad [^o/s]$$
$$\dot{\psi}_g(t) = \dot{\psi}(t) + d_\psi(t) \quad [^o/s]$$
$$\dot{\theta}_g(t) = \dot{\theta}(t) + d_\theta(t) \quad [^o/s]$$

where $\dot{\phi}_g(t)$, $\dot{\psi}_g(t)$ $\dot{\theta}_g(t)$ are the velocities obtained from the gyroscopes, $\dot{\phi}(t)$, $\dot{\psi}(t)$ and $\dot{\theta}(t)$ are the true angular velocities, and $d_\phi(t)$, $d_\psi(t)$ and $d_\theta(t)$ are the drift rates about the x, y, and z axes, respectively.

With this measurement model, we can correct the velocity measurement with estimates for the

[3]After the gyro is warmed up

drift rates as follows

$$\dot{\phi}(t) = \dot{\phi}_g(t) - d_\phi(t) \quad [^o/s]$$
$$\dot{\psi}(t) = \dot{\psi}_g(t) - d_\psi(t) \quad [^o/s]$$
$$\dot{\theta}(t) = \dot{\theta}_g(t) - d_\theta(t) \quad [^o/s]$$

assuming the drift rates are known.

Accelerometers

The three on-board accelerometers measure accelerations along orthogonal x, y, z axes of their local reference frame. These accelerations can be integrated to arrive at estimates for velocity. The velocity estimates may then be integrated to arrive at estimates for position. This portion of the filter has not been implemented.

FILTER COMPUTATIONS

In order to maximally exploit our understanding of the dynamics of planetary rover operations, we defined two distinct *modes* of operation for the filter. These are defined to be *rest* and *maneuvering*. During rest, we utilize the assumption that the rover is stationary (in a fixed but unknown orientation) in a vertically oriented gravitational field. During maneuvering, we make no assumptions about the movement of the vehicle.

Determination of Mode

We have designed a transient detector to distinguish between these modes of operation. This detector utilizes hysteresis to avoid becoming confused by outliers (the data from both the gyrometers and accelerometers are reasonably noisy.) Each gyrometer data point is compared against a running average of the previous 30 samples. If it is greater than 0.5 degrees/s from this average, that data point is defined to be a transient data point. If 5 consecutive data points are labelled as transient data points, the state is defined to be transient. Leaving transient mode should be a more conservative transition, so 30 consecutive non-transient data points are required to leave transient mode. If fewer than these thresholds are reached, no mode changes are made. All of these thresholds are defined experimentally and are tunable. This transient detector allows robust determination of the motion state of the rover.

Gyro Drift Estimates - Rest Mode

If the robot is at rest, the measured angular velocities consist completely of drift. In this case, simple one-dimensional discrete Kalman Filters are used to estimate drift about each axis. The assumed models are

$$d_\theta(k+1) = d_\theta(k) + w(k) \qquad \text{(Motion Model)}$$
$$\dot{\theta}_g(k) = \dot{\theta}(k) + d_\theta(k) + v(k) = d_\theta(k) + v(k) \qquad \text{(Measurement Model)}$$

leading to a filter implementation of

$$K_\theta(k) = P_\theta(k-1)(P_\theta(k-1) + R(k))^{-1} \quad \text{(Kalman Gain)}$$
$$\widehat{d}_\theta(k) = \widehat{d}_\theta(k-1) + K_\theta(k)(\theta_g(k) - \widehat{d}_\theta(k-1)) \quad \text{(Estimate Update)}$$
$$P_\theta(k) = (I - K_\theta(k))P_\theta(k-1) + Q(k) \quad \text{(Uncertainty Update)}$$

where $w(k)$ and $v(k)$ are assumed to be zero-mean Gaussian white noise of covariance $Q(k)$ and $R(k)$, respectively. The filters for the ϕ and ψ rotations are analogous.

Attitude Estimate - Rest Mode

At rest, the attitude of the robot can be estimated based on the projection of gravity (which is assumed to be directed along the $+z$ axis of the inertial frame)[5],

$$\psi(t) = -sin^{-1} g_x/g$$
$$\phi(t) = sin^{-1} \frac{g_y}{gcos(\psi(t))}$$

Instead of direct estimation, these *measurements* of attitude are combined with previous estimates of attitude in one-dimensional Kalman filters to achieve smoothing and outlier rejection.

Gyro Drift Estimates - Maneuvering Mode

If the ERA is maneuvering, the simplifying assumptions made in the previous sections are invalid. Therefore, we use different models for this mode. We simply maintain a constant drift estimate and increase the uncertainty of the estimate with time. In essence, we are neglecting the observation by setting the Kalman gain to zero.

$$\widehat{d}_\theta(k) = \widehat{d}_\theta(k-1) \quad \text{(No Estimate Update)}$$
$$P_\theta(k) = P_\theta(k-1) + Q(k) \quad \text{(Uncertainty Update)}$$

Angular Rate Estimates - Maneuvering Mode

To estimate the actual angular rates in this case, we subtract the gyro drift estimates from the gyrometer reading:

$$\widehat{\dot{\phi}}(k) = \dot{\phi}_g(k) - d_\phi(k) \quad [^o/s]$$
$$\widehat{\dot{\psi}}(k) = \dot{\psi}_g(k) - d_\psi(k) \quad [^o/s]$$
$$\widehat{\dot{\theta}}(k) = \dot{\theta}_g(k) - d_\theta(k) \quad [^o/s]$$

Attitude Estimation - Maneuvering Mode

As the vehicle acceleration is superimposed on the gravitational acceleration, the attitude estimates during maneuvering are derived from integration of the angular acceleration, corrected by the drift estimates as described above.

$$\phi_g(t) = \phi_g(t-\Delta t) + \int_{t-\Delta t}^{t} \left[\dot{\phi}_g(t) - \widehat{d}_\phi(t)\right] dt$$
$$\psi_g(t) = \psi_g(t-\Delta t) + \int_{t-\Delta t}^{t} \left[\dot{\psi}_g(t) - \widehat{d}_\psi(t)\right] dt$$
$$\theta_g(t) = \theta_g(t-\Delta t) + \int_{t-\Delta t}^{t} \left[\dot{\theta}_g(t) - \widehat{d}_\theta(t)\right] dt$$

where Δ is the sampling period. This integration needs to be done via a numerically sound (e.g. rectangular, trapezoidal, Runge-Kutta) algorithm. These estimates are folded into one-dimensional Kalman filters to achieve smoothing and outlier rejection.

RESULTS

Figures 4 and 5 illustrate the performance of the filters for the gyro drifts and orientation angles. Figure 6 illustrates the behavior of the standalone head stabilization.

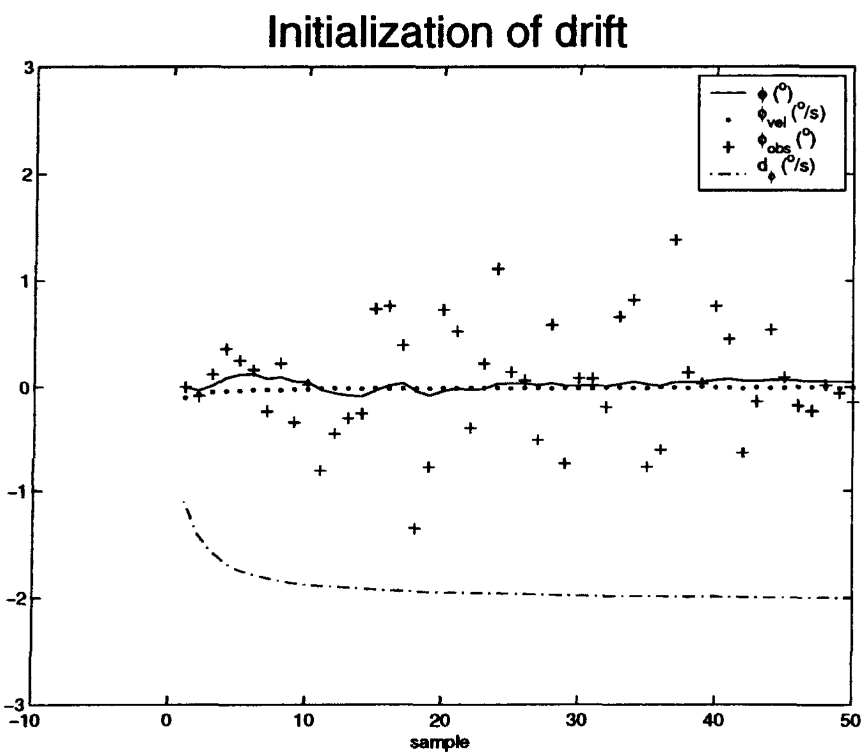

Figure 4: Drift Estimation I (Roll only)

Figure 4 shows the initialization of the drift estimate d_ϕ while the base is at rest. Initially, the uncertainty associated with the drift estimate is high. Therefore, the drift measurements ϕ_{obs} affect the drift considerably. After the drift estimates become more certain, new measurements begin to affect the drift estimates less. The computed velocity ϕ_{vel} quickly approaches zero.

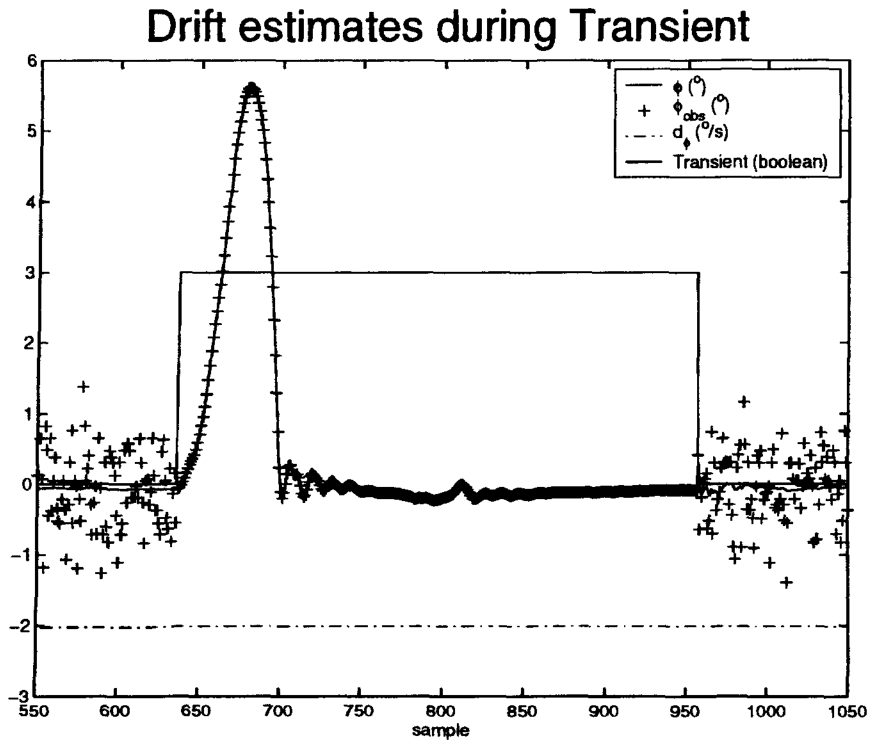

Figure 5: Drift Estimation II (Roll only)

Figure 5 illustrates both sets of Kalman filters: the orientation angles and drift estimates. After many samples, the estimate for the drift is fairly certain. Upon entering an angular transient, there is a detection lag of several samples. During this time (near sample 635) the drift estimate does not change. As described above, once a transient is detected, updates to the drift estimates are suspended for the duration of the transient. In this test, the robot begins at rest, drives over an obstacle, then is at rest again.

This filter also shows the difference in uncertainty between the at-rest observations of the attitude (derived from the accelerometers) and the observations derived by integrating the gyro measurements. The derived measurements are more precise, but are subject to a slow drift over time, while the accelerometer-derived measurements are bias-free, but have a high degree of uncertainty. Both types of measurements are used over time, yielding the behavior shown in Figure 5: a filter that responds quickly and accurately to measure transient behavior, but will reset the attitude estimates any time the base is at rest.

Figure 6 shows the location in image coordinates (u along the horizontal direction, v along the vertical) of an object of interest. This object drifts slowly lower in the image as the rover moves forward toward the object (it is located slightly below the PTV head on the rover). As can be seen from the figure, with fixed gaze there is a large vertical transient near samples 50-100. This corresponds to the front tire of the rover encountering an obstacle. The other transient (near samples 190-220) corresponds to the rear tire encountering the same obstacle. With stabilization turned on, both transients are smaller.

There is a tradeoff for the stabilization of the image, however. As can be seen from Figure 6,

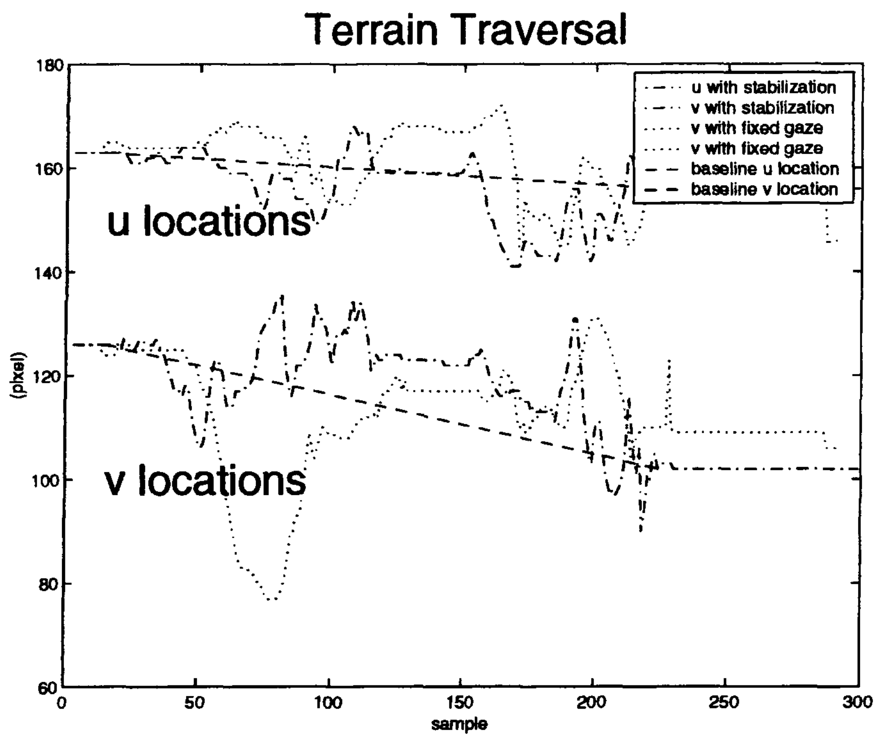

Figure 6: Stabilization Results

stabilization currently induces a low-frequency vibration in image location. The object of interest remains roughly in the center of the center of the image, as intended, but the picture appears to shake. We believe that this effect is due to the point-to-point move commands currently used to command the PTV heads. We are working to integrate the ego-motion estimation with existing stereo tracking work that drives the PTV heads in a smoother fashion, which may eliminate or reduce this effect.

FUTURE WORK

The primary extension to this work will be to complete the integration of the ego-motion estimates generated by this filter with the existing JSC stereo tracking software and to evaluate the efficacy of this upgrade. Evaluation of the behavior of the angular estimates in the field may take place in September 2000, during the scheduled tests in Arizona.

Less immediate extensions include the elimination of the explicit notion of *modes* of operation, to be replaced by a continuous scale of *"transientness"* that can be used to smoothly transition between exploiting rest-mode assumptions and the general form of the filter. Feedback on actual camera motion could be generated by the stereo vision software and incorporated into the attitude estimates.

Finally, positional estimates have not been addressed at this point. Ideally, this filter would also receive input from a Global Positioning System (GPS) receiver and from the wheel encoders. This information would be combined with measurements from the linear accelerometers to arrive at estimates for the position, linear velocity, and linear acceleration of the robot. This information could be used, for example, to generate a three-dimensional path that the rover has followed.

CONCLUSION

Inertial data can be used to compensate for ego-motion in images taken from an outdoor rover. This compensation can be treated as a standalone behavior, to keep a specified object of interest centered in an image, or as an input to a more complex object tracking algorithm. Initial tests reveal that some low-frequency oscillation was introduced as a result of the stabilization, but that the amplitude of image location transients due to obstacles in the path of an outdoor rover decreased. This should expand the range of speed and surface roughness over which the rover should be able to visually track and follow a field geologist.

REFERENCES

[1] R. G. Brown. *Introduction to Random Signal Analysis and Kalman Filtering*. John Wiley & Sons, New York, 1983.

[2] C. K. Chui and G. Chen. *Kalman Filtering with Real-Time Applications*. Springer-Verlag, Berlin, 1987.

[3] E. Foxlin. Inertial head-tracker sensor fusion by a complementary separate-bias kalman filter. In *Proc. 1996 Virtual Reality Annual International Symposium*, 1996.

[4] M. Spong and M. Vidyasagar. *Robot Dynamics and Control*. John Wiley & Sons, New York, 1989.

[5] J. Vaganay, M. J. Aldon, and A. Fournier. Mobile robot attitude estimation by fusion of inertial data. In *Proceedings IEEE International Conference Robotics and Automation*, pages 277–282, 1993.

Development and Engineering Design in Support of "Rover Ranch", A K-12 Outreach Software Project

Raresh Pascali
Marine Engineering Department
Texas A&M University at Galveston
Galveston, TX 77553
August 11, 2000

Dr. Robert Shelton
Learning Technologies. GT4 Branch
Information Technology Office, GT Division
Information Systems Directorate

Raresh Pascali

Dr. Robert Shelton

Development and Engineering Design in Support of "Rover Ranch", A K-12 Outreach Software Project

Final Report
NASA/ASEE Summer Faculty Fellowship Program – 2000
Johnson Space Center

Prepared by:	Raresh Pascali (12)
Academic Rank:	Senior Lecturer
University & Department:	Texas A&M University at Galveston Marine Engineering Department Galveston, TX 77553

NASA/JSC

Directorate:	Information Systems
Division:	Information Technology
Branch:	Systems and Applications
JSC Colleague:	Robert Shelton
Date Submitted:	August 11, 2000
Contract Number:	NAG 9-867

ABSTRACT

A continuation of the initial development started in the summer of 1999, the body of work performed in support of "ROVer Ranch" Project during the present fellowship dealt with the concrete concept implementation and resolution of the related issues. The original work performed last summer focused on the initial examination and articulation of the concept treatment strategy, audience and market analysis for the learning technologies software.

The presented work focused on finalizing the set of parts to be made available for building an AERCam Sprint type robot and on defining, testing and implementing process necessary to convert the design engineering files to VRML files. Through reverse engineering, an initial set of mission critical systems was designed for beta testing in schools. The files were created in ProEngineer, exported to VRML 1.0 and converted to VRML 97 (VRML 2.0) for final integration in the software. Attributes for each part were assigned using an in-house developed JAVA based program.

The final set of attributes for each system, their mutual interaction and the identification of the relevant ones to be tracked, still remain to be decided.

INTRODUCTION

Every new wave of media, from filmstrips to video to the many iterations of computer-delivered training, has spawned wild enthusiasm in the past. Each promising a better and more effective learning environment than the last. Despite years of visionary predictions of the inevitable triumph of technology-delivered training, the vast majority of training today is still delivered in the classroom testament to the enduring human preference for face to face, real-time, interactive learning environments.

In order to design a successful new learning tool, it is essential to first identify the elements contributing to the effectiveness of classroom teaching. In physical sciences in general, and in engineering in particular, a course has two interdependent parts: a lecture session, in which the material is usually presented and a laboratory session in which application and experimentation takes place. While it tends to be easier to implement the former in new media – and by new media one refers here to the convergence of many industries such as cable and television broadcasting, film and video, publishing, software, and the IT -, the latter proves more elusive: short of building a physics laboratory in every student's house, how does one allow pupils to practice free thinking through experimentation? Virtual reality (VR) may prove to be the answer.

Virtual Reality is a promising technology for corporate and industrial training applications as well as for the classroom. VR simulations are an effective and inexpensive alternative in situations requiring hands-on training with equipment that is hazardous or expensive; anything from learning how to dock a super tanker or operate a nuclear power plant, to developing microsurgery techniques or teaching procedures for proper wafer handling in semi-conductor manufacturing.

While in the past, large-scale VR simulators required powerful workstations, the advances in computer technology make this type of training attainable in schools. And today, head-mounted displays, or custom control environments prove to be highly effective but they are expensive and can be operated by only one trainee at a time. PC-based simulations can be accessed by many over a corporate intranet and an increasing number of VR training programs are also being developed for delivery over the web.

Creating user-friendly interactive systems is complex and expensive in time and effort. With the increased penetration of 3D solid modeling MCAD (mechanical computer aided design) software in all types of industries, the opportunity exists to use the generated models outside the design loop, and in particular, in the training process. This is especially true for an organization such as NASA, which is globally recognized as a proficient generator of knowledge and a user of advanced CAD tools. However, it can be difficult to train astronauts to operate in environments which are impossible to duplicate on earth.

As the ISS (International Space Station) continues assembly, the opportunity of informing, educating and ultimately involving students in the new challenges, was seized by NASA's JSC Learning Technologies Project by conceiving the "Rover Ranch" software. The NASA Johnson Space Center Learning Technologies Project (http://prime.jsc.nasa.gov) is in charge of developing and implementing new software, methods and methodologies that create learning opportunities with focus on mathematics, science and engineering. Within this context, JSC created a set of Internet tools for K-12 teachers and students. A three-year NASA sponsored project, with the first full operating beta system to be delivered in September 2000, the software's first phase is based on the AERCam Sprint (Autonomous Extravehicular Activity Robotic Camera Sprint – http://tommy.jsc.nasa.gov/projects/Sprint/index.htm) concept (Figure 1). The "Rover Ranch" would represent a departure from today's flight simulation software and their instantaneous input/correction capabilities. Mimicking the engineering design process, the robot would expect the mission to be planned ahead. The planning process involves selecting the various components needed to successfully complete the set tasks after which the simulation would begin thereby allowing students to observe the consequences. Unlike the majority of the learning software on the market today, the "Rover Ranch" would be targeted towards average and above average students. Since the software will emphasize planning and before-fact thinking rather that hand-eye coordination and speed of movement, it should appeal to physically disabled students as well.

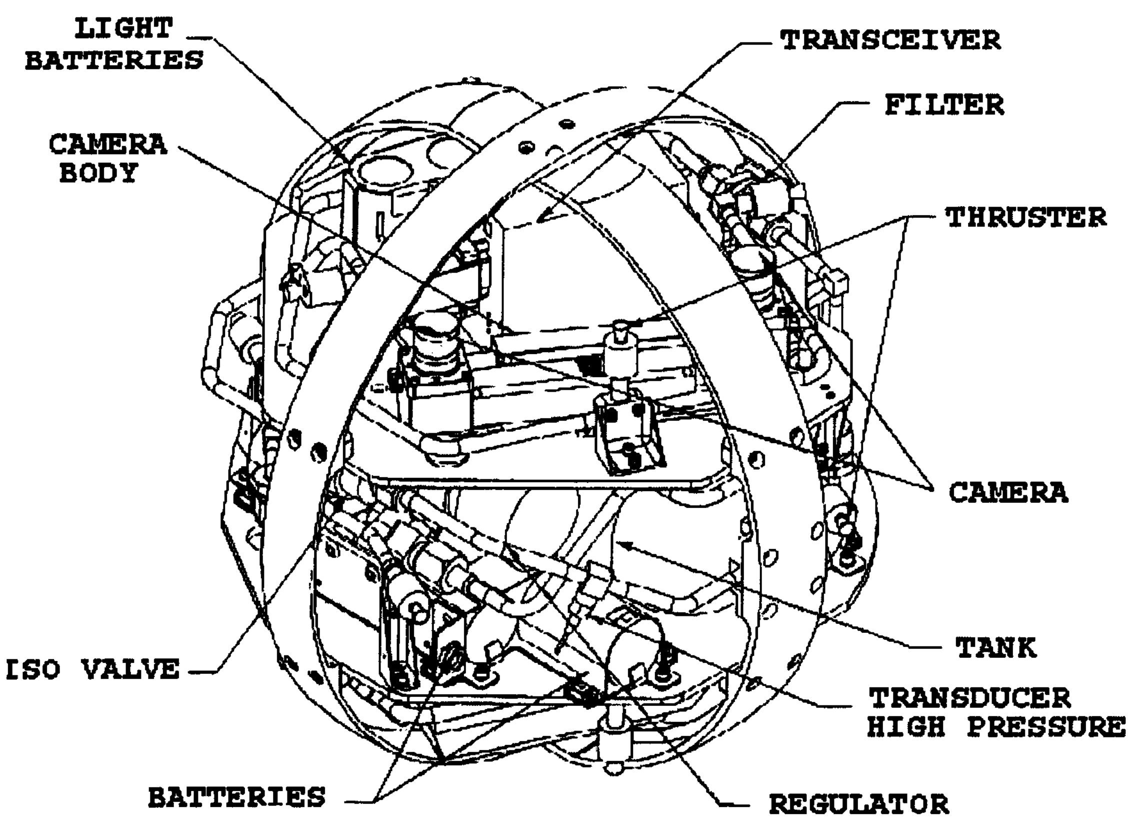

Figure 1: NASA's AERCam Sprint

Since there could be a wide variation in the type of systems used by students, the initial set of requirements for an effective product were that the product be platform independent. Such product must also be visually exciting and easily extendable after the initial phase was completed. These issues were resolved by using JAVA, a platform independent language, capable of creating applets that would run on common browsers. The parts would be displayed in VRML (virtual reality modeling language) which through the use of plug-ins can also be seen in common browsers. As NASA is currently standardizing on Parametric Technologies Corporation (PTC) products (www.ptc.com), ProEngineer was chosen as the software in which the parts would be constructed. This will allow future elimination of preliminary part construction in the initial screening phase, as the parts are created by engineers during the design process.

1. ProEngineer

Pro/ENGINEER is the industry's de facto standard 3D mechanical design suite. It is based on a robust, parametric, feature-based modeler -- so wholesale design changes can be made with ease. While creating the parts in ProE proved more efficient, two issues were encountered.

Although ProE has capabilities to export to VRML, it does so in ver. 1.0. This represented a concern in terms of interaction with the rest of the software. In addition, learning and keeping track of two sets of commands represents a potential future productivity loss. This issue was resolved by converting files from VRML 1.0 to VRML 2.0. Due to the fact that ProE generates several files for each model, made the selection of the translator challenging.

The second issue, the fact that the VRML files were monochrome, was resolved by changing various settings.

2. Virtual reality

Aristotle enumerated five senses through which humans perceive or interact with the world around them. These were: hearing, smell, touch, taste and sight. Medicine is continuously discovering additional ways through which human body "reads" the environment such as carbon dioxide sensed by the skin.

Virtual reality is a system by which the senses are "tricked" into untrue perception (i.e. different than what they would normally detect). Various tools for virtual reality were created throughout history: artificial flavors for taste and smell, gramophones, radios and later stereo and surround sound for hearing, fabrics, faux fur, etc. for touch and television and cinema for sight. However, computers hold the potential for making the virtual reality meaningful through (a) total immersion and (b) by allowing interactivity with the environment. Hence, educators are in the process of experimenting with virtual reality in a number of teaching applications. As with other computer mediated teaching, virtual reality provides the student with the advantage of learning the subject at their own pace with opportunities to explore a broad band of knowledge relating to a specific subject rather than acquiring such knowledge in a passive manner. One advantage that a three-dimensional environment has over a two-dimensional page in this field is the ability to illustrate concepts. Most importantly the immersive element of VR can make the experience more appealing and unique which will, often, attract the interest of a student who might otherwise be hard to motivate. The applications that have been created for education vary. For example historical reconstruction can provide students with the opportunity to re-live any moment in history thereby creating a more in-depth look at that particular point in history. Similarly, the use of simulation can produce a virtual lab that can be used for experimenting with mathematical and physical laws. VR can also be adopted to illustrate principles in a variety of other subjects, for instance the urban impact of an area that is due for development in geography and molecular arrangement in chemistry.

Although VR has not been adopted as a standard tool for teaching basic curriculum, preliminary trials have shown that the quality of learning is comparable to that achieved by using other computer aided learning and in some subjects a superior quality is achieved when using VR. The value of such a learning tool does not lie in replacing, but in complementing and enhancing traditional forms of learning.

3. Concept Definition

It is envisioned that when completed, ROVer Ranch would have three types of robots:

1. Free-flying
2. Mars rover and
3. AUV (autonomous underwater vehicle).

The initial phase would concentrate on a free-flying robot based on AERCam Sprint. The number of systems that can be incorporated was decided to be limited to six. The systems and possible subsystems are enumerated below:

1. Propulsion: cold gas, hot gas, variable specific impulse magnetoplasma rocket (VASIMIR), internal combustion engine, warp drive, electric motor, solar powered.
2. Body: material – steel, stainless steel, aluminum, titanium; shape: spherical, cylindrical, cube, humanoid; color: white, black, glow-in-the-dark, yellow.
3. Power: zinc-carbon, lithium, car battery, rechargeable, fuel cells, fly wheel, ultracapacitors.
4. Control: teleoperated, autonomous
5. Tools: grip only, humanoid arm, continuous deformation, snake.

6. Sensors: visual: digital still camera, digital DV camcorder, SLR camera, VHS Camcorder, light sensors; hearing: commercial microphone, parabolic antenna; smell and taste: spectrometer, nitrogen detector; touch: force sensor.

The Rover Ranch software is meant to be educational and informative about NASA's challenges and current projects, while challenging students' imaginations and encouraging out-of-the-box thinking. Hence, once the systems have been established, the available choices for subsystems varied from common, to high-tech research, to science fiction. It is the aim that in the finalized package that each of the systems as well as subsystems be followed by a short narrative to inform the user of the possible pros and cons as well as the trade offs a one would face during the design process. In addition, web links would be provided, such that individual teacher can elect the depth of the knowledge to be pursued.

CONCLUSION

The final system (Figure 2) will be ready for beta testing in September. Based on the feedback from students and teachers, limited changes are anticipated to the current system. With the proven system defined, design on the Mars Rover will begin in October followed by the AUV parts. As new technologies evolve, it is expected that enhancements to subsystems will have to be added. Due to the modular nature of the software, this should prove relatively easy.

Figure 2: The Developed System in VRML Format

SENSORY MOTOR COORDINATION IN ROBONAUT

Richard Alan Peters II

Vanderbilt University School of Engineering

JSC Mail Code: ER4

30 October 2000

Robert O. Ambrose

Robotic Systems Technology Branch

Automation, Robotics, & Simulation Division

Engineering Directorate

Richard Alan Peters II

Robert O. Ambrose

SENSORY MOTOR COORDINATION IN ROBONAUT

Final Report
NASA/ASEE Summer Faculty Fellowship Program – 2000
Johnson Space Center

Prepared By:	Richard Alan Peters II, Ph.D.
Academic Rank:	Associate Professor
University and Department:	Vanderbilt University Department of Electrical Engineering and Computer Science Nashville, TN 37235

NASA/JSC

Directorate:	Engineering
Division:	Automation, Robotics, & Simulation
Branch:	Robotic Systems Technology
JSC Colleague:	Robert O. Ambrose
Date Submitted:	30 October 2000
Contract Number:	NAG 9-867

ABSTRACT

As a participant of the year 2000 NASA Summer Faculty Fellowship Program, I worked with the engineers of the Dexterous Robotics Laboratory at NASA Johnson Space Center on the Robonaut project. The Robonaut is an articulated torso with two dexterous arms, left and right five-fingered hands, and a head with cameras mounted on an articulated neck. This advanced space robot, now driven only teleoperatively using VR gloves, sensors and helmets, is to be upgraded to a thinking system that can find, interact with and assist humans autonomously, allowing the Crew to work with Robonaut as a (junior) member of their team. Thus, the work performed this summer was toward the goal of enabling Robonaut to operate autonomously as an intelligent assistant to astronauts.

Our underlying hypothesis is that a robot can *develop* intelligence if it learns a set of basic behaviors (*i.e.*, reflexes – actions tightly coupled to sensing) and through experience learns how to sequence these to solve problems or to accomplish higher-level tasks. We describe our approach to the automatic acquisition of basic behaviors as *learning sensory-motor coordination* (SMC). Although research in the ontogenesis of animals (development from the time of conception) supports the approach of learning SMC as the foundation for intelligent, autonomous behavior, we do not know whether it will prove viable for the development of autonomy in robots. The first step in testing the hypothesis is to determine if SMC can be learned by the robot. To do this, we have taken advantage of Robonaut's teleoperated control system. When a person teleoperates Robonaut, the person's own SMC causes the robot to act purposefully. If the sensory signals that the robot detects during teleoperation are recorded over several repetitions of the same task, it should be possible through signal analysis to identify the sensory-motor couplings that accompany purposeful motion.

In this report, reasons for suspecting SMC as the basis for intelligent behavior will be reviewed. A robot control system for autonomous behavior that uses learned SMC will be proposed. Techniques for the extraction of salient parameters from sensory and motor data will be discussed. Experiments with Robonaut will be discussed and preliminary data presented.

INTRODUCTION

To interact naturally with people in a human-centered environment, a robot must be able to coordinate sensing with action. That is, it must have Sensory-Motor Coordination (SMC). It is possible to program a certain degree of SMC into a robot prior to its deployment. But it is impossible for a programmer to anticipate every physical contingency that may arise in a robot's interactions with people. This is due to the intrinsic complexity of a human-centered environment. Only animals (including people) have SMC that permits them to work effectively in a complex natural world. If SMC in animals were well understood – if the structures and functions of the systems that manifest it were known – then analogous systems could be implemented in robots.[1] SMC in animals is not completely understood, but research in it has recently advanced to the point where plausible mechanisms for it have been described. Evidence from studies in neurophysiology [1], ontogenesis [2,3], and cognitive science [4] suggests that to interact effectively and efficiently with its environment, an animal must learn through its own experiences the reciprocal causative relationships between sensing and action that foster its success or survival (cf. below). That is, SMC must be learned, or at least refined, through an animal's direct experience with acting in the world.

Schema theory [4] can be used to describe the functional aspects of an animal's behavior without exact specification of the biological systems that support it. Schemas exist at a frame of reference higher than that of the individual computational elements (neurons in the case of animals). A schema description of the behavior of an animal is inherently modular. It provides a framework for the description of behaviors in terms of the interactions of modules that control motion, process sensory information, create and recall memories, etc. In animals, the modules may more or less directly correspond to specific networks of neurons. But this separation of function from structure affords the possibility of realizing the behavior of an animal in a robot by substituting computers and electro-mechanical devices for neuron networks and bio-mechanical subsystems. Behavior-based robots (BBR) [5,6] are particularly amenable to this. BBRs act through the combination of *basic behaviors*, which are motor actions tightly coupled to sensory stimuli – both external to the robot and internal (*i.e.*, proprioceptic).

This report proposes a method for the learning of sensory-motor coordination through the teleoperation of a behavior-based robot. The goal of the work is to enable a robot to learn SMC by finding the correlations between sensory events and motor control events that co-occur during task execution. The robot is guided by a human operator through repeated trials of a specific task while recording all its incoming sensory data. The motor and sensory data gathered throughout the trials will be analyzed to find representative couplings between sensory stimuli and motor actions. If successful this will not

[1] Implementation is possible if the *functionality* of the biological systems can be reproduced in electro-mechanical systems. Schema theory suggests that it can. (cf. below).

only permit the robot to perform the task autonomously, but also (with an appropriate control system) enable the robot to adapt to variations in the task or in the environment.

SENSORY-MOTOR COORDINATION

Sensory-Motor Coordination underlies the physical behavior of an animal in response to its environment. More than a response, SMC is a feedback loop that changes both the animal and the environment. An animal's motions are caused by muscle contractions. These contractions are elicited by electrochemical signals that are generated by circuits of motor neurons. When the animal moves, it causes a relative shift in the environment. As the environment shifts, energy patterns sweep across the animal's sensory organs. Sensory organs are transducers that, in effect, transform external, spatio-temporally dynamic energy fields into electrochemical signals carried by circuits of sensory neurons internal to the animal. These sensory signals (more or less directly) modulate the signals in the original motor circuits. Learning occurs in the mapping from sensory response signal to motor control signal. Thus, an animal senses the environment and acts. The action changes the environment relative to the animal, which senses those changes and acts accordingly.

SMC is likewise needed by a sensory-guided robot. The basic behaviors of a BBR are independent units of SMC. They include what are commonly called reflex actions. When a basic behavior is enabled[2] and the stimuli associated with it occur, the action is performed -- without resort to modeling or deliberation. Basic behaviors are canonical in the sense that all actions exhibited by the robot are generated through the cooperation and competition of basic behaviors operating concurrently or in sequence. At any given point in time, some of the basic behaviors will be enabled and others suppressed depending on the task and environmental context of the robot. Since a BBR exhibits any and all its behaviors through the combination and sequencing of basic behaviors, a BBR is wholly dependent on, and to a large extent defined by, sensory motor coordination.

Sensory-motor coordination is fundamental for another compelling reason. It forms a foundation for higher level learning and perception. In particular, the categorization of sensory stimuli can be accomplished through SMC [7]. A mobile agent can learn the sensory patterns that correspond to an obstacle by associating stimuli with its motor responses, as when a characteristic stimulus pattern routinely accompanies the sudden inability to move. Similarly, as Pfeifer has demonstrated, an agent can learn to distinguish between objects that it can manipulate and those which it cannot [8]. If the internal sensation of a need (a drive or a goal) having been satisfied accompanies a set of actions performed in the presence of specific stimuli, that stimuli can be recognized as

---

[2] A BBR typically has a suite of basic behaviors, not all of which are operational at the same time. Depending on the task and environmental contexts, various basic behaviors will be enabled or disabled. If a behavior is enabled – made operational – it will remain quiescent until its triggering sensory stimuli are present.

being beneficial to the agent (*e.g.*, an energy source -- food). Recent experiments by Pfeifer and others have demonstrated that such SMC events can be used to learn classifications of objects and events in the environment more easily and more accurately than can traditional machine sensing strategies such as model-based vision [9,10].

SCHEMA THEORY

Since the behavior of animals is mediated by their nervous systems, the understanding of their behavior from first principles requires an understanding of nervous systems. Neuroscience has provided a structural description that includes neurons (individuals and networks) and layers, columns, and modules in the brain [11]. But the *function* of these structures is not completely understood and it is function more than structure that determines behavior. Functional analysis is complicated by the fact that many of the neuronal structures participate in different functions. With certain exceptions there are no discernible one-to-one mappings of low-level structure to high-level function [4].

Arbib *et al.* employ schema theory "as a framework for the rigorous analysis of [animal] behavior that requires no prior commitment to hypotheses on the location of each *schema* (unit of functional analysis) but can be linked to a structural analysis as and when it becomes appropriate." [4] (p. 33). Thus schemas are descriptions of functions that are performed by networks of neurons and the muscles and appendages that they control. Schema theory enables the top-down analysis of a complex behavior by providing a structure for logically dissembling it, that is it facilitates the analytical decomposition of a complex behavior into sets of simpler behaviors. On the other hand, schemas also enable the bottom-up analysis of sets co-occurring behaviors. The collective behavior of a set of simple schemas can be deduced if the framework for their competition, cooperation, and sequencing is known. This collective behavior is a higher-level schema called an *assemblage*. Not only are the behaviors of animals describable by schemas but also are the control systems of behavior-based robots. BBRs are, given their modular architectures, particularly amenable to such description. The theory of behavior-based robotics is grounded on the idea that complex behavior in an agent emerges through the competition and cooperation of simple behaviors in the context of an environment, which is precisely the idea of assemblage in schema theory.

To the extent that function can be separated from structure, a schema representation enables a specific behavior to be performed by agents with dissimilar computational hardware. In particular, a behavior observed in an animal that can be described accurately by schemas could be implemented on an appropriately structured robot. Schemas, therefore, provide for comparative analysis of similar behaviors on dissimilar agents, be they bio-chemical or electro-mechanical.

Arbib *et al.* group schemas in two categories. *Motor schemas* are "the control systems which can be coordinated to effect the wide variety of movement. A set of basic motor schemas is hypothesized to provide simple, prototypical patterns of movement." *Perceptual schemas* "are those used for perceptual analysis. They embody the processes whereby the system determines whether a given domain of interaction is present in the environment. They not only serve as pattern-recognition routines but can also provide the appropriate parameters concerning the current relationship of the organism with its environment." [4] (p. 42).

Research in the ontogenesis of animals has demonstrated that the ability to move exists prior to an animal's ability to sense its environment. Arbib *et al.* state that this "does not, however, imply that motility is an end in itself. Rather this, 'motor foundation' serves to group the later development of sensory maps and sensorimotor representations in a self-directed manner." [4] (p.10). Thus, in animals the formation of the musculo-skeletal system and the neuro-circuits for motor control precedes the development of perceptual schemas. Such a development schedule makes sense. Perceptual schemas in animals, even if passed on phylogentically, must be tuned; sensory stimuli is required for a perceptual modality to develop. Other perceptual schemas (*e.g.*, a semantic description of a visual object) must be learned. On the other hand, an animal must, to a certain extent, "hit the ground running" to survive. Motion must precede perception so that the animal can move at birth and so that the effects of its motion can be perceived and learned. Perceptual schemas, must therefore be learned or tuned in concert with motion. Simultaneously, motor schemas must be tuned to enable efficient sensing. Thus, sensory-motor coordination requires the coupling of perceptual schemas and motor schemas into assemblages. Perceptual schemas provide goal and trajectory information to the motor schemas, whereas the latter provide a physical framework within which a perceptual schema can extract salient information. Arbib *et al.* place motor schemas and perceptual schemas at the foundation of animal function. Under the influence of the environment these schemas self-organize to control an animal's behavior.

For the designers of robots the main implication of the onset of motility prior to sensation in animals is that reflexes are not primary. (See [4] Sec. 2.1.1, p. 13 f.f.) Put in another way, basic behaviors are not truly basic. Motion is primary; it can happen without sensing. Reflexes develop with the onset of sensing. Then sensory signals modulate the signaling of motor circuits and reflexes emerge.

SCHEMAS AND SMC IN BEHAVIOR BASED ROBOTS

The following four examples of behavior-based robot control systems depend on SMC and can be described through assemblages of schemas. Each of the architectures has basic behaviors at its foundation. In each case, the basic behaviors are selected by the designer of the robot. Each of the architectures can be designed to learn, and as a result exhibit emergent SMC. The learning, however, occurs at levels above basic behaviors.

Brooks' subsumption architecture

Brooks' subsumption architecture controls a robot through a collection of augmented finite state machines (AFSM) organized into layers [5]. A subsumptive robot has no central planner or controller. Each AFSM can be activated by sensory inputs and produces outputs that drive actuators or are passed to the inputs of other modules. Within subsumption, the AFSMs are motor schemas. The sensory inputs are perceptual schemas. An AFSM with well-defined sensory input implements a basic behavior. Assemblages are formed dynamically as AFSMs at one level are activated or inhibited by AFSMs at a higher level. Usually the basic behaviors in the lowest layer are preprogrammed; the sensory signals that trigger an AFSM are not learned. Learning can take place in a subsumption architecture, (*e.g.*, Brooks' robot, Ghengis [12]) but generally this occurs in layers above the first.

Mataric's action-oriented representations.

Mataric designed, using subsumption, a mobile robot that learns to navigate an environment through the use of action-oriented representations [13]. The robot both generates and operates from an "action map" of the environment. While wandering in the environment and reacting to sensory input according to its basic behaviors (*e.g.*, wall following, object avoidance, etc.) the robot generates the map by building up a directed graph. Each node of the graph contains a description of the motor state at the time of its formation and description of the sensory data that was received as the robot performed the actions described by the motor state. Adjacent nodes in the graph correspond to adjacent areas in the environment. Once the environment has been mapped, the robot can reach a physical location by activating the corresponding node of the graph. The graph is searched (using spreading activation) back from the goal node to the node that represents the current position of the robot. The nodes along the shortest connecting path are enabled. The robot reaches the goal by moving according to the motor commands of its current node until its sensory input more closely matches the data from the next node. Then it executes the motor commands from next node and proceeds successively from node to node until the goal is reached.

Mataric's robot learns while acting by forming a spatio-temporal sensory-motor description of the environment. The map indicates the sensory and motor status of the robot at a particular point in space at a particular time relative to the current position. Thus, the robot learns how to sequence and basic behaviors from sensory input. This is undoubtedly a form of SMC but it learns the sequencing of basic behaviors rather than the SMC that defines the basic behaviors themselves.

Arkin's Motor Schema.

A robot controlled by Arkin's motor schema[3] architecture follows gradients in a vector field map of its environment [14]. Computational modules such collision detectors and obstacle or object recognizers are perceptual schemas since they compute the vectors at points in space that serve to impel the robot. Motor schemas (in Arbib's sense) within Arkin's architecture are assemblages of motor controllers that respond individually to components of the vector field map. A motor controller generally has a fixed response

[3] *Motor Schema* is the name that Arkin has given his control architecture. It makes use of both perceptual schemas and motor schemas in the sense that Arbib describes them.

to its input vector. The response is a function of the magnitude and direction of the input vector, but that function is generally preprogrammed and does not change. Any learning that occurs happens in the perceptual schemas that compute the vector field.

Pfeifer's SMC-based categorization.

Pfeifer's robots are based on an extended Braitenberg architecture, another type of BBR [15]. A number of basic behavior modules (Pfeifer calls these "reflexes") operate in parallel, receiving sensory inputs (including proprioception) and summing their outputs onto the motor controllers [8]. The response of each behavior module to its inputs is preprogrammed. The overall robot system does learn, however, as it interacts with the environment, guided by a "value system." Values are, essentially, the preprogrammed reflexes and reinforcement schemes, that cause the robot to seek some sensory stimuli and to avoid others. Learning occurs through the adaptive modulation of sensory signals that are fed to the behavior modules.

Pfeifer defines categorization of an object as the robot's appropriate interaction with the object. Through the value-based learning scheme the robot learns how to couple sensing with actuation so that appropriate behaviors are learned for different stimulus patterns. Thus the objects that project the different stimulus patterns are classified *de facto* without forming an abstract model of the object. Pfeifer's robot learns about objects by finding the correlations between sensory signals and behaviors that lead to favorable results and by decoupling behaviors from stimuli when that coupling leads to unfavorable results. Thus, an appropriate linkage between sensing and action at the task level is learned by trial and error.

LEARNING BASIC BEHAVIORS

Behavior-based robots employ schemas implicitly. Their complex behaviors emerge through the interaction of a canonical set of basic behaviors, each of which is a sensory-driven motor controller. Therefore, in a BBR high-level behavior emerges from assemblages of perceptual schemas linked to motor schemas, just as in animals. In terms of schema theory, the practice of designing BBRs differs from the ontogenesis of animals. The designer of a BBR must decide *ad hoc* or through trial and error, exactly which coupling of sensory data to motor controller constitutes a useful basic behavior. And the designer must decide which basic behaviors to include in the canonical set. He or she determines the perceptual to motor schema linkage at the base level and decides which of these first-order assemblages to include on the robot.[4] In other words, the designer programs SMC into the robot at the lowest level.

BBRs that learn, such as those described in the previous section, learn at the level above basic behaviors. They learn which behaviors to activate and which to inhibit or to suppress under various sensory conditions, or they learn an appropriate sequence of be-

[4] In some BBRs the higher-order assemblages are also completely specified by the designer. Such robots cannot learn.

haviors in response to sensory input, or they learn a control function that modulates the sensory signals before they reach the basic behaviors. While these robots might work well, they are still subject to the errors and oversights of their designers in programming SMC into the functional base-level of the robot.

How, then, does one enable a robot to learn SMC at the level of basic behaviors? There are at least two possibilities:

1. Design and implement on the robot the fundamental motor circuits that enable actuation. Have the robot move randomly while sensing. Reinforce any sensory-motor coupling (a temporal coincidence of sensory signals and motor actions) that leads to purposeful motion. approach such as this is necessary for a fully autonomous agent, like an animal. This approach has been used successfully by researchers in artificial life [16]. Learning SMC this way with a robot could require much time.
2. Take advantage of the fact that a robot can be teleoperated. When a person teleoperates a robot, the person's SMC causes the robot to act purposefully. If the robot records all of its sensory signals during repeated teleoperations, through signal analysis it should be able to identify the sensory-motor couplings that accompany purposeful motion.

Both of these approaches require signal analysis algorithms that will detect signal correlations or coincidences. Moreover, the detected sensory-motor couplings must be used to construct basic behavior modules. Both of these problems are open research issues.

ROBONAUT

Robonaut is NASA's most sophisticated humanoid system (See figure 1). Its mechanical systems have been designed to operate within the conditions of space in low-earth orbit. The Robonaut upper body is an articulated torso with two dexterous arms, left and right five-fingered hands, and a head with cameras mounted on an articulated neck, packaged in less volume than an Astronaut's EMU. Robonaut is fully functional at the level of motor control and is operated via full-immersion VR. It has a large set of proprioceptic sensors and an active pan-tilt stereo vision system. Robonaut brings to the project, a high degree of dexterity, sophisticated teleoperability, and a rich sensor suite, but no autonomy. At this point in time it only works through teleoperation

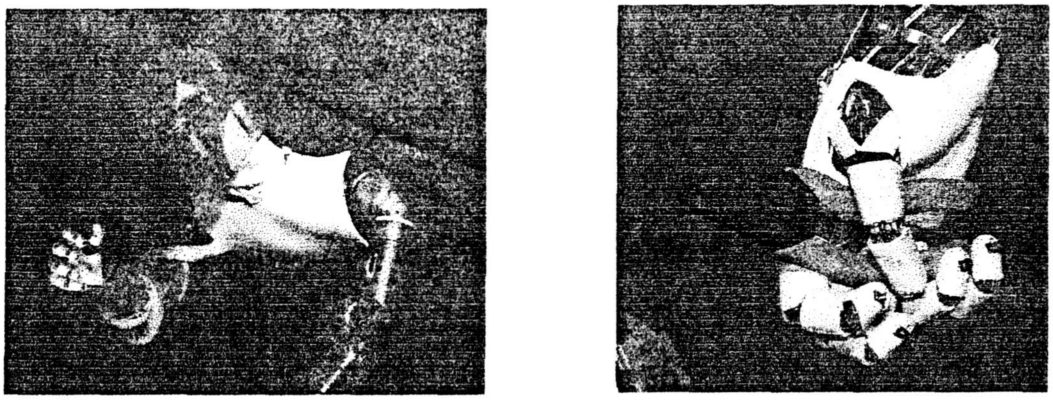

Figure 1. Left: Robonaut; right: Robonaut's hand.

EXPERIMENTS

The objective of the research began during the summer of 2000 is to enable Robonaut to learn the sensory-motor control couplings that define a canonical set of basic behaviors and to learn the sensory signals that precede and follow behavior changes during task execution. The approach is to have a person teleoperate the robot through a task a number of times while the robot records the motor control sequence and the signals from its sensors. For the experiments reported herein, Robonaut's task was to find, to reach toward, and to grasp one stationary object followed by another across the workspace. This was accomplished through teleoperation, wherein the teleoperator controlled the action of the robot through a full-immersion VR station. The signals recorded were the end-effector position and the 6-axis force and torque above the wrist on the forearm.

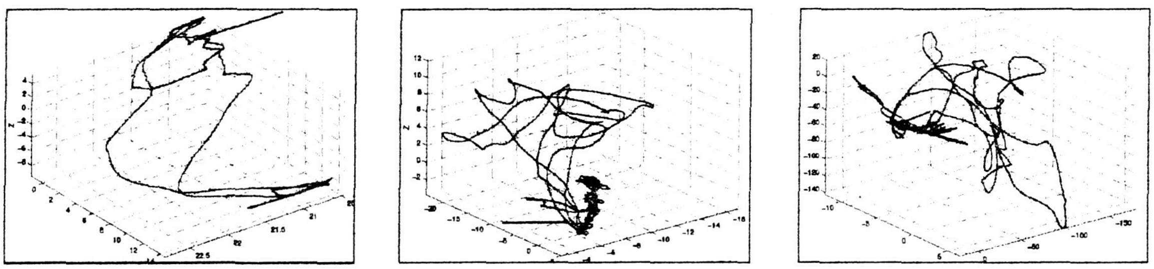

Figure 2. Left: end-effector position; middle: force on wrist; right: torque on wrist

LEARNING SMC

The motor control sequence within each trial will be used to determine the motor events -- the times of transition between continuous motor operation states. The motor events from a trial will be used to partition all the sensory signals within that trial. Since the same task is repeated by the same operator several times there should be the same number of motor events in each trial, although the time between them will vary. After all the trials are completed, the signals will be time warped to align the motor events across trials. Then in a time interval bracketing the motor event, the signals from a single sensor will be correlated across all trials to determine if there is a corresponding sensory event (the signal exhibits a change consistently near the motor event.) Only the signals that exhibit a consistent sensory event within an interval of a motor event will be considered to be salient to that motor event and analyzed further. (A signal that is constant or that changes inconsistently near a motor event across multiple trials of the same task is presumed to be superfluous to the SMC of that event.) Through averaging (or some nonlinear combination such as median filtering) a characteristic signal for that sensory event at the given motor event will be formed. Then the signals from different sensors will be correlated within individual trials to determine which sensors react together near the motor events. To each motor event, the characteristic signals from the salient sensors are coupled to form a sensory-motor coordination event. An SMC event is, therefore, a motor state transition, that is either preceded or followed by a consistent signals in more than one sensor.

CONCLUSIONS AND FUTURE WORK

At the time of this writing, the first experiments in SMC data gathering during teleoperation had been performed. We found that the teleoperation procedure is repeatable in the way needed for the analysis: Having the same number of motor events yet having sufficient variability to detect true sensory events and to average out the spurious ones. It remains to perform the analysis described herein.

REFERENCES

[1] Hamburger, V, "The developmental history of the motor neuron," *Neurosciences Research Program Bulletin*, no. 15, pp.~1-37, April, 1977.

[2] Bushnell, E. W. and J. P. Boudreau, "Motor development and the mind: The potential role of motor abilities as a determinant of aspects of perceptual development," *Child Development* vol.~64, pp.~1005-1021, 1993.

[3] Thelen, E. AND L. B. Smith, *A Dynamic Systems Approach to the Development of Cognition and Action*, MIT Press, Cambridge, MA, 1994.

[4] Arbib M. A., P. Érdi, and J. Szentágothai, *Neural Organization: Structure, Function, and Dynamics*, MIT Press (Bradford), Cambridge, MA, 1998.

[5] Brooks, R. A., "A Robust Layered Control System for a Mobile Robot," *IEEE Journal of Robotics and Automation*, vol.~2, no.~1, pp.~14-23, March 1986; also MIT AI Memo 864, September 1985.

[6] Arkin, R. C., *Behavior-Based Robotics*, MIT Press, Cambridge, MA, 1998.

[7] Scheier, C. and R. Pfeifer, "Classification as sensory-motor coordination," *Proc. 3rd European Conf. on Artificial Life*, pp.~656-667, 1995.

[8] Pfeifer, R. and C. Scheier, "Sensory-motor coordination: the metaphor and beyond," *Robotics and Autonomous Systems*, Special Issue on "Practice and Future of Autonomous Agents," vol.~20, no.~2-4, pp.~157-178, 1997

[9] Lambrinos, D. and C. Scheier, "Building complete autonomous agents: a case study on categorization," *Proceedings IROS'96, IEEE/RSJ Int'l Conf. on Intelligent Robots and Systems*, November 4-8, 1996.

[10] Pfeifer, R. and C. Scheier, "Representation in natural and artificial agents: an embodied cognitive science perspective," *Zeitschrift für Naturforschung*, vol.~53c pp.~480-503, 1998.

[11] Carter, R., *Mapping the Mind*, University of California Press, Berkeley, CA, 1998.

[12] Brooks, R. A., "A Robot That Walks; Emergent Behaviors from a Carefully Evolved Network," MIT AI Lab Memo 1091, MIT Artificial Intelligence Laboratory, Cambridge, MA, February, 1989.

[13] Mataric, M. J., "Navigating with a rat brain: a neurobiologically inspired model for robot spatial representation,", in From *Animals to Animats I*, J.-A. Meyer and S. Wilson, eds, MIT Press, 1991.

[14] Arkin, R. C., "Motor schema-based navigation for a mobile robot: An approach to programming by behavior," *Proc. IEEE Conf. on Robotics and Automation*, Raleigh, NC, pp.~264-271, 1987.

[15] Lambrinos, D. and C. Scheier, *Extended Braitenberg Architectures*, AILab Technical Report, No.~95-10, University of Zurich, 1995.

[16] Terzopoulos, D., X. Tu, R. Grzeszczuk, "Artificial fishes: Autonomous locomotion, perception, behavior, and learning in a simulated physical world," *Artificial Life*, vol.~1, no.~4, pp.~327-351, December, 1994.

DESIGN THROUGH MANUFACTURING:
THE SOLID MODEL - FINITE ELEMENT ANALYSIS INTERFACE

Carol Rubin
Vanderbilt University
EM3
August 4, 2000

Raymond Aronoff
Manufacturing Integration and Technology Branch
Manufacturing, Materials, and Process Technology Division
Engineering Directorate

Carol Rubin

Carol Rubin

Raymond Aronoff

DESIGN THROUGH MANUFACTURING:
THE SOLID MODEL - FINITE ELEMENT ANALYSIS INTERFACE

Final Report

NASA/ASEE Summer Faculty Fellowship Program - 2000

Johnson Space Center

Prepared by:	Carol Rubin, Ph.D. P.E.
Academic Rank:	Professor
University & Department:	Vanderbilt University Mechanical Engineering Nashville, TN 37235

NASA/JSC

Directorate:	Engineering
Division:	Manufacturing, Materials, and Process Technology
Branch:	Manufacturing Integration and Technology
JSC Colleague:	Raymond Aronoff
Date Submitted:	August 4, 2000
Contract Number:	NAG 9-867

ABSTRACT

State-of-the-art computer aided design (CAD) presently affords engineers the opportunity to create solid models of machine parts which reflect every detail of the finished product. Ideally, these models should fulfill two very important functions: (1) they must provide numerical control information for automated manufacturing of precision parts, and (2) they must enable analysts to easily evaluate the stress levels (using finite element analysis - FEA) for all structurally significant parts used in space missions. Today's state-of-the-art CAD programs perform function (1) very well, providing an excellent model for precision manufacturing. But they do not provide a straightforward and simple means of automating the translation from CAD to FEA models, especially for aircraft-type structures.

The research performed during the fellowship period investigated the transition process from the solid CAD model to the FEA stress analysis model with the final goal of creating an automatic interface between the two. During the period of the fellowship a detailed multi-year program for the development of such an interface was created. The ultimate goal of this program will be the development of a fully parameterized automatic ProE/FEA translator for parts and assemblies, with the incorporation of data base management into the solution, and ultimately including computational fluid dynamics and thermal modeling in the interface.

INTRODUCTION

State-of-the-art computer aided design (CAD) presently affords engineers the opportunity to create solid models of machine parts which reflect every detail of the finished product. Ideally, these models should fulfill two very important functions:

(1) they must provide numerical control information for automated manufacturing of precision parts, and

(2) they must enable analysts to easily evaluate the stress levels (using finite element analysis - FEA) for all structurally significant parts used in space missions.

Today's state-of-the-art CAD programs perform function (1) very well, providing an excellent model for precision manufacturing. But they do not provide a straightforward and simple means of automating the translation from CAD to FEA models, especially for aircraft-type structures. Presently, the process of preparing CAD models for FEA consumes a great deal of the analyst's time.

The aim of the research performed during the Summer Faculty Fellowship Program period was to explore the transition from the solid CAD model to the FEA stress analysis model with the aim of making it uncomplicated and automatic. The ultimate goal of this work will be the development of an Automatic CAD/FEA Interface (ACFI) for parts and assemblies. ACFI will be able to (a) extract a fully parameterized part or assembly of parts, (b) identify and test its individual features for possible suppression, (c) suppress the appropriate features, (d) rework the part geometries to prepare the model for finite element meshing, (e) export the revised geometries to a preprocessor, (f) identify element type to be associated with each feature geometry, (g) rerun the solution based on any design changes made, (h) import the part/assembly back to the CAD program after analysis, (i) update any geometries which have been changed as a result of the analysis, and (j) resume all previously suppressed features on the updated design.

This project is consistent with the Intelligent Synthesis Environment (ISE) initiative (http://www.ise.nasa.gov/) which NASA has recently set in motion. ISE is an Agency objective which seeks to place NASA operations on the leading edge of technology. This effort includes automation of many manual processes, interactive-collaborative design through manufacturing efforts, hologram visualization of designs, and automatic assessment and modification analysis based on changes in requirements and/or design.

The Johnson Space Center (JSC), specifically, has focused on the areas of design-through-delivery of hardware, including data mining and repository issues. The goals of design-through-delivery for JSC are to define the tools required for the design through manufacturing process as well as automate the interaction among these tools.

The project described herein will play a vitally important part in this process by providing a seamless link between the design and analysis processes.

BACKGROUND

This project examines one aspect of the design-through-manufacturing process, that is, the process by which computer aided design (CAD) models are translated into finite element analysis (FEA) models. Ideally, this process should be an automatic and parameterized two-way street: After the part has been designed on the computer it is moved to the FEA program for analysis, it is analyzed, optimized in some way, and then seamlessly moved back to the CAD program which sends it to the numerical control (NC) program for manufacture (see Figure 1).

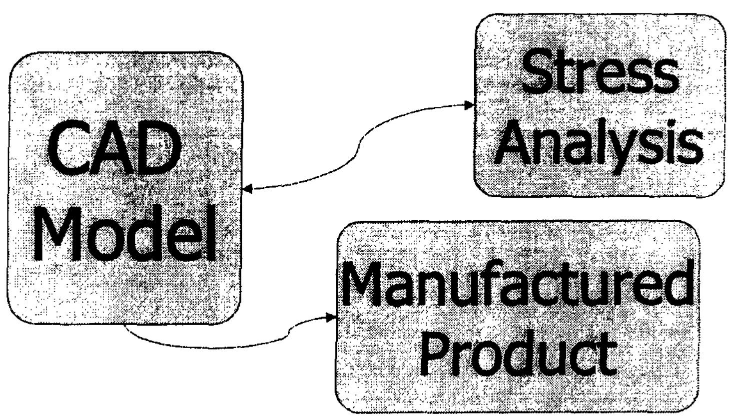

Figure 1. The Idealized Design-Through-Manufacturing Model

While the programs which translate from the CAD model to the NC model, in fact, are automatic and simple, that is not the case for the interface between the CAD model and the FEA stress analysis model. This process is extremely software and model dependent. We shall examine some of the tools that are used for both CAD and FEA at NASA/Johnson Space Center (JSC) and describe the development of a program for an Automatic CAD to FEA Interface (ACFI).

Figure 2 summarizes the most common design/analysis processes used at JSC on parts and assemblies for the International Space Station, the X38, and other systems. The design tool used most widely at JSC is PTC's ProEngineer; this is a state-of-the-art CAD package which is used by the major aerospace companies worldwide. Stress analysis packages consist of a combined pre- and post-processor, and a processing program. The packages most widely available at JSC are (pre- and post-processor/processor):

- Mechanica/Mechanica
- PATRAN/NASTRAN
- I-DEAS/NASTRAN
- ProMesh/NASTRAN

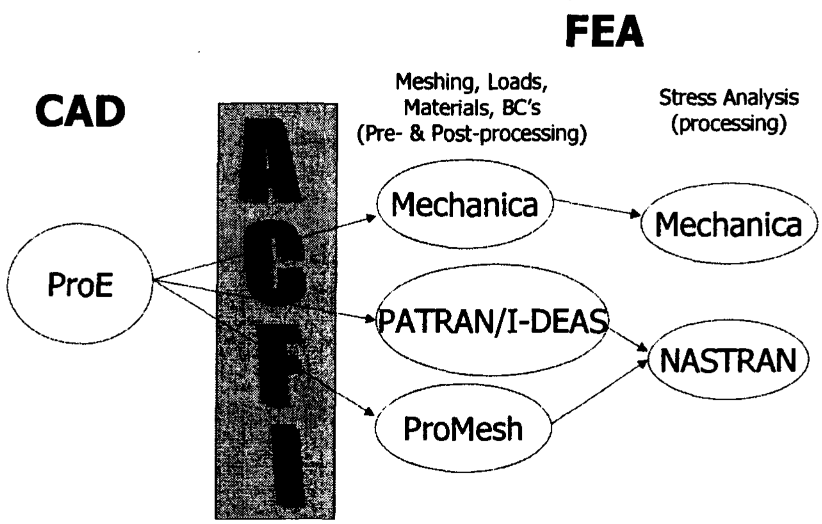

Figure 2. Tools for the CAD-to-FEA Process at NASA/JSC

There are a few other programs in use (e.g. Stress-Check), but the list above covers the major packages; in addition, it is hoped that whatever interface tools are developed will be extended to work with other platforms as well.

The processing programs Mechanica and NASTRAN are theoretically quite different. Mechanica is a P-version FEA code, and NASTRAN is an H-version code; the basic difference between them lies in the way the analysis elements are formulated. But there are other differences as well. NASTRAN is a state-of-the-art code which includes sophisticated material capabilities and advanced elements, loading and constraints which permit treatment of much more sophisticated problems than Mechanica. It is felt that the initial implementation of a CAD/FEA interface will be from ProE to PATRAN and I-DEAS, although there is another possibility which includes the use of ProMesh, a preprocessing code which comes with ProE and is meant to be used as an interface to other preprocessors and processors. ProMesh has certain capabilities that PATRAN and I-DEAS presently lack (although they are under development), namely the ability to extract midsurface planes from thin features, and beam axes from long, thin features in CAD models. This is an enhancement that can be used together with PATRAN/I-DEAS to simplify the interfacing process (see Figure 3).

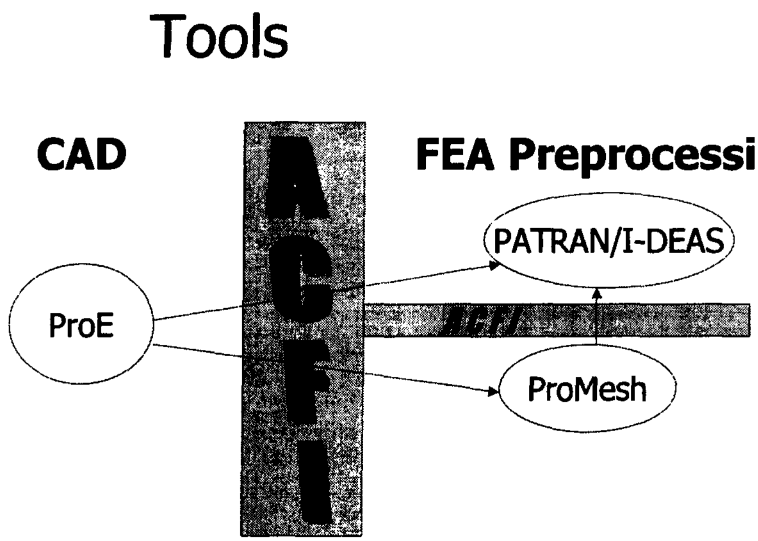

Figure 3. ProMesh and PATRAN/I-DEAS Used in Combination

What are the problems that the analyst faces when importing a CAD model? We will look at several examples. The first is a longeron from the X38 (See Figure 4). If this part were imported from ProE, without first making any changes to it, using the NASTRAN automatic import facility, it would be imported as over 150 geometric surfaces. These surfaces would need to be altered dramatically by the analyst in order to obtain an FEA mesh. It has been found that removing some of the ProE features will yield a geometry that will be imported directly into PATRAN as a single solid. Figure 5 shows the longeron with all the fillets, holes and bosses removed. Removal of certain features (e.g. fillets) will increase the stresses in a part, so that the results of the FEA analysis will be conservative. Removal of other parts (e.g. holes) will result in an analysis showing lower stresses than the actual case; this must somehow be taken into account so that the final design will have sufficient strength. When the simplified model is exported to PATRAN, it consists of a single solid which can be easily meshed for FEA; however, using PATRAN automatic meshing with this model will produce an inferior mesh with many solid elements, not the appropriate type of element for this type of shell structure. The best solution, in this case, is to first use ProMesh to create midsurface planes which represent the shell nature of this part, and then extract them (in this case 9 planes) to PATRAN. In PATRAN the planes can be quickly meshed using shell elements, yielding a very accurate mesh with a minimal number of excellent elements. Once proper loading, boundary conditions, and material behavior are inserted into the preprocessor, the finite element analysis can be performed yielding accurate results using a minimum amount of computer time.

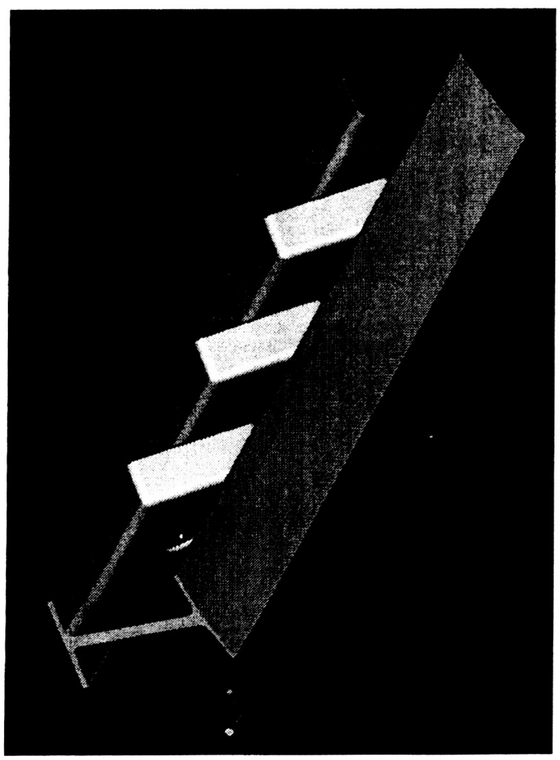

Figure 4. Longeron Part from the X38

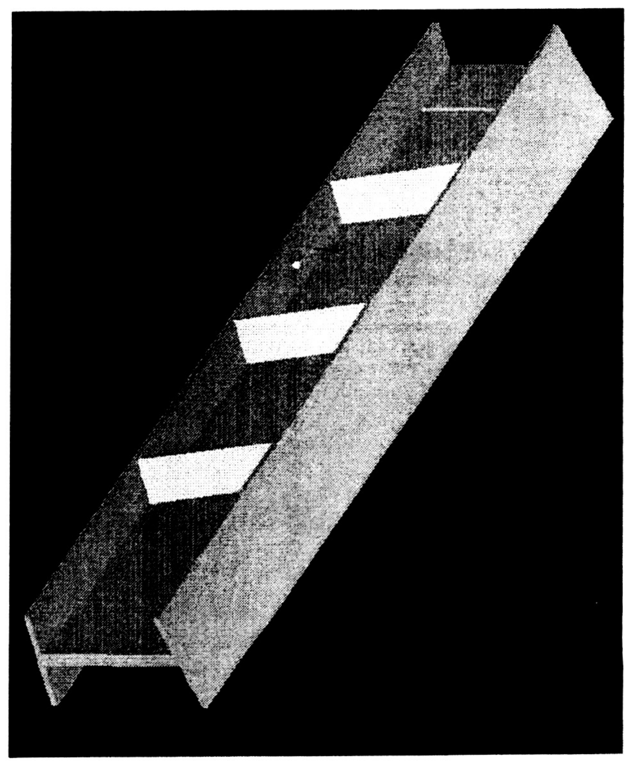

Figure 5. Longeron with Features Removed

Another example is a waffle part from the skid bracket on the X38 (see Figure 6). This part has also been simplified with fillets, rounds and holes removed (see Figure 7). Once the features have been removed, all thin features are replaced by midsurfaces using ProMesh, the results are exported to PATRAN and then the end bars are modeled in PATRAN ultimately resulting in an efficient and accurate mesh, which can be rapidly created, containing a combination of shell and beam elements.

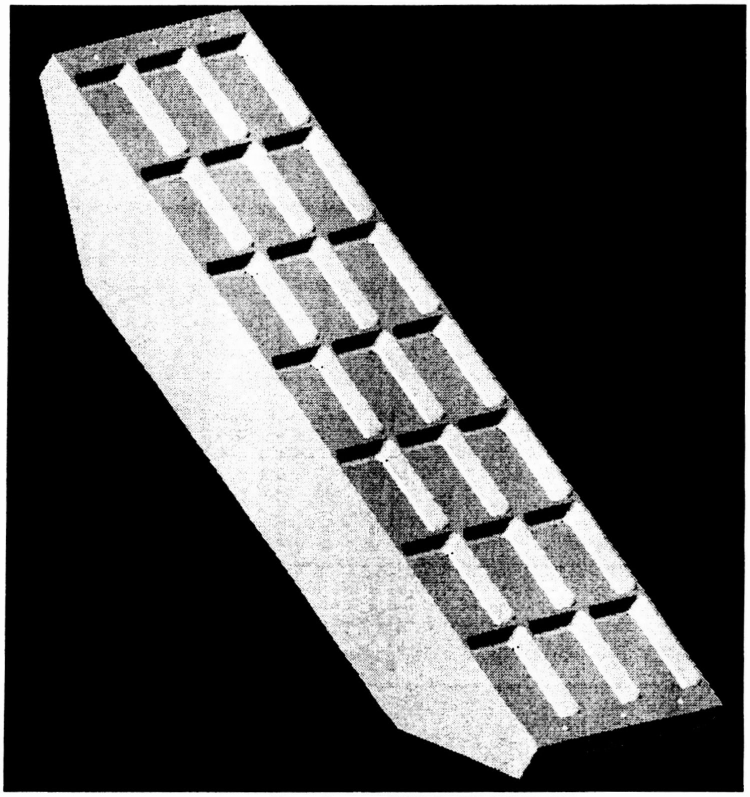

Figure 6. Waffle from X38 Skid Bracket

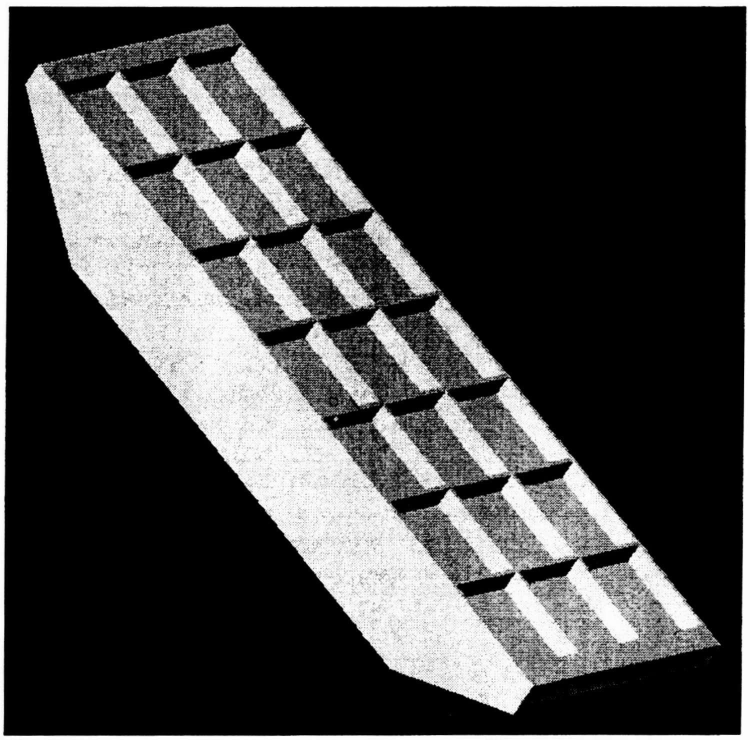

Figure 7. Waffle with Features Removed

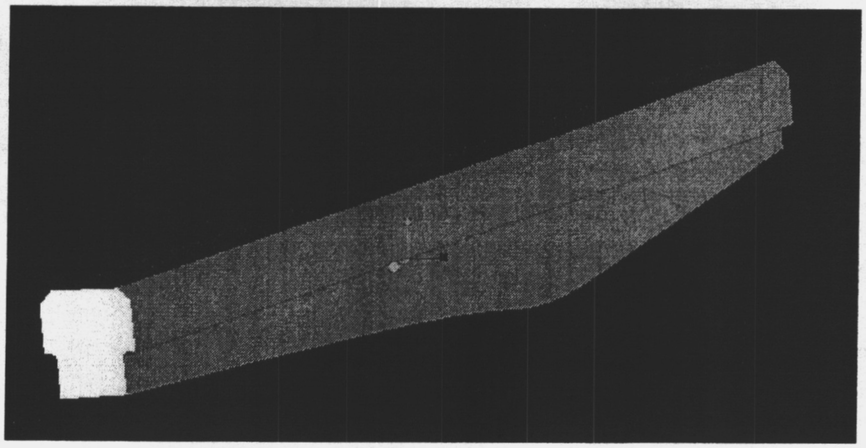

Figure 8. Bulky X38 Part

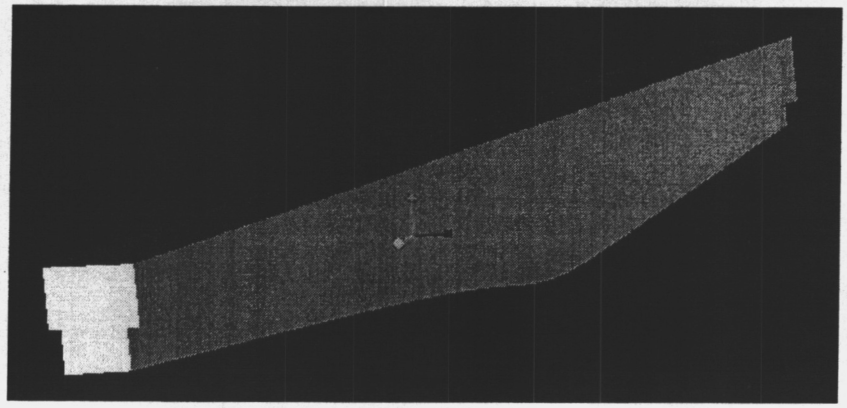

Figure 9. Bulky Part with Features Removed

In general, parts that are bulky, rather than thin, are easier to translate from the CAD program for FEA meshing. However, an automatic interface would help even with these. Figures 8 and 9 show a bulky X38 part fully featured, and with chamfers and rounds removed. When translated directly to PATRAN, the part with features removed will be easier to mesh with better shaped elements, and the resulting stress analysis will be conservative.

The ACFI program, developed at NASA/JSC this summer, is based on the concept that automating the process of translation from CAD model to FEA model will result in tremendous improvements in the design-through-manufacturing process at NASA/JSC. It will increase analyst productivity; at the present time it is not uncommon for analysts to spend days or weeks modifying the solid model to prepare it for analysis, and they often just use the dimensions from the CAD model to rebuild the

FEA model from scratch. ACFI, when fully implemented, will also enable analysts to rapidly transfer design improvements back to the original model for manufacturing. Smoother interfacing between programs will also enable designers and analysts to concentrate their efforts on what they do best, designing and analyzing, respectively.

ACFI is based on the current capabilities of the common CAD and FEA programs presently in use at JSC. The resources used in the above examples are shown in Table 1. These tools are not automatic, but will be automated as part of the proposed program. Additional development tools available within the software packages are listed in Table 2. It is expected that these tools will provide the resources for developing the capabilities described in the program.

Table 1. Existing Software Features

ProE	ProMesh	PATRAN/ I-DEAS
Manual feature suppression	Manual midsurface, beam extraction	Automatic geometry interpretation

Table 2. Development Tools within Existing Software

ProE	ProMesh	PATRAN/ I-DEAS
▪ Mapkey ▪ ProProgram ▪ J-Link ▪ Pro/TOOLKIT ▪ Config.pro, Win.pro ▪ UDF ▪ IGES and PATRAN export	▪ Mapkey ▪ Pro/TOOLKIT ▪ IGES export	▪ IGES & PATRAN import ▪ PCL - PATRAN Control Language

PROGRAM FOR THE DEVELOPMENT OF AN AUTOMATIC CAD/FEA INTERFACE

Task 1 - Establishment of program at Vanderbilt

- Installation of computers, software
- Training of graduate/undergraduate students, thorough investigation of software
- package capabilities: ProE, ProMesh, PATRAN/NASTRAN, I-DEAS, Mechanica

Task 2 - Collect information on typically removed features from CAD parts

Task 3 - Development of strategy for treatment (removal/extraction and export) of each class of feature prior from CAD software

- Thin features - midsurface extraction
- Solid 3-D features – export
- Fillets, rounds, chamfers - possible removal
- Holes - possible removal
- Beam type features - midline/cross-section extraction
- Two-force features - midline extraction
- Other features (springs, contact, etc.)

Task 4 - Development of routine for feature evaluation

- Incorporation of on-the-fly FEA analysis of individual features
- Evaluation and assessment of feature importance
- Incorporation of stress concentration factors of removed features for inclusion with analysis results

Task 5 - Development of automatic capability for CAD geometry export and FEA import

- Automatically remove features which do not impact design
  fillets, rounds, holes
- Automatically evaluate importance (via stress concentration factor, SCF) of features which do impact design, but should be removed for analysis
- Automatically replace removed features which impact design with their appropriate SCF's
- Automatically export revised CAD geometry
  thin, solid features
  beam type, two-force, others
- Automatically import revised CAD geometry to FEA program

- Automatically create report describing alterations in the model

Task 6 - Implement model export so that loading, constraints, and material properties automatically translate across the interface and are permanently attached to the model

Task 7 - Address data base management issues

- Develop method for management of part versions with removed/altered features
- Develop method for maintenance of revision status for original CAD models

Task 8 – Development of routine for automatic specification of element type required for each feature

Task 9 - Parameterization of Interface

- Development of strategy for parameterization of geometry by interface
- Implementation of automatic parameterization

Task 10 - Web implementation of interface

Task 11 - Extension of interface to include assemblies

Task 12 - Development of platform-independent interface

Task 13 - Expansion of interface to include CFD and thermal analyses

The total time required for completion of the program will depend on the level of funding. It will be performed at Vanderbilt University by Dr. Carol Rubin and graduate/undergraduate students maintaining close contact with EM and ES Design and Analysis colleagues at NASA/JSC.

SUMMARY OF SUMMER, 2000 ACTIVITIES

Consistent with the tasks listed above, the work performed at NASA/JSC this summer included:

- Investigation of the capabilities of most of the CAD and FEA tools used at JSC
- Establishment of the **ACFI** program requirements with advice from EM & ES designers and analysts

- Creation of a detailed development plan for **ACFI**
- Initial development of specific tools for **ACFI**
- Collection of parts which will be useful for testing **ACFI** during development
- Preparation of a Director's Research Grant proposal

ACKNOWLEDGMENTS

I would like to thank the EM3 Branch for their help and encouragement this summer; especially Raymond Aronoff my project colleague, Hector Saenz who provided prompt and efficient IT support, and Carolyn Krumrey EM3 Branch Chief.

I would also like to thank the following people who shared ideas with me during my work at JSC, and have expressed their interest in seeing this project through to completion. I expect to maintain extensive continued contact with them:

Steve Caperton
John Edgecombe
Brent Evernden
Chris Hansen
Chris Lupo
Galen Overstreet
Brandan Robertson
James Smith
Ted Tsai
Dave Wade

Countermeasure Evaluation and Validation Project (CEVP) Database
Requirement Documentation

Sung Y. Shin
South Dakota State University
SD3
August 4, 2000

Charles M. Lundquist
SD3/Life Sciences Research Laboratories Branch
Medical Science Division
Space and Life Science Directorate

Charles M. Lundquist

Sung Y. Shin

Countermeasure Evaluation and Validation Project (CEVP) Database Requirement Documentation

Final Report

NASA/ASEE Summer Faculty Fellowship Program – 2000

Johnson Space Center

Prepared By:	Sung Y. Shin, Ph.D.
Academic Rank:	Associate Professor
University & Department:	South Dakota State University Computer Science Department Brookings, SD 57007

NASA/JSC

Directorate:	Space and Life Science
Division:	Medical Science
Branch:	Life Sciences Research Laboratories
JSC Colleague:	Charles M. Lundquist
Date Submitted:	August 4, 2000
Contract Number:	NAG 9-867

Abstract

The initial focus of the project by the JSC laboratories will be to develop, test and implement a standardized complement of integrated physiological test (Integrated Testing Regimen, ITR) that will examine both system and intersystem function, and will be used to validate and certify candidate countermeasures. The ITR will consist of medical requirements (MRs) and non-MR core ITR tests, and countermeasure-specific testing. Non-MR and countermeasure-specific test data will be archived in a database specific to the CEVP. Development of a CEVP Database will be critical to documenting the progress of candidate countermeasures.

The goal of this work is a fully functional software system that will integrate computer-based data collection and storage with secure, efficient, and practical distribution of that data over the Internet. This system will provide the foundation of a new level of interagency and international cooperation for scientific experimentation and research, providing intramural, international, and extramural collaboration through management and distribution of the CEVP data.

The research performed this summer includes the first phase of the project. The first phase of the project is a requirements analysis. This analysis will identify the expected behavior of he system under normal conditions and abnormal conditions; that could affect the system's ability to produce this behavior; and the internal features in the system needed to reduce the risk of unexpected or unwanted behaviors. The second phase of this project have also performed in this summer. The second phase of project is the design of data entry screen and data retrieval screen for a working model of the Ground Data Database. The final report provided the requirements for the CEVP system in a variety of ways, so that both the development team and JSC technical management have a thorough understanding of how the system is expected to behave.

1. Introduction

This document specifies the requirements that the University of Wyoming development team and the JSC Space Life Science Division deem necessary for development of the Countermeasure Evaluation and Verification Project (CEVP) database and Internet-based data transfer system. The goal of this work is a fully functional software system that will integrate computer-based data collection and storage with secure, efficient, and practical distribution of that data over the Internet. This system will provide the foundation for a new level of interagency and international cooperation for scientific experimentation and research, providing intramural, international, and extramural collaboration through management and distribution of the CEVP data.

This document describes the requirements for the CEVP system in a variety of ways, so that both the development team and JSC technical management have a thorough understanding of how the system is expected to behave. The requirements are divided into three sections.

The first section, Functional Requirements, provides a textual description of each major function that briefly states the purpose of the function and the activities performed by that function. These functions are then described in more detail through the use of Work Breakdown Structures (WBSs), data flow diagrams, input/output design diagrams, and data dictionaries. Where a functional requirement is directly related to a function on the WBS, the WBS number will follow the requirement number in parentheses. The document then describes the general outputs of the system and the user inputs required for each major function.

The second section describes the non-functional requirements for the system. These requirements include physical environment, interface, users and human factors, performance, documentation, and security. The information about each requirement will vary according to the requirement type. The final section of the document outlines the administrative requirements, including team organization, tentative project schedule, and review procedures.

The requirements in this document address the major issues as currently defined for the CEVP system. At this point, all the data items to be contained in the CEVP database have not been identified, nor has the mechanism for approving distribution and access been completed, reviewed, and approved. It is expected that these constraints on the system will be evolving for some time. As those constraints change, the system requirements will also need to be changed. This nature of the project must be kept in mind by the development team and technical liaisons.

In addition, the system is expected to eventually provide an interface with other independent databases managed by other groups, as shown in Figure 1. The protocol of connecting those systems to the CVEP database is a major concern. However, those systems are also under construction, and solid information about them is not yet available. The current International Space Station (ISS) Data and Communications requirement stipulates that an "Interface Engine" be used to connect the databases, but that Interface Engine is not yet in place. Therefore, this document should be viewed as a first attempt to define the requirements for the CEVP database and data transfer system, and that changes to these requirements are to be both expected and accommodated in the design, implementation, and testing of the system.

2. Functional Requirements

System overview

The overall goal of the CEVP system will be to efficiently disseminate Integrated Testing Regimen (ITR) data, in accordance with Data Sharing Agreement (DSAs) signed by participating investigators and crewmembers, to JSC Discipline Experts, ISS International Partner facilities, and extramural investigators collaborating with NASA experts. The Internet-based data transfer system will support addition to and extraction of ITR data for the CEVP database. Ultimately, the CEVP database should interface with other Medical Operations databases (including LSAH/CMIS and LSDA), which house Medical Requirements information, as well as support the inclusion of data from in-flight research.

Security will be an issue of major concern since the CEVP database will contain confidential human medical and non-medical information that will be distributed over the Internet. All functions described below will be available only to those persons who have been authorized to do so, either through a DSA or for administrative purposes, as explained under "Users" in the nonfunctional requirements section.

CEVP Components and Interface Overview

SEE FIGURE 1.1 (attached)

CEVP Ground Data Dbase Overview

SEE FIGURE 1.2 (attached)

Major Functions Overview

Access and Update – The Access function will provide access to the data in the CEVP Ground Data Database. Access is provided in three modes: Intramural, Extramural, and International; research-oriented users at JSC, other users in the US, and at International Partner sites will be able to access the CEVP Ground Data Database through the Internet. Direct (non-Internet) access to the database will be limited to administrative users.

Authorized users will be able to extract and view a listing of selected data from the CEVP Ground Data Database in a variety of ways. This function also supports the download of collected data by all approved users for subsequent analysis. This module will be secure in that only authorized users will have access to the data, and that the data to which these users have access are only those items or records described in the applicable Request forms(s). In addition, data distributed to authorized users outside of JSC will be protected from unauthorized viewing through encryption, tunneling protocols, or similar mechanisms.

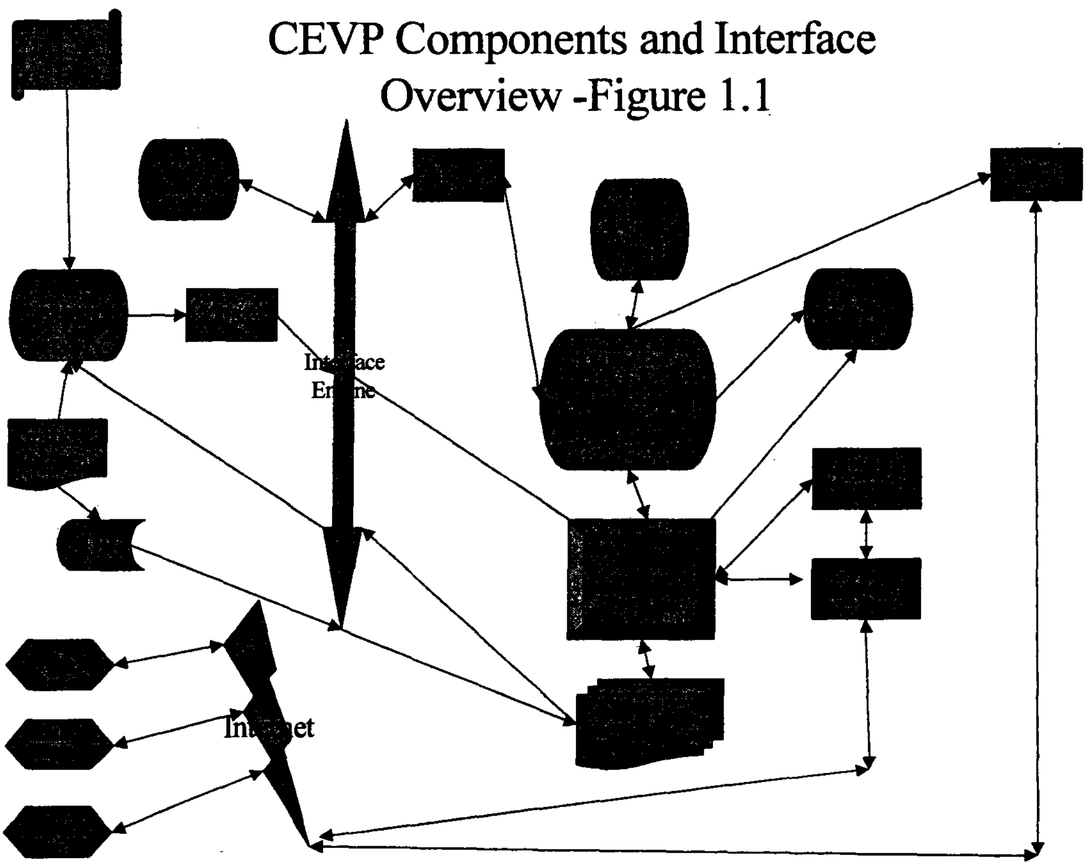

CEVP Components and Interface Overview -Figure 1.1

The Update function will allow users to download data into the CEVP Ground Data Database for subsequent analysis. Only authorized users will be permitted to download data to the database. Updates will be checked for consistency with the CEVP Ground Data Database structure so that they do not corrupt the existing database or any records that it contains.

Backup, Archive, and Restore - The Backup and Archive functions will support copying records from the CEVP Ground Data Database to other storage devices. This will ensure availability and integrity of the "active" database in case of equipment failure

CEVP Ground Data Database Overview
Figure 1.2

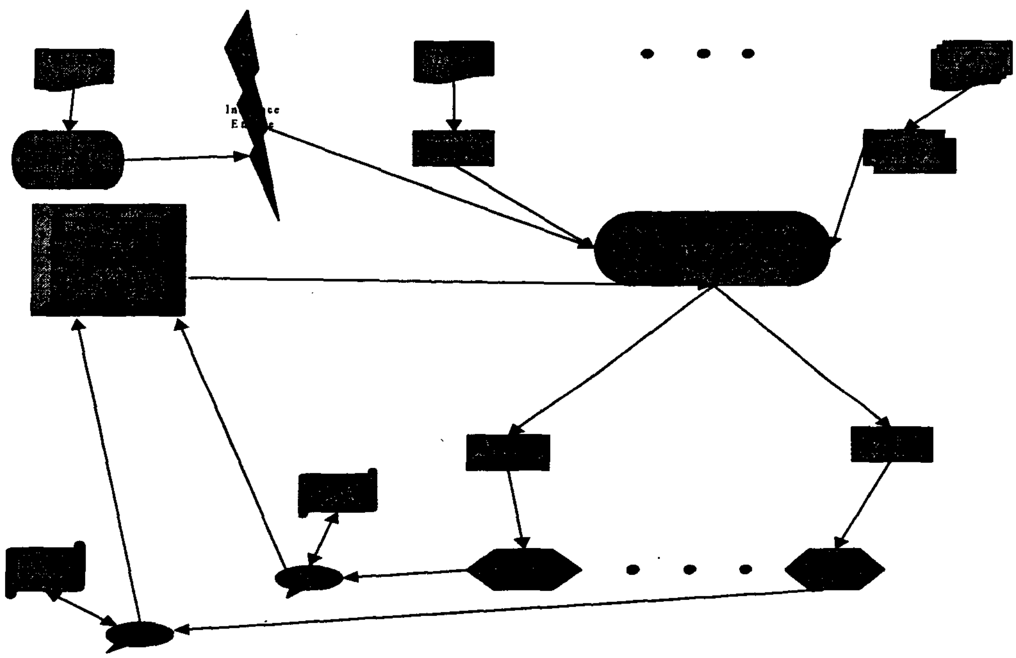

or external damage. The Backup function will allow the system administrator to create a mirror copy of the entire database on a separate hard drive or external medium (tape or Zip drive). The device to which backups are performed should be configurable by the administrator.

The Archive function will allow the administrator to selectively remove records from the active database and move them into an archive or other database, such as LSDA. The Restore function will allow records in an archive to be reinserted into the active database.

Modify and Download – These functions are restricted to the system administrator. Modify allows the administrator to add/delete/modify data fields in the database. This function will also allow the administrator to add, delete, or modify data items for each field in the database in a manual mode. The download function allows the administrator to modify and move data downloaded from other systems (such as LSAH/CMIS or LSDA) into the CEVP database.

Report Generator – This function will be used by the system administrator to view or print data from the CEVP Ground Data Database. It will be able to generate, view, and print reports for the various laboratories at JSC or other remote sites. If a specific user wants a standard report or customized report, the request will be made to the system administrator.

Analysis – This function will support analysis of the data in the CEVP Ground Data Database for the users. This function will have three sub-forms: Statistics, Computation, and Modeling.

3. Non-functional Requirements

Physical Environment

The database should be maintained on a dedicated machine connected to the Internet through the JSC network. The operating environment should be the most recent version of Microsoft Windows NT. The database should be implemented in the most recent version of Microsoft Access 2000 or Microsoft SQL. (Note: it is unlikely that Access will support the number of records expected in the CEVP Ground Data Database. However, the working model may be implemented in Access and later converted to SQL. The user interface of the system may also be programmed in Access 2000.) This server should have the following minimum configuration:

- Pentium III 750 Mz
- 256 Mb RAM
- Dual hard drive, 10 Gb capacity
- 19" Monitor
- HP Laser Printer (direct attachment)
- External High-Capacity Tape/Zip Drive for backups
- Uninterruptible power supply

Interface with other Systems

An Interface Engine will be used to support sharing of data between the CEVP Ground Data Database and other systems in JSC and other related networks. The CMIS project is going to use HIE Cloverleaf Interface Engines for connecting existing systems to ISS data systems at JSC.

According to its designers, the HIE Cloverleaf Interface Engine is a core technology suitable for any industry that replaces costly point-to-point interface development with a configurable hub and spoke architecture. The engine creates a high-performance messaging platform that supports asynchronous and synchronous connections to a range of programs, databases, objects, and protocols. Graphical configurations clients allow quick development of flow logic to direct, modify, and support business integration rules. Proactive management, alerting, and testing functions are all included. The system is available for both UNIX and native Windows NT platforms. HIE Cloverleaf supports multi-user interface development environment and popular communications protocols, including TCP/IP, SNA, and MQSeries.

Users and Human Factors

User Type: System Administrator (or Super User)
User Role: Responsible for activities relating to managing the CEVP Ground Data Database, including but not limited to network management, database update, database management, security management, answering user's questions, and technical support for the CEVP Ground Data Database.
Experience and Technical background: Computer Science and/or Science

User Type: Life Science Laboratories Staff
User Role: Access the CEVP Database without special authorization. High priority user.
Experience and Technical background: Science

User Type: PIs (General User)
User Role: Access the CEVP Database with special authorization as defined in applicable request from lower priority user.
Experience and Technical background: Science

User Type: LSAH/CMIS and LSDA Staff
User Role: Define interfaces to CEVP database, help in downloads between databases. Low priority user.
Experience and Technical background: Science

Performance

Any query of the CEVP Ground Data Database should be as efficient as possible. Most queries should take less than 10 seconds, and any query that takes more than 30 seconds for fewer than 2000 records is unacceptable. A progress indicator will be displayed for a query that takes more than 10 seconds. Note: these requirements do not consider delays caused by network congestion or routing failures.

Documentation

The following lists the deliverable documentation for the CEVP Ground Data Database and data transfer system:

- Users Manual (On-line help will be provided as well)
- System Administration Manual

- Requirements Documentation
- Design Documentation
- Source Code
- Test Plan and Results of Testing

Security and reliability

All human clinical or research data obtained will be subject to the Privacy Act of 1974 and secured using the "level two" security status set out by the Johnson Space Center Automated Information Systems Security Manual for the LSAH. To this end, the following requirements apply.

The CEVP Ground Data Database server should be located in a physically secured area at JSC so manual/non-networked access to the machine can be limited to administrators or designated JSC personnel. The CEVP Ground Data Database server and any peripheral machines used for data distribution should be within the JSC security firewall and thus protected from unauthorized logins and attacks to the extent possible with the existing mechanisms or future upgrades.

The CEVP Ground Data Database system will be logically isolated from other systems and accessible only as described in the interface section above. Access to the CEVP Ground Data Database will be limited to administrators or other specifically authorized JSC personnel, as described in the users and human factors section. No PI or other end user will be allowed to update or query the database directly.

Data marts in the CEVP Ground Data Database system will be constructed only by administrators, and only in response to a legitimate request from an authorized PI or other end user. The requests will be verified as to the user's identity and conformance to an approved the request form that explicitly specifies the information to be made available to the user through a data mart.

Data transmitted between the CEVP Ground Data Database system and an authorized PI or other end user will be secure according to the policy stated above. All data will be transmitted using virtual private networking (or a similar technology) to encrypt and encapsulate the data and prevent its interception or viewing by unauthorized persons. This technology will support encryption to the fullest extent allowed by United States policy for the end user location.

A formal security policy for all data distributed between the CEVP Ground Data Database system and end users will be developed, including guidelines for protecting the confidentiality of both data and authorization at the end user site. However, it will be the end user's responsibility to follow these guidelines, as well as any set out in the request form, and maintain security in accordance with all applicable NASA policies. The security policy to be developed will not supersede any existing or future NASA policy.

To prevent attempts to penetrate or attack the CEVP Ground Data Database system, no publication or presentation about the system will explicitly describe or identify any machine, location, or security mechanisms used. Any such publication describing the techniques or mechanisms used in this system will avoid discussion of the specifics of CEVP security.

The CEVP Ground Data Database system is not intended to be a highly available system. The Backup and Archive function described above is intended to assure that no data is lost in the event of a system or server failure, although it is possible that some transactions may need to be restarted should the system fail during query or update of the database or a data mart. If a security breach is detected, the system will shut down until the problem is resolved; however, the security of the data will be not be compromised due to a shutdown or failure of the system

4. Administrative Requirements

Team Organization

The development effort will be coordinated by Dr. Rex Gantenbein of the University of Wyoming. His primary responsibilities will be the supervision of the participants and preparation of deliverables as outlined here and in the original Offer to Perform Services.

Requirements gathering of the working model will be the responsibility of Dr. Sung Shin of South Dakota State University. In addition, Dr. Shin will assist with demonstrating the fulfillment of the system requirements through scenario analysis, determining the appropriate interfaces with other systems established at JSC, and obtaining cooperation with other JSC entities regarding data gathering, distribution, and archiving.

Mr. John Kim, a M.S. student at the South Dakota State University, will support the database implementation of the working model, with funding from NASA JSC grant NAG91176 (as revised). Security implementation of the working model will be performed by Mr. Tom James, a Ph.D. student at the University of Wyoming, with funding from a NASA JSC Graduate Student Research Program Fellowship. Mr. James will be assisted in the development of the secure Web interface by another University of Wyoming student to be hired for the Fall 2000 semester with funding from NASA JSC grant NAG91176 (as revised).

The technical monitor for this project is the CEVP manager, Mr. Charles M. Lundquist of the Life Sciences Research Laboratories at JSC.

Project Schedule

In Phase I of the project, the development team will deliver a revised version of the requirements documentation for the CEVP Ground Data Database and an implementation of the working model for the ground data. The Phase II system will incorporate these interfaces, as well as refine the number, types, and structure of the actual database items as they change in response to the interfaces and experiments developed during this period.

The Phase I prototype and documentation will be delivered no later than April 30, 2001. The Phase II system will be completed no later than August 31, 2001.

Review Process and Procedures for Change

Dr. Gantenbein will provide monthly progress reports to Mr. Lundquist. These reports will detail progress to date, issues and/or problems, costs in relation to the agreed-upon budget, and near-term goals. Mr. Lundquist and other parties at JSC will review these reports and discuss them with Dr. Gantenbein and other members of the development team. Through these reviews, desired changes to the development plan or project structure can be voiced and decided upon.

Once the definition of the CEVP system as specified by the Requirements Documentation is agreed to, all changes must be approved by the development team and the technical monitor.

5. A Working model Implementation for CEVP Ground Database

The goals of developing the CEVP Working model for the CEVP Ground Data Database are as follows:

1. Review mechanisms available for security in the CEVP project.
2. Review the current design of the CEVP project.
3. Investigate the advantages and disadvantages of the current approach to the CEVP project.
4. Investigate possible data input and output modes for the CEVP project.
5. Investigate the interface requirements with respect to other systems or archive databases at JSC.
6. Write and validate a complete requirements document for the CEVP project.
7. Store Ground Data into the CEVP Ground Data Database by the summer of 2001.

Architectural Design for CEVP Ground Data Database

The proposed operating system for the implementation will be WINDOWS NT. The project team will use Microsoft ACCESS 2000 and Microsoft Active Server Pages (ASP) technology for the implementation.

Data Entry for each lab

Authorized labs will be able to enter the ground data into the CEVP Ground Data Database only through Data Marts (DMs), which will be accessible over the Internet (and through the JSC intranet) using a Web browser such as INTERNET EXPLORER or NETSCAPE. It is may be necessary to specify a particular browser in order to assure that all features of the data entry system integrate properly.

A Menu Driven System will be used for the data entry by each lab. Each lab will be authorized to access only its own DM(s) for data entry.

The DMs and the CEVP Ground Data Database itself will be located on a secure database server within the JSC firewall. Security from Data entry to DM will include both user authentication (password) and Windows NT-provided virtual private networking. Security between the DM and the database will be provided by the secure database server.

CEVP Administration & Committee

The CEVP Administrator & Committee will review a request for access to data in the CEVP Ground Data Database through a request form submitted by each PI. On approval of the request, the Administrator will create a DM for the PI. The data items listed on the request form will be extracted from the CEVP Ground Data Dbase to the DM for the appropriate PI.

The CEVP Administrator will maintain the CEVP Ground Data Database and DM for each PI.

The CEVP Administrator will update the DM for PI if PI requests an update for a structure of an appropriate DM.

Data Retrieval for each PI

All authorized PIs will be able to view a listing of selected data from the CEVP Ground Data Database as specified by the appropriate DSA. This function also supports the download of collected data from the DM by all approved PIs for subsequent analysis. This function will be secure in that only authorized users will have access to the data, and that the data to which users have access is only those items or records previously approved.

The DM for each PI has a limited lifetime, which will be specified individually for each DM. The DM will be deleted once its lifetime has terminated.

The Update function will allow only the CEVP Administrator to update the CEVP Ground Data Database. This function will be protected by authentication on the database itself.

The CEVP Ground Data database server will provide security from the CEVP Ground Data Database to each DM. Security from the DM to the PI will include authentication (password) and Windows NT-provided virtual private networking.

Data Entry Screen Design for Each Lab.

Architectural Design for the Data Entry
Data Entry for Patient Information
Screen Design for Cardio Lab
Screen Design for Bone Lab
Screen Design for Exercise Lab
Screen Design for Nutritional Status Assessment

Data Retrieval flowchart and Screen Design

Ground Data Retrieval Flowchart
Architectural Design for Retrieval

Appendix

Acronyms

CEVP – Countermeasure Evaluation and Verification project
DFD – Data Flow Diagram
I/O – Input and Output
RD – Requirement Documentation
DSA – Data Sharing Agreement
ITR – Integrated Testing Regimen
WBS – Work Breakdown Structure

MiniAERCam Ranging

Dr. T. J. Talley P.E.
Tarleton State University
EV21
8/02/2000

Dr. G. D. Dickie Arndt Deputy Branch Chief
Chau T. Phan Project Engineer
Electronic Design & Development Branch (EV2)
Avionics Systems Division
Engineering Directorate

Tom Talley

Dr. T. J. Talley
Faculty Summer Fellow

Chau Phan

Chau T. Phan
Project Engineer

MiniAERCam Ranging

Final Report

NASA/ASEE Summer Faculty Fellowship Program – 2000

Johnson Space Center

Prepared By:	**Tom Talley, D.Eng., P.E.**
Academic Rank:	**Associate Professor**
University and Department:	**Tarleton State University** **Math, Physics and Engineering** **Stephenville, Texas 76402**

NASA/JSC

Directorate:	**Engineering**
Division:	**Avionics Systems Division**
Branch:	**Electronic Design & Development Branch (EV2)**
JSC Colleagues:	**Dickie Arndt, Chau Phan**
Date Submitted:	**August 3, 2000**
Contract Number:	**NAG 9-867**

ABSTRACT

Johnson Space Center (JSC) is designing a small, remotely controlled vehicle that will carry 2 color and one black and white video camera in space. The device will launch and retrieve from the Space Vehicle and be used for remote viewing. Off the shelf cellular technology is being used as the basis for communication system design. Existing plans include using multiple antennas to make simultaneous estimates of the azimuth of the MiniAERCam from several sites on the Space Station and use triangulation to find the location of the device. Adding range detection capability to each of the nodes on the Space Vehicle would allow an estimate of the location of the MiniAERCam to be made at each Communication And Telemetry Box (CATBox) independent of all the other communication nodes. This project will investigate the techniques used by the Global Positioning System (GPS) to achieve accurate positioning information and adapt those strategies that are appropriate to the design of the CATBox range determination system.

THE NASA SUMMER FACULTY FELLOWS PROGRAM

The NASA Summer Faculty Fellows Program offers university faculty an opportunity to participate in active, state-of-the-art projects and associate with other engineers and scientists. The experience gained is extremely valuable as it allows the participant to enrich the classroom experience for the students with discussions of real applications of the theory that is being taught. Further, students who graduate from programs that are well connected to current engineering and scientific challenges and practice graduate with a much fuller understanding of what is expected of them in the work place thus making them more diligent students and ultimately more valuable as future engineers and scientists. This enrichment has been shown to be an extremely valuable motivator for the students. In addition, the faculty can bring "new eyes" to projects that allow fresh perspectives to be examined by the design teams already deeply involved in projects.

Classroom enrichment, project contributions and the establishment of personal and professional relationships between academic and NASA personnel are good for all the individuals and institutions concerned. I am particularly grateful to have been able to participate as a NASA Summer Faculty Fellow and to be able to work on the MiniAERCam project.

The MiniAERCam is a small, free flying device that will use cellular communications techniques, which in some ways are similar to those, used by the Global Positioning System (GPS). This report will discuss the design objectives for the MiniAERCam, review GPS communications and analysis methods and make estimates of the ability of the MiniAERCam to determine its range from a known location. The nature of the signals involved in location using GPS, a comparison of the signals used by MiniAERCam, and expected performance of the system will be discussed.

Raw data and other information used by the author and not included in this report can be had by contacting the author at talley@tarleton.edu, or 254-968-9164.

MiniAERCam HISTORY AND DESIGN CONSIDERATIONS

MiniAERCam - System Objectives: The MiniAERCam project is a follow on to the AERCam (Autonomous EVA Robotic Camera) Sprint project that first flew on STS-87 in November 1997. The Sprint version was a 13" diameter ball shaped vehicle that traveled at about 0.25 ft/s (.076 m/s) and was cushioned to prevent damage should it run into anything. Sprint had an attitude hold function, gas thrusters controlled by UHF radio link and could send television from a color camera back to the shuttle using S Band microwave. The lack of navigation and control capability meant that the astronaut operated Sprint by looking out the window or by using the television image from Sprint to determine attitude and general location. The operation of the sprint was limited to locations where it could be observed.

In an effort to further reduce size and expense of AERCam, as well as enhance its capabilities, MiniAERCam was proposed. A 7"-8" diameter spherical vehicle will fly at a maximum rate of 0.15 m/s, or about twice as small (Dia., Volume = 16% of Sprint) and twice as fast as Sprint. The 10-lbm vehicle will be propelled by inert gas thrusters with an ultimate energy supply capable of giving the vehicle a Delta V of 40 ft/s (12.2 m/s). It is proposed to use cellular telephone based technology as a communications link between the flier and the control location, since cellular technology provides sufficient bandwidth, stable standards and parts are becoming less expensive. In addition to passing telemetry and video signals to and from MiniAERCam, the cellular communications signals can be used to find the position of the device with relation to the CATBox.

An antenna array (or several arrays) will be used to determine the relative bearing of the MiniAERCam from the Communications and Telemetry Box (CATBox). Signal processing of the cellular communications link signals using TOA (Time of Arrival) techniques will yield an estimate of the range from the CATBox to the MiniAERCam. It is desired to achieve a range resolution to within 1 meter.

Design Basis

For communication and location design purposes, the assumptions listed in Table 1 are used.

Table 1. MiniAERCam Ranging Design Basis Assumptions

Max Relative Velocity	1 m/s (Vehicle spec is 0.152 m/s)
Max Trans Accel	5-10 (cm/s^2)
Energy Capacity	40 fps Delta V
Mass	10 lbm
One CATBox only	
Eb/No	9.6 dB for 10^{-5} BER
Osc Stability	10^{-8}
Osc Stability	10^{-9} aided

Since the MiniAERCam flies in 3 space, it is necessary to solve at least three equations for three unknowns (x, y, z, in rectangular coordinates or r, Θ, Φ in spherical) in order to know where MiniAERCam is at any given time. If, however, there are timing errors in any of the measurements of the three equations, then a fourth equation must be added in order to resolve the timing error term. The spherical coordinate system lends itself well to this particular application, as two variables, (Θ,Φ) can be found using phase difference techniques at the antenna array, while the remaining variable r (range), can be found by Time of Arrival (TOA) techniques in the receivers. The TOA technique used in the MiniAERCam application is much like the distance measuring techniques used by

RADAR, in that a signal is sent out, the time between transmission and receipt of the returned signal is measured. Knowing that the radio frequency energy and signals traveled at roughly the speed of light, an estimate of the distance traveled is given by the following general equation. The division by 2 in this case is required since the time measured is the time for signals to travel both directions over the path.

$$\text{Distance} = C * \Delta t/2$$

The CATBox will send out a Pilot Code imbedded in the Radio Frequency signal, which the communication system on the MiniAERCam will use to set its clock. Then, using its own clock, the MiniAERCam will send information streams out using the same Pilot Code. The delay between the time that the CATBox transmits the Pilot code and when it returns to the CATBox will be proportional to the time necessary to travel the distance between the CATBox and the MiniAERCam. Timing errors will be introduced along the way, and reducing them to a minimum and accounting for them will be necessary in order to arrive at an accurate estimate of the range.

Communication Link

The communication link between the CATBox and the MiniAERCam is in the cellular telephone band with a center frequency of approximately 850 MHz. The modulation scheme is based on a spread spectrum signaling technique now in wide commercial use known as CDMA (Code Division Multiple Access). During World War II, secure communications techniques were necessary in order to coordinate between the leaders of the Allies. A technique was invented [6][7] that mixed a very wide band noise with the very narrow band signal of a voice. The very wide mostly noise signal was then transmitted. Anyone receiving the signal would think that the noise was simply noise, but it actually contained within it the information of the voice signal. At the desired receiving location, there existed an exact copy of the noise that had been used to modulate the signal originally. The noise was synchronized with the transmitted noise, subtracted from the signal and what was left was the original voice signal.

In today's modern digital communications systems, similar signaling techniques are used, but the noise is created by using what are called PRN (Pseudo Random Number) or PN (Pseudo Noise) Codes. These codes are mixed with the intelligence signal in much the same way that the original spread spectrum signals were created. Once mixed and transmitted, the PN code (being known to the intended receiver) can be subtracted from the data stream leaving the original data in tack. The important feature of this kind of code is that unless the receiver has the correct code, and is able to line the code up exactly with the code that was originally sent, it is virtually impossible to unscramble the original data stream. In fact, different data streams can be sent within the same band of frequencies using only different, or time delayed versions of the same PN codes to separate them.

Once modulated with a PN code (referred to as a chipping code), the data stream can be transmitted using different modulation schemes. The EIA-2000A [9] specification for CDMA cellular equipment spells out the details of the modulation schemes to be used. MiniAERCam will use Offset Quadrature Phase Shift Keying (OQPSK) where the phase of the outgoing signal is varied based on the information stream to be transmitted taken two bits at a time (one in the In Phase "I" channel, the other in the Quadrature "Q" channel).

Spread Spectrum And Pseudo Noise

In order to decode the incoming signal, it is necessary to mix (correlate) the incoming information stream with the PN code. The correlation will allow the information contained within the signal to then be detected. Part of the demodulation process in the receiver requires the PN code be lined up exactly in time with the incoming signal's PN code. This lining up process is accomplished in a circuit known as a Delay Locked Loop.

Good PN Code Properties

- They don't correlate well with themselves
- If they don't line up, they don't produce large outputs from the code locked loop correlators
- They don't have too many consecutive 0's (or 1's)
- They can be generated simply in hardware
- Really good ones are called "Gold Codes"
- You can use the same code at different start times to separate different data streams (remember, they don't line up)

GPS Location Techniques

Perhaps the best known, currently in use, location system is the Global Positioning System (GPS). The GPS uses information gained by receiving a signals from a number of satellites in order to make an estimate of the location of the observer. Each of the satellites is at a "known" location, transmits timing information and is in high-speed relative motion with the observer. GPS uses an array of satellites, which broadcast their locations, and the time using CDMA modulation techniques similar to those used in cellular telephony. A review of the GPS system specifications [1][3] reveals the following.

Table 2. Global Positioning System (GPS) Signal Characteristics

- Standard Positioning System (SPS)
  - 100m Hz (2 drms, 95%)
  - 156m vert
  - 340 nsec time accuracy
- Precise Positioning System (PPS)
  - encrypted
- CDMA Based
  - Short Code C/A repeats every 1ms
  - Long Code P(Y) repeats every week
- Selective Availability (25m sigma variation)
  - Off for the time being
- Two frequencies
  - L1 Frequency 1575.42 MHz
  - C/A 1.023 x 10^6 chips/sec
  - AND P(y) 10.23 x 10^6
  - L2 Frequency 1227.6 MHz
  - C/A 1.023 x 10^6 chips/sec
  - OR P(y) 10.23 x 10^6
- Time Of Arrival techniques
  - 4 or 5 equations (Sats in View)
  - 4 unknowns (x,y,z,t)
  - 5 unknowns (x,y,z,t,v)
- Carrier Based Techniques
  - Resolve Carrier Phase Ambiguity using multiple receptions. (5-10 wavelengths (1-2 meters)
  - Carrier Phase Resolution 1.7-2.3° (1.2-1.6 mm)

The GPS and MiniAERCam ranging system will use many of the same signaling and calculation techniques. Both GPS and MiniAERCam were examined to determine whether any of the techniques well known to GPS could be adapted to the MiniAERCam thus reducing development cost and uncertainty. The following is a comparison of the Signaling Parameters involved in each technique.

Table 3. GPS Vs Cellular Signaling Parameters

GPS	Cellular

▪ CDMA
▪ PN Code (C/A)
  ▪ 1.023 Mb/s chip rate (100/150 m)
  ▪ Repeats every ms
▪ P(Y) Code
  ▪ 10.23 Mb/s chip rate
  ▪ Repeats Once a Week
▪ TOA estimate
▪ High Doppler from Satellites
▪ Multiple, independent information streams (4 sats can solve 4 equations for 4 unknowns (5 is better)
▪ Code Locked Loop for PN Tracking
▪ Multipath considerations
▪ Carrier Tracking Techniques improve resolution
▪ 1-2 m (wavelength ambiguity)
▪ 1.2 - 1.6 mm (Phase Angle)
	▪ CDMA
	▪ PN Code
	▪ R3 3*1.2288 MBPS chip rate
	▪ 3.6864 MBPS chip rate
	▪ Repeats 26.6… ms
	▪ TOA estimate of range
	▪ Little or no Doppler
	▪ Single (dependent) data stream
	▪ Code Locked Loop for PN Tracking
	▪ Multipath considerations
	▪ Carrier Tracking Techniques improving resolution

Comparison of GPS and AERCam

While there would appear to be many similarities between GPS and MiniAERCam Ranging, the GPS environment is very different from the communication environment expected for the MiniAERCam. For example, the receiver in GPS has several independent streams of information originating on widely spaced satellites from which the receiver can calculate its position. The relative velocity between the GPS receiver and the satellites is very high. Multipath signals (signals arriving at slightly different times because of reflections from nearby objects) presents a problem for both GPS and MiniAERCam, but GPS uses the fast change in relative positions of the satellites to remove the artifacts produced by multipath, while MiniAERCam will be moving very slowly indeed by comparison.

GPS uses comparison, combination and filtering techniques to remove some of the signaling artifacts caused by the atmosphere and the timing errors between GPS satellites. MiniAERCam, on the other hand, will not fly far from the CATBox (160 m) and will only fly in space, so the measures used to resolve GPS errors caused by propagation through the ionosphere are of little use to MiniAERCam. Conversely, since the basis for timing the signal traveling between the CATBox and MiniAERCam involves only the CATBox's knowledge of its clock status, there is no need to resolve clock differences between various satellites. The one exception to this is the assumption that the MiniAERCam will (Per EIA-2000) maintain its PN code response in exact synchronism with the incoming PN code from the CATBox. This time difference tracking, if done in comparison to a stable clock, will yield a phase resolution of approximately 15 Degrees, or approximately 0.8 m relative to initial clock synchronization position. The short-term stability of the local MiniAERCam clock produces variation on the order of 3 meters (1×10^{-8}), so the use of the phase variation of the 10 MHz reference clock could not be used as a primary location mechanism with its current stability. However, phase locking the MiniAERCam clock to the incoming signals will produce relative clock errors as the MiniAERCam changes position.

GPs Accuracy

An examination of the GPS positioning error analysis shows the following contributions to error.

Table 4. GPS Error Sources [1]

Sources of Error	SA On	SA Off
Space	Space	Space
o Sat clock stability	o 3.0	o 3.0
o Sat perturbations	o 1.0	o 1.0
o Selective Availability	o 32.3	o -
o Other	o 0.5	o 0.5
Control	Control	Control
o Ephemeris prediction error	o 4.2	o 4.2
o Other	o 0.9	o 0.9
User	User	User
o Ionospheric delay	o 5.0	o 5.0
o Tropospheric delay	o 1.5	o 1.5
o Receiver noise and resolution	o 1.5	o 1.5
o Multipath	o 2.5	o 2.5
o Other (interchannel bias, etc)	o 0.5	o 0.5
Total (rss) User UERE	**33.3**	**8.0**

With the Selective Availability feature of GPS currently turned off, the one σ variation of the position estimate for the generally available location from GPS has improved significantly from 33 meters to 8 meters. MiniAERCam's PN code chipping rate is 3 times the C/A rate of the GPS system, which implies that resolutions of at least 3 meters are achievable all else being equal, but they are not.

The resolution of the range estimate that can be made by the MiniAERCam communication system is controlled by the ability of the system to resolve the time of arrival of PN codes. Further reductions in variation will be achievable with MiniAERCam due to the difference in nature of the application. There will be error induced in MiniAERCam due to clock stability, but not the same kind of errors produced in GPS.

In GPS, each satellite thinks it knows what time it is. It is left to the receiver to figure out what time it really is and then correct its location estimates based on its "corrected " estimate of the current time. In the MiniAERCam application, the PN code signal is being sent out and then received back by the same CATBox, so short term clock stability, or even accuracy is not as much of a factor as it is in GPS applications. The error is more related to the amount of jitter (statistical very short term phase noise) available from the clock in the CATBox combined with the same variation on the MiniAERCam will determine the accuracy of the signal transit time and hence range. A number of 1×10^{-11} has been suggested as a goal for the proposed system.

Receiver Noise and resolution

The MiniAERCam receiver will be using under sampling techniques in order to gain an estimate of the early and late signals present in the delay locked loop circuit. These techniques involve using an Analog to Digital conversion of 10 bits resolution. Such a conversion offers a dynamic range of approximately 60 db (volts), which insures that the output of the early and late correlators of the delay locked loop, will provide suitable range resolution. A model of a generic correlator run on SPW indicated that resolutions of 30 db could be expected for full scale, no noise Intermediate Frequency signals yielded range resolutions on the order of 1/1000 th of the chipping period which is equivalent to range resolutions on the order of .08 m. Previous stages processing, noise, and time reference will all contribute to reducing such precision by one or more orders of magnitude.

Other experience with Cellular Ranging

MiniAERCam is not the only application for location using CDMA techniques [2]. The Federal Communications Commission (FCC) has proposed that by October of 2001, a cellular phone service provider should be able to provide an estimate of the location of a cellular customer within 125 meters. This requirement is designed to facilitate emergency response much as is currently available in the wired networks using the 911 system. Two studies by Motorola [4][5] and one by a university in Australia [8] point to range resolutions in the 10s - 100s of meters as being possible.

Table 5. Cellular E911 Trials on Ranging

▪ University of Technology, Sydney± 9 m ▪ Simulation - no multipath ▪ MultiCell Detection with post processing ▪ 38.4 MBPS (Msps) ▪ 1.2 MBPS Chip Rate
▪ Motorola Labs, Texas (2/99) ▪ 96-302 m Single Site ▪ 99-93 m Multi Site ▪ 1.2 MBPS Chip Rate
▪ Motorola Labs, IL. (2/99) ▪ 85-189 m Single Site ▪ 169-357 m Multi Site ▪ 1.2 MBPS Chip Rate

These studies indicate that higher sampling rates produce better range resolution. And that ranges out to several miles are obtained using cellular system receiver transmitter equipment.

Signal and Timing within MiniAERCam

The receiver system for the MiniAERCam and the CATBox will use similar signaling techniques all based on Rate 3, EIA 2000a standards for Cellular Systems. These standards call for the following signals to be present. The particular implementation of the signal is left to the designer and those implementations are shown as frequencies (and their resulting resolution basis in meters).

Table 6. AERCam Basic Resolutions

Chip Rate (3.6864 Mcps)	81.38 m
VCO Resolution (29.4912 Mpps)	10.17 m
Input Sample Rate (36.864 Msps)	8.12 m
Oscillator Short Term Stability unaided (1×10^{-8})	3 m
FPGA Propagation Delay (5×10^{-9} s)	1.5 m
Oscillator Short Term Stability aided (1×10^{-9})	0.3 m
Oscillator Jitter (1×10^{-11})	0.003 m (3 mm)

The implication of the nature of these signals is generally that the lower the frequency, the lower the resolution with which the Time of Arrival of the PN code signal can be assessed.

System Operational Requirements

In order for the CATBox to make an accurate Estimate of Range to the MiniAERCam, the following system operations must be performed.

- RxVCO is locked to the correct arrival time of MiniAERCam PN code sequence (± 1/8 chip time) in the Delay Locked Loop (DLL).
- Residue of the summer is related to difference between RxVCO and PN code sequence arrival time.
- Range = c*[(RxVCO-TxVCO)+k*Residue) / 2]
- Additional delays inserted (i.e. to mitigate multipath [5]) in the MiniAERCam and CATBox system must be deterministic, measured and subtracted from the total delay in order to arrive at a correct range estimate.
- Three antennas/receivers with "the same" data at the CATBox location offer the opportunity for further improvement in noise and clock estimates.

FINDINGS AND CONCLUSIONS

After reviewing the performance of the GPS system, the experience of others performing ranging using cellular technologies and the design concepts involved in the MiniAERCam, the following conclusions are drawn.

- The MiniAERCam, CATBox combination should be able to resolve the range between them with accuracy on the order of 1 meter using Time of Arrival CDMA techniques.

- Adding a Phased Locked Loop to the MiniAERCam receiver in an attempt to improve internal oscillator short term stability from 1×19^{-8} to 1×10^{-9} seems to be warranted.

- Multipath will be present, and if compensated for by using delay mechanisms in the system, the amount of such delay must be transmitted to the device calculating the range so that overall travel time estimate can be corrected.

- Techniques such as double differencing used in GPS for the reduction of noise and atmospheric effects will add little to the accuracy of position estimates of the MiniAERCam.

- Careful attention must be paid in the construction of the FPGA devices of the MiniAERCam and the CATBox to account for and match signal delays in the paths being used for measurement of range.

- The clock of the MiniAERCam, if locked to the incoming signals from the CATBoxes will wander based on the relative distance between them. If not locked to the incoming signals, the MiniAERCam clock will produce 1/8 chip (10 Meter distance equivalent) steps in delay based on the operation of the code locked loop circuitry, as range varies. This design element is critical to the proper functional operation of any ranging determination and should be examined further.

The MiniAERCam will be improved by the ability to locate it in space with sufficient accuracy. Use of Time of Arrival techniques added to Angle of Arrival techniques already under development will add another dimension to the flexibility of the MiniAERCam system.

2000 NASA/ASEE SUMMER FACULTY FELLOWSHIP PROGRAM

JOHNSON SPACE CENTER
UNIVERSITY OF HOUSTON

A Subjective Assessment of Alternative Mission Architecture Operations Concepts for the Human Exploration of Mars at NASA Using a Three-Dimensional Multi-Criteria Decision Making Model

By

Madjid Tavana, Ph.D.
Chairman, Management Department
La Salle University
Philadelphia, PA 19141-1199, USA
Phone: 215-951-1129 • Fax: 215-951-1271
Chapter 17 Internet: tavana@lasalle.edu

NASA/JSC

Directorate:	**Mission Operations Directorate**
Division:	**Advanced Operations Development Division**
Branch:	**Advanced Projects Branch**
NASA Colleague:	**Anthony Griffith**
Date:	**July 2000**

A Subjective Assessment of Alternative Mission Architecture Operations Concepts for the Human Exploration of Mars at NASA Using a Three-Dimensional Multi-Criteria Decision Making Model

ABSTRACT

The primary driver for developing missions to send humans to other planets is to generate significant scientific return. NASA plans human planetary explorations with an acceptable level of risk consistent with other manned operations. Space exploration risks can not be completely eliminated. Therefore, an acceptable level of cost, technical, safety, schedule, and political risks and benefits must be established for exploratory missions. This study uses a three-dimensional multi-criteria decision making model to identify the risks and benefits associated with three alternative mission architecture operations concepts for the human exploration of Mars identified by the Mission Operations Directorate at Johnson Space Center. The three alternatives considered in this study include split, combo lander, and dual scenarios. The model considers the seven phases of the mission including: 1. Earth Vicinity/Departure, 2. Mars Transfer, 3. Mars Arrival, 4. Planetary Surface, 5. Mars Vicinity/Departure, 6. Earth Transfer, and 7. Earth Arrival. Analytic Hierarchy Process (AHP) and subjective probability estimation are used to captures the experts' beliefs concerning the risks and benefits of the three alternative scenarios through a series of sequential, rational, and analytical processes.

Key Words: *Multicriteria Decision Making, Group Decision Support Systems, Analytic Hierarchy Process, and Subjective Probabilities.*

THE PROCEDURE

This study considers a five-step procedure that guides the Human Exploration Operations Team (HEOT) at Johnson Space Center through a systematic evaluation of the three mission architecture scenarios including: split, combo lander, and dual.

Split Mission Scenario: In this scenario, the mission is split into two steps: pre-deployment of mission assets to the planet surface followed by the mission crew. During the assets deployment, the Return Habitat/Ascent Vehicle is launched to Mars. Upon arriving Mars's orbit, the Return Habitat will stay in the orbit while the Ascent Vehicle lands on Mars and starts producing fuel. After the mission equipment are configured and tested to be viable, the Transit Habitat/Surface Habitat is sent initially to Earth's orbit. The crew will be transferred to the Transit Habitat/Surface Habitat in Earth's orbit at a later date. Next, the Transit Habitat/Surface Habitat and the crew are sent to Mars to land near the Ascent Vehicle. After the completion of surface exploration, the Ascent Vehicle is used to transfer the crew to Return Habitat orbiting Mars's orbit. Return Habitat will be used to return the crew to Earth. In all scenarios, travel to and from Mars will take approximately six months each way and surface exploration is scheduled for 520-580 days.

Combo Lander Scenario: In this scenario, the mission assets travel to and from Mars with the crew. Initially Transit Habitat/Surface Habitat/Ascent Vehicle are launched to Earth's orbit. The crew will be transferred to the Transit Habitat/Surface Habitat/Ascent Vehicle in Earth's orbit at a later date. Next, the Transit Habitat/Surface Habitat/Ascent Vehicle are sent to Mars with the crew. Upon arriving Mars's orbit, the Transit Habitat separates and remains in Mars's orbit while the crew uses the Surface

Habitat/Ascent Vehicle to land on Mars. After the completion of surface exploration, the Ascent Vehicle is used to transfer the crew to Transit Habitat which will return the crew to Earth.

Dual Scenario: In this scenario, Transit Habitat/Surface Habitat/Ascent Vehicle/Descent Vehicle is launched to Earth's orbit. The crew will be transferred to the Transit Habitat/Surface Habitat/Ascent Vehicle/Descent Vehicle in Earth's orbit at a later day. Next, the Transit Habitat/Surface Habitat/Ascent Vehicle/Descent Vehicle is sent to Mars with the crew. In Mars's orbit, Transit Habitat will stay in the orbit, Surface Habitat is landed on Mars unmanned, and the crew uses Ascent/Descent Vehicle to land on Mars near the Surface Habitat. After the completion of surface exploration, the Ascent Vehicle is separated and used to transfer the crew to Transit Habitat which will return the crew to Earth. The five steps are described below:

(i) The HEOT identifies Mission Phases. In this step, the HEOT identifies the phases of mission to be included in the evaluation process. Mission phases considered by the team included Earth Vicinity/Departure, Mars Transfer, Mars Arrival, Planetary Surface, Mars Vicinity/Departure, Earth Transfer, and Earth Arrival.

(ii) HEOT utilizes AHP and EC to determine the importance weight of each Phase. AHP was introduced by Saaty (1972) to assist decision makers in the evaluation of complex judgmental problems. AHP allows the HEOT to assign numerical values to qualitative attributes by making trade-off among them. The process is confined to a series of pairwise comparisons. Saaty (1972) argues that a decision maker naturally finds it easier to compare two things than to compare all the items in a list. AHP also evaluates the consistency of the HEOT and allows for the revision of the responses. Because of the intuitive nature of the process and its power in resolving the complexity in a judgmental problem, AHP has been applied to many diverse decisions. A comprehensive list of the major applications of AHP, along with a description of the method and its axioms, can be found in Saaty (1972, 1977a, 1977b, 1980, and 1990), Weiss and Rao (1987) and Zahedi (1986). AHP has proven to be a very popular technique for determining weights in multicriteria problems (Zahedi 1986 and Shim 1989).

There has been some criticism of AHP in the operations research community. Harker and Vargas (1987) show that AHP does have an axiomatic foundation, the cardinal measurement of preferences is fully represented by the eigenvector method, and the principles of hierarchical composition and rank reversal are valid. On the other hand, Dyer (1990a) has questioned the theoretical basis underlying AHP and argues that it can lead to preference reversals based on the alternative set being analyzed. In response, Saaty (1990) explains how rank reversal is a positive feature when new reference points are introduced. In this study we use the geometric aggregation rule to avoid rank reversal which has had varying degrees of importance to different researchers (Dyer 1990a, Saaty 1990, Harker and Vargas 1990, and Dyer 1990b).

Once the mission phases were identified, the HEOT used a pairwise comparison questionnaire based on AHP to determine the importance weight of each phase. These judgments are synthesized by EC. The normalized geometric means of the HEOTs importance weights of mission phases are calculated at the end of this step.

(iii) The HEOT identifies the criteria to be used for each mission phase and utilize EC to determine the importance weight of their criteria. HEOT as a tem identifies the set of criteria to be used for evaluating the alternative mission architectures. Assume team member i believes $c_1, c_2, \ldots, c_I$ are the I criteria that contribute to the success of a mission architecture. The team member's next task is to assess the relative importance of these criteria using a questionnaire provided based on AHP. The questionnaire asks the team member to compare each possible pair of criteria c_j, c_k and to indicate which of the criteria is more important and by how much.

These judgments are represented by an $I \times I$ matrix:

$$A = (a_{jk}) \qquad (j,k=1, 2, \ldots, I)$$

If c_j is judged to be of equal importance as c_k, then $a_{jk}=1$

If c_j is judged to be more important than c_k, then $a_{jk}>1$

If c_j is judged to be less important than c_k, then $a_{jk}<1$

$$a_{jk} = 1/a_{kj} \qquad a_{jk} \neq 0$$

Thus, matrix A is a reciprocal matrix so that the entry a_{jk} is the inverse of the entry a_{kj}. a_{jk} reflects the relative importance of c_j compared with criteria c_k. For example, $a_{12}=1.25$ indicates that c_1 is 1.25 times as important as c_2.

Then, the vector w representing the relative weights of each of the I criteria can be found by computing the normalized eigenvector corresponding to the maximum eigenvalue of matrix A. An eigenvalue of A is defined as λ which satisfies the following matrix equation:

$$A\,w = \lambda\,w$$

where λ is a constant, called the eigenvalue, associated with the given eigenvector w. Saaty has shown that the best estimate of w is the one associated with the maximum eigenvalue (λ_{max}) of the matrix A. Because the sum of the weights should be equal to 1.00, the normalized eigenvector is used. Saaty's algorithm for obtaining this w is incorporated in the software Expert Choice utilized in this study.

One of the advantages of AHP is that it assesses the consistency of the team member's pairwise comparisons. Saaty suggests a measure of consistency for the pairwise comparisons. When the judgments are perfectly consistent, the maximum eigenvalue (λ_{max}) should equal the number of criteria that are compared (I). Typically, the responses are not perfectly consistent, and λ_{max} is greater than I. The larger the λ_{max}, the greater is the degree of inconsistency. Saaty defines a consistency index (CI) as $(\lambda_{\max} - I)/(I-1)$ and provides a random index (RI) table for matrices of order *3* to *10*. This RI is based on a simulation of a large number of randomly generated weights.

n	*3*	*4*	*5*	*6*	*7*	*8*	*9*	*10*
RI	*0.58*	*0.90*	*1.12*	*1.32*	*1.41*	*1.45*	*1.49*	*1.51*

Saaty recommends the calculation of a consistency ratio (CR) that is the ratio of CI to RI for the same order matrix. A CR of *0.10* or less is considered acceptable. When the CR is unacceptable, the team member is informed that the pairwise comparisons are logically inconsistent and is encouraged to revise the EC judgments.

(iv) The HEOT members identify probabilities of occurrence for each factor and each mission phase: Subjective probabilities are commonly used in multicriteria decision making because they require no historical data (Schoemaker 1993, Schoemaker and Russo 1993, Vickers 1992, and Weigelt and Macmillan 1988). Some researchers conclude that the difficulty of obtaining relevant historical information on which to base probabilities inhibits their use. However, probabilistic phrases such as "possible," "likely," "certain," etc. provide an opportunity to elicit the required information verbally and then convert these verbal phrases into numeric probabilities (Brun and Teigen 1988, Budescu and Wallsten 1985, and Tavana et al. 1997). Other commonly used approaches include reasoning (Koriat and Lichtenstein 1980), scenario construction (Schoemaker 1993) and this cross-impact analysis (Stover and Gordon 1978). Merkhofer (1987) and Spetzler and Stael von Holstein (1975) review probability elicitation procedures that are used in practice.

This study utilizes verbal probabilistic scales with probabilistic phrases, like "possible," "likely," and "certain" to elicit the required information and then converts them into numeric probabilities as suggested by Tavana et al. (1997). Alternatively, the HEOT can use numeric probabilities rather than the probabilistic phrases. Each team member receives a listing of all three mission architectures under consideration and assigns probabilities of occurrence to its set of criteria for each mission architecture.

(v) EXCEL is utilized to provide a consensus ranking of the mission architecture scenarios. Microsoft Excel is used in this step to calculate an attractiveness score for each mission architecture scenario using the model presented next.

THE MODEL

To formulate an algebraic model, let us assume:

S^m = Mission architecture score of the *m-th* scenario; ($m = 1, 2, ..., q$)

W_i = The importance weight of the *i-th* mission phase; ($i = 1, 2, ..., I$)

F_{ij} = The Importance Weight of the *j-th* Criterion for the *i-th* mission phase; ($i = 1, 2, ..., I$ and $j = 1, 2, ..., J$)

P_{ij}^m = The *m-th* Probability of Occurrence of the *j-th* Criterion for the *i-th* mission phase; ($m = 1, 2, ..., q; i = 1, 2, ..., I$; and $j = 1, 2, ..., J$)

I = Number of mission phases

J = Number of Criteria for the *i-th* mission phase

Given the above notations, the overall score of the *m-th* mission architecture scenario is:

$$S^m = \sum_{i=1}^{I} W_i \left(\sum_{j=1}^{J} F_{ij} \left(P_{ij}^m \right) \right)$$

Where:

$$0 \le P_{ij}^m \le 1$$

$$\sum_{i=1}^{I} W_i = 1$$

$$\sum_{j=1}^{J} F_{ij} = 1$$

RESULTS AND CONCLUSION

Tables 1 and 2 present the final results of this study. Table 1 shows the average normalized weights assigned to mission architecture phases by the HEOT members. The table also shows the evaluation factors within each phase along with their impact, whether they are perceived as risk or benefit. Risky factors are represented by a (-1) while beneficial factors are represented by a (+1). Table 2 shows the average probabilities of occurrence assigned by the HEOT members along with a final score for each mission architecture scenario. Give the goal of maximizing the overall score, split scenario with an overall score of (-0.124) is the optimal choice followed by dual scenario (-0.145) and the combo lander (-0.169). Further analysis could be done to study the detailed risks and benefits associated with each scenario for each phase.

Insert Tables 1 and 2 Here

This study is not intended to replace human judgment in mission architecture evaluation at Johnson Space Center. In fact, human judgment provides the basic input of to this study. The model used in this study helps HEOTs think systematically about complex mission architecture selection problems and improves the quality of the resulting decisions. Objective data on the characteristics of most scenarios is somewhat limited because of inherent uncertainties. However, experienced HEOTs are often able to provide reasonably accurate estimates of values for these characteristics as a substitute for objective data. This study combines these subjective values numerically to provide an overall score for each mission architecture. It is important to realize that human beings are imperfect information processors and their judgments and preferences about uncertainty can be limited. An awareness of human cognitive limitations is critical in developing the necessary judgmental inputs.

REFERENCES

Dyer, J. S. Remarks on the Analytic Hierarchy Process. *Management Science*. 1990a, 36 (3), 249-258.

Dyer, J. S. A clarification of 'Remarks on the analytic hierarchy process.' *Management Science*, 1990b, 36 (3), 274-275.

Harker, P. T. and Vargas, L. G. Reply to 'Remarks on the analytic hierarchy process' by J. S. Dyer. *Management Science*, 1990, 36 (3), 269-273.

Koriat, A., Lichtenstein, S., and Fischoff, B. Reasons for confidence. *Journal of Experimental Psychology*. 1980, 6, 107-118.

Merkhofer, M. W. Quantifying Judgmental Uncertainty: Methodology, Experiences, and Insights. *IEEE Transactions on Systems, Man, and Cybernetics*. 1987, SMC-17, 741-752.

Saaty, T. L. *An Eigenvalue Allocation Model for Prioritization and Planning*. Energy Management and Policy Center, University of Pennsylvania, 1972.

Saaty, T. L. "A Scaling Method for Priorities in Hierarchical Structures", *Journal of Mathematical Psychology*, 15 (1977a), 234-281.

Saaty, T. L. "Modeling Unstructured Decision Problems: A Theory of Analytical Hierarchies", *Proceedings of the First International Conference on Mathematical Modeling*, (Conference) (1977b), 69-77.

Saaty, T. L. *The Analytic Hierarchy Process*. New York, NY: McGraw-Hill, 1980.

Saaty, T. L. *Multicriteria Decision Making: The Analytic Hierarchy Process*. Pittsburgh: RWS Publications, 1990.

Saaty, T. L. An exposition of the AHP in reply to the paper 'Remarks on the analytic hierarchy process.' *Management Science*, 1990, 36(3), 259-268.

Shim, J. P. Bibliographical research on the Analytic Hierarchy Process (AHP). *Socio-Economic Planning Sciences*. 1989, 23, 161-167.

Spetzler, C. S. and Stael von Holstein, C.- A.S. Probability Encoding in Decision Analysis. *Management Science*, 1975, 22, 340-358.

Stover, J. G., & Gordon, T. J. This study-impact analysis. In J. Fowles (Eds.), *Handbook of futures research*. Westport, CN: Greenwood, 1978.

Tavana, M., Kennedy, D., and Mohebbi, B. An Applied Study Using the Analytic Hierarchy Process to Translate Common Verbal Phrases to Numerical Probabilities. *Journal of Behavioral Decision Making.* 1997, 10(2), 133-150.

Weiss, E. N. and Rao, V. R. "AHP Design Issues for Large-Scale Systems," *Decision Sciences*, 18 (1987), 43-61.

Zahedi, F. "The Analytical Hierarchy Process--A Survey of the Method and Its Applications", *Interfaces*, 16 (1986), 96-108.

TABLE-1: MISSION ARCHITECTURE FACTORS ALONG WITH THEIR PERCEIVED WEIGHTS AND IMPACT

FACTOR	IMPACT	WEIGHT
1. Earth Vicinity/Departure Operations (EV): LUT clear through Trans-Mars Injections		0.111
EV1: Possibility of TMI miss due to problems with vehicles.	-1	0.066
EV2: Possibility of loss of vehicle due to problems with TMI.	-1	0.130
EV3: Possibility of loss of crew due to problem with TMI.	-1	0.430
EV4: Availability of Post-TMI Earth-return abort options.	+1	0.225
EV5: Availability of existing resources for full operations support for all exploration vehicles during Near Earth	+1	0.088
EV6: Possibility of unplanned shuttle mission to fix problem on MTV.	-1	0.061
2. Mars Transfer Operations (MT): Burnout of the TMI maneuver until x hours before Mars Orbital		0.084
MT1: Possibility of need to perform non-surface contingency EVA (Challenging EVA suit design implications –	-1	0.478
.MT2: Probability of adequate in-situ crew skill development (Computer-based proficiency training and failure	+1	0.186
MT3: Ability to support crew activities (physical and mental health maintenance, warning of and protection from	+1	0.094
MT4: Ability of the crew/vehicle to resolve serious systems problems without the help of the MCC.	+1	0.186
MT5: Possibility of Art. Gravity not being used (no spin-up), resulting in deconditioned crew.	-1	0.056
3. Mars Arrival Operations (MA): MOI minus x hours through the post landing, Crew Adaptation Phase		0.190
MA1: Possibility of errors in the post-insertion orbit plane or altitude.	-1	0.110
MA2: Possibility of an Extended Mars Vicinity Phase.	-1	0.124
MA3: Possibility of errors in aerocapture leading to loss of Crew.	-1	0.402
MA4: Possibility of NO GO for Surface descent.	-1	0.051
MA5: Possibility of crew having a need to perform strenuous activities during CAP.	-1	0.077
MA6: Possibility of injury to crew during CAP.	-1	0.143
MA7: Possibility of descent problem to cause crew to abort back to Mars Orbit.	-1	0.094
4. Planetary Surface Operations (PS): End of CAP to the initiation of the Surface Ascent Terminal		0.149
PS1: Possibility of needing contingency surface EVA to restore ascent capability.	-1	0.159
PS2: Possibility of crew stranded on Mars.	-1	0.437
PS3: Possibility of bad weather or other anomaly which could delay ascent, and even require extra EVAs to return	-1	0.131
PS4: Possibility of early surface mission termination and ascent to Mars orbit.	-1	0.091
PS5: Ability to meet surface mission constraints and schedule.	+1	0.078
PS6: Ability to meet Go/No-Go criteria for EVA.	+1	0.103
5. Mars Vicinity/Departure Operations (MV): The initiation of the SATC through the Trans-Earth		0.109
MV1: Probability of NO-GO for ascent.	-1	0.277
MV2: Probability of NO-GO for TEI.	-1	0.161
MV3: Possibility of crew stranded in Mars orbit.	-1	0.328
MV4: Possibility of ascent to lower-than-desired orbit, requiring the return vehicle coming to rescue.	-1	0.092
MV5: Possibility of problems with rendez and docking.	-1	0.096
MV6: Possibility of problems with transferring items to return vehicle.	-1	0.045
6. Earth Transfer Operations (ET): Post-TEI to x hours prior to Earth Orbital Insertion		0.127
ET1: Possibility of need to perform non-surface contingency EVA.	-1	0.494
ET2: Crew's ability to meet their physical fitness activities.	1	0.230
ET3: Possibility of Art. Gravity not being used (no spin-up), resulting in deconditioned crew.	-1	0.163
ET4: Possibility of problems with MCCs.	-1	0.113
7. Earth Arrival Operations (EA): Defined as x hours prior to EOI to Crew Egress.		0.229
EA1: Possibility of loss of Payload	-1	0.036
EA2: Possibility of loss of crew during direct entry.	-1	0.308
EA3: Possibility of loss of crew during Earth orbit insertion and Shuttle recovery.	-1	0.308
EA4: Ability to address planetary protection issues.	1	0.122
EA5: Possibility of problem ditching the NTR stage.	-1	0.130
EA6: Possibility of deconditioned crew having trouble during contingency recovery operations.	-1	0.095

TABLE-2: MISSION ARCHITECTURE SCENARIOS ALONG WITH THEIR PROBABILITIES OF OCCURRENCE

FACTOR	SPLIT	COMBO	DUAL
1. Earth Vicinity/Departure Operations (EV)			
EV1	35.71%	45.71%	45.71%
EV2	27.14%	31.43%	24.29%
EV3	17.14%	22.86%	22.86%
EV4	47.14%	38.57%	47.14%
EV5	45.71%	37.14%	38.57%
EV6	24.29%	32.86%	30.00%
2. Mars Transfer Operations (MT)			
MT1	32.42%	41.43%	60.56%
.MT2	78.57%	74.29%	75.71%
MT3	74.29%	74.29%	81.43%
MT4	65.71%	65.71%	65.71%
MT5	71.43%	72.86%	64.29%
3. Mars Arrival Operations (MA)			
MA1	24.29%	25.71%	28.57%
MA2	34.29%	30.00%	31.43%
MA3	37.14%	32.86%	32.86%
MA4	24.29%	25.71%	25.71%
MA5	31.43%	31.43%	32.86%
MA6	25.71%	24.29%	25.71%
MA7	27.14%	21.43%	21.43%
4. Planetary Surface Operations (PS)			
PS1	32.86%	37.14%	41.43%
PS2	12.22%	55.71%	28.57%
PS3	34.29%	37.14%	38.57%
PS4	30.00%	28.57%	35.71%
PS5	52.86%	55.71%	57.14%
PS6	58.57%	54.29%	61.43%
5. Mars Vicinity/Departure Operations (MV)			
MV1	31.43%	30.00%	25.71%
MV2	25.71%	30.00%	31.43%
MV3	25.71%	24.29%	27.14%
MV4	24.29%	24.29%	22.86%
MV5	25.71%	22.86%	37.14%
MV6	30.00%	27.14%	20.00%
6. Earth Transfer Operations (ET)			
ET1	40.00%	44.29%	41.43%
ET2	61.43%	62.86%	60.00%
ET3	55.71%	60.00%	55.71%
ET4	24.29%	27.14%	24.71%
7. Earth Arrival Operations (EA)			
EA1	24.29%	21.43%	18.57%
EA2	22.86%	27.14%	27.14%
EA3	21.43%	31.43%	22.86%
EA4	60.00%	58.57%	68.57%
EA5	28.57%	31.43%	38.57%
EA6	50.00%	42.86%	50.00%
TOTAL SCORE	**-0.124**	**-0.169**	**-0.145**

Section 18 was intentionally omitted

Performance Evaluation and Software Design for

EVA Robotic Assistant Stereo Vision Heads

Daniel DiPaolo
Trinity University
ER4

August 11, 2000

Kenneth Baker
ER4/Robotic Systems Technology Branch
Automation, Robotics, and Simulation Division
Engineering Directorate

Daniel DiPaolo

Ken Baker

Performance Evaluation and Software Design for EVA Robotic Assistant Stereo Vision Heads

Final Report

NASA/ASEE Summer Faculty Fellowship Program – 2000

Johnson Space Center

Prepared By:	Daniel DiPaolo
Academic Rank:	Undergraduate Student
University & Department:	Trinity University Dept. of Engineering Science San Antonio, Texas 78212

NASA / JSC

Directorate:	Engineering
Division:	Automation, Robotics and Simulation
Branch:	Robotic Systems Technology
JSC Colleague:	Kenneth Baker
Date Submitted:	August 11, 2000
Contract Number:	NAG 9-867

ABSTRACT

The purpose of this project was to aid the EVA Robotic Assistant project by evaluating and designing the necessary interfaces for two stereo vision heads – the TracLabs Biclops pan-tilt-verge head, and the Helpmate Zebra pan-tilt-verge head. The first half of the project consisted of designing the necessary software interface so that the other modules of the EVA Robotic Assistant had proper access to all of the functionalities offered by each of the stereovision heads. This half took most of the project time, due to a lack of ready-made CORBA drivers for either of the heads. Once this was overcome, the evaluation stage of the project began. The second half of the project was to take these interfaces and to evaluate each of the stereo vision heads in terms of usefulness to the project. In the key project areas such as stability and reliability, the Zebra pan-tilt-verge head came out on top. However, the Biclops did have many more advantages over the Zebra, such as: lower power consumption, faster communications, and a simpler, cleaner API. Overall, the Biclops pan-tilt-verge head outperformed the Zebra pan-tilt-verge head.

1 Introduction

The broad focus of the ERA[1] project is to provide an astronaut with a mobile assistant during EVA on another planet. The continuing example used for this project is one where the astronaut is a field geologist who is studying the surface of the planet, and this is what the project is focused on providing – a robot that can perform the duties necessary to assist a geologist on another planet. Very few assumptions are made about the planet by this project. Every other possibility has to be taken into consideration in the design of this robot. One of the more distinct and more likely possibilities is that the design produced by this project may someday produce an actual robotic assistant for an astronaut who must traverse the Martian surface. With this in mind, one must consider the rocky and unpredictable terrain of the Martian surface. Normally, this would suggest that a robot with a suspension system would behoove the project. However, before this was taken into consideration, the testbed robot was already purchased, and it in fact had *no suspension* at all. Also, it had been decided that a stereo vision system was going to be used as a key part in the guidance system of the robot. Of course, driving a robot with no suspension over rocky terrain does a great deal of damage to the viability of a stereo vision system because the gaze of the robot would constantly shift as a result of the rocky terrain.

That is where this project comes in. In conjunction with the stabilization and attitude prediction project of Dr. Kevin Nickels, the aim of this project was to help cancel out the negative effects of a non-smooth terrain on the performance of the stereo vision guidance system. To do so would require a high-performance pan-tilt-verge (PTV) head that could communicate with all of the other modules of the ERA project. However, the project already had two heads as candidates for use on the testbed robot – one was the Traclabs Biclops PTV head that was already being used as the development platform for our stereo tracking developer, Eric Huber, who had helped develop the head; the other was the Helpmate Zebra head which had been used in previous stereo tracking projects and, as such, already had some driver code written for it that we could use. However, neither of the heads had been field tested on the testbed robot while the stereo vision

[1] ERA = EVA Robotic Assistant

tracker was operating. So, before settling on one platform or another, an evaluation was necessary.

2 The Two PTV Heads

2.1 Traclabs' Biclops

The Traclabs Biclops PTV head was brought to the project by our stereo tracking developer, Eric Huber, who helped design the Biclops head before this project. Actually, the Biclops used for this project is one of the first functional prototypes for the design. The Biclops is a much smaller head than the Zebra, having dimensions of 155mm high by 160mm wide by 101mm long, and having a mass of 1.1kg without cameras attached. It uses a relatively standard cabling interface as well. The input into the Biclops PTV is a simple RS-232 serial port. However, within the Biclops head, there are two different voltages necessary for operation instead of the RS-232 standard of simply 7.5V and ground. The motors require a 24V power supply, and the RS-232 logic requires a 7.5V source. So, the serial connector takes input from a special power adapter which takes the normal serial connection from the computer *and* a 24V DC input. The other power requirement is that the Biclops may draw as much as 1A (ampere), with the motor pulling a maximum of 750mA and the logic circuitry pulling a constant 300mA.

The operation of the Biclops PTV head is fairly basic. The pan and tilt axis are driven by belts that are each controlled by an independent (not coupled) servo motor. The verge axis uses a metal spring which is drawn in and out by a motor-driven screw threaded through it. Each of these motors has an accompanying encoder that it uses to determine its position, velocity, and acceleration as well. The motors are independently controlled, with each having a PIC Servo Controller dedicated to it. The PIC controllers are in turn commanded by the Biclops firmware which was designed by Traclabs. Traclabs exposes a basic API (applications programming interface) for creation of drivers so that the Traclabs firmware in the Biclops can appropriately handle commands received via serial communication. So, once the software drivers are written, all one needs is a basic client program that takes advantages of these drivers and allows the user to command the Biclops head.

2.2 Helpmate's Zebra

The Helpmate Zebra PTV head had been used by the stereo image tracking team in previous projects, and because of the team's familiarity with the head and all of its capabilities (as well as the several Zebra heads available for this project), this PTV head was also selected as a candidate for the ERA project. This head is physically much larger than the Biclops head, and it is also shaped much differently. The Zebra PTV head consists of a tall base topped with a wide head. The base dimensions are: 3.875in. long by 2.25in. wide by 9.5in. high[2]. The head itself is 8.75in. wide, however, greatly adding to the dimensions of this PTV head. The communications and power scheme is similar to the Biclops. The Zebra communicates via a standard RS-232 serial port like the Biclops, and also like the Biclops, requires special power conversions to supply both logic power and motor power to the PTV head. Instead of a small inline connector adapter (like the Biclops), the Zebra instead has a controller box that, while greatly increasing the necessary space to operate the PTV head, affords a few other options as well. Under normal operation, the controller box requires two things to properly operate the PTV head – that motor power be enabled by the push of a button on startup, and that an emergency stop switch be plugged in. Both of these can be overridden, however, so as to automate the process much more. The controller box does very similar power conversions as well. It supplies the motors with 24V DC, and the logic circuitry with 5V DC (regulated). The current requirement is a bit steeper for the Zebra PTV head, 1.5A for the logic power and up to 6A for motor power. However, with this added power, the motors are given more torque, allowing faster movement of the head. The added power, however, has not proven either necessary or useful in our testing. For the majority of the functions required of the PTV head on this project (fixed gaze, slow motion tracking), the added velocity of the Zebra proves neither to be necessary or useful.

The Zebra head operates in a manner that is also very similar to the Biclops PTV head. The main difference between the two is that the Zebra has a pair of coupled axes – the pan and tilt axes. This means that any motion in the pan axis will cause a corresponding motion on the tilt axis. This has to be compensated for in the control of the PTV head. However, aside from that, the hardware operates essentially the same way

[2] *This is the total height, not just the base height*

as the Biclops does, with motors for each axis and encoders for each motor. Helpmate also gave a basic API for their Zebra PTV head for us to use, along with many little code snippets and examples. Utilizing those pieces of code, one can create the appropriate drivers to drive the head over the simple RS-232 serial port connection.

3 The Implementations

As mentioned in the abstract, the majority of time spent on this project was on the design and programming of the software for each of the two PTV heads. The ERA project requires that many other software modules of the project be able to communicate with the PTV head as well as one another, and to do such things, it was decided that using CORBA (Common Object Request Broker Architecture, a communications protocol) on the two Linux computers mounted on the robot was to be the way of interfacing all of the components together. So, it was necessary to design drivers for the heads that would be able to receive CORBA calls, interpret them appropriately and then issue the necessary calls to the PTV head in the head's own language via Linux serial port commands. Also, one of the requests of the project is that there be a standard PTV CORBA API so that everyone would be able to communicate with *either* of the PTV heads in the same fashion. So, to any CORBA clients, it is transparent as to which PTV head you are actually communicating.

3.1 CORBA Basics

CORBA is the proverbial "glue" that unifies all of the modules of this project into a cohesive unit. Using CORBA and its services, the ERA project can successfully run a number of different servers that interact with one another simultaneously and even on different computers running different operating systems. CORBA is simply another layer of abstraction that sits on top of other layers that handle things that are normally important to servers: initialization, requests, exceptions, etc. Any CORBA interface is well-defined by the IDL (Interface Definition Language) file of that interface. So, to establish the transparency described above, it was necessary to establish a standard set of commands that could be done by both PTV heads and to create a standard IDL.

However, since the other end of the server (that had to communicate with the PTV via serial commands) was *necessarily* different between the two heads due to the different APIs of each, the layers underneath the CORBA IDL had to be customized.

3.2 The Biclops Implementation

The Biclops PTV head was developed under a Windows environment, and with a Windows environment in mind. As such, the only code available for the Biclops head was not Linux compliant (due to uses of MFC (Microsoft Foundation Classes) functions among other things). However, the Windows code was two-layered in nature, using two separate C++ classes to describe a Biclops object. The first class was a simple *Serial* class that provided nothing more than a few simple functionalities for serial connections such as: opening/closing a port, setting port parameters, sending/receiving data, etc. This class was mostly unusable due to the heavy use of MFC function calls. The second class was a more general *SerialBiclops* class which contained an instance of the *Serial* class, as well as general calls to actually drive the motion of the PTV head. This code was relatively portable, as many of the calls were either using the *Serial* pointer class member or doing other simple operations. What needed to be done to get this working was to essentially use existing serial code from the Zebra PTV head (whose development began before the Biclops's development), and to turn it into a reasonable facsimile of the original *Serial* class that was implemented in the Windows NT code.

3.3 The Zebra Implementation

The Zebra head was not designed with a particular computing platform in mind. The documentation for the Zebra provides fairly portable (though very basic) code as a jumping off point for the coding of a driver for the PTV head. However, the portability of the code often encumbered it with many things that were unnecessary to the project. For example, the code provided by Helpmate is mostly written in C instead of C++. It is definitely more portable in that respect but it is not nearly as easy to work with as C++ which is object oriented. It also makes using that code to create a CORBA client even more difficult because the interface system of CORBA is made much simpler when dealing with objects defined by classes instead of dealing with a collection of functions.

However, the code for the Zebra was still divided in a very similar fashion. Most of the low-level serial code was written to be independent of the code that actually runs the head itself. It would not be a great undertaking to rewrite the code into C++ form, but there was not enough time to do so.

3.4 Comparison

Although the Biclops was actually developed with a different operating system in mind, implementing its functionalities into a Linux CORBA server was actually significantly simpler than it was for the Zebra. The usage of C++ in the code provided by Traclabs greatly helped the development of the Biclops driver. By separating the serial code and the Biclops-specific code, it was easy to overcome the Windows-specific serial code and to plug in working Linux serial functions. With the Zebra, although the code was already designed to work on Linux, the code that was provided was all very low-level code with no higher-level interface, and therefore required much more design for that driver than the Biclops did, as Traclabs provided code for some of the simpler and more useful functions like moving.

4 Performance Evaluation

Once the drivers for each of the heads was completed and ready to be used on the ERA robot, the actual performance evaluation began. Keeping in mind that the purpose of these PTV heads is to be used for the stereo tracking software that is currently being developed for this project, certain things are of greater importance in terms of performance. The main traits that were tested were:

1. Response time
2. Smoothness of move

4.1 Response Time

Response time is always an important issue in performance evaluations, but even more so with this project because of the nature of stereo tracking. Stereo tracking depends upon the ability to know where the object of interest is through correlations made by looking at the video provided by the cameras mounted on the PTV head. The tracker then sends commands telling the head where to look next in order to try to center the object of interest in the video (that is, in the PTV's gaze). However, without an adequate response time from the PTV head, the object of interest may go out of frame. Once the object of interest is out of frame, it is impossible to track it, and the only way tracking can continue is through an exhaustive search of the area in an attempt to reacquire the object.

To gauge head response time, we will record the amount of time between the issuing of a move command and the time visible movement is seen. The easiest and most reliable way to record the latter is to have a utility analyzing the video stream which will record the time at which it shifts significantly enough. However, since that utility is not available at the time of this writing, we had to rely upon a keypress from someone watching the head.

The setup for the tests was:

- PTV head – mounted on the robot, connected to serial port on robot computer
- PTV server – running on robot computer
- PTV client – running remotely, across a wireless network connection, on a PC

As it turns out, even with a wireless network connection setup, the heads respond much more quickly than a person can react and press a key. The fastest response that was measured was approximately 200ms for each head. So, 200ms was essentially the resolution of our test, but the response time of each head was better than our resolution could measure.

4.2 Smoothness of move

For the purpose of this project, a smooth move is a very big plus. With smoother moves, tracking is much easier and much more efficient. This is because with the way the stereo tracking is done is that it likes to begin searching for the object of interest at or near the last known position of the object. The more accurate the PTV head is at moving to the goal and not overshooting it, the more likely it is that tracking will be successful.

The test designed to measure the smoothness of each head's moves was that each head was to be set to move at a fairly high speed, and that it would make a significant move at that speed while we log the position of the head and then analyze it – computing overshoot and settling time for each, and then comparing them.

The setup for these tests was identical to the response time tests:

- PTV head – mounted on the robot, connected to serial port on robot computer
- PTV server – running on robot computer
- PTV client – running remotely, across a wireless network connection, on a PC

As mentioned in the description of the test, this test was supposed to use a high-speed move. However, the Zebra server was not to the point where the velocities were easily modified, so we had to use the default velocities, giving a slower move, and hence, giving it an advantage in this test because it is less likely to overshoot at a slower speed.

For this test, only the pan and tilt axes were measured for overshoot for two reasons. First, we aren't using vergence, and second, because the movements in vergence are generally so small that any overshoot is almost trivial. The move performed was a simultaneous 45 degree move in both the pan and tilt axes, with the Biclops moving at its maximum velocity on both axes and the Zebra moving at its default velocities (due to the problems mentioned above).

The results of the test confirmed the hypothesis for the Zebra head. There was no measurable overshoot in its movement at the sampling rate we used – the maximum for that head, about 100Hz (this value was obtained through experimentation). The Biclops, of course, did have some overshoot. It overshot on the pan axis by 0.6073° and on the tilt axis by 0.4183°, settling to the eventual goal in 1.24s and 2.02s, respectively. These results are fairly good. The overshoot in the pan axis only translates to 0.032m (3.2cm) shift at a verge depth of 3m, the amount we are currently using, and the tilt overshoot only translates to 0.022m (2.2cm) shift at that verge depth. Within those settling times, the tracking software can more than make up for that small a shift.

So, the Zebra's results don't really say much, since how the move was relatively slow. The Biclops results, however, confirm that it performs relatively well, with an acceptable amount of overshoot.

5 Conclusions

The first objective of the program, to design a common software interface for the two stereo vision heads, was very successful. It has proven to be fairly reliable in the constant testing it has undergone, and has proven to be a complete enough system for use in the upcoming field tests in Arizona.

The second objective of the program, the evaluation of each of the stereo vision heads using the common software interface, was quite telling. The performance evaluation tests of each head didn't reveal much, as both performed fairly equally. The Zebra head's best quality was its superior reliability, with its track record of zero failures sharply contrasting the three Biclops failures encountered during the design and testing. However, the other evaluations such as considerations of power, size, and API showed the Biclops to be a clear winner. Its lower power consumption (without reducing the responsiveness to a substandard level), more compact size, and much more amenable API put the Biclops ahead of the Zebra in just about every other category. As a result, the Biclops has been chosen by the ERA project team as the head to be used for the field tests in Arizona.

Development of a Poincaré Software to Predict Arrythmias

Samer Maaliki, M.S.
University of Miami

August 14, 2000

Todd Schlegel, M.D.
SD3
Medical Sciences
Space and Life Science

Todd T. Schlegel, MD

Samer Maaliki, M.S.

Todd Schleggel, M.D.

Development of a Poincaré Software to Predict Arrythmias

Final Report

NASA/ASEE Summer Faculty Fellowship Program – 2000

Johnson Space Center

Prepared By:	Samer Maaliki, M.S.
University &Department:	University of Miami Biomedical Engineering Coral Gables, Florida 33146

NASA/JSC

Directorate:	Space and Life Science
Division:	Medical Sciences
Branch:	SD3
JSC Colleague:	Todd Schlegel, M.D.
Date Submitted:	August 11, 2000
Contract Number:	NAG 9-867

Abstract

The most distressing types of heart malfunction occur because of an abnormal rhythm of the heart. Cardiac arrythmias can be caused by abnormal rhythmicity of the pacemaker, electrolyte disturbances, blockage of the transmission of the electric impulse through the heart, and other abnormalities. There is strong evidence that space flight is associated with decreased cardiac electrical stability that may pose a life threatening risk to astronauts. For example, during the Skylab missions, a crewmember had a five beat run of ventricular tachycardia during lower body negative pressure. Also, analysis of nine 24-hour Holter monitor recordings obtained during long term spaceflight on Mir revealed one 14-beat run of ventricular tachycardia. A Mir cosmonaut was replaced in 1986 because of cardiac dysrhythmias. Most recently, in July of 1997, a Mir commander was unable to participate in the Spektr module repair due to complaints of an irregular heart rhythm. Despite these examples, possible mechanisms of arrhythmias and countermeasure strategies have barely been addressed.

The Poincaré method has been proposed as a technique that might potentially predict life-threatening arrhythmias before they occur. According to this method, each RR interval obtained from an EKG recording is plotted sequentially vs. the previous RR interval. Several studies using the method have demonstrated a strong correlation between the shape of the Poincaré plot and ventricular arrhythmia. Our purpose was to develop an automated software program that detects the "R" peaks from an EKG recording while simultaneously displaying the Poincaré plot and other related parameters.

INTRODUCTION

The pumping action of a heart is regulated by a conduction system that spreads electrical impulses from the sinoatrial node to the rest of the heart. The signal generated in the sinoatrial node first disperses through the atrial tissues causing the atria to contract. The signal then moves through the Purkinje fibers into the ventricular septum. Finally, the signal is conducted to the outer ventricular walls causing the ventricles to contract. In a normal heart, this process is very organized. However, in a diseased heart, the conduction system can be damaged. The degree of irregularity in the conduction of the impulse depends greatly on the extent and location of the disease in the heart.

Electrical potentials that originate in the heart spread out into neighboring tissues. Electrodes that are placed on the chest opposite to the heart can record these potentials. Such a recording is known as an electrocardiogram (EKG). A sample EKG is shown in Figure 1. There are three distinct peaks in an EKG signal: the P wave, the QRS complex, and the T wave. Electrical potentials, generated when the atria depolarize at the onset of atrial contraction, cause the P wave. The QRS complex is caused by potentials generated by ventricular depolarization before contraction. When the ventricle recovers from depolarization, the T wave is generated.

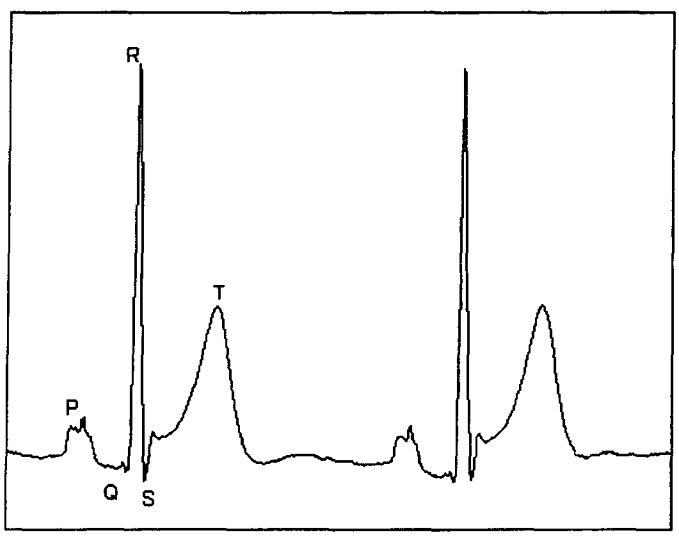

Figure 1. A Sample EKG Showing the Characteristic P, Q, R, S and T Waves.

The P-Q or P-R interval is the amount of time it takes from the onset of atrial contraction to the onset of ventricular contraction. The Q-T interval is the time of ventricular contraction. The time between successive QRS complexes is the time it takes for a complete heart beat. This is also known as the RR interval.

By analyzing the peaks and intervals in an EKG, clinicians can determine whether the heart is functioning properly or if it is diseased. Such analysis also provides a good way of determining the type of cardiac disease that may be present. Recently, there has been an increasing interest in one method that relies on the RR interval. This method, called the Poincaré plot (2,5,12), is simply a plot of the current RR interval (RR_{n+1}) vs. the previous RR interval (RR_n). If A, B, and C are consecutive RR intervals, their Poincaré plot consists of two points with the coordinates (A,B) and (B,C). This is shown in Figure 2. When EKG recordings are of longer duration (i.e., minutes to hours), the Poincaré method provides a visual way of analyzing overall heart rate variability (HRV) (5,8). When the RR intervals are very similar, i.e., low standard deviation, the points in the Poincaré plot form a tight pattern. When the RR intervals vary a lot from beat to beat, i.e., high standard deviation, the points on the Poincaré plot are spread out. Since several studies suggest that both heart failure and impending arrhythmias can be associated with a decreased HRV (3,4,7), the Poincaré plot provides a useful diagnostic tool.

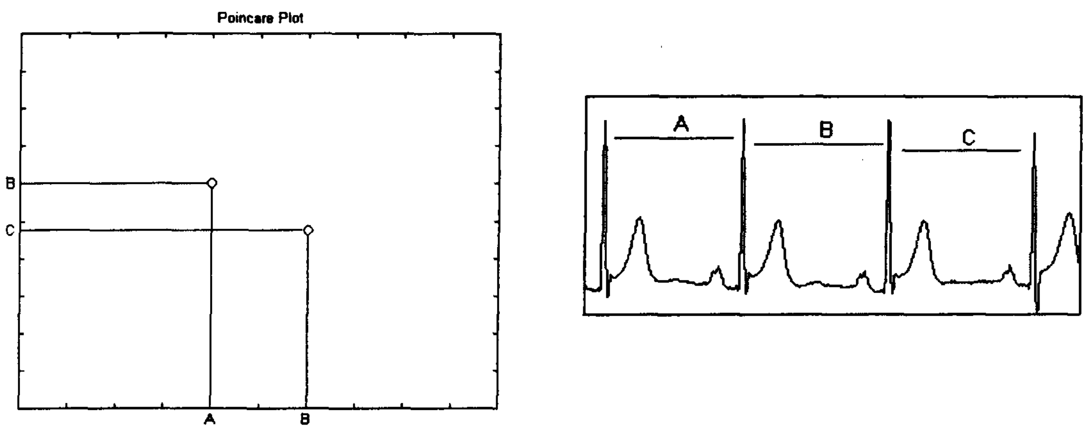

Figure 2. Poincaré Plot of Three Consecutive RR Intervals

Healthy subjects usually have a so called "comet" shaped (13) 24-hour Poincaré plot (Figure 3). The range of RR intervals is usually between 500 to 1000 ms. On the other hand, 24-hour Poincaré plots obtained from patients with heart failure may exhibit three different abnormal patterns. The most common one is the "cigar" shape. This shape is attributed to little or no increase in R-R variability at lower heart rates. The second Poincaré plot pattern from unhealthy subjects is the "fan" shape. Both of the cigar and fan patterns have a much lower RR interval range. The third pattern is a "complex" pattern that is a combination of the cigar and fan patterns that are spread out over the entire plot.

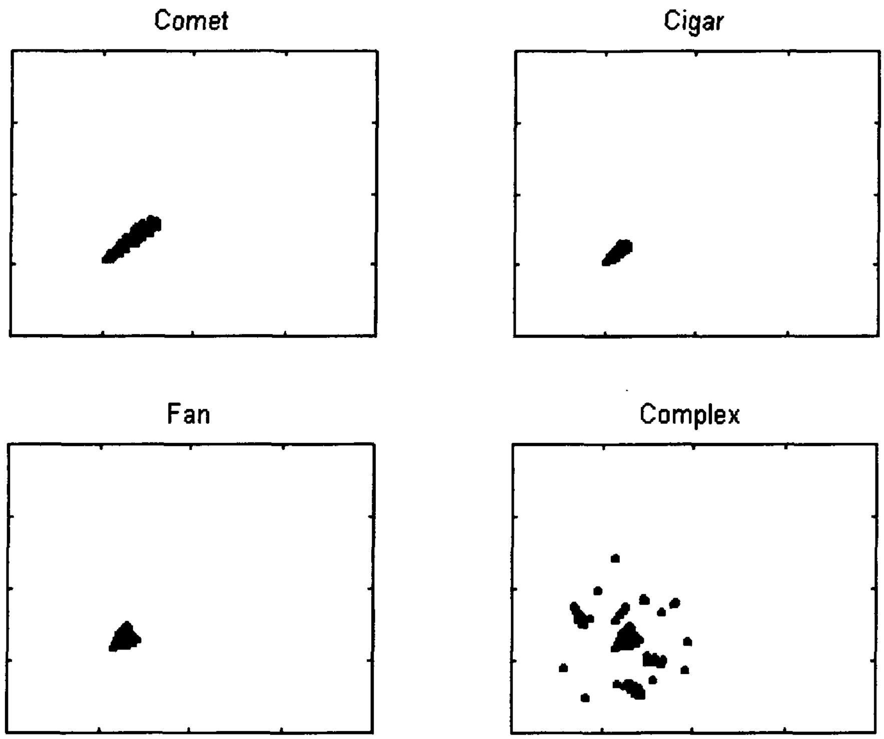

Figure 3. Different Patterns of a 24-hour Poincaré Plot.

METHODS

The first step in generating a Poincaré plot is to acquire the locations of the R-peaks in the signal. To accomplish this goal, an R-wave detector was developed that functions as follows: First, the Fast Fourier Transform (FFT) of the EKG signal is determined. Next, the lower frequencies of the Fourier spectrum are filtered out. Figure 4 shows the Fourier spectrum of an EKG signal before and after filtering. By filtering the spectrum, the slower components of the EKG signal are removed. Finally, the Inverse Fast Fourier Transform (IFFT) is computed from the filtered spectrum, and a modified version of the EKG signal is obtained. The only significant peaks in this modified signal are the R waves (Figure 5).

The locations of the R peaks were determined using a custom made peak detector. This detector first divides the signal up into different windows. For each window it then computes the maximum. Finally, the detector scans through the maxima to determine which windows have a maximum that has a higher value than the two maxima in the surrounding windows. The location of that maximum in the EKG signal is then determined and saved as an R peak.

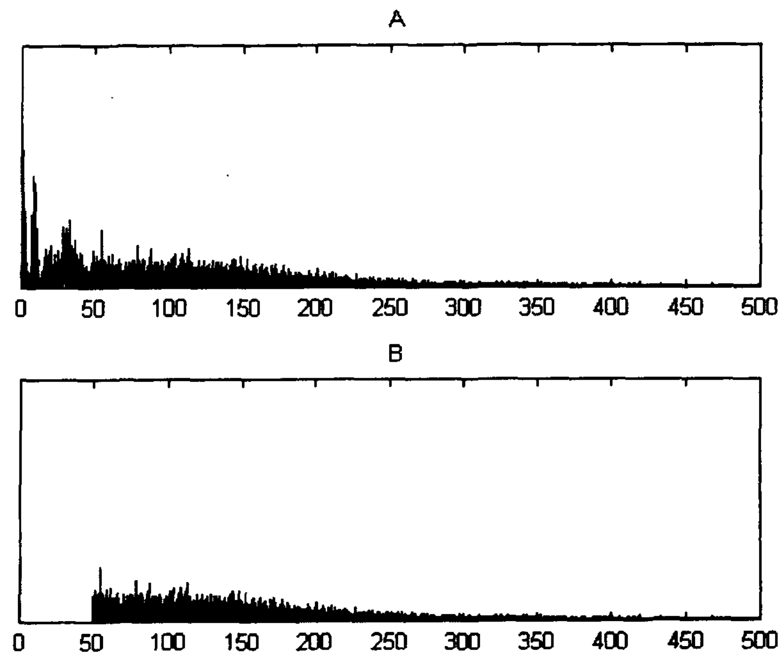

Figure 4. (A) FFT of EKG Signal Before Filtering. (B) FFT After Filtering.

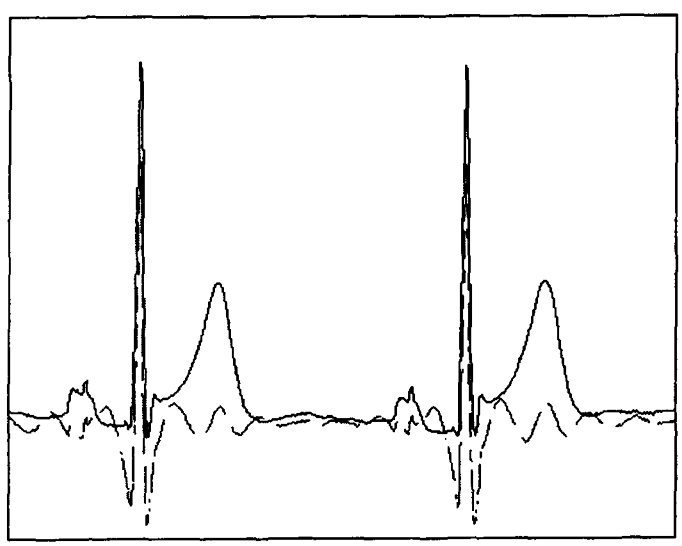

Figure 5. The EKG Signal Before (solid) and After (dashed) Filtering.

From the locations of the R peaks, the RR intervals can then be calculated. Most of the important information regarding HRV can be obtained from the RR intervals. The following is a short list of some of these variables and their descriptions (9).

RRmean	Average of RR intervals
RRstd	Standard deviation of RR intervals
ΔRR	Difference between elements of RR_{n+1} and RR_n
ΔRRstd	Standard deviation of ΔRR
RR_nstd	Standard deviation of RR_n
RR_{n+1}std	Standard deviation of RR_{n+1}
nRR_nstd	RR_nstd / RRstd
nRR_{n+1}std	RR_{n+1}std / RRstd
NN50	Sum of elements of ΔRR that are less than 50 ms
pNN50	NN50 divided by length of ΔRR

By plotting RR_{n+1} vs. RR_n, a Poincaré plot is generated. Once the Poincaré plot is acquired, an ellipse (3) is fitted to the data (Figure 6). To produce such an ellipse, the confidence interval method was used. Knowing the means (μ_1,μ_2), standard deviations (σ_1,σ_2) and the correlation coefficient (ρ) of RR_n and RR_{n+1}, one can define an ellipse that encloses a desired percentage of the data. The equation for such an ellipse is the following:

$$\frac{1}{2(1-\rho^2)}\left(\frac{(x-\mu_1)^2}{\sigma_1^2}-\frac{2\rho(x-\mu_1)(y-\mu_2)}{\sigma_1\sigma_2}+\frac{(y-\mu_2)^2}{\sigma_2^2}\right)=-\log\left(\frac{n}{100}\right), \qquad \text{Eq. 1}$$

where n is the desired percentage of data to be enclosed within the ellipse. In Equation 1, one can assume that RRn and RRn+1 have the same mean ($\mu_1 = \mu_2 = \mu$) and standard deviations ($\sigma_1 = \sigma_2 = \sigma$), which simplifies the equation into the following:

$$\frac{1}{2\sigma^2(1-\rho^2)}\left((x-\mu)^2-2\rho(x-\mu)(y-\mu)+(y-\mu)^2\right)=-\log\left(\frac{n}{100}\right). \qquad \text{Eq. 2}$$

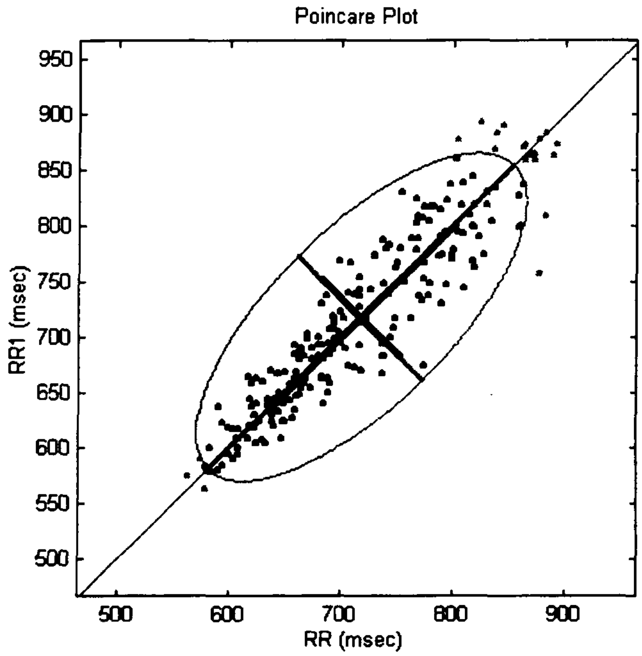

Figure 6. A Poincaré Plot with its Ellipse and Axes.

The only variables in this equation are x and y. Therefore, by substituting for either of these variables, the other variable can be determined. Using x and y the ellipse can be superimposed on the Poincaré plot. The major and minor axes of the ellipse can then be determined. These axes are directly proportional to RR_nstd and RR_{n+1}std, respectively.

The histograms of RR and ΔRR can also be determined (Figure 7). These histograms are then analyzed to calculate the HRV triangular index and the triangular index of RR (TIRR) (7). The HRV triangular index is defined as the number of RR intervals divided by the maximum of the RR histogram. TIRR is the base (B) of the triangule fit to the histogram. To find B, the area under the histogram is first computed. The area of a triangle is the product of B and the height (H), divided by 2. If H is equal to the maximum of the histogram, then B can be calculated from the area of the triangle. To plot the triangular fit, the ratio of the area of the histogram before the maximum to the area of the histogram after the maximum is first calculated. The base is then positioned so that the ratio of its length before the maximum to its length after the maximum is equal to the ratio of the areas.

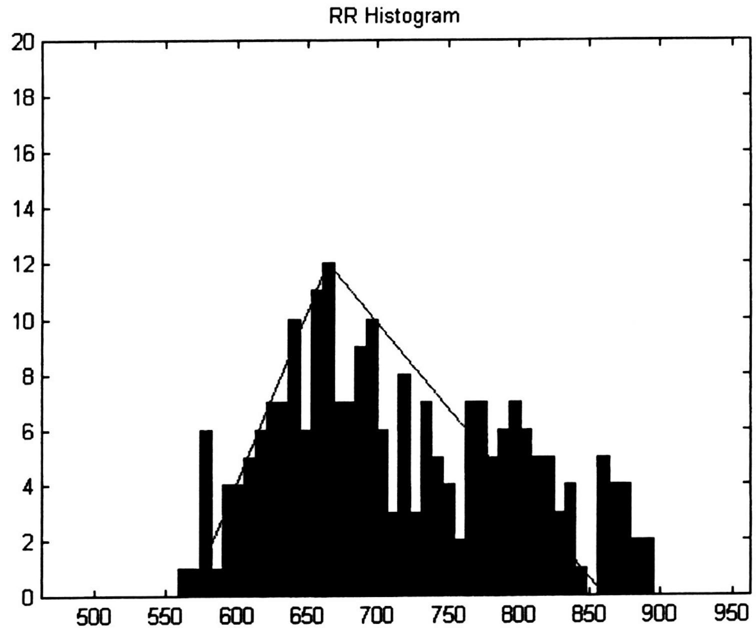

Figure 7. RR Histogram Showing the Triangular Fit.

RESULTS

Software Package

To carry out these methods and calculations in an automatic an easy manner, a graphical user interface package was developed using Matlab. This package allows the user to open several formats of EKG signals. The electrocardiogram is immediately displayed when the data file is successfully opened. The user can then analyze the data using several options in the package. The first option is detecting the R peaks in the signal. When this method is called from the menu, a window like that shown in Figure 8, is opened. In this window, there is a plot of the EKG signal with the R-wave peaks marked by asterisks, a slider to scroll through the signal, an edit box to change the size of the window used to detect the R peak, and a [Recalculate] button that recalculates the peaks according to the window size that is defined in the edit box.

The second option in this package is the Poincaré analysis. When this menu item is chosen, the Poincaré plot is displayed along with the ellipse that fits a default percentage of data. This plot also shows the major and minor axes. The third option is to plot the histograms of RR and ΔRR.

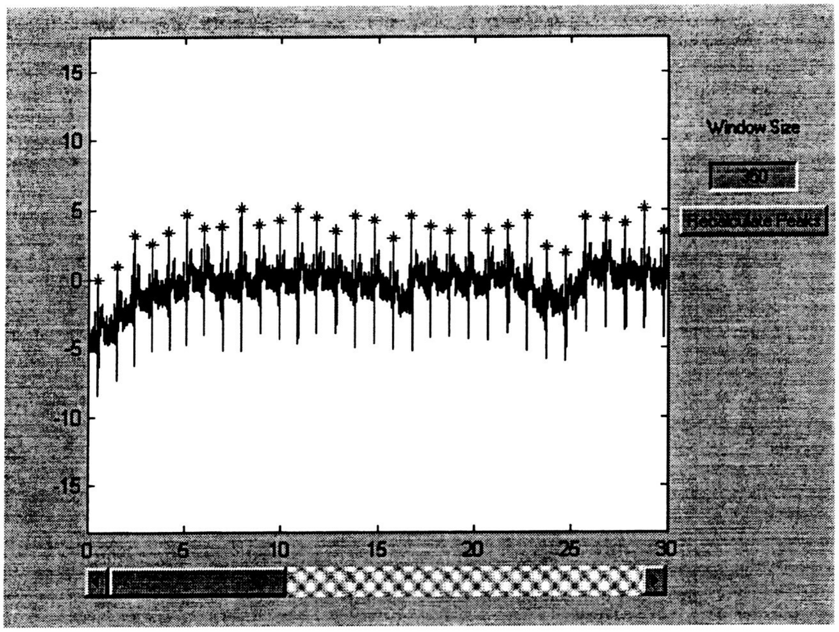

Figure 8. The R Detector Window

It is also possible to generate a 3D Poincaré plot (10,11). In such a plot (Figure 9), each point's coordinates are (RR_{n+2}, RR_{n+1}, RR_n). Once the analysis is finished, the user can print out a list of all the variables associated with the methods described in this paper.

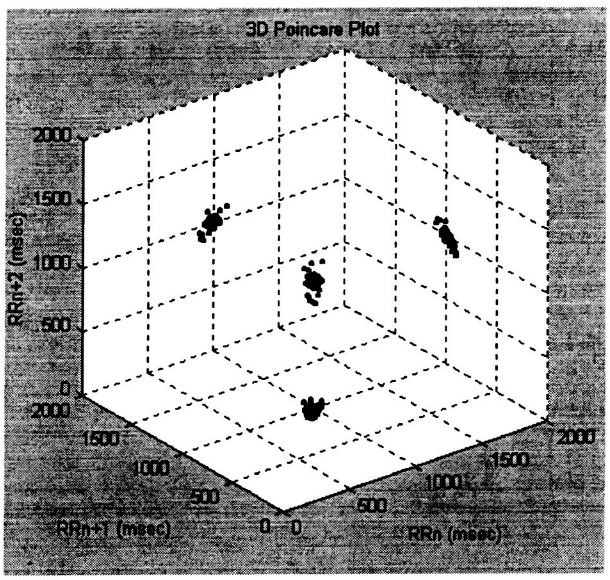

Figure 9. 3D Poincaré Plot Example

Data Analysis

Two EKG signals obtained from a healthy and non-healthy subject were analyzed to obtain the Poincaré plots shown in Figure 10. There is a remarkable difference between the healthy subject's Poincaré plot and that of the unhealthy subject. This shows that the methods integrated into this software provide reliable data.

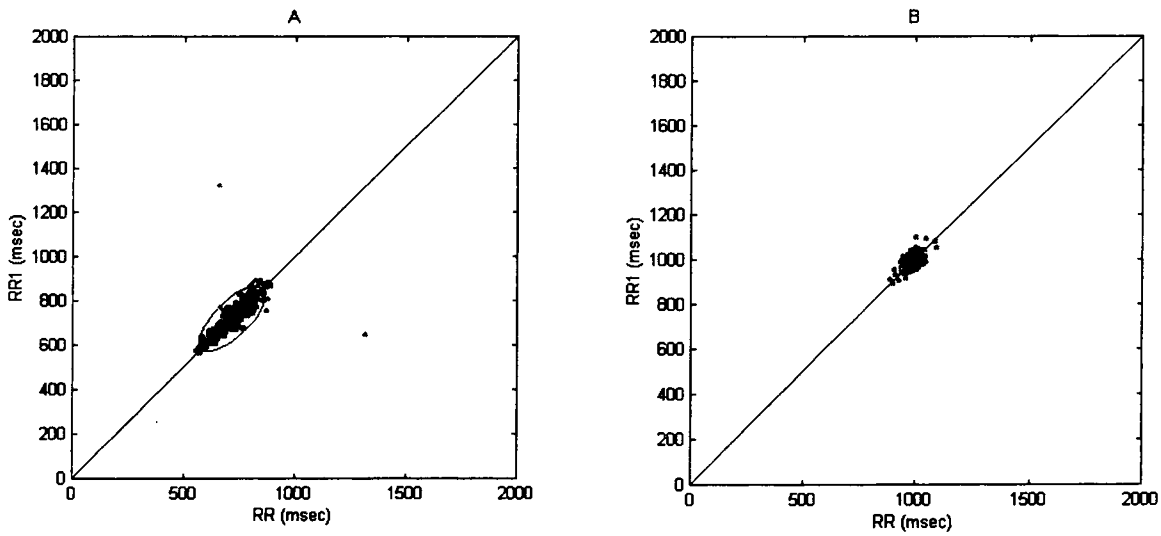

Figure 10. Poincaré Plots From a (A) Healthy Subject and a Subject with Heart Disease

CONCLUSION

In this project, the Poincaré method of analyzing HRV was automated. The software package that was developed allows the user to open an EKG file and process the data to obtain a Poincaré plot, histograms of RR intervals, and variables that can help physicians determine whether the patient's heart is functioning normally or abnormally.

The Poincaré package developed in this project can only be used in a Matlab compiler. Therefore, for further research, the methods involved in this package should be integrated into a standalone software package. The R wave detector is also a very rudimentary one. A more sophisticated R wave detector where no user input is needed would automate the software even further. Also, this package works offline only. It would be a greater asset for physicians to be able to monitor the Poincaré plot in real time.

Several other analysis tools can be added to this package to enhance its diagnostic use. The approximate entropy (ApEn) method (1,6) for assessing complexity of the EKG signal provides a sensitive marker for changes in HRV. The power spectral density (PSD) of RR intervals can also be added to this package. PSD (2,9) is used to study the sympathetic and parasympathetic neural control to the heart.

REFERENCES

1. Goldberger, A. L., J E. Meitus, D. R. Rigney, M. L. Wood and S. M. Fortney "Effects of head-down bed rest on complex heart rate variability: response to LBNP testing." *J. Appl. Physiol.* 1994; 77(6): 2863-2869.

2. Hayano, J., H. Takahashi, T. Toriyama, S. Mukai, A. Okada, S. Sakata, A. Yamada, N. Ohte and H. Kawahara "Prognostic value of heart rate variability during long-term follow-up in chronic haemodialysis patients with end-stage renal disease." *Nephrol. Dial. Transplant.* 1999; 14(6): 1480-1488.

3. Huikuri, H. V., T. S. Seppänen, M. J. Koistinen, K.E. Juhani Airaksinen, M.J. Ikäheimo, A. Castellanos and R. J. Myerburg "Abnormalities in beat-to-beat dynamics of heart rate before the spontaneous onset of life-threatening ventricular tachyarrhytmias in patients with prior myocardial infarction." *Circulation* 1996; 93: 1836-1844.

4. Kamen, P. W. and A. M. Tonkin "Application of the Poincaré plot to heart rate variability: a new measure of functional status in heart failure." *Aust. NZ J. Med.* 1995; 25: 18-26.

5. Kamen, P. W., H. Krum and A. M. Tonkin "Poincare plot of heart rate variability allows quantitative disply of parasympathetic nervous activity in humans." *Clinical Science* 1996; 91: 201-208.

6. Kaplan, D. T., M. I. Furman, S. M. Pincus, S. M. Ryan, L. A. Lipsitz, and A. L. Goldberger "Aging and the complexity of cardiovascular dynamics." *Biophys. J.* 1991; 59: 945-949.

7. Malik, Marek "Heart rate variability: standards of measurement, physiological interpretation, and clinical use." *Eur. Heart J.* 1996; 17: 354-381.

8. Otzenberger, H., C. Gronfier, C. Simon, A. Charloux, J. Ehrhart, F. Piquard and G. Brandenberger "Dynamic heart rate variability: a tool for exploring sympathovagal balance continuously during sleep in men." *Am. J. Physiol.* 1998; 275: H946-H950.

9. Pieper, S. J. and S. C. Hammill "Heart rate variability: Technique and investigational applications in cardiovascular medicine." *Mayo Clin. Proc.* 1995; 70: 955-964.

10. Schmidt, G. and G. E. Morfill "Complexity diagnostics in cardiology: Fundamental considerations." *PACE* 1994; 17: 1174-1177.

11. Schmidt, G. and G. E. Morfill "Complexity diagnostics in cardiology: Methods." *PACE* 1994; 17: 2336-2341.

12. Woo, M. A., W. G. Stevenson, D. K. Moser, H. R. MiddleKauff "Complex heart rate variability and serum norepinephrine levels in patients with advanced heart failure." *J. Am. Coll. Cardiol.* 1994; 23: 565-569.

13. Woo, M. A., W. G. Stevenson, D. K. Moser, R. B. Trelease and R. M. Harper "Patterns of beat-to-beat heart rate variability in advanced heart failure." *Am. Heart J.* 1992; 123: 704-710.

Sections 21 and 22 were intentionally omitted

Interactions of Hydrazine and Blowby Gases

Nancy E. Meagher, Ph.D.
Texas Woman's University
Lyndon B. Johnson Space Center
White Sands Test Facility – RF
August 3, 2000

Regor Saulsberry
Laboratories Office
White Sands Test Facility

Nancy E. Meagher

Nancy E. Meagher

Regor Saulsberry

Regor Saulsberry

Interactions of Hydrazine and Blowby Gases

Final Report
NASA/ASEE Summer Faculty Fellowship Program 2000
Johnson Space Center – White Sands Test Facility

Prepared By:	Nancy E. Meagher, Ph.D.
Academic Rank:	Assistant Professor
University & Department:	Texas Woman's University Department of Chemistry & Physics Denton, Texas 76204

NASA/JSC

Directorate:	White Sands Test Facility
Division:	Laboratories Office
JSC Colleague:	Regor Saulsberry
Date Submitted:	August 3, 2000
Contract Number:	NAG-9-867

ABSTRACT

The interactions between hydrazine and blowby gases from pyrovalves was explored in this research project. Investigating the decomposition chemistry of hydrazine through detailed chemical kinetic modeling is a project started last summer while participating in the Summer Faculty Fellowship program. During the 1999-2000 academic year, the chemical kinetic mechansim for hydrazine decomposition developed while a SFF at NASA's White Sands Test Facility was further revised and validated against the limited experimental data in the literature. This mechanism was then used in assessing the effects of blowby gas species on hydrazine decomposition.

The combustion products introduced into the fuel line by pyrovalve actuation consist primarily of hydrogen gas. Hydrogen is also a product of the decomposition of hydrazine. Additional gaseous chemical species are introduced into the fuel, as well as metals and metal salts that deposit onto the walls of the fuel line. The deposition process is undoubtedly very rapid, and exothermic. Therefore, the major focus of this summer's work was examining the effects of hydrogen presence on hydrazine decomposition, with some representative calculations including the remaining gaseous species found to exist in blowby gases.

Since hydrogen is a product of hydrazine decomposition, all reactions necessary to evaluate its effect on hydrazine decomposition chemistry were in the original mechanism developed. However, the mechanism needed to be considerably expanded to include the reactions of the other gaseous blowby species with hydrazine, all the intermediate species formed in its decomposition, and each other. The expanded mechanism consists of 70 species interacting via a network of 452 reactions.

Calculations with molecular hydrogen introduced into hydrazine gas in an inert bath gas indicate that H_2 presence as an initial reactant in substantial amounts can dramatically impact the decomposition process for hydrazine. The other gaseous blowby species (CO, CO_2, H_2O, CH_4, O_2, and N_2) were found to have little effect compared to the inclusion of hydrogen itself as an initial reagent. This result is undoubtedly due, in part, to the fact that the blowby gas used in these calculations consisted of 94.6% H_2. A more rigorous examination of the behavior of the full detailed mechanism under a variety of conditions was not performed.

INTRODUCTION

Hydrazine decomposition has been the subject of scientific study for a considerable time.[1-10] The final products of hydrazine decomposition change with the temperature at which the decomposition is initiated. N_2H_4 decomposition can be described by the following two reactions:

$$2\ N_2H_4 \rightarrow 2\ NH_3 + N_2 + H_2 \qquad \Delta H_r = -141.3\ \text{kJ/mol}\ N_2H_4 \qquad \text{(R1)}$$

$$N_2H_4 \rightarrow N_2 + 2\ H_2 \qquad \Delta H_r = -95.4\ \text{kJ/mol}\ N_2H_4 \qquad \text{(R2)}$$

Experimentalists have noted that at lower initial temperatures, the decomposition of hydrazine is dominated by R1, while at higher temperatures, the product mixture observed is more accurately represented by R2.

The study of hydrazine decomposition is of basic scientific interest, however, the main reasons for this study are found in the results of research conducted at NASA's White Sands Test Facility (WSTF). The Mars Observer failure review board indicated that propulsion and pyrotechnic systems may have contributed to the loss of the spacecraft.[11] Experiments performed at WSTF revealed that pyrovalve actuation could result in uncontrolled fuel decomposition which fragmented a simulated fuel line.[12-14] These results suggested that a more thorough understanding of the decomposition chemistry of N_2H_4, and the potential effects of blowby gases on the process, is needed.

Actuating a pyrovalve is known to introduce combustion products from the valve into the fuel line. Although the valves are designed to minimize the contamination of the fuel system, some gases escape the combustion chamber in the valve. These hot gases entering the fuel system will result in both a localized temperature increase in the fuel as well as an alteration of the chemical composition of the fuel or fuel vapors immediately adjacent to the valve. WSTF has designed and produced a pyrovalve simulator connected to instrumentation capable of measuring pressure increases in an evacuated line upon valve cycling, and more importantly, chemical species escaping the confines of the combustion chamber.[15]

The chemical species measured in the blowby gases provided a starting point for a chemical kinetic analysis of possible chemically, rather than thermally, initiated local decomposition near the pyrovalve that could ultimately result in a thermal runaway of the fuel. It is highly likely that both thermal and chemical effects from the interaction of the blowby gases with the fuel resulted in the observed destruction of simulated fuel lines. The importance of understanding the chemistry of N_2H_4 decomposition must not be forgotten while focusing on the interaction of blowby gases and hydrazine; interactions between the blowby gases and hydrazine will be a very localized phenomenon near the pyrovalve. Propagation of fuel decomposition will result from the chemistry of the fuel itself, combined with various physical factors within the fuel system.

EXPERIMENTAL

The decomposition mechanism developed last summer was further updated in February of 2000 by the addition of a chemical species and its associated reactions overlooked in the earlier mechanism. A revision of some of the rate expressions in the first version of the mechanism was also completed. This fully updated mechanism for the N/H system was used in modeling the interactions of hydrazine and hydrogen gas. The majority of the rate expressions were obtained from Ref. 16 or primary references therein. This mechanism comprises 12 species interacting in a network of 51 elementary reactions (not counting duplicates); it was validated during the 1999-2000 academic year. Although a fair number of experimental studies have been published in the open literature, the amount of reliable thermal decomposition data available for mechanism validation is rather limited. Nonetheless, the mechanism proved to be quite accurate at modeling the decomposition process of hydrazine in a diluent gas in the temperature regime typical of shock-tube studies.[17]

The mechanism used for the modeling work completed this summer is presented in Table 1. Due to space considerations, the larger, more inclusive mechanism for all blowby species will not be presented in this report.

Table 1. N/H Mechanism for Hydrazine Decomposition

Reactions Considered		k = A T**b exp(-E/RT))		
		A	b	E
1. NH2+NH2=N2H4		3.200E+49	-11.18	13988.0
2. N2H3=HNNH+H		1.800E+45	-9.39	70141.0
3. HNNH=NNH+H		3.100E+41	-8.42	76102.0
Declared duplicate reaction...				
4. HNNH=NNH+H		1.300E+44	-9.22	77096.0
Declared duplicate reaction...				
5. HNNH=H2NN		1.300E+45	-10.13	77096.0
6. H2NN=NNH+H		5.100E+33	-6.52	54245.0
Declared duplicate reaction...				
7. H2NN=NNH+H		5.000E+36	-7.43	57226.0
Declared duplicate reaction...				
8. NNH=N2+H		3.000E+08	0.00	0.0
Declared duplicate reaction...				
9. NNH+M=N2+H+M		1.000E+13	0.50	3080.0
Declared duplicate reaction...				
10. NH3+M=NH2+H+M		2.200E+16	0.00	93470.0
N2 Enhanced by	1.500E+00			
11. NH2+M=NH+H+M		1.200E+15	0.00	76004.0
N2 Enhanced by	1.500E+00			
12. NH+M=N+H+M		2.650E+14	0.00	75510.0
N2 Enhanced by	1.500E+00			
13. N2H4+H=N2H3+H2		9.600E+08	1.50	4838.0
14. N2H4+H=NH2+NH3		4.460E+09	0.00	3100.0
15. N2H4=H2NN+H2		2.500E+39	-8.19	69744.0
16. NH2+NH2=N2H3+H		1.200E+12	-0.03	10084.0
17. N2H3+H=NH+NH3		1.000E+11	0.00	0.0

18. HNNH+H=NNH+H2	4.800E+08	1.50	1579.7
19. NNH+H=N2+H2	2.400E+08	1.50	-894.0
20. NH3+H=NH2+H2	5.420E+05	2.40	9917.0
21. NH2+H=NH+H2	4.800E+08	1.50	7938.0
22. N+H2=NH+H	1.600E+14	0.00	25140.0
23. N2H4+NH=NH2+N2H3	1.000E+12	0.50	1987.0
24. HNNH+NH=NNH+NH2	2.400E+06	2.00	-1192.0
25. H2NN+NH2=NH3+NNH	1.800E+06	1.94	-1153.0
26. NNH+NH=N2+NH2	5.000E+13	0.00	0.0
27. NH+NH=NH2+N	1.990E+11	0.50	1987.0
28. NH+NH=NNH+H	7.940E+12	0.50	994.0
29. N2H4+NH2=N2H3+NH3	3.700E+06	1.94	1629.0
30. N2H3+NH2=HNNH+NH3	9.200E+05	1.94	-1152.5
31. N2H3+NH2=H2NN+NH3	3.000E+13	0.00	0.0
32. HNNH+NH2=NNH+NH3	1.800E+06	1.94	-1152.5
33. HNNH+NH2=NH+N2H3	1.000E+11	0.50	33779.0
34. NNH+NH2=N2+NH3	9.200E+05	1.94	1152.0
35. NH3+NH2=N2H3+H2	7.940E+11	0.50	2146.0
36. NH2+NH2=NH+NH3	9.200E+05	1.94	2444.0
37. NH2+NH=HNNH+H	1.500E+15	-0.50	0.0
38. NH2+N=N2+H+H	7.200E+13	0.00	0.0
39. N2H4+HNNH=N2H3+N2	2.510E+10	0.50	9935.0
40. HNNH+N2H3=N2H4+NNH	1.000E+13	0.00	9935.0
41. HNNH+HNNH=NNH+N2H3	1.000E+13	0.00	9935.0
42. NNH+NNH=HNNH+N2	1.000E+13	0.00	9935.0
43. NH+N=N2+H	1.500E+13	0.00	0.0
44. NNH+N=NH+N2	3.160E+13	0.00	1987.0
45. NH+NH=N2+H+H	5.100E+13	0.00	0.0
46. N2+M=N+N+M	3.710E+21	-1.60	225000.0
47. H+H+M=H2+M	1.000E+18	-1.00	0.0
48. 2H+H2=2H2	9.200E+16	-0.60	0.0
49. N2H3+N=NH+HNNH	1.000E+13	0.00	2000.0
50. N2H4+N=N2H3+NH	1.000E+13	0.00	4000.0
51. N2H3+N=NH+H2NN	1.000E+13	0.00	2000.0
52. N2H3+H=H2NN+H2	2.400E+08	1.50	0.0
53. N2H3+H=HNNH+H2	2.400E+08	1.50	0.0
54. H2NN+H=H2+NNH	4.800E+08	1.50	-894.0

Computations were performed using the same computer software and hardware that was utilized last summer.[18] An additional computer program for producing pathway diagrams was also used.[19] The reader is directed to contact the authors of the pathways analysis code directly for obtaining the software.

Discussions with personnel at WSTF resulted in enough information to begin computations to predict the results of blowby gases entering a mixed-phase hydrazine fuel system. Any thermal runaway of the liquid hydrazine present in a fuel line is almost certainly initiated in the gas phase of a mixed phase system. As a result, only gas-phase reactions were considered in this study.

The typical constituents of blowby gases as described in a pyrovalve handbook currently being written at WSTF[20] were used as initial reagents, along with hydrazine, for this project. Although the molar ratio of the blowby gases to fuel vapor present in the line is unknown, an attempt was made to ascertain reasonable initial conditions for homogenous gas-phase chemical kinetics modeling. Due to the fact that the blowby gases measured indicate a very high percentage of hydrogen in the gas, a 1:1 ratio of H_2 to N_2H_4 was used as a starting point to begin examining the effect of blowby gases on the rate of hydrazine decomposition. This ratio was chosen because the presence of a stoichiometric amount of H_2 can change the exothermicity and products of hydrazine decomposition by shifting the overall decomposition of hydrazine from R1 or R2 to R3, below.

$$N_2H_4 + H_2 \rightarrow 2\ NH_3 \qquad \Delta H_r = -187.2\ \text{kJ/mol}\ N_2H_4 \qquad \text{(R3)}$$

Several assumptions were made in carrying out this research. As mentioned above, a 1:1 stoichiometry of hydrogen to hydrazine was assumed. Additionally, to begin calculations, some thought was given as to what gas-phase species would be present near the valve at actuation. The ullage gas used in the fuel systems is helium, and it is prudent to assume if bubbles form in the fuel line, they will consist principally of helium saturated with hydrazine. At the equilibrium fuel temperature measured in an experiment prior to a destructive event initiated by a pyrovalve, the vapor pressure of hydrazine relative to the total pressure in the system (80 p.s.i.) would result in helium bubbles containing slightly under 3% hydrazine. The equilibrium fuel temperature in this experiment was below the temperature range in which several of the most important reactions in the decomposition mechanism are known. As a result, the baseline temperature decided upon for the calculations was 600 K, roughly 300 K higher than the measured temperature in the experiment cited. The rate expression for the initiation reaction for hydrazine decomposition (without the presence of blowby gases, which can change the initiation step for the mechanism) is known with a fair degree of certainty at this temperature. Three percent hydrazine in an inert bath gas at 600 K and 10 atm. was used as the baseline case.

Unfortunately, many of the key reactions in the decomposition of hydrazine are in fall-off in this temperature and pressure region, and their rate expressions have only been calculated in an N_2 bath gas. Extrapolating beyond the temperature and/or pressure region of a reaction exhibiting fall-off behavior is inadvisable, as is making assumptions as to the collider efficiency of various bath gases in a fall-off region. Due to these considerations, all calculations were performed with N_2 as the bath gas. To more properly model the behavior of the system in He will require QRRK calculations to determine the rate expressions in He bath gas for the reactions in fall-off. It should be noted that performing the modeling in N_2, rather than He, should result in a lower overall temperature rise, as well as a shallower slope in the temperature curve than what would result in He, due to N_2's greater heat capacity.

RESULTS

Decomposition With and Without Molecular Hydrogen Initially Present

The results of calculations of the decomposition of 3% N_2H_4 in N_2 at 600 K and 10 atm. indicate the compound is extremely stable at that temperature and pressure. Traditionally, the homogenous gas-phase chemical kinetic codes utilized are used to evaluate situations involving relatively rapid reactions, so the absolute value of the half-life of hydrazine at the conditions stated is somewhat questionable. Nevertheless, the calculated half-life of hydrazine at the baseline conditions was on the order of 10^6 seconds. Essentially, it is infinitely stable. The decay curve for hydrazine is shown in Figure 1.

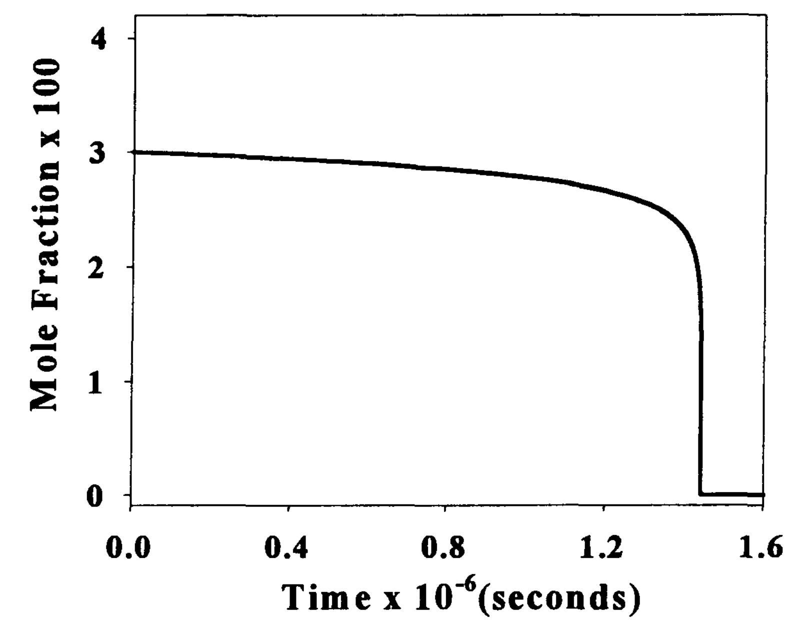

Figure 1. Hydrazine Mole Fraction vs. Time for the Thermal Decomposition of Hydrazine at 600 K, 10 atm, N_2 bath gas, 3% Hydrazine.

As seen in the figure, the hydrazine concentration remains fairly stable for a long period of time, then enters a period of rapid decrease. This induction period is indicative of a very gradual build up of reactive radicals in the gas mixture, until some critical concentration is reached, enabling a rapid decomposition of hydrazine, with concomitant rapid increase in heat release rate and temperature. A similar decay curve results from the decomposition of hydrazine in a 1:1 mixture of hydrazine and hydrogen gas, with a very substantial and prominent difference in the half-life of hydrazine. For both of these scenarios, the initiation step of the decomposition remains the same: the breakage of the N-N bond in hydrazine. What is of particular interest, and somewhat surprising, is the extent to which molecular hydrogen in the initial mixture accelerates the decomposition of hydrazine. The change in hydrazine half-life from the baseline case (i.e., no H_2 initially present) to the case where a 1:1 H_2:N_2H_4 starting ratio exists is *five orders of magnitude*.

The first solid symbols in Figure 2 represent the values obtained with molecular hydrogen as a reagent. All data in Figure 2 was calculated assuming a 1:1 H_2:N_2H_4 ratio at 600 K and 10 atm. The dramatic change in the thermal stability of hydrazine in the presence of molecular hydrogen is extremely important. The finding must be considered in the context of the possibility of a thermal runaway situation. Hydrogen gas is a final product of N_2H_4 decomposition as shown in R1 and R2; its presence as a reagent dramatically increases the rate of hydrazine decomposition. In practical terms, the meaning of this feature of hydrazine chemistry is clear: once started, the thermal decomposition of additional hydrazine present in a fuel line would be accelerated by one of the products of that decomposition. Such behavior within a neat chemical system can easily lead to thermal runaway once the process is initiated.

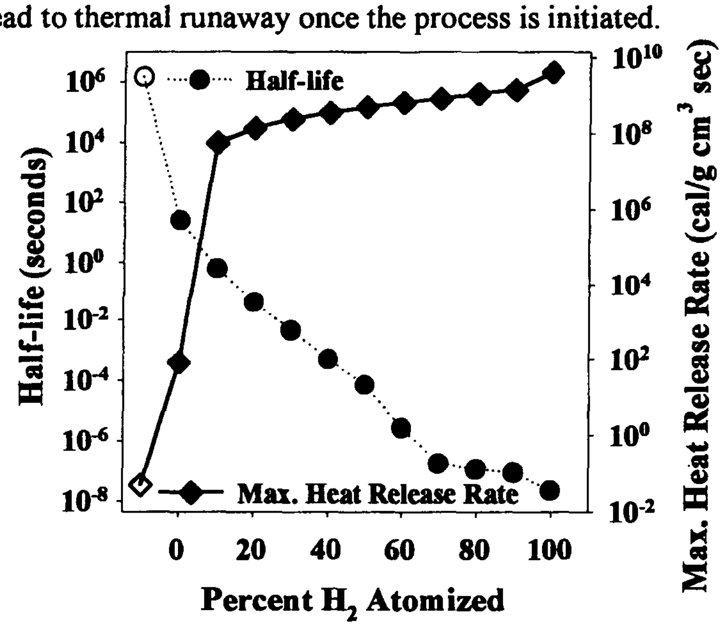

Figure 2. Plot of Hydrazine Half-life and Maximum Heat Release Rate vs. Percent of H_2 Atomized. The hollow symbols represent the values when no H_2 is initially present.

The chemical process by which H_2 gas so profoundly accelerates the destruction of N_2H_4 is primarily due to one elementary step in the mechanism. As stated earlier, without H_2 as a reagent, the reverse of Step #1 in Table 1 initiates decomposition. This N-N bond breakage produces two radicals. At 600 K this reaction is extremely slow. That same reaction is the initiation step for hydrazine decomposition when H_2 is present. However, the reverse of Step #35 in Table 1 is an extremely fast reaction that is both exothermic and chain propagating. Thus, a rapid propagation step is activated in the mechanism early on in the decay process when H_2 is present initially, leading to a more rapid buildup of radicals and subsequently shorter half-life. The NH_2 radicals produced by reversing Step #35 in turn attack hydrazine itself, a propagation step independent of H_2 presence. These differences in behavior can be visualized by examining the pathway diagrams in Figures 3 and 4.

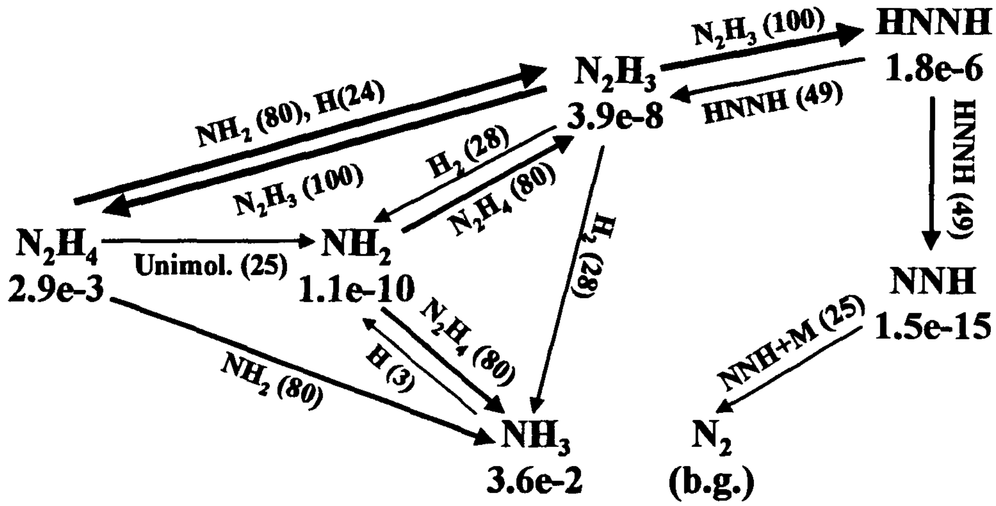

Time at 1.4e6 sec (max. heat release), 100 = 9.4e-9 mol/cm³ sec

Figure 3. Pathway Diagram for N_2H_4 Decomposition at Time of Maximum Heat Release Rate. Initial Conditions of 3% N_2H_4 in N_2, 600 K, 10 atm.

Figure 3 shows the pathway diagram for hydrazine decomposition when H_2 is not an initial reagent. The time at which this diagram is accurate is the time of maximum heat release rate. The values directly underneath the species in the diagram represent the mole fractions of the species at that time. N_2 does not have a numerical value for the concentration because it is the bath gas for all the calculations, hence, its concentration is relatively unimportant. For both Figures 3 and 4, the rates of the various reactions shown are scaled to a value of 100, and the absolute rate of the reaction against which the others are normalized is given.

The pathway diagram presented as Figure 3 has several interesting features. Even at the time of maximum heat release rate, there is a considerable back reaction of N_2H_3 with itself to regenerate hydrazine. The reactions that result in a net destruction of hydrazine at this point in time consist of the reactions of the NH_2 and H radicals with hydrazine. Also of interest is the fact that the formation of two products of decomposition, ammonia and nitrogen, are represented. The nitrogen produced is reached only through one sequence of reactions, while the ammonia is produced via two reactions, one of which directly consumes hydrazine. This diagram is indicative of the overall stoichiometry of R1.

Figure 4 presents the pathway diagram for hydrazine decomposition when an equamolar amount of H_2 is initially present. The chemical pathways leading to the destruction of N_2H_4 are considerably simpler in this case, due to the dominance of the $H_2+N_2H_3=NH_3+NH_2$ reaction and subsequent reaction of the NH_2 radical produced with hydrazine. Also, there are no reactions producing hydrazine present at the time of maximum heat release, which results in a steeper slope in the N_2H_4 concentration curve at that point.

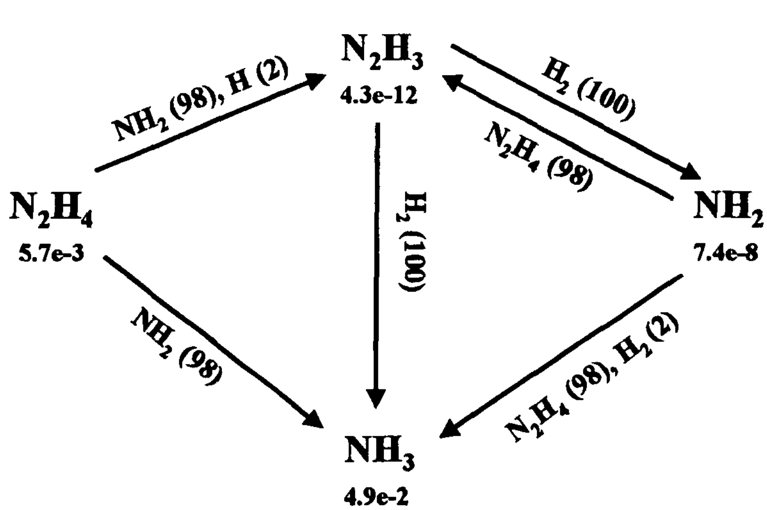

Time at 25.52 sec (max. heat release), 100 = 9.95e-6 mol/cm³ sec

Figure 4. Pathway Diagram for N_2H_4 Decomposition at the Time of Maximum Heat Release Rate. Initial Conditions of 3% N_2H_4 and 3% H_2 in N_2 at 600 K, 10 atm.

The decomposition of hydrazine in the presence of a stoichiometric amount of molecular hydrogen is accomplished through a much "cleaner" process; fewer intermediate species are produced in any significant amount during the decomposition. Additionally, the sequence of reactions leading to the production of N_2 gas under these conditions is suppressed, due to the rapid consumption of N_2H_3 radical by H_2. Because N_2H_3 is quickly destroyed through reaction with molecular hydrogen, the formation of HNNH and subsequent reactions to yield nitrogen are negligible. The overall stoichiometry for this condition is represented by R3.

Decomposition in the Presence of Molecular and Atomic Blowby Species

There is considerable uncertainty about the actual composition of the blowby gas as it reaches the fuel line. This uncertainty arises as a result of the measurement technique currently employed. The residual gas analyzer used to measure the total mass and relative concentrations of the gas-phase species in the blowby is not an instantaneous technique – therefore, only stable species are measured. Any radicals reaching the evacuated simulated fuel line are long since converted to molecular species prior to the time of the actual measurements. Calculations were performed wherein varying amounts of the molecular hydrogen is present as atomic hydrogen in the initial mixture while maintaining the same overall stoichiometry resulting in R3. The results of these calculations are shown in Figure 2, which presents the half-life and maximum heat release rate vs. percent atomization of hydrogen in a 1:1 mixture of H_2:N_2H_4.

Examination of Figure 2 indicates a considerable decrease in the half-life of N_2H_4 and increase in the maximum heat release rate when the initial conditions include 10% of the hydrogen existing as H atom as compared to all the hydrogen existing as the molecular species. This is expected, due to the attack of the H atom on N_2H_4. That reaction generates N_2H_3 radical, which can then rapidly react with the molecular hydrogen present as discussed above. The fact that the half-life curve in Figure 2 shows some tendency toward leveling off as the percentage of hydrogen atomized is increased is due to the reverse of Step #10 in the mechanism. This chain termination step becomes increasingly important as the atomic hydrogen concentration increases, which limits the rate at which the N_2H_4 half-life decreases.

The rate of maximum heat release vs. percentage of molecular hydrogen atomized shows a steady increase after 10% atomization is assumed, as shown in Figure 2. This fact is not surprising, since the reactions of H atom with N_2H_4 are exothermic, and very rapid. Results of calculations for the lower percentages of hydrogen atomization produced heat release rate curves with very steep initial slopes which then level off until a secondary heat release peak occurs. This secondary peak in the heat release rate occurs simultaneously with a sharp drop in the concentration of hydrazine. Above 60% atomization of the hydrogen, this feature of the heat release rate and N_2H_4 concentration curves disappears.

A major concern in conducting this study is the fact that the species that actually contact the fuel or fuel vapor present are, in fact, unknown. It is rather unlikely, but not impossible, that the molecular species measured that have weaker bonds are reaching the fuel as wholly atomized species. Likewise, it is possible, but not likely, that the blowby gases reach the fuel as they are measured, consisting only of molecular species. The probability is quite high that some mixture of molecular and atomic species reaches the fuel, rather than either extreme. Hydrogen gas is known to heat up when forced through a small orifice in going from a region of higher pressure to one of lower pressure at most temperatures, due to its Joule-Thompson coefficient.[21] This process alone could produce some atomic hydrogen in the mixture of combustion products that reaches the fuel.

Representative calculations using the inclusive mechanism and all the gaseous species measured in the blowby gas were performed. Three conditions were used: the first with the assumption that the blowby gases exist only as molecular species, the second with the assumption that 10% of the species likely to be atomized (based on bond energies) reach the fuel in the atomic state, and thirdly, that 50% of the species likely to atomize will have done so at the time of contact with the gas-phase hydrazine. A 1:1 H_2:N_2H_4 stoichiometry was maintained for all three cases, with the concentrations of the other blowby species scaled according to their mole fractions as measured.

The results of the calculations of all three cases indicate that the other blowby species contribute little to the acceleration of hydrazine decomposition. In the first case (no atomization), the decrease in N_2H_4 half-life was slightly less than that seen from assuming the blowby gas was pure H_2. Both cases of atomization resulted in slight increases in the accelerating effect on the decomposition of hydrazine. However, the changes in N_2H_4 half-life as calculated with pure H_2 added vs. all blowby species included as compared to the pure N_2H_4 in an inert bath gas were minor.

CONCLUSIONS

Hydrazine is resistant to thermal decomposition at low temperature (600 K) due to the slow rate of the initiation reaction. The calculations performed for this study, however, indicate that a readily accessible means of decomposition initiation exists under conditions likely to occur in a fuel line due to blowby from pyrovalves. Equally important, the research revealed a chemical mechanism for propagation of hydrazine decomposition throughout a fuel line due to the accelerating effects of molecular hydrogen, which is a decomposition product, on the decomposition process itself. This aspect of hydrazine decomposition chemistry has not been previously noted in the literature. Although physical processes would have effects and must be considered in any thermal runaway scenario, the chemistry of hydrazine itself would play a key role in such an event.

The results of this investigation into hydrazine chemistry raises some technical issues that need to be addressed to fully understand the conditions under which a destructive decomposition of N_2H_4 can occur in "real life" situations. Clearly, the rate expressions for key fall-off reactions need to be revised to more accurately reflect conditions in spacecraft fuel lines, i.e., QRRK calculations should be performed to get smooth-fit pressure dependent rate expressions in He.

Another deficiency with the current chemical mechanism relating to the rate expressions for the fall-off reactions is their lack of pressure dependency as used. The reference from which those expressions were taken did not include true fall-off forms, rather, the published expressions used were presented for three constant pressure cases. Therefore, the rate coefficients for the reactions in fall-off are not entirely valid as the decomposition proceeds and the pressure of the system changes. The rate expressions used in this work were those which most closely corresponded to what is presumed to exist in the simulated fuel line in the experiments cited earlier.

Ideally, experimental work to validate the effect of molecular hydrogen on N_2H_4 decomposition should be performed. Experiments involving a multiphase hydrazine system with the inclusion of H_2 into the initial mixture should be completed. Accelerating Rate Calorimetry (ARC) would be a particularly useful technique for such a study. Liquid hydrazine could be placed into a bomb, with a small amount of He above the liquid, thus generating a multiphase system. Data could then be taken as the system is gradually heated until thermal runaway begins. The experiment could then be repeated with hydrogen gas added to the He in an amount close to 1:1 stoichiometry with the known vapor pressure of hydrazine at the initial temperature. The time/temperature at which thermal runaway starts for the two conditions could then be established, and any differences observed could provide some experimental validation of the results of this work. Although ARC does not give direct information about the concentrations of species as decomposition proceeds, the gross properties of the system itself that are measured in this type of experiment, and any changes resulting from the addition of molecular H_2, could provide valuable information.

Additional experimental studies to validate the computational results obtained using the current chemical kinetic mechanism should be performed via shock-tube or high-temperature photochemistry (HTP) research of hydrazine decomposition, and hydrazine/hydrogen mixture behavior. Shock-tube work is generally limited to fairly high temperatures (usually exceeding 1500 K), but it would be useful to quantitate the decomposition behavior under those conditions as a check on the ability of the mechanism to predict hydrazine decomposition rates in a variety of conditions. HTP studies can be run at considerably lower temperatures, and can include the ability to generate radical species (such as H atom) in situ to ascertain their effects on hydrazine decomposition.

The determination of the amount and composition of blowby gases as performed with the current experimental apparatus at WSTF has proven useful in this research. More rapid determination of the composition of the gases that provided real-time values as the blowby gases escape the combustion chamber of the valve would be invaluable for the purposes of input into a chemical model. It should be noted that experiments providing real time measurements of blowby gases would undoubtedly prove to be extremely challenging due to the exceptionally short duration of the events being measured, and the need to measure multiple transient species simultaneously. Other system measurements that would prove helpful in further development of this modeling effort could include studies of He solubility in hydrazine over a wide temperature range, and a window in a simulated fuel line to observe any bubbles that form prior to, or after, firing a pyrovalve so as to obtain a reasonably reliable measure of the relationship of blowby mass to fuel vapors adjacent to the valve.

A complete, detailed computational model of the initiation and propagation of the destructive decomposition of hydrazine in a spacecraft fuel line has not yet been developed. However, it may be possible to devise a less-sophisticated model that could be utilized in determining the maximum amount of blowby that could safely be introduced into a fuel system for different temperatures. Such a model would have to include heat transfer effects, and the safe upper limit for the amount of blowby would likely be established by looking at the heat release rate and total heat release calculated from the chemical kinetics and their relationship to overall heat transfer within the system. Undoubtedly, there is some lower limit to blowby mass that will result in a locally quenched reaction, rather than an uncontrolled decomposition of the fuel, and modeling may be a method for determining that limit within a reasonable margin of error.

The modeling work that was carried out this summer provides some clues as to what contributed to the destruction of a simulated fuel line observed in WSTF experiments. Chemical kinetics modeling provides insight into the detailed chemistry underlying the behavior of very complex physical and chemical systems. Although this work was specific to a particular situation, the techniques can be applied to other fuels, and/or other blowby species produced by different pyrotechnic materials as a means of screening for unanticipated hazards due to the chemistry unique to a given system.

REFERENCES

1. Birse, E. A. B.; Melville, H. W. *Proc Roy. Soc. (London)* **1940**, *A175*, 164.
2. Shiavello, M.; Volpi, G. G. *J. Chem. Phys.* **1962**, *37*, 1510.
3. Moberly, W. H. *J. Phys. Chem.* **1962**, *66*, 366.
4. Diesen, R. W. *J. Chem. Phys.* **1963**, *39*, 2121.
5. Husain, D.; Norrish, R. G. W. *Proc. Roy. Soc. (London)* **1963**, *A273*, 145.
6. Gray, P.; Lee, J. C.; Spencer, M. *Combust. Flame* **1963**, *7*, 315.
7. McHale, E. T.; Knox, B. E.; Palmer, H. B. *Tenth Symposium (Int.) on Combustion* (The Combustion Institute), **1965**, 345.
8. Michel, K. W.; Wagner, H. Gg. *Tenth Symposium (Int.) on Combustion* (The Combustion Insitute), **1965**, 353.
9. Eberstein, I. J.; Glassman, I. *Tenth Syposium (Int.) on Combustion* (The Combustion Institute), **1965**, 353.
10. Halat-Augier, C.; Dupre, G.; Paillard, C. E. *Proceedings of the 20th International Symposium on Shock Waves* (World Scientific Publishing Company), **1996**, *Vol. II*, 893.
11. NASA Headquarters. *Report of the Mars Observer Mission Failure Investigation Board.* Washington, D. C.; December 31, 1993.
12. Saulsberry, R.; Julien, H. L.; Liming, S; Maes, M. *33rd AIAA/ASME/SAE/ASEE Joint Propulsion Conference and Exhibit*, AIAA 97-3102, Seattle, WA, July 6-9, 1997.
13. Saulsberry, R.; Julien H. L.; Liming, S.; Maes, M. *34th AIAA/ASME/SAE/ASEE Joint Propulsion Conference and Exhibit*, AIAA 98-3916, Cleveland, OH, July 13-15, 1998.
14. Saulsberry, R.; Ramirez, J; Hart, M.; Julien, H; Smith, W. *35th AIAA/ASME/SAE/ASEE Joint Propulsion Conference and Exhibit*, AIAA 99-2305, Los Angeles, CA, June 20-23, 1999.
15. Saulsberry, R.; Ramirez, J.; Bement, L.; Julien, H. L.; Hart, M.; Smith, W.; Meagher, N. E. *36th AIAA/ASME/SAE/ASEE Joint Propulsion Conference and Exhibit*, AIAA 2000-3514, Huntsville, AL, July 16-19, 2000.
16. Dean, A. M.; Bozzelli, J. W. in Gas-Phase Combustion Chemistry, Gardiner, W. C., Jr. ed., Springer-Verlag New York, Inc., **2000**, Chap. 2.
17. Meagher, N. E.; Bates, K. R.; Hart, M.; Smith, S. G. *To be published.*

18. Meagher, N. E. *A Detailed Chemical Kinetic Mechanism of Hydrazine Decomposition*, Final Report NASA/ASEE Summer Faculty Fellowship Program, Johnson Space Center White Sands Test Facility, August 1999.

19. Anderson, R. J.; Anderson, W. R. *Elemap: An Interactive, Portable, JAVA Computer Code for the Rapid Visualization of Chemical Pathways Diagrams Related to Complex Chemical Kinetic Code Outputs*, U.S. Army Research Laboratory, developed 1999-2000.

20. Julien, H. L. *private communication.*

21. Zemansky, M. W. *Heat and Thermodynamics*, Fourth Edition, McGraw-Hill Book Company, Inc. 1957, Chap. 14.

REPORT DOCUMENTATION PAGE

Form Approved
OMB No. 0704-0188

1. REPORT DATE *(DD-MM-YYYY)*
01-03-2003

2. REPORT TYPE
Contractor Report

3. DATES COVERED *(From - To)*

4. TITLE AND SUBTITLE
National Aeronautics and Space Administration (NASA)/American Society of Engineering Education (ASEE) Summer Faculty Fellowship Program - 2000

5a. CONTRACT NUMBER

5b. GRANT NUMBER
NAG9-867

5c. PROGRAM ELEMENT NUMBER

6. AUTHOR(S)
Richard B. Bannerot (University of Houston) and Donn G. Sickorez (JSC), Editors

5d. PROJECT NUMBER

5e. TASK NUMBER

5f. WORK UNIT NUMBER

7. PERFORMING ORGANIZATION NAME(S) AND ADDRESS(ES)
Lyndon B. Johnson Space Center
Houston, Texas 77058

8. PERFORMING ORGANIZATION REPORT NUMBER

9. SPONSORING/MONITORING AGENCY NAME(S) AND ADDRESS(ES)
National Aeronautics and Space Administration
Washington, DC 20546-001

10. SPONSORING/MONITOR'S ACRONYM(S)
NASA

11. SPONSORING/MONITORING REPORT NUMBER
CR-2003-208934

12. DISTRIBUTION/AVAILABILITY STATEMENT
Available from the NASA Center for AeroSpace Information (CASI)
7121 Standard
Hanover, MD 21076-1320 subject category: 99

13. SUPPLEMENTARY NOTES

14. ABSTRACT
The 2000 Johnson Space Center (JSC) National Aeronautics and Space Administration (NASA)/American Society for Engineering Education (ASEE) Summer Faculty Fellowship Program was conducted by the University of Houston and JSC. The 10-week program was operated under the auspices of the ASEE. The program at JSC, as well as the programs at other NASA Centers, was funded by the Office of University Affairs, NASA Headquarters, Washington, D.C. The objectives of the program, which began in 1965 at JSC and 1964 nationally, are to (1) further the professional knowledge of qualified engineering and science faculty, (2) stimulate an exchange of ideas between participants and NASA, (3) enrich and refresh the research and teaching activities of participants' institutions, and (4) contribute to the research objectives of the NASA Centers. Each faculty fellow spent at least 10 weeks at JSC engaged in a research project commensurate with her/his interests and background, and worked in collabroation with a NASA/JSC colleague. This document is a compilation of the final reports on the research projects done by the faculty fellows during the summer of 2000.

15. SUBJECT TERMS
Reports

16. SECURITY CLASSIFICATION OF: a. REPORT	b. ABSTRACT	c. THIS PAGE	17. LIMITATION OF ABSTRACT	18. NUMBER OF PAGES	19b. NAME OF RESPONSIBLE PERSON / 19b. TELEPHONE NUMBER *(Include area code)*
Unclassified	Unclassified	Unclassified	Unlimited	294	